

A COMPUTATIONAL TOOLKIT TO UNDERSTAND ORBITAL OVERLAP AND
CHEMICAL REACTIVITY

by

ARSHAD MEHMOOD

M.Sc. Chemistry, 2009
The Islamia University of Bahawalpur, Pakistan

M.Phil. Physical Chemistry, 2011
The Islamia University of Bahawalpur, Pakistan

Submitted to the Graduate Faculty of the
College of Science and Engineering
Texas Christian University
in partial fulfillment of the requirements
for the degree of

Doctor of Philosophy

December 2020

Acknowledgments

I am grateful to my advisor, Dr. Benjamin G. Janesko, for his support, motivation, and guidance throughout the years of my Ph.D. Your help in my professional development, personal life, and career planning is exemplary. I am deeply indebted to you for your support in official matters, encouraging me to be independent and supporting me in expanding my skills. I have grown greatly as a researcher and person under your guidance. *Thank you for being my mentor and a role model for my future life.*

I am thankful to the members of my committee, Prof. Jeffery L. Coffey, Prof. Sergei V. Dzyuba, and Prof. Jing Kong (Middle Tennessee State University), for their guidance at each step of my Ph.D. I am also thankful to Prof. Eric E. Simanek and Prof. Kayla N. Green for their help and collaborations. I am grateful to Prof. Onofrio Annunziata and Dr. Yulia V. Sevryugina, for their support and encouragement. Many thanks to my colleague, collaborator, and outrageously talented close friend, Dr. Stephanie I. Jones, who helped me and supported me to succeed during the years of my graduate study at TCU. I am thankful to my friends Dr. Alan E. Enciso, Dr. Vishal Sharma, Dr. Akop Yepremyan, and Dr. Adam Montoya. Thank you, Page Kimbrell, for your appreciated help in administrative matters and for being so cheerful about it. I want to thank the TCU College of Science and Engineering for their funding, travel grants, and financial support. I am also thankful to GC University Lahore, Pakistan, for granting me the study leave to complete my Ph.D.

I must express my very profound gratitude to my parents, my sisters, and especially to my brother Maqsood Ahmed. He has always been a significant support to me and encouraged me in all my endeavors.

Finally, a big thanks to my wife, Aisha, for listening to my complaints, excitements, and for her patience. Thank you for completing my life, supporting me through every desperation and every triumph, and going through the journey of Ph.D. together.

Contents

| | |
|-------------------------------------------------------------------|-------------|
| Acknowledgments | ii |
| List of Figures | vi |
| List of Tables | xii |
| List of Abbreviations | xiii |
| Chapter 1 Introduction | 1 |
| 1.1 Interpreting Quantum Chemistry Calculations | 1 |
| 1.2 Orbitals | 5 |
| 1.3 Our Interpretive Tools..... | 6 |
| 1.4 The Chemistry of the Orbital Overlap | 11 |
| 1.5 Specific Objectives and Organization | 13 |
| Chapter 2 Electron Delocalization in Stretched Bonds | 15 |
| 2.1 Background | 15 |
| 2.2 Ground-state Singlet H ₂ | 16 |
| 2.3 van der Waals Interaction: He ₂ | 21 |
| 2.4 Polar Covalent Bond: HF | 24 |
| 2.5 Charge-shift Bond: F ₂ | 27 |
| 2.6 Ionic Interaction: LiH | 30 |
| 2.7 Concluding Remarks | 33 |
| 2.8 Computational Details..... | 34 |
| Chapter 3 Quantifying the Reactivity of Atoms in Molecules | 35 |
| 3.1 Background | 35 |
| 3.2 The Relation Between Q_A and D_A | 37 |
| 3.3 Quantifying the Effects of Substituents..... | 39 |
| 3.4 D_A and Aromaticity | 43 |
| 3.5 Quantifying the Reactivity of Isomers..... | 45 |
| 3.6 Quantifying the Site-dependent Reactivity | 48 |
| 3.7 Quantifying the Angle Strain Effects | 50 |

| | | |
|------------------|-----------------------------------------------------------------|-----------|
| 3.8 | Concluding Remarks..... | 51 |
| 3.9 | Computational Details..... | 51 |
| Chapter 4 | Quantifying Protein-ligand Interactions | 52 |
| 4.1 | Background..... | 52 |
| 4.2 | Combination of ESP and Overlap Distance – An Illustration | 54 |
| 4.3 | Visualizing Protein-ligand Interactions | 55 |
| 4.3.1 | Avidin-Biotin Binding..... | 55 |
| 4.3.2 | Thyroxine-Globulin Binding | 58 |
| 4.4 | Quantifying Protein-metal Interactions..... | 61 |
| 4.4.1 | Gold–GolB Binding..... | 61 |
| 4.4.2 | Selective Binding in Formylglycine-Generating Enzyme | 63 |
| 4.5 | Applications for Structure-based Drug Design..... | 66 |
| 4.5.1 | Promiscuous Binding | 66 |
| 4.5.2 | Designing of CENP-E Inhibitor | 67 |
| 4.6 | Concluding Remarks..... | 70 |
| 4.7 | Computational Details..... | 70 |
| 4.7.1 | Preparation of Systems for MD Simulations..... | 70 |
| 4.7.2 | Initial Energy Minimization | 72 |
| 4.7.3 | MD Simulations | 73 |
| 4.7.4 | Molecular Orbital Calculations and Analysis..... | 74 |
| Chapter 5 | Quantifying Solvent Softness | 75 |
| 5.1 | Background..... | 75 |
| 5.2 | Empirical Solvent Softness Scales..... | 76 |
| 5.3 | Quantifying Softness Using Electronic Structure | 77 |
| 5.4 | Predicting Marcus Softness Scale Using Overlap Distance | 78 |
| 5.5 | Extension to Other Solvent Softness Scales..... | 82 |
| 5.6 | Development of Solvent Versatility Scale..... | 83 |
| 5.7 | Applications to Ionic Liquids..... | 84 |
| 5.8 | Applications to Ionic Liquids/co-solvents..... | 88 |
| 5.9 | Concluding Remarks..... | 89 |
| 5.10 | Computational Details..... | 89 |
| Chapter 6 | Quantifying the Reactivity of Graphene Defects | 91 |
| 6.1 | Background..... | 91 |
| 6.2 | Quantifying the Reactivity of Intrinsic Defects..... | 93 |
| 6.3 | Quantifying the Reactivity of Extrinsic Defects..... | 97 |
| 6.4 | Quantifying the Adsorption of Metal Atoms..... | 99 |
| 6.5 | Concluding Remarks..... | 102 |

| | | |
|-------------------|--------------------------------------------------------------------------------|------------|
| 6.6 | Computational Details..... | 102 |
| Chapter 7 | Visualizing the σ-hole Using Orbital Overlap Distance | 104 |
| 7.1 | Background..... | 104 |
| 7.2 | σ -holes on p-Block Elements | 108 |
| 7.3 | σ -holes on Transition Metal Nanoclusters..... | 113 |
| 7.4 | Quantifying σ -holes Interactions | 118 |
| 7.5 | Concluding Remarks..... | 121 |
| 7.6 | Computational Details..... | 122 |
| Chapter 8 | Assessment, Implications, and Outlook | 123 |
| 8.1 | Discussion | 123 |
| 8.2 | Broader Impacts of the Tools..... | 124 |
| 8.3 | Limitations of the Tools | 125 |
| 8.4 | Future Directions..... | 125 |
| Appendix A | The Electronic Structure Methods | 127 |
| A.1 | Fundamentals | 127 |
| A.2 | The Hartree-Fock (HF) Approximation | 128 |
| A.3 | Correlated Ab Initio Methods..... | 132 |
| A.3.1 | Configuration Interaction (CI)..... | 133 |
| A.3.2 | Møller-Plesset Perturbation Theory..... | 134 |
| A.3.3 | Coupled-Cluster Methods..... | 136 |
| A.4 | Density Functional Theory (DFT) | 137 |
| A.5 | Basis Sets..... | 145 |
| Appendix B | The One-particle Density Matrix | 148 |
| Appendix C | The Atomic Partial Charges | 151 |
| Appendix D | The Electrostatic Potential | 154 |
| Appendix E | The Chemical Softness in Conceptual DFT | 157 |
| Appendix F | Multiwfn Implementations | 158 |
| Appendix G | Supplementary Computational Data | 165 |
| | References | 195 |
| | Vita | |
| | Abstract | |

List of Figures

| | | |
|-----|---------------------------------------------------------------------------------------------------------------------------------------------------------------------------------------------------------------------------------------------------------------------------------------------------------------------------------------------------------------------------------|----|
| 1.1 | ESP surface plot of the XIAP–SMAC binding site. The electrostatics of regions highlighted using white lines is proposed to controls the affinity of ligands..... | 2 |
| 1.2 | Plots of electrostatic potential on electron density isosurface of 0.001 e/bohr ³ for (a) Pristine (b) 2P doped and (c) SW defects of graphene..... | 3 |
| 1.3 | The orbital overlap distance in mercaptoethanol. (a) Optimized gas-phase geometry. (b) Evaluation of $D(\vec{r})$ at two points \vec{r}_1 and \vec{r}_2 near O and S lone pairs, respectively. (c) $D(\vec{r})$ grid obtained for entire molecule plotted across the entire electron density isosurface on 0.001 e/bohr ³ electron density surface..... | 9 |
| 1.4 | (top) Optimized structures and 0.001 e/bohr ³ density isosurface plots of electrostatic potential and overlap distances of three selective Lewis bases. (bottom) The most negative value of ESP on the surface, the largest value of $D(\vec{r})$ on surface and DFT based gas-phase interaction energies with H ⁺ and Au ⁺ for each base..... | 12 |
| 2.1 | H–H bond length of ground-state singlet H ₂ molecule plotted <i>vs.</i> bond dissociation energy ΔE_{bond} (a), The expectation value of KE (b), System-averaged D_{max} (c), System averaged $\overline{\text{EDR}(d)}$ plot of H atom, stretched FCI H ₂ , and stretched H ₂ ⁺ (d)..... | 18 |
| 2.2 | Bond delocalization shift $\overline{\Delta \text{EDR}(\text{H}_2; d)}$ of ground-state singlet H ₂ plotted <i>vs.</i> delocalization distance d and H–H bond length. (a) RHF, (b) UHF, (c) FCI and (d) FCI at minimal basis set calculations..... | 19 |
| 2.3 | Real-space plots of $\text{EDR}(\vec{r}; d = 4.0 \text{ bohr}) = 0.75$ shown using the transparent red surface for H ₂ molecule stretched to bond length of 1.4Å (a) RHF (b) FCI..... | 21 |

| | | |
|------|----------------------------------------------------------------------------------------------------------------------------------------------------------------------------------------------------------------------------------------------------------------------------------------|----|
| 2.4 | He–He bond length of He ₂ molecule plotted <i>vs.</i> bond dissociation energy ΔE_{bond} (a), The expectation value of KE (b) and System-averaged D_{max} (c)..... | 22 |
| 2.5 | CCSD bond delocalization shift, $\overline{\Delta\text{EDR}}(\text{He}_2;d)$ of He ₂ molecule, plotted against length scale d and He–He bond length..... | 23 |
| 2.6 | CCSD EDR($\vec{r};d = 0.8$ bohr) = 0.75 plot shown using the transparent red surface for He ₂ at 2.0 Å bond length..... | 23 |
| 2.7 | H–F bond length of HF molecule plotted <i>vs.</i> bond dissociation energy ΔE_{bond} (a) Expectation value of KE (b) and System-averaged D_{max} (c)..... | 24 |
| 2.8 | Bond delocalization shift $\overline{\Delta\text{EDR}}(\text{HF};d)$ of HF molecule plotted <i>vs.</i> delocalization length d and H–F bond length. (a) RHF, (b) UHF, (c) CCSD..... | 25 |
| 2.9 | Isosurfaces of the RHF EDR($\vec{r};d$) in H–F molecule shown using red surface..... | 26 |
| 2.10 | F–F bond length of F ₂ molecule plotted <i>vs.</i> bond dissociation energy ΔE_{bond} (a), the expectation value of KE (b), and System-averaged D_{max} (c) | 27 |
| 2.11 | Bond delocalization shift $\overline{\Delta\text{EDR}}(\text{F}_2;d)$ of F ₂ molecule, plotted <i>vs.</i> delocalization distance d and F–F bond length. (a) RHF, (b) UHF, (c) CCSD. The dotted line denotes the equilibrium bond length..... | 28 |
| 2.12 | Isosurfaces of the EDR($\vec{r};d$) in F ₂ molecule shown using red surface at two different F–F bond lengths..... | 29 |
| 2.13 | Li–H bond length of LiH molecule plotted <i>vs.</i> bond dissociation energy ΔE_{bond} (a), the expectation value of KE (b), System-averaged D_{max} (c), and Hirshfeld charge on Li atom (d). The vertical dotted line shows the equilibrium bond length..... | 31 |
| 2.14 | CCSD EDR($x;d$) of spin-up electrons in stretched LiH at $R = 2.0\text{Å}$ (a) and at $R = 3.8\text{Å}$ (b)..... | 32 |
| 2.15 | $\overline{\Delta\text{EDR}}(\text{LiH};d)$ of LiH molecule, plotted <i>vs.</i> delocalization distance d , and Li–H bond length. (a) RHF, (b) UHF, (c) CCSD..... | 33 |
| 3.1 | The relation between D_{C} and Q_{C} for molecules used in this study..... | 38 |

| | | |
|------|-------------------------------------------------------------------------------------------------------------------------------------------------------------------------------------------------------------------------------------------------------------------------------------------------------------------------------------------------------|----|
| 3.2 | Partial charge Q_C and overlap distance D_C of the central carbon in $\text{CH}_n\text{R}_{4-n}$, $\text{R} = \text{Me}, \text{F}, \text{Br}$ | 40 |
| 3.3 | Partial charge Q_C and overlap distance D_C of the central carbon in (a) $[\text{CH}_n\text{R}_{3-n}]^-$, $\text{R} = \text{Me}, \text{Br}, \text{CN}$ and (b) $[\text{CH}_n\text{R}_{3-n}]^+$, $\text{R} = \text{F}, \text{Br}, \text{CN}$ | 41 |
| 3.4 | Correlation between experimental Hammett substituent effects at meta and para positions of 30 monosubstituted benzenes..... | 42 |
| 3.5 | Atomic average overlap distance calculated for H atom's 1s (left), 2s (middle), and 2p (right) orbitals. The α -spin orbitals are shown in red and green. The $\text{EDR}(\vec{r}; d)$ test function is shown in blue. The width of the test function which maximizes overlap with orbitals to give D_H is highlighted for each orbital..... | 43 |
| 3.6 | The relation between Q_C and D_C of carbon atoms in aromatic (black dots), nonaromatic (red boxes), and antiaromatic (blue triangles) conjugated molecules..... | 44 |
| 3.7 | The relation between Q_C and D_C of carbon atoms in aromatic (black dots), nonaromatic (red boxes), and antiaromatic (blue triangles) (a) cationic (b) anionic charged conjugated systems..... | 45 |
| 3.8 | The trend in Q_C and D_C of carbon atom in different positional isomers highlighting their relative stability and reactivity..... | 46 |
| 3.9 | Chemical structures and atomic overlap distance of 5-norbornenyl anions isomers..... | 47 |
| 3.10 | (top) Z:E tautomerization of an alkenyl anion intermediate. (bottom) Tautomerization equilibrium constants K_{eq} predicted for anionic intermediate and protonated product..... | 48 |
| 3.11 | Au atom charge <i>vs.</i> overlap distance in 60 cationic gold clusters. Chemically interesting outliers are highlighted..... | 49 |
| 3.12 | Propane's central carbon Q_C (red triangles) and D_C (black circles) plotted <i>vs.</i> C–C–C bond angle..... | 50 |
| 4.1 | Optimized structure and 0.001 e/bohr ³ electron density molecular surfaces of (b) electrostatic potential and (c) overlap distance of deprotonated cysteine..... | 54 |

| | | |
|------|--------------------------------------------------------------------------------------------------------------------------------------------------------------------------------------------------------------------------------------------------------------------------------------------------------------------------------------------------------------------------------------------------------------------------------------------------------------------------------------------------------------------------------------------------------------------------------|----|
| 4.2 | Graphic depictions of biotin molecule inside the binding pocket of streptavidin; (a) molecular geometry, and 0.001 e/bohr ³ electron density molecular surface plots (b) electrostatic potential (c) overlap distance..... | 56 |
| 4.3 | 0.001 e/bohr ³ molecular electron density surface plots of streptavidin binding pocket; (a) electrostatic potential (b) overlap distance..... | 57 |
| 4.4 | Graphic depictions of thyroxine molecule inside the binding pocket of TBG; (a) molecular geometry, and 0.001 e/bohr ³ electron density molecular surface plots (b) electrostatic potential (c) overlap distance..... | 59 |
| 4.5 | 0.001 e/bohr ³ molecular electron density surface plots of TBG binding pocket; (a) electrostatic potential (b) overlap distance..... | 60 |
| 4.6 | 0.001 e/bohr ³ molecular electron density surface plots of GolB binding pocket holding Au ⁺ atom; (a) electrostatic potential (b) overlap distance... | 62 |
| 4.7 | 0.001 e/bohr ³ molecular electron density surface plots of FGE binding pocket; (a) ESP of Cu ⁺ binding pocket, (b) ESP of Ca1 and Ca2 binding pockets, (c) $D(\vec{r})$ of Cu ⁺ binding pocket, and (d) $D(\vec{r})$ of Ca1 and Ca2 binding pockets..... | 64 |
| 4.8 | (a) Optimized geometry and HOMO-1, and 0.001 e/bohr ³ molecular electron density surface plots of (b) ESP, and (c) $D(\vec{r})$ of benzylidene-substituted rhodanine..... | 66 |
| 4.9 | (top) Structures, <i>in vitro</i> CENP-E IC ₅₀ values (in nM), and <i>in vivo</i> HeLa cell proliferation values (in nM) [p-HH3 EC ₅₀ (nM)] of CENP-E inhibitors 6a, 1e, 1j, and 1h and inhibitors A and B proposed here. R ₁ = p-fluorobenzene; R ₂ = m-methyl-p-fluorobenzene; R ₃ = C(=O)N(C ₂ H ₄ NMe ₂)PhCl ₂ . 0.001 e/bohr ³ molecular electron density surface plots of (middle) predicted ESP and (bottom) $D(\vec{r})$ of the fused-ring regions..... | 68 |
| 4.10 | Full chemical structure of the proposed CENP-E inhibitor. R = -O-CF ₃ and R = -F are the new inhibitors based on Fig. 4.9 molecule A and B respectively proposed here..... | 69 |
| 5.1 | Measured Marcus μ parameters plotted <i>vs.</i> computed mean $D(\vec{r})$ (a) and computed global softness $1/\eta$ (b). Important outliers are highlighted..... | 78 |

| | | |
|-----|-------------------------------------------------------------------------------------------------------------------------------------------------------------------------------------------------------------------------------------------------------------------------------------------------------------------------------------|-----|
| 5.2 | (a) Correlation between Marcus's μ -scale and $1/Gap$ and (b) Correlation between $1/Gap$ and mean $D(\vec{r})$ of solvents. The important outliers are highlighted..... | 80 |
| 5.3 | Correlation between Marcus's μ -scale and mean $D(\vec{r})$ (a) and $1/Gap$ (b) of solvents mentioned in Table 2 of Ref. [301]..... | 81 |
| 5.4 | Correlation between mean $D(\vec{r})$ and RMSD $D(\vec{r})$ of solvents elaborating the versatility of solvents..... | 84 |
| 5.5 | Correlation between mean $D(\vec{r})$ and RMSD $D(\vec{r})$ of conventional solvents and ILs elaborating the dissolution versatility..... | 86 |
| 5.6 | Optimized geometries and calculated mean $D(\vec{r})$ and RMSD $D(\vec{r})$ of two 1-butyl-3-methylimidazolium (a) Trans – trans (b) Gauche – trans conformations..... | 87 |
| 6.1 | 0.001 e/bohr ³ density isosurface plots of ESP on left for (a) pristine (c) SW (e) reconstructed V_1 and (g) reconstructed V_2 defects. The right of the figure represents similar density isosurface plots of $D(\vec{r})$ for (b) pristine (d) SW (f) reconstructed V_1 and (h) reconstructed V_2 defects..... | 94 |
| 6.2 | 0.01 e/bohr ³ alpha electron density surface plots of frontier orbital plots (top) HOMO and (bottom) LUMO for optimized geometries of pristine, Stone-Wales (SW), reconstructed single vacancy (V_1) and double vacancy (V_2) defects..... | 95 |
| 6.3 | 0.001 e/bohr ³ density isosurface plots of ESP on left for (a) 2N (c) 2P (e) 2B and (g) 2Si doped graphene. The right of figure represents similar density isosurface plots of $D(\vec{r})$ for (b) 2N (d) 2P (f) 2B and (h) 2Si doping..... | 98 |
| 6.4 | The relation between binding energies of some selected transition metals atoms on V_1 defect and surface $D(\vec{r})$ calculated at 0.001 e/bohr ³ density isosurface..... | 101 |
| 6.5 | Plots of $D(\vec{r})$ on 0.001 e/bohr ³ electron density isosurface for chemisorbed transition metal atoms (a) Co (b) Fe (c) Mn at the V_1 defect site of graphene flakes..... | 102 |

| | | |
|------|-----------------------------------------------------------------------------------------------------------------------------------------------------------------------------------------------------------------------------------------------------------------------------------------|-----|
| 7.1 | Optimized geometry of bromofluoromethane at ω B97-XD/6-311G(d,p) level. (b) Molecular ESP plots on 0.001 e/bohr ³ electron density surface..... | 104 |
| 7.2 | Valence p orbital arrangement on halogen atom in C–X bond. The lobes of p _x orbital are shown using green, p _y orbital using red and p _z orbital using blue colors. Both C and X atoms are represented using black dots..... | 105 |
| 7.3 | σ_p -holes on representative trifluorohalomethanes. (left) molecule structure (middle-right) molecular ESP and $D(\vec{r})$ plotted on the and 0.001 e/bohr ³ electron density isosurface..... | 109 |
| 7.4 | The relation between molecular ESP and $D(\vec{r})$ evaluated on the and 0.001e/bohr ³ electron density isosurface of halomethanes (a) on H atom along the extension of C–H bond and (b) at the center of σ -hole of halogen atom shown in red (<i>italic</i>)..... | 110 |
| 7.5 | σ_p -holes on CFHBr ₂ and CFH ₂ I molecules. (left) molecule structure (middle-right) molecular ESP and $D(\vec{r})$ plotted on the 0.001 e/bohr ³ electron density isosurface..... | 111 |
| 7.6 | σ_p -holes on group IV-VI elements in representative molecules. (left) molecule structure (middle-right) molecular ESP and $D(\vec{r})$ plotted on the and 0.001 e/bohr ³ electron density isosurface..... | 112 |
| 7.7 | Representative examples of σ_s and σ_d on transition metal nano-clusters Au ₂ and Pt ₄ respectively. The left side of the figure shows the gas phase optimized geometry..... | 114 |
| 7.8 | ESP and $D(\vec{r})$ of transition metals Au, Pt, and Ir TM ₈ nanoclusters in O_h and T_d symmetry. The left side of the figure shows the gas phase geometries..... | 115 |
| 7.9 | Surface plots of ESP and $D(\vec{r})$ of Au ₁₃ and Au ₅₅ nanoclusters. The left side of the figure shows the gas phase geometries..... | 117 |
| 7.10 | The relation between reported and predicted binding energies using Eq. 7.3 for F–Cl complexes with CN–R and SiN–R acceptors..... | 120 |

List of Tables

| | | |
|-----|--------------------------------------------------------------------------------------------------------------------------------------------------------------------------------------------------------------------|-----|
| 1.1 | Calculated atomic charge Q_C and atomic overlap distance D_C of carbon atom in representative allotropes..... | 10 |
| 5.1 | Linear fits of experimental Marcus μ parameter to computed $D(\vec{r})$, global softness $1/\eta$ (Eq. E.2), or HOMO-LUMO Gap (Eq. E.3). Fits are performed for the 34 solvents in Table I of Ref. [301]..... | 79 |
| 5.2 | Linear fits of μ , Ds and DN solvent scales to computed mean $D(\vec{r})$ (bohr), mean ESP and global softness $1/\eta$ (a.u) and electronegativity χ (a.u) of 26 solvents..... | 82 |
| 5.3 | Predicted μ values for selected ionic liquids..... | 85 |
| 5.4 | Predicted μ values for selected ionic liquids and ionic liquids/cosolvents along with mean and RMSD $D(\vec{r})$ (bohr)..... | 88 |
| 6.1 | Hirshfeld charges Q_C (e) and atomic overlap distance D_C (bohr) for selected atoms (labelled in the figure) of defected graphene systems relative to the central carbon atom of pristine graphene..... | 96 |
| 6.2 | Trends in transition metal binding..... | 100 |
| 7.1 | Correlation coefficients and RMS errors in reported and predicted binding energies..... | 120 |

List of Abbreviations

| | |
|-------|---------------------------------------|
| CCSD | Coupled-cluster Singles and Doubles |
| CI | Configuration Interaction |
| DFT | Density Functional Theory |
| DN | Donor Number |
| ELF | Electron Localization Function |
| ESP | Electrostatic Potential |
| FCI | Full Configuration Interaction |
| GGA | Generalized Gradient Approximation |
| GTO | Gaussian-type Orbitals |
| HF | Hartree Fock |
| HOMO | Highest Occupied Molecular Orbital |
| HSAB | Hard and Soft Acids and Bases |
| IL | Ionic Liquid |
| KE | Kinetic Energy |
| LCAO | Linear Combination of Atomic Orbitals |
| LDA | Local Density Approximation |
| LOL | Localized Orbital Locator |
| LUMO | Lowest Unoccupied Molecular Orbital |
| MD | Molecular Dynamics |
| MP | Møller-Plesset |
| NBO | Natural Bond Orbitals |
| NCI | Non-covalent Interaction |
| 1-RDM | One-particle Reduced Density Matrix |
| QTAIM | Quantum Theory of Atoms in Molecules |
| RMSD | Root-mean-square Deviation |
| SAR | Structure-activity Relationship |
| STO | Slater-type Orbitals |
| SW | Stone–Wales |
| VDD | Voronoi Deformation Density |

Chapter 1

Introduction

1.1 Interpreting Quantum Chemistry Calculations

The fundamental objectives of quantum chemistry are to provide the quantum mechanical description of chemical bonding and devise tools to model the molecular structure, properties, thermodynamics, reaction mechanisms, reactivity indices, molecular spectroscopy, and inter- and intramolecular forces, *etc.*¹ The applications of these methods have become a “standard tool” for diverse materials modeling problems in chemistry, physics, materials sciences, and multiple branches of engineering.² Most of the present-day quantum chemical methods ([Appendix A](#)) yield energy-related results approaching chemical accuracy, *i.e.*, with errors less than 2 kcal/mol.³ In addition, quantum chemistry provides means to estimate the fundamental bonding concepts such as delocalization, aromaticity, electrophilicity, nucleophilicity, electronegativity, hard–soft behavior and atomic partial charges, *etc.*, which are difficult to measure empirically but are essential for the prediction and analysis of chemical reactions. Some of the contemporary achievements of quantum chemistry include the rapid screening of reaction model mechanisms in organic and polymer chemistry,^{4, 5} quantification of non-covalent interactions^{6, 7} which leads towards the development of crystal engineering,⁸⁻¹¹ characterization of functional nano-¹² and molecular

materials¹³⁻¹⁵ and structure-based *in silico* screening and development of drugs¹⁶ such as 5-HT_{1B/1D} receptor agonist Zolmitriptan, angiotensin II receptor antagonist Losartan and development of DNA intercalating DNMTs inhibitors.¹⁷⁻¹⁹

Among various molecular and atomic descriptors obtained from electronic structure methods, electrostatic potential (ESP) (Appendix D) and partial atomic charges (Q_A) (Appendix C) are fundamental quantities used to predict and interpret the chemical reactivity of molecules, solids, surfaces, and nanoparticles.²⁰⁻²² Computational methodologies such as molecular dynamics simulations and molecular docking largely depend on these computed properties. The ESP molecular surface plots of proteins and ligands and their complementarity establish the basis of drug discovery and are critically important to design ligands with optimal affinity and selectivity.²³ As an illustration, Fig. 1.1 shows the protein

ESP surface plot for the apoptosis protein SMAC active site, which was exploited recently to design the highly potent X-linked inhibitors of apoptosis protein (XIAP).^{24, 25} XIAPs have been proposed as targets for anticancer therapy, and some of these inhibitors have been entered in clinical trials.²⁵ Optimization of the protein-ligand ESP complementarity by controlling the electrostatics of the indoline ring with electron-donating or withdrawing R-substituents allowed to significantly increase the XIAPs binding affinities.^{24, 25}

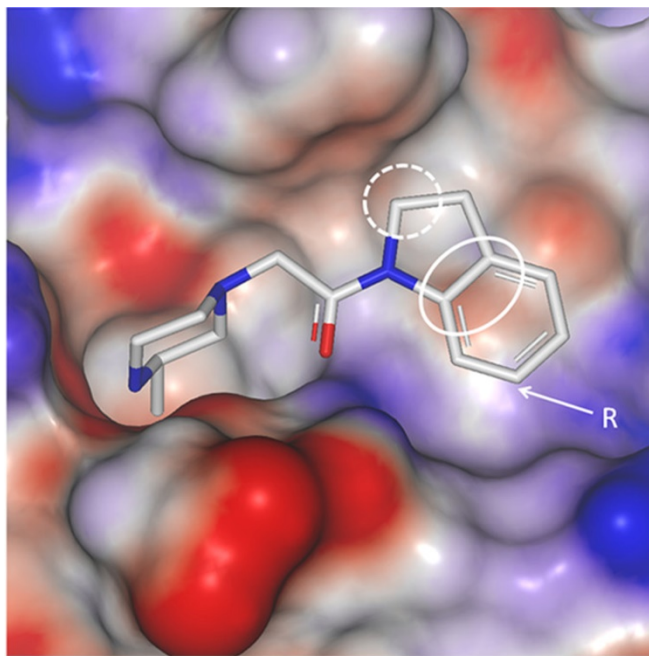


Figure 1.1 ESP surface plot of the XIAP–SMAC binding site. The electrostatics of regions highlighted using white lines is proposed to controls the affinity of ligands. Image is adopted from Ref. [24].

However, there are many systems where the partial charge or ESP alone gives an incomplete picture of reactivity. For example, PhS^- is a much better nucleophile compared to PhO^- in $\text{S}_{\text{N}}2$ reactions with MeI , though PhO^- has a more negative charge on the nucleophilic atom.²⁶ Deprotonated amides perform nucleophilic attack via the less negative nitrogen, rather than the more negative oxygen in the base-catalyzed anionic cyclization of *o*-alkynyl benzamides.^{27, 28} Halides F^- , Cl^- , Br^- , and I^- have identical charges but different nucleophilicities. Many nucleophiles attack α,β -unsaturated ketones at the softer β carbon, not at the more positively charged carbonyl carbon.^{29, 30} Allotropes such as diamond, graphene, and C_{60} have identical partial atomic charges of zero, but different heats of formation. Carbon atoms in aromatic benzene and anti-aromatic cyclobutadiene have nearly identical partial charges but very different reactivities. Close-packed surfaces of different transition metals have partial atomic charges near zero but very different chemisorption behaviors.³¹ Adsorbates such as oxygen atoms can have nearly identical charges, but very different adsorption energies on different transition metals surfaces.³²

As illustrated in Fig 1.2, the variations in surface ESP of graphene with Stone-Wales (SW) intrinsic defects are small relative to the graphene with extrinsic defects (e.g., P doping). The surface ESP cannot effectively distinguish the variations in the reactivity of different carbon atoms on the surface of the SW defects relative to the underlying pristine

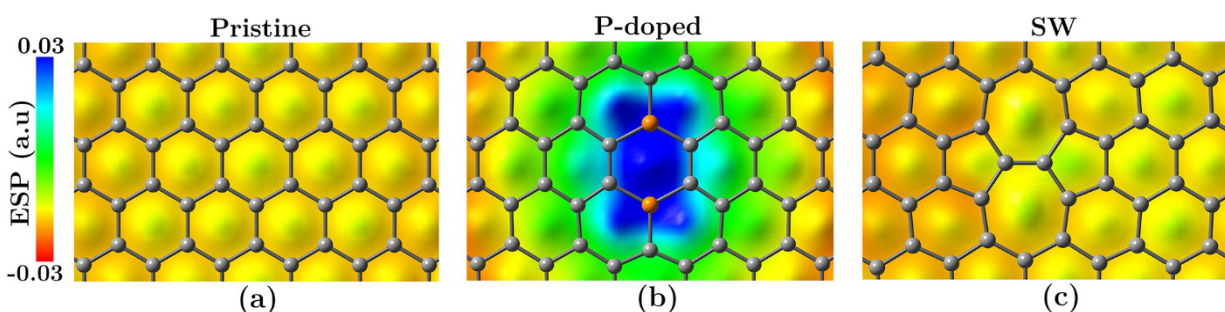


Figure 1.2 Plots of electrostatic potential on electron density isosurface of 0.001 e/bohr^3 for (a) Pristine (b) 2P doped and (c) SW defects of graphene. Electrostatic potential itself cannot effectively distinguish the reactivity of individual atom at the SW defect site.

graphene. However, previous studies have demonstrated that the carbon atoms at the defect site show markedly different binding energies to H_2OH , H_2OCO , NO , $-\text{H}$, $-\text{F}$, and $-\text{Ph}$ groups.^{33, 34} The pentagons of SW defects are more prone to oxidation, while the octagons prefer reduction and provide favorable sites for radical attacks.³⁵ The dopants such as N and P or B, Al and Si, *etc.*, impart nearly similar electrostatic changes to graphene sheets but Si and P lower the activation energy for Diels-Alder and other cycloaddition reaction. Also, B, N, and S doped graphene undergo [2+2] cycloaddition while Si, P, and Al doped graphene favors [4+2] cycloadditions.³⁶ Similarly, transition metal atoms having the same charge and ionic radius, give another example by showing different coordination chemistries and adsorption behavior with metalloproteins. For example, the ESP alone cannot distinguish the binding affinities of Ca^{2+} and Cu^+ to the formylglycine-generating enzyme.

There have been many efforts to quantify aspects of reactivity missing from partial atomic charges and ESP. Conceptual density functional theory (DFT) ([Appendix E](#)), a branch of DFT which deals with the extraction of chemically relevant concepts and principles from the computational DFT³⁷ provides valuable alternatives such as global hardness³⁸ global softness³⁹, local hardness¹, local softness¹, hardness, and softness kernels,¹ reactivity indices and Fukui functions⁴⁰⁻⁴², *etc.* These descriptors have been extensively applied in areas including organic reactivity⁴³⁻⁴⁶, aromaticity⁴⁷, coordination complexes⁴⁸⁻⁵⁰, surface chemistry⁵¹, biological systems⁵², and so on^{37, 51, 53, 54}. However, previous studies have demonstrated that the chemical hardness calculated using the conceptual DFT based method provides sufficiently accurate results at Hartree Fock (HF) level ([Appendix A](#)).⁵⁵⁻⁵⁷ Beyond HF and at DFT level this method becomes strongly dependent on the basis set and exchange-correlation potential used in DFT calculations.^{37, 58} Also, conceptual DFT quantifies global properties only, and these methods struggle to distinguish the chemistry of different sites on a single molecule.^{37, 59, 60} Local information are usually provided by

coordination numbers⁶¹; atomic radii⁶² and kinetic energies⁶³, the quantum theory of atoms-in-molecules (QTAIM)⁶⁴, local kinetic energies⁶⁵, steric energies⁶⁶, and ionization potentials⁶⁷; *d*-band filling³¹; the electron localization function (ELF)^{68, 69}; and many other tools⁷⁰⁻⁷². However, most of these tools are *arguably* under-utilized by practicing chemists.^{73, 74}

1.2 Orbitals

This dissertation involves developing a new orbital-based toolkit for interpreting electronic structure calculations. Orbitals and orbital overlap are fundamental in chemistry, both conceptually in general and to model the chemical reactions in particular. Orbital overlap in chemical bonds,⁷⁵ frontier orbital interactions,⁴² isolobality,⁷⁶ and charge versus orbital control of reactivity⁷⁷ are central to the chemical theory. For instance, interactions of frontier molecular orbitals form the basis of molecular orbital theory taught in general chemistry courses and at advance level, interacting molecular orbitals establish the foundations of the pericyclic selection or Woodward–Hoffmann rules^{78, 79} applicable to the majority of reactions in organic chemistry⁸⁰ including electrocyclizations, cycloadditions, sigmatropic, group transfer, *ene*-, cheletropic and dyotropic reactions.^{79, 80} These molecular orbital calculations are not limited to organic chemistry but are increasingly important in biological and medicinal chemistry, as illustrated in recent applications to quantitative structure-activity relationships (QSARs),⁸¹ ligand-target interactions,⁸² mechanistic proposals for enzyme catalysis,⁸³ and simulations of entire proteins⁸⁴. However, these classical applications of orbital overlap are limited to the analysis of one orbital at a time, though useful for small systems, but are insufficient to large systems such as large ligands and active sites, nanoclusters, and extended materials like graphene. Instead, medicinal chemists often focus on electrostatic and hydrophobic interactions visualized across a biomolecule’s entire surface.⁸⁵ Materials chemists mainly rely on the calculated energies or

density of states, *etc.*⁸⁶ To overcome these limitations, many orbitals-based descriptors have been developed, such as the aforementioned conceptual DFT based methods or tools like ELF^{68, 69}. However, hampered by the associated difficulties in their learning and interpretations, the applications of these tools have been limited to the theoretical chemists and are unfamiliar to many experimentalists.⁷³ These shortcomings of contemporary interpretative tools of electronic structure calculations motivate for the development of more powerful tools, in a way that are easy to apply and interpret, accessible to experimentalists, and complement the classical concepts of chemistry which can help to make quantum chemistry a more useful for experimentalists.

1.3 Our Interpretive Tools

We develop a descriptor of the electronic structure intended to more effectively bridge the gap between classical analyses of individual orbitals and visualization of chemically intuitive quantities on the surface of the molecule. The Orbital Overlap Distance, $D(\vec{r})$ complements atomic partial charges and ESP, characterizing the hybridization and localization of orbitals as distinct from the polarization of charge. It quantifies whether the occupied orbital lobes around the point \vec{r} are small and compact or large and diffuse.⁸⁷⁻⁹⁰ $D(\vec{r})$ is based on electron delocalization range function, $\text{EDR}(\vec{r}; d)$ built from the nonlocal one-particle density matrix (1-RDM), $\gamma(\vec{r}, \vec{r}')$ described in [Appendix B](#).

The electron delocalization range function, $\text{EDR}(\vec{r}; d)$ is designed to extract information from six variable 1-RDM and complements other 1-RDM based tools by focusing on the distance between points \vec{r} and \vec{r}' in $\gamma(\vec{r}, \vec{r}')$.⁹¹ The $\text{EDR}(\vec{r}; d)$ quantifies the extent to which the molecular orbitals around point \vec{r} overlap with a hydrogen atom's 1s orbital type test function, $g_d(\vec{r}, \vec{r}')$ of width d centered at \vec{r} .⁹²

$$\text{EDR}(\vec{r}'; d) = \int d^3r g_d(\vec{r}, \vec{r}') \gamma(\vec{r}, \vec{r}') \quad (1.1)$$

For Eq. 1.1, $\gamma(\vec{r}, \vec{r}')$ is constructed from all spin-orbitals with nonzero occupancies and,

$$g_d(\vec{r}, \vec{r}') = \rho^{-1/2}(\vec{r}) \left(\frac{2}{\pi d^2} \right)^{3/4} \exp \left(-\frac{|\vec{r} - \vec{r}'|^2}{d^2} \right) \quad (1.2)$$

In Eq. 1.2, factor $(2 / \pi d^2)^{3/4}$ ensures that the value of the $\text{EDR}(\vec{r}; d)$ is bound between -1 and $+1$.⁹⁰ The $g_d(\vec{r}, \vec{r}')$ is unitless while $\gamma(\vec{r}, \vec{r}')$ has units of inverse volume, both of these parameters make $\text{EDR}(\vec{r}; d)$ a unitless function. $\text{EDR}(\vec{r}; d)$ is a four-variable function and cannot be visualized in its entirety. However, different tools can be extracted from it to obtain and visualize the chemically relevant information. The first tool is the “system-averaged delocalization length” defined as:⁹¹

$$D_{\max} = \arg \max_d \overline{\text{EDR}}(d) \quad (1.3)$$

Constructed from density-weighted averages over $\text{EDR}(\vec{r}; d)$:

$$\overline{\text{EDR}}(d) = \int d^3\vec{r} \rho(\vec{r}) \text{EDR}(\vec{r}; d) \quad (1.4)$$

Value of D_{\max} increases if the system’s electrons become diffuse and weakly bound. It is inversely related to the average kinetic energy and will be discussed in the next [chapter](#).

The second tool, $\overline{\Delta\text{EDR}}(AB; d)$, represents the “bond delocalization shift,” which shows how $\overline{\text{EDR}}(d)$ of a molecule differs from its separated atoms, e.g., for a diatomic molecule:

$$\overline{\Delta\text{EDR}}(AB; d) = \overline{\text{EDR}}(d)_{AB} - \overline{\text{EDR}}(d)_A - \overline{\text{EDR}}(d)_B \quad (1.5)$$

Two-dimensional plots of $\overline{\Delta\text{EDR}}(AB; d)$ as a function of delocalization length d (bohr) and bond length R (Å) illustrate the localization of the 1-RDM due to bonding. Compressing

bonds tends to localize electrons, giving a positive $\overline{\Delta\text{EDR}}(AB;d)$ at small distances d , and a negative $\overline{\Delta\text{EDR}}(AB;d)$ at large d . The applications of these tools are also described in the next [chapter](#). The third tool derived from $\text{EDR}(\vec{r};d)$ is the real-space plots of isosurfaces $\text{EDR}(\vec{r};d_{\text{special}})$ evaluated at “special” length scales d_{special} . It represents the real space locations where electrons tend to be localized to distance d_{special} .

The Orbital Overlap Distance, $D(\vec{r})$ is defined as the value of length d that maximizes $\text{EDR}(\vec{r};d)$ at the point the \vec{r} :⁹³

$$D(\vec{r}) = \arg \max_d \text{EDR}(\vec{r};d) \quad (1.6)$$

$D(\vec{r})$ represents the value of test function $g_d(\vec{r},\vec{r}')$ width d that maximizes the test function’s overlap with the occupied orbitals of the molecule. $D(\vec{r})$ is calculated by evaluating $\text{EDR}(\vec{r};d)$ at each point \vec{r} on a grid of different d_i values, then the value of d_i that maximizes $\text{EDR}(\vec{r};d)$ is determined followed by performing a three-point numerical fit about that value. Implementation of these tools to Gaussian 16⁹⁴ and Mutliwfn⁹⁵ (version 3.4 and above, see [Appendix F](#)) allows us to choose the different grids of d_i values and output the grid of $D(\vec{r})$ covering the entire molecule. Surface plots of $D(\vec{r})$ represent the value of $D(\vec{r})$ at the point \vec{r} on the surface of the molecule, following the common practice of plotting electrostatic potentials on the molecular electron or spin density isosurface.⁹⁶ We opt for the commonly used isovalue of 0.001 e/bohr³, which has been established to contain 96% of molecular electronic charge.⁹⁷ These surface plots of $D(\vec{r})$ quantifies whether the electrons at a given point are held by compact and small or diffuse and large orbitals hence distinguish the hard and soft regions on the surface of the molecule and complement the molecular electrostatic potential. [Fig. 1.3](#) shows an illustration of evaluation, analysis, and findings of overlap distance by taking the optimized geometry ([Fig. 1.3\(a\)](#)) of

mercaptoethanol as an example. This molecule contains a compact oxygen atom and a relatively diffuse sulfur atom. Fig. 1.3(b) shows the highest occupied molecular orbitals HOMO and HOMO-1 surfaces represented using green and red transparent colors. The test function $g_d(\vec{r}, \vec{r}')$ (Eq. 1.2) shown as blue spheres is evaluated at two points \vec{r}_1 and \vec{r}_2 near O and S lone pairs, respectively. The test function's overlap with O atom is maximized at relatively small distance $D(\vec{r}_1) = 2.8$ bohr while for S atom this overlap is maximized at relatively large distance $D(\vec{r}_2) = 3.4$ bohr, indicating that electrons in former are held by small and compact orbitals while the electrons of latter are occupying relatively diffuse and large orbitals. Evaluation of $D(\vec{r})$ on entire molecule and using it to color the electron density surface as shown in Fig. 1.3(c) distinguishes the regions of molecule with large overlap distance from those regions which have small value of $D(\vec{r})$. These findings of overlap distance complements the classis concept of chemistry of oxygen being a hard atom and sulfur being a relatively chemically soft.

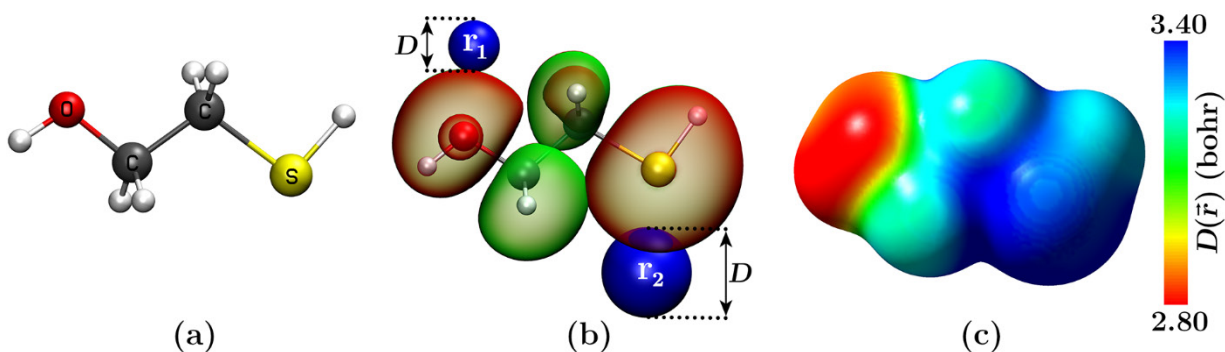


Figure 1.3 The orbital overlap distance in mercaptoethanol. (a) Optimized gas-phase geometry. (b) Evaluation of $D(\vec{r})$ at two points \vec{r}_1 and \vec{r}_2 near O and S lone pairs respectively. Green and red surfaces are representative occupied orbitals HOMO and HOMO-1, plotted on the $|\Psi(\vec{r})|^2 = 0.001$ e/bohr³ surface. Blue surfaces are the test function (Eq. 1.2), plotted at 80% of its maximum value. The overlap of test functions with all occupied MOs is maximized for widths $D(\vec{r}_1) = 2.8$ bohr and $D(\vec{r}_2) = 3.4$ bohr. (c) $D(\vec{r})$ grid obtained for entire molecule plotted across the entire electron density isosurface on 0.001 e/bohr³ electron density surface.

Atom averaged overlap distance D_A is defined as the average overlap length of electrons (N_A) assigned to atom A in the molecule:

$$D_A = \frac{1}{N_A} \int d^3\vec{r} w_A(\vec{r}) \rho(\vec{r}) D(\vec{r}) \quad (1.7)$$

Where $w_A(\vec{r})$ represents the weight assigned to an atom A in the molecule using either the Hirshfeld, Voronoi, Becke, and Hirshfeld-I partitioning schemes. The implementations of these tools in Mutliwfn allow calculating D_A and atomic partial charges Q_A using any of these partitioning methods. D_A distinguishes the relative nature of each atom in the molecule and complements the atomic partial charges. For example, though the isolated carbon atom and its allotropes diamond, graphene, and C_{60} have identical charge of zero, but as shown in [Table 1.1](#), their atom averaged overlap distance, D_C , decrease with the order of $C_{\text{atom}} > C_{60} > \text{graphene} > \text{diamond}$, mirroring the trend in their relative thermodynamic stability and providing information which is not given by the atomic partial charges alone.

The 1-RDM used for the calculations of $\text{EDR}(\vec{r}; d)$ and all of its derived descriptors can be calculated using Hartree–Fock theory, Kohn–Sham DFT, generalized Kohn–Sham DFT, coupled-cluster singles and doubles (CCSD) theory, and complete active space self-consistent field (CASSCF) approaches. The details are given in [Appendix A](#).

Table 1.1 Calculated atomic charge Q_C and atomic overlap distance D_C of carbon atom in representative allotropes.

| Allotrope | Q_C (e) | D_C (bohr) |
|-----------------|-----------|--------------|
| Diamond | 0.00 | 1.54 |
| Graphene | 0.00 | 1.58 |
| C_{60} | 0.00 | 1.60 |
| Isolated C atom | 0.00 | 2.12 |

1.4 The Chemistry of the Orbital Overlap

The combination of molecular surface plots of electrostatic potential and overlap distance and the quantitative analysis of these surfaces provide rich information about the chemistry of small molecules, ions, nanomaterials, protein, enzymes, and low dimensional materials like graphene. The quantitative analysis includes the determination of their surface maxima, minima, average, and root-mean-square deviation (RMSD) values, which can be carried out using Multiwfn implementations. Combining the obtained results of ESP and $D(\vec{r})$ provides classical information about the hard-soft acid-base chemistry. Fig. 1.4 illustrates the power of this combination to rationalize trends in coordination chemistry. The figure shows the electron density isosurface plots of ESP and $D(\vec{r})$ of three small representatives Lewis bases MeO^- , MeS^- , Me^- , and computed gas-phase binding affinities to hard Lewis acid H^+ and soft Lewis acid Ag^+ . The large negative ESP and small $D(\vec{r})$ of MeO^- make it a strong-hard Lewis base while less negative ESP and large $D(\vec{r})$ of MeS^- make it a weak-soft Lewis base. Similarly, moderate negative ESP and very large value of $D(\vec{r})$ for carbanion Me^- show that it is a very soft and very strong Lewis base. The associated table illustrates that the interaction energy of H^+ is higher for MeO^- over MeS^- , indicating its preferred interaction for the former over the latter. Similarly, soft acid Au^+ prefers MeS^- over MeO^- , and both acids prefer strong base Me^- . These findings are consistent with Pearson's hard-soft acid-base principle that acids & bases of comparable strength prefer hard-hard and soft-soft interactions, and with the fact that strong Lewis bases tend to be soft.⁹⁸⁻¹⁰¹

It is important to note that ESP alone cannot capture all of the trends in binding affinities. For example, the surface minimum of ESP follows the order $\text{MeS}^- > \text{Me}^- > \text{MeO}^-$, but the H^+ binding affinities decrease with the order of $\text{Me}^- > \text{MeO}^- > \text{MeS}^-$. $D(\vec{r})$

also captures the coordination chemistry of the Me^- carbanion. The substantial value of $D(\vec{r})$ for the Me^- carbanion is consistent with its ability to share electrons in strong covalent bonds. ESP alone clearly cannot capture the carbanion's reactivity, as MeO^- has an electrostatic potential more negative than Me^- . These findings suggest that $D(\vec{r})$ captures

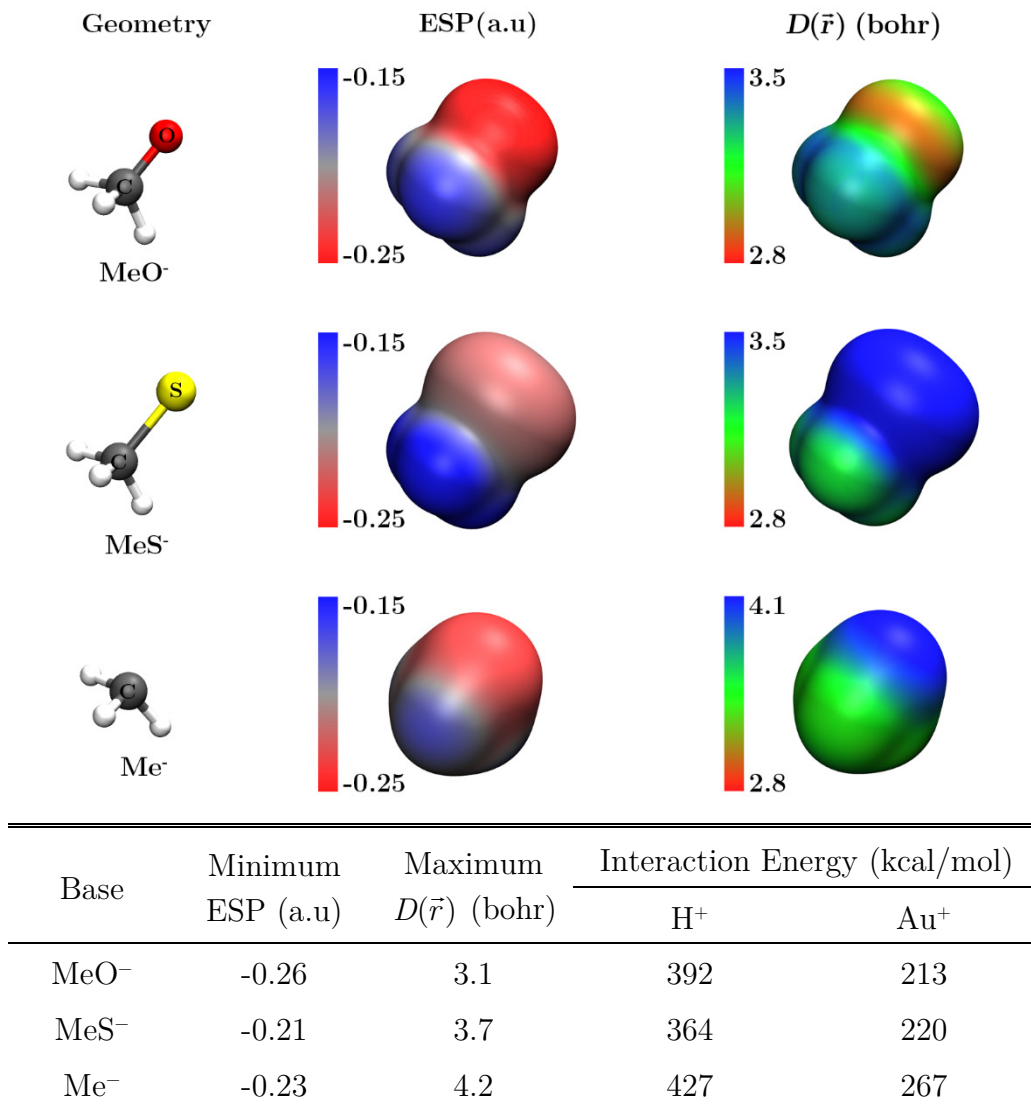


Figure 1.4 (top) Optimized structures and $0.001 \text{ e}/\text{bohr}^3$ density isosurface plots of electrostatic potential and overlap distances of three selective Lewis bases. (bottom) The most negative value of ESP on the surface, the largest value of $D(\vec{r})$ on surface and DFT based gas-phase interaction energies with H^+ and Au^+ for each base.

orbital-dependent aspects of chemical reactivity that are different from and complementary to the aspects captured by electrostatic potentials alone.

1.5 Specific Objectives and Organization

The objectives of the studies mentioned in this dissertation are to implement the $\text{EDR}(\vec{r}; d)$ and its derived tools to open-source package Multiwfn ([Appendix F](#)) and to use these tools primarily orbital overlap distance to capture the trends of reactivities in systems ranging from small molecules to enzymes, proteins, and graphene sheets. The objective of each study and organization of this dissertation are mentioned below.

[Chapter 2](#) describes the applications of $\text{EDR}(\vec{r}; d)$ and its tools to study the stretched and compressed chemical bonds. The objective of this chapter is to quantify the aspects of fractional occupancy and left-right correlation in stretched covalent bonds using these tools. These studies considered the molecules of H_2 , HF, He_2 , F_2 , and LiH, and calculations use Hartree–Fock, DFT, CCSD, and FCI methods.

[Chapter 3](#) presents the applications of atomic averaged overlap distance, D_A , and its combination with atomic partial charges to captures trends in aromaticity, nucleophilicity, allotrope stability, and substituent effects. The objective of this chapter is to distinguish the comparative reactivity of each atom in the molecule and to highlight the effects of substituents on these reactivities. The systems studied in this chapter range from organic molecules and carbon allotropes to gold nanoclusters.

[Chapter 4](#) deals with the application of $D(\vec{r})$ for problems in medicinal chemistry. The combination of $D(\vec{r})$ and ESP surface plots are invoked to distinguish the binding pockets for hard versus soft cations in formylglycine-generating enzyme and other proteins as prototype examples. The applications of this combination are extended to get a novel

and experimentally testable predictions for promiscuous bindings and improving the *in vivo* activity of centromere-associated protein E inhibitors.

Chapter 5 describes the use of $D(\vec{r})$ to model the solvent softness. The objective of this chapter is to use the computed properties of the solvent molecule to reproduce the solvent empirical softness scales, such as the Marcus μ -scale. The softness values modelled using $D(\vec{r})$, are compared with those obtained from conceptual DFT descriptors. The applications of these methods are extended to model the μ -parameters for widely used ionic liquids and ionic liquid–cosolvent systems. This chapter also introduces a “solvent versatility” scale to quantify the solvation power of solvents.

Chapter 6 extends the applications of $D(\vec{r})$ based tools to quantify the reactivity of graphene defects. The objective of this chapter is to distinguish the comparative reactivity of each carbon atom at the defect site of graphene sheets, which are not possible to model using ESP or atomic partial charges alone. Three types of defects are considered in these studies, namely intrinsic (SW and vacancy) defects, extrinsic defects (N, P, B, and Si dopants), and transition metal atoms adsorbed at the sites of the defects.

Chapter 7 presents the modelling of halogen bonding and other sigma(σ)-hole interactions using the combination of molecular surface plots of $D(\vec{r})$ and ESP. The objective of this chapter is to predict the interactions energies of molecules involving σ -hole interactions by using this combination. The applications of these combinations are extended to visualize and rationalize the different types of the σ -holes on the molecules of group IV to VI elements and transition metal nanoclusters.

Finally, the last chapter describes the conclusions, broader impacts, limitations, and future potential of this work.

Chapter 2

Electron Delocalization in Stretched Bonds

2.1 Background

Electron delocalization provides fundamental grounds to understand chemical bonding. The formation of a covalent bond delocalizes the valence electrons between the participating atoms, and bond stretching increases this delocalization. The development of quantum mechanical methods to visualize, quantify, and interpret the aspects of chemical bonding remains a topic of active study. Novel bonding motifs, from sigma aromaticity¹⁰² to σ -hole¹⁰³ and charge-shift¹⁰⁴ bonding, are regularly proposed in the literature. One of the core objectives of new electronic structure approximations is to address the classic problems, including non-dynamical correlation,¹⁰⁵⁻¹⁰⁷ fractional occupancies, and dissociation of odd-electron^{105, 108, 109}, and multiple bonds.^{110, 111}

Several quantum chemical interpretative tools have been developed to elaborate the chemical bonding based on electronic structure calculations and to deduce the useful information from those calculations. These tools can be broadly divided into three categories; the first category includes tools that are computed directly from calculated N-electron wavefunctions. Examples are weights of resonance structures,¹¹² valence bond

theory,¹¹³ block-localized wavefunctions,¹¹⁴ natural bond orbitals,¹¹⁵ sharing indices,¹¹⁶ and adaptive natural density partitioning.¹¹⁷ The tools in the second category are calculated from the electron density, including the quantum theory of atoms in molecules,^{64, 118} inhomogeneity,¹¹⁹ bond ellipticity¹²⁰, and the single exponential decay detector.¹²¹ The third category includes tools that are derived from density matrices, e.g., parity function, ELF and localized orbital locator (LOL), *etc.* Our $\text{EDR}(\vec{r};d)$ based tools belong to the third category and complement other bonding descriptors by providing useful information about the electron localization-delocalization in various bonding interactions. In this chapter $\text{EDR}(\vec{r};d)$ and its derived tools are applied to study the stretched and compressed chemical bonds of types polar, non-polar, charge-shift, van der Waals and ionic interactions. The bonding descriptions obtained from these tools are compared with the results of calculated kinetic energies to capture the effects of delocalization, left-right correlation, and fractional occupancies in stretched bonds. The results obtained from different electronic structure approximations are compared to provide an in-depth description of a chemical bond. The end of the chapter reports the computational methodologies adopted for these studies.

2.2 Ground-state Singlet H_2

The ground state of the H_2 molecule provides a prototype model of the system with a left-right electron correlation.¹²² Before moving towards applications of $\text{EDR}(\vec{r};d)$ and its tools, a brief description of the state-of-the-art is provided. In the exact solution of stretched H_2 bond, each electron is half on each atom, and at dissociation, the wavefunction may be thought of as incorporating the two Lewis structures, $\text{H}^\uparrow\text{H}^\downarrow$ and $\text{H}^\downarrow\text{H}^\uparrow$.¹⁰⁵ The accurate description require multireference calculations. In single-determinant methods, stretching the H-H bond beyond the Coulson-Fischer point,¹²³ makes the restricted Hartree-Fock (RHF) wavefunction unstable, leading to the symmetry breaking that localizes spin-up and

spin-down electrons to different atoms. Further stretching makes the RHF singlet, and unrestricted Hartree-Fock (UHF) triplet dissociation energy curves cross. The study of single-determinant RHF and UHF methods are essential because they underly Kohn–Sham DFT (Appendix A) and single-reference-correlated methods. Previous studies have shown that interpretative tools such as ELF fails to adequately capture these effects. The value of ELF obtained from the single-determinant calculations on H_2 is identically one at all points in space and at all bond lengths.^{124, 125} Other tools such as basin-point sharing indices and the shared-electron distribution index highlight the interplay of delocalization and correlation in this system.^{126, 127} Critical points in the off-diagonal 1-RDM are associated with the covalent bond.¹²⁸

Figure 2.1 provides a global picture of H_2 bond stretching starting from the compressed bond, plotting the bond energy ΔE_{bond} , total electronic kinetic energy KE, and system-averaged delocalization length D_{max} (Eq. 1.3) plotted as a function of bond length. The vertical red dotted line represents the equilibrium bond length. The technical details about the calculations are given in section 2.8. The obtained plots of ΔE_{bond} (Fig. 2.1a) and KE (Fig. 2.1b) reproduces the previous work.¹²⁹⁻¹³⁵ A comparison of plots shows that trends in D_{max} (Fig. 2.1c) mirrors trends in KE; when KE is large, D_{max} is small, and *vice versa*. At the equilibrium bond length, KE calculated using the exact electronic structure method full configuration interaction (FCI), is larger than that of two H atoms, consistent with the virial theorem.¹³⁶⁻¹³⁸ Stretching the bond gives a minimum of KE at modest bond lengths,¹³⁹ and converges to the isolated atom limit. RHF calculations predict an excessively large D_{max} and too low KE at dissociation. This is a well-known consequence of RHF theory's nonzero probability for finding both electrons on the same atom at dissociation, a spurious Coulomb repulsion that produces a spuriously over-delocalized density matrix and a spurious low KE. Symmetry-restricted R-B3LYP DFT calculations, partly correct for this over-delocalization.

UHF calculations show a derivative discontinuity in KE and D_{\max} at the Coulson-Fischer point and “over-localization” with too small D_{\max} and too large KE at bond lengths around 2\AA . These findings complement the literature that the UHF kinetic energy of correlation is negative in this region.¹⁰⁶

The bond delocalization shift $\overline{\Delta\text{EDR}}(\text{H}_2;d)$ (Eq. 1.5), of \uparrow -spin electrons plotted as a function of bond length (Fig. 2.2), gives further insight into the dissociation. $\overline{\Delta\text{EDR}}(\text{H}_2;d)$

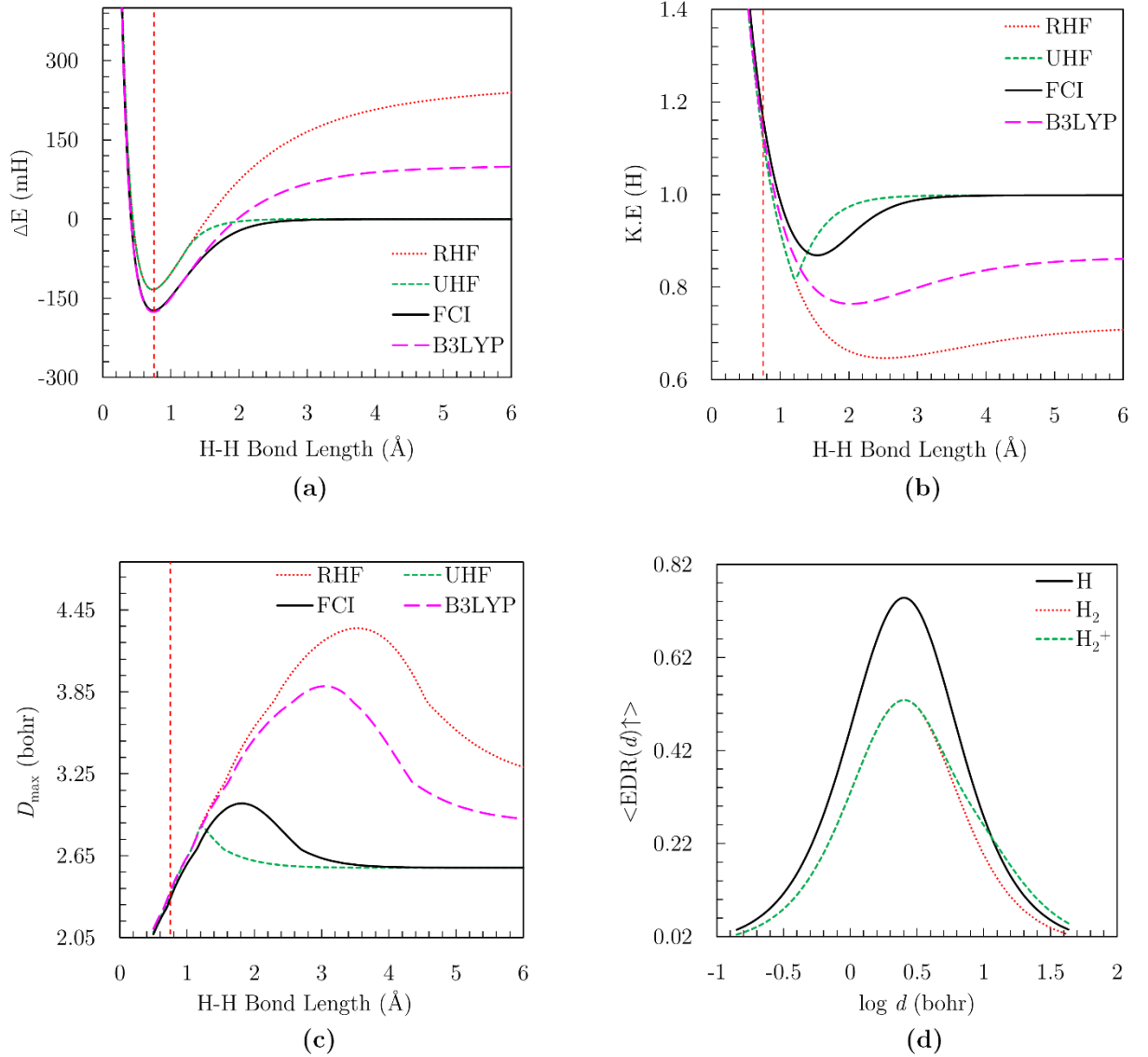


Figure 2.1 H–H bond length of ground-state singlet H₂ molecule plotted *vs.* Bond dissociation energy ΔE_{bond} (a), The expectation value of KE (b), System-averaged D_{\max} (c), System averaged $\overline{\text{EDR}}(d)$ plot of H atom, stretched FCI H₂, and stretched H₂⁺ (d).

shows how a $\overline{\text{EDR}}(\text{H}_2; d)$ of an H_2 differs from its separated H atoms. Fig. 2.2 uses the alpha-spin density matrix, compared to a single isolated H atom. At equilibrium (red dotted line), the electrons are more localized¹³⁹ and more tightly bound than in the isolated atoms, giving a positive peak at small distance d , highlighted with the letter “A” in Fig. 2.2 and a negative peak at large d . Compressing the bond further localizes the electrons and intensifies these peaks. It can be inferred from Fig. 2.2, that $\overline{\Delta\text{EDR}}(\text{H}_2; d)$, can visualize the “fractional

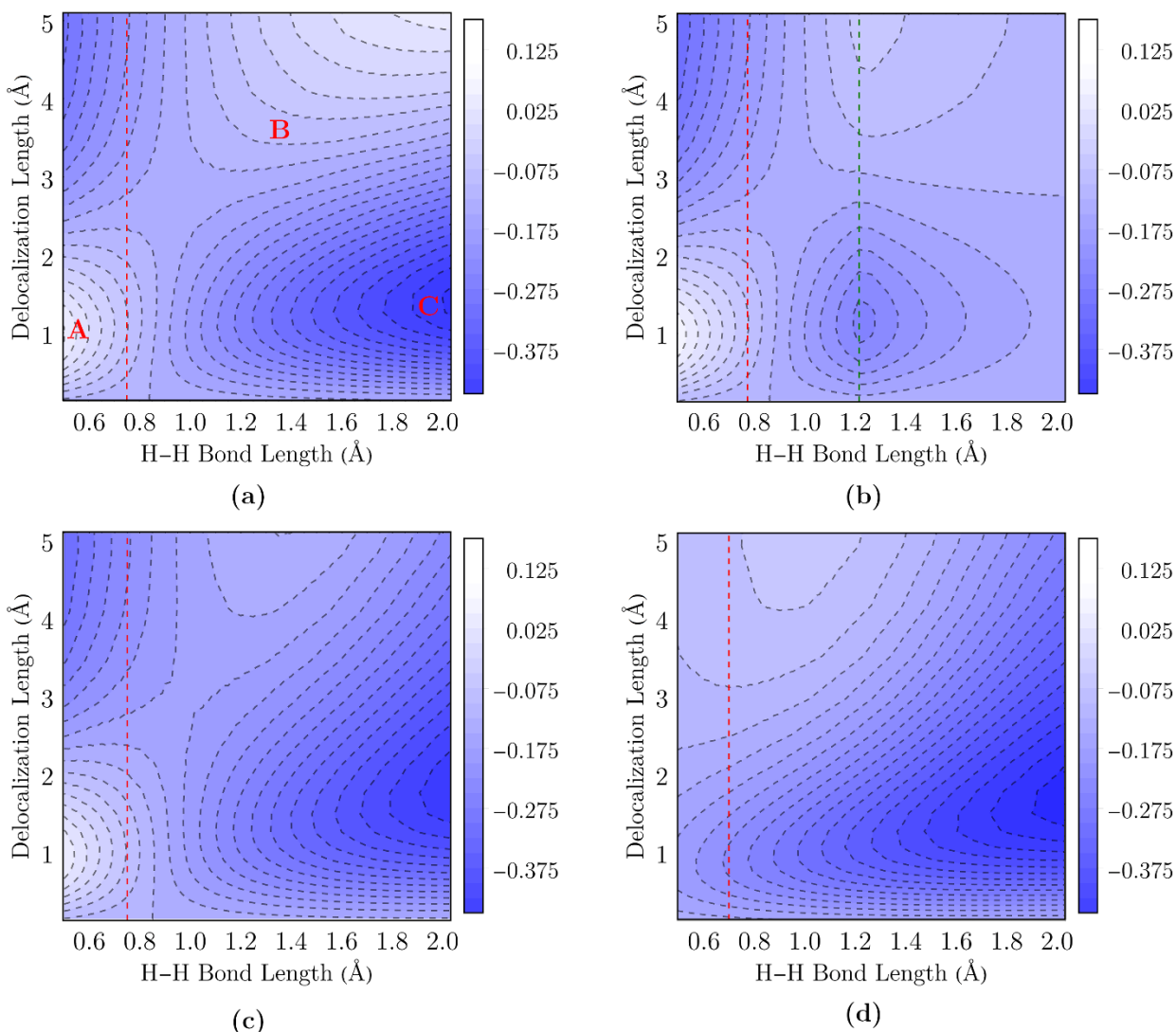


Figure 2.2 Bond delocalization shift $\overline{\Delta\text{EDR}}(\text{H}_2; d)$ of ground-state singlet H_2 , plotted *vs.* delocalization distance d and H–H bond length. (a) RHF, (b) UHF, (c) FCI and (d) FCI at minimal basis set calculations. Vertical red line denotes the equilibrium bond length and green line corresponds to the Coulson-Fischer point.

spin” critical to non-dynamical correlation in chemical bonds.¹⁴⁰ At stretched bond lengths, both RHF (Fig. 2.2a) and FCI (Fig. 2.2c) calculations show that the \uparrow -spin electron has an equal probability of being found on either the left or right atom. The RHF and FCI bond delocalization shifts have a small positive peak at all plotted bond lengths. The distance d of this peak increases with bond length as highlighted using the letter “B”. This peak arises from the overlap between the density matrix on the atoms and the of $\text{EDR}(\vec{r};d)$ test function (Eq. 1.2) at the bond midpoint. Projecting this delocalized electron's 1-RDM onto the localized 1-RDM gives a value much less than one, regardless of distance d because the exact solution gives 1/2 alpha electron, not 1 alpha electron, on each atom. This shows up as a dark (negative) region growing at large bond lengths highlighted with the letter “C”. This region of the bond delocalization shift thus precisely identifies the fractional occupancy of atoms in a dissociated covalent bond. Fig. 2.1(d) provides additional proof of this effect, showing the system-averaged, $\overline{\text{EDR}}(d)$ for isolated H atom and dissociated H_2 and H_2^+ . The two dissociated bonds have half spin-up electron on each atom, which rescales the entire system-averaged $\overline{\text{EDR}}(d)$ by a factor of $1/\sqrt{2}$ (a small “bump” at very large d arises from the finite bond lengths used here). This result clearly illustrates how the positive and negative regions of the bond delocalization shift highlight the interplay of bond stretching and fractional occupancy in dissociating bonds. Moreover, the UHF delocalization shift in Fig. 2.2(c) smoothly converges to zero past the Coulson-Fischer point (green dotted line), highlighting the absence of fractional occupancy effects in the symmetry-broken calculation.

To further highlight an example of how the bond delocalization shift can visualize a classic concept in chemical bonding, Fig. 2.2(d) shows the delocalization shift for FCI wavefunction for H_2 evaluated using a minimal basis set. The bond delocalization shift in this figure highlights the well-known contraction of the electron density towards the nuclei in covalent bonds.¹³⁶⁻¹³⁸ Minimal-basis calculations that prevent density contraction yield an

overall delocalization of the electrons at equilibrium, unlike the large-basis calculations in Fig. 2.2(c), the electrons are more delocalized than in the isolated atoms, giving a negative peak at small d and a positive peak at large d . This analysis isolates the critical role of delocalization in covalent bonding.

While system-averaged values plotted in Figs. 2.1 and 2.2 are suffice to strengthen the conclusion drawn above, the real-space picture of the effects of stretching of individual bonds will provide additional insights. Fig. 2.3(a) shows the real-space EDR($\vec{r};d$) at a relatively large distance $d = 4$ bohr, bond length R stretched to 1.4 \AA . The RHF isosurface shows that these relatively delocalized electrons reside near the middle of the bond, as expected from conventional pictures of chemical bonding. Plots of the EDR at $d = 1$ bohr and the equilibrium bond length were found to be qualitatively similar. The FCI isosurface also sits near the bond midpoint, as shown in Fig. 2.3(b), but occupies a smaller volume, consistent with RHF over-delocalization.

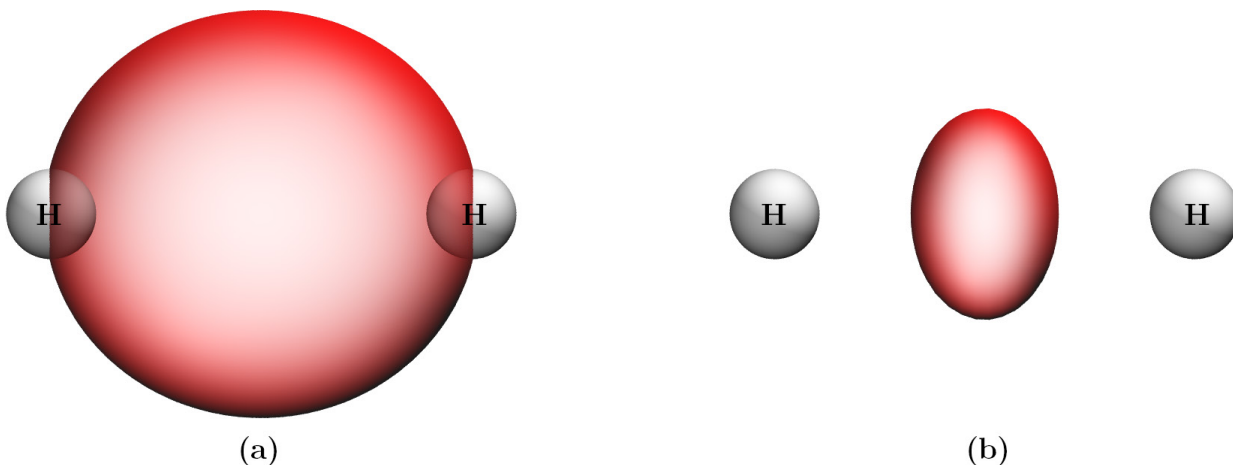


Figure 2.3 Real-space plots of $\text{EDR}(\vec{r};d = 4.0 \text{ bohr}) = 0.75$ shown using transparent red surface for H_2 molecule stretched to bond length of 1.4 \AA (a) RHF (b) FCI.

2.3 van der Waals Interaction: He_2

Helium atoms in the dimer are linked by a weak van der Waals interactions.¹⁴¹ These interactions arise from electron pair fluctuations, and will not appear in the 1-RDM. A weak

antibonding interaction in the He₂ 1-RDM is identified by the topological analysis, as distinct from the coupled fluctuations of electron pair probability, giving rise to the van der Waals interaction.¹²⁸ As illustrated for the atoms linked by non-covalent interactions, the electron sharing index for He₂ decays exponentially with distance.¹⁴² Therefore, it is expected that the EDR($\vec{r};d$) will not capture bonding interactions in He₂, and will only highlight Pauli repulsion between the atoms.

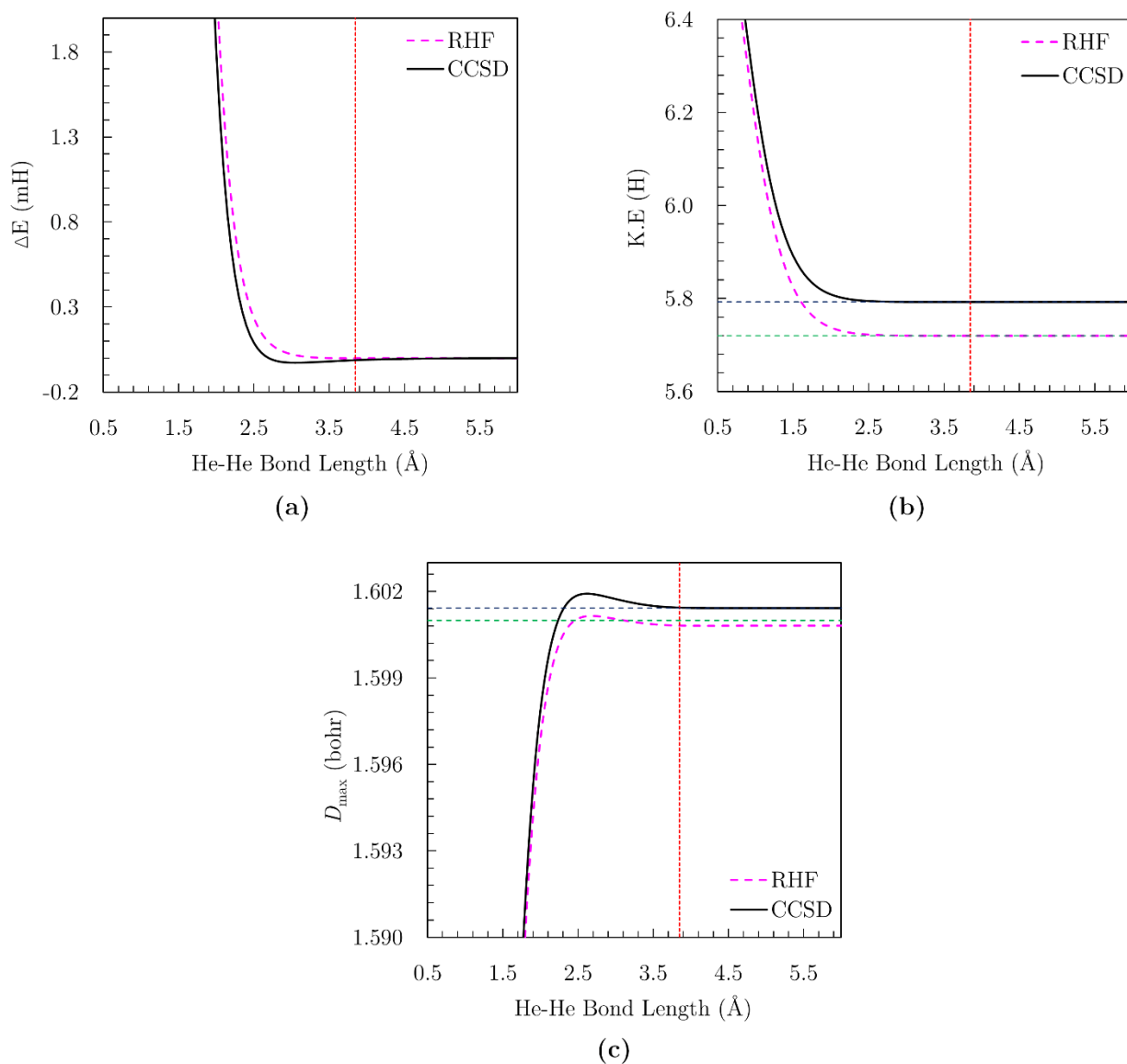


Figure 2.4 He–He bond length of He₂ molecule plotted *vs.* bond dissociation energy ΔE_{bond} (a), Expectation value of KE (b) and System-averaged D_{\max} (c). The horizontal dotted lines correspond to the isolated-atom limit while vertical line shows equilibrium bond length.

Figure 2.4 illustrates the calculated ΔE_{bond} , KE, and D_{max} of the helium dimer plotted as a function of bond length. Following the line of Fig. 2.1, trends in D_{max} mirror trends in KE. The KE converges from above to the isolated-atom limit represented using the horizontal dotted line in Fig. 2.4(b). D_{max} instead shows a tiny peak at modest bond lengths. This artifact of the EDR($\vec{r}; d$) in nonbonded regions is

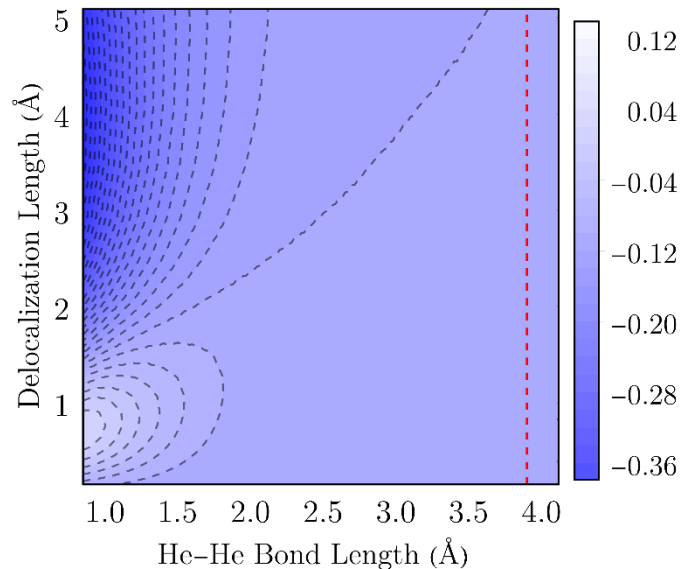


Figure 2.5 CCSD bond delocalization shift, $\Delta\text{EDR}(\text{He}_2; d)$ of He_2 molecule, plotted against length scale d and He–He bond length.

associated with the normalization effects of the test function of Eq. 1.2 and its overlap with 1-RDM.⁸⁹ Fig. 2.5 plots the CCSD bond delocalization shift of He_2 as the function of He–He interaction length. Compressing the distance below the equilibrium, localizes the electrons, giving a positive peak at small d . Stretching the He–He bond makes the 1-RDM smoothly converge to the isolated-atom limit, such that the $\overline{\Delta\text{EDR}(\text{He}_2; d)}$ goes to zero.

Figure 2.6 plots the EDR($\vec{r}; d$) in real space and exhibit a nearly spherically symmetric region about each atom. Therefore, as mentioned at the beginning of this section, it can be concluded that 1-RDM and EDR($\vec{r}; d$) give limited information about the van der Waals interaction.



Figure 2.6 CCSD EDR($\vec{r}; d = 0.8$ bohr) = 0.75 plot shown using transparent red surface for He_2 at 2.0 Å bond length.

2.4 Polar Covalent Bond: HF

Polar covalent bonds such as hydrogen fluoride (HF) have an unequal sharing of electrons¹⁴³ between bonding atoms but dissociate to neutral atoms in the gas phase.¹⁴⁴ Fig. 2.7 shows the ΔE_{bond} , KE, and D_{max} of the HF molecule plotted as a function of bond length. Following the trends of Fig. 2.1, D_{max} mirror trends in KE. The KE exhibits nearly similar trends as the H_2 molecule. At equilibrium bond length, KE is larger than the isolated-atom limit,

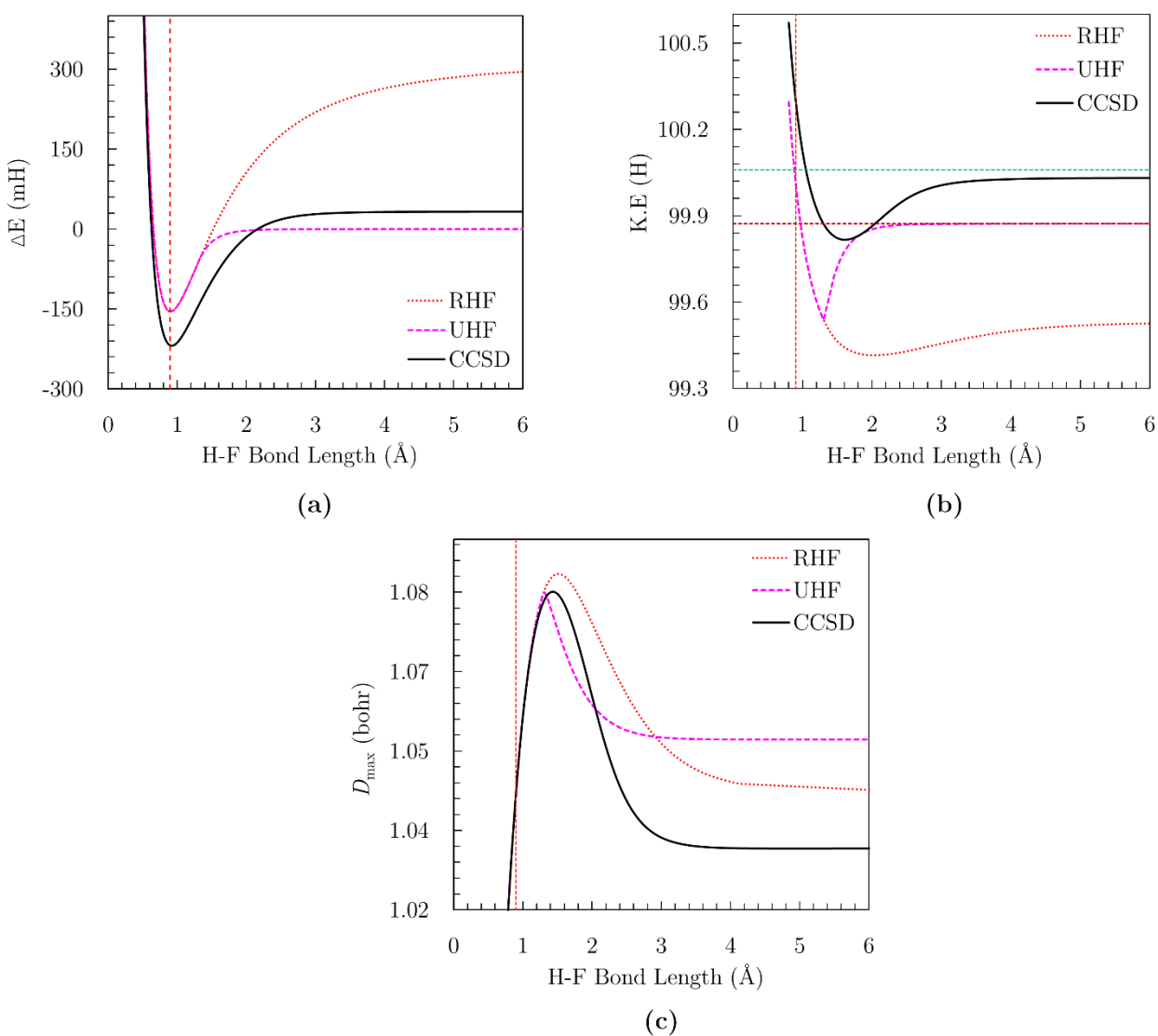


Figure 2.7 H–F bond length of HF molecule plotted *vs.* bond dissociation energy ΔE_{bond} (a), Expectation value of KE (b) and System-averaged D_{max} (c). The horizontal dotted lines correspond to the isolated-atom limit while vertical line shows equilibrium bond length.

minimized past equilibrium, and upon further stretching, converges into the isolated-atom limit in UHF calculations as represented using the horizontal green dotted line in Fig. 2.7(b). On the contrary to the H_2 molecule, the variations in D_{\max} are small, as the system average is dominated by fluorine's localized core electrons. These limitations of the global picture further highlight the importance of real-space images $\text{EDR}(\vec{r}; d)$, as represented in Figs. 2.3, and 2.6. Fig. 2.8 shows the HF molecule's bond delocalization shift $\overline{\Delta\text{EDR}(\text{HF}; d)}$. As for

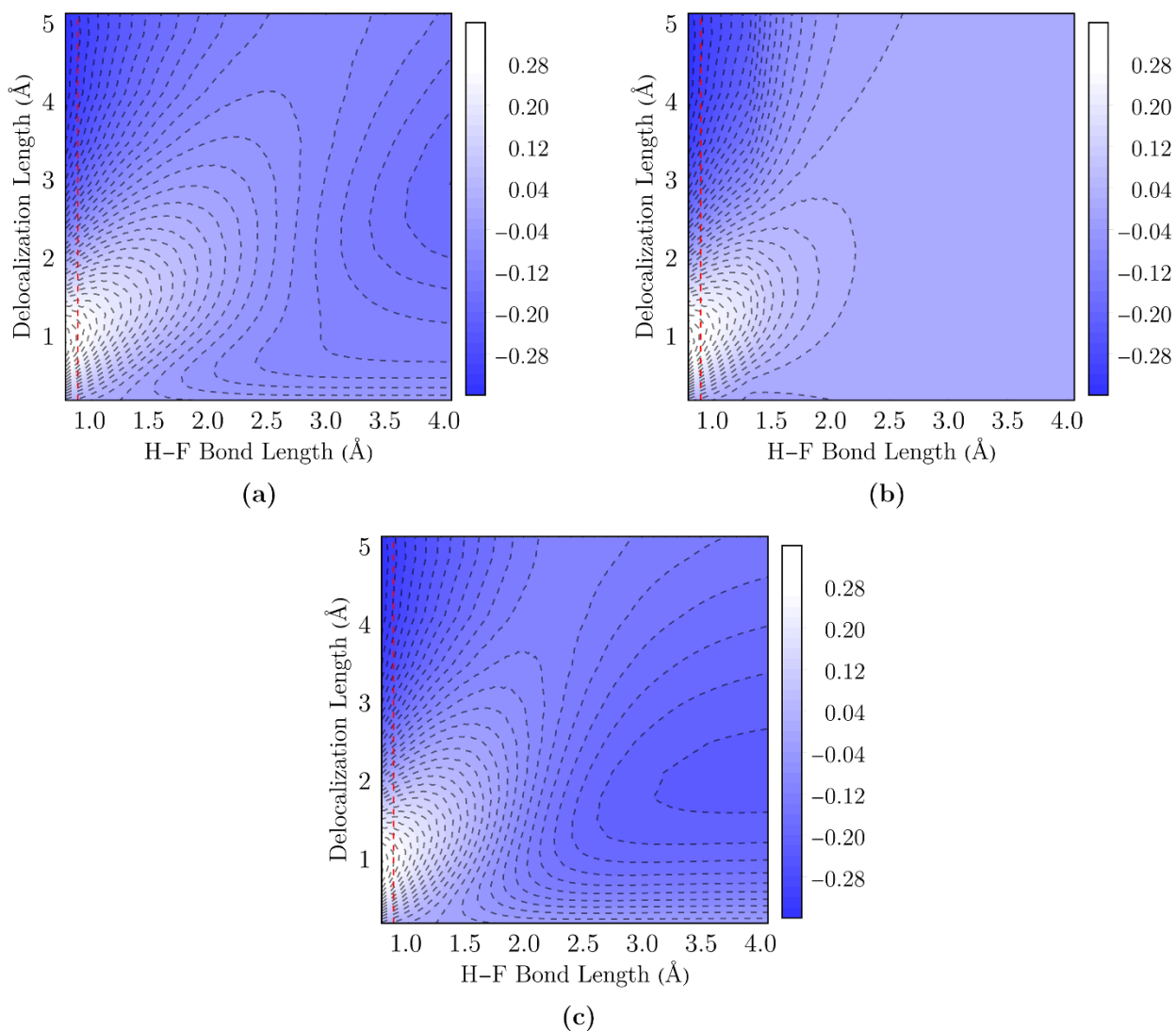


Figure 2.8 Bond delocalization shift $\overline{\Delta\text{EDR}(\text{HF}; d)}$ of HF molecule, plotted *vs.* delocalization length d and H–F bond length. (a) RHF, (b) UHF, (c) CCSD. Dotted line denotes the equilibrium bond length.

H_2 , the bond delocalization shift at the equilibrium bond length has a positive peak at small d and a negative peak at large d , highlighting electron localization in the stable bond. As exhibited for H_2 molecule, bond stretching in HF gives fractional occupancy in RHF and CCSD wavefunctions, yielding negative $\overline{\Delta\text{EDR}}(\text{HF}; d)$ at considerable bond length at length scale $d = 4$ bohr. One notable difference between HF and H_2 is that the Coulson-Fischer point in HF molecule appears at relatively short bond lengths. Therefore, the UHF wavefunction's bond delocalization shift does not show the negative region as appeared in H_2 , but the wavefunction smoothly converges to the isolated-atom limit.

The extension of the real-space analysis of $\text{EDR}(\vec{r}; d)$ in the stretched bond of the HF molecule provides another perspective on this system. Stretching the bond to the length $R = 2.5 \text{ \AA}$ leaves the relatively delocalized electrons at $d = 4$ bohr, mainly in the bonding region and in the vicinity of the H atom, as exhibited in Fig. 2.9(a). At small length $d = 2$ bohr, these electrons are relatively localized on F atom, as shown in Fig. 2.9(b). At equilibrium bond length, the relatively localized electrons at the test function size of $d = 2$ bohr are located between F and H atoms, as demonstrated in Fig. 2.9(c). These findings

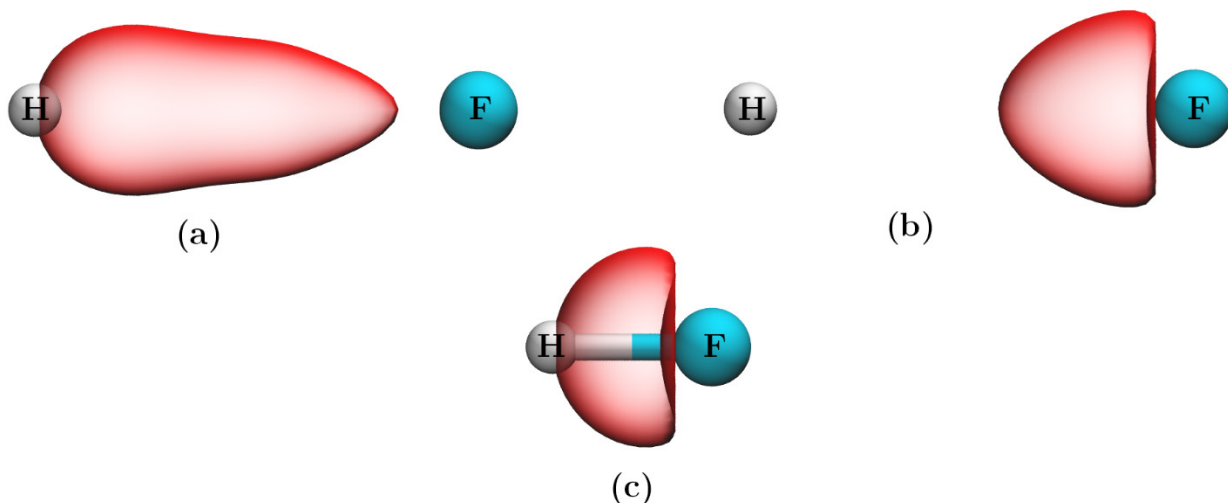


Figure 2.9 Isosurfaces of the RHF $\text{EDR}(\vec{r}; d)$ in H–F molecule shown using red surface. (a) $\text{EDR}(\vec{r}; d = 4.0 \text{ bohr}) = 0.50$ at bond length of 2.5 \AA , (b) $\text{EDR}(\vec{r}; d = 2.0 \text{ bohr}) = 0.70$ at bond length of 2.5 \AA and (c) $\text{EDR}(\vec{r}; d = 2.0 \text{ bohr}) = 0.70$ at equilibrium bond length.

complement the atomic electronegativities, as electrons on H are expected to be bound less tightly than electrons on F atom.

2.5 Charge-shift Bond: F₂

The type of chemical bonding in the F₂ molecule is termed as charge-shift bonding,^{104, 145} arising largely from the resonance between F⁺F⁻ and F⁻F⁺ Lewis structures. Like the dipole-

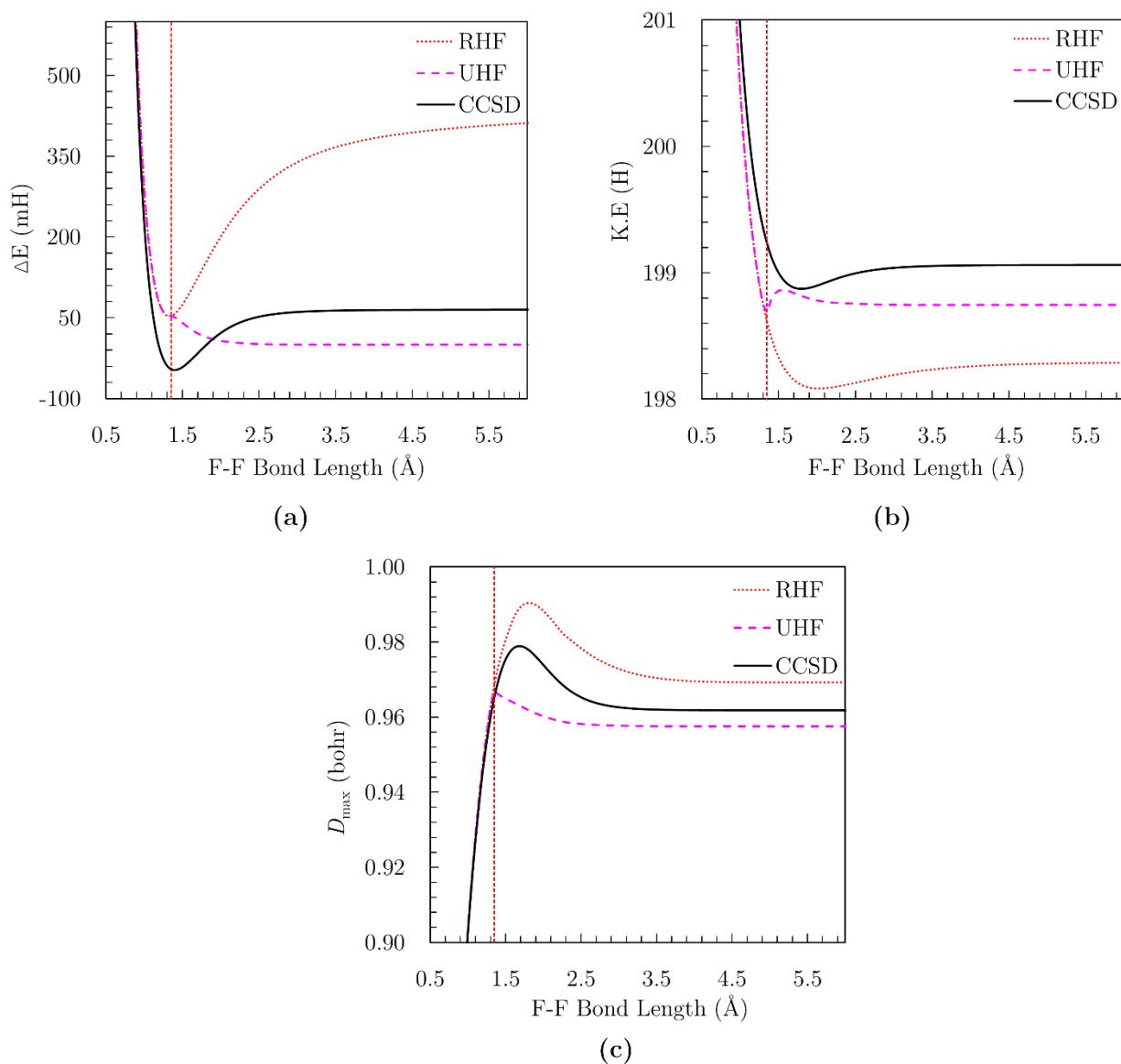


Figure 2.10 F–F bond length of F₂ molecule plotted *vs.* bond dissociation energy ΔE_{bond} (a), Expectation value of KE (b) and System-averaged D_{\max} (c). The vertical dotted line shows equilibrium bond length.

dipole interactions binding the He_2 , the charge-charge fluctuations in the F_2 are most evident in the pair density, such that the 1-RDM gives limited information about the bond. Tools such as ELF demonstrates a negligibly small value near the bond midpoint¹⁰⁴; therefore, the F_2 molecule provides an opportunity to extend the applications of $\text{EDR}(\vec{r}; d)$ and its derived tools on this molecule and compare the results with the findings of other descriptors.

Figure 2.10 shows the calculated ΔE_{bond} , KE, and D_{max} of the F_2 molecule as functions of F–F bond length. The trends of these plots nearly mirror those for the H_2 molecule. The

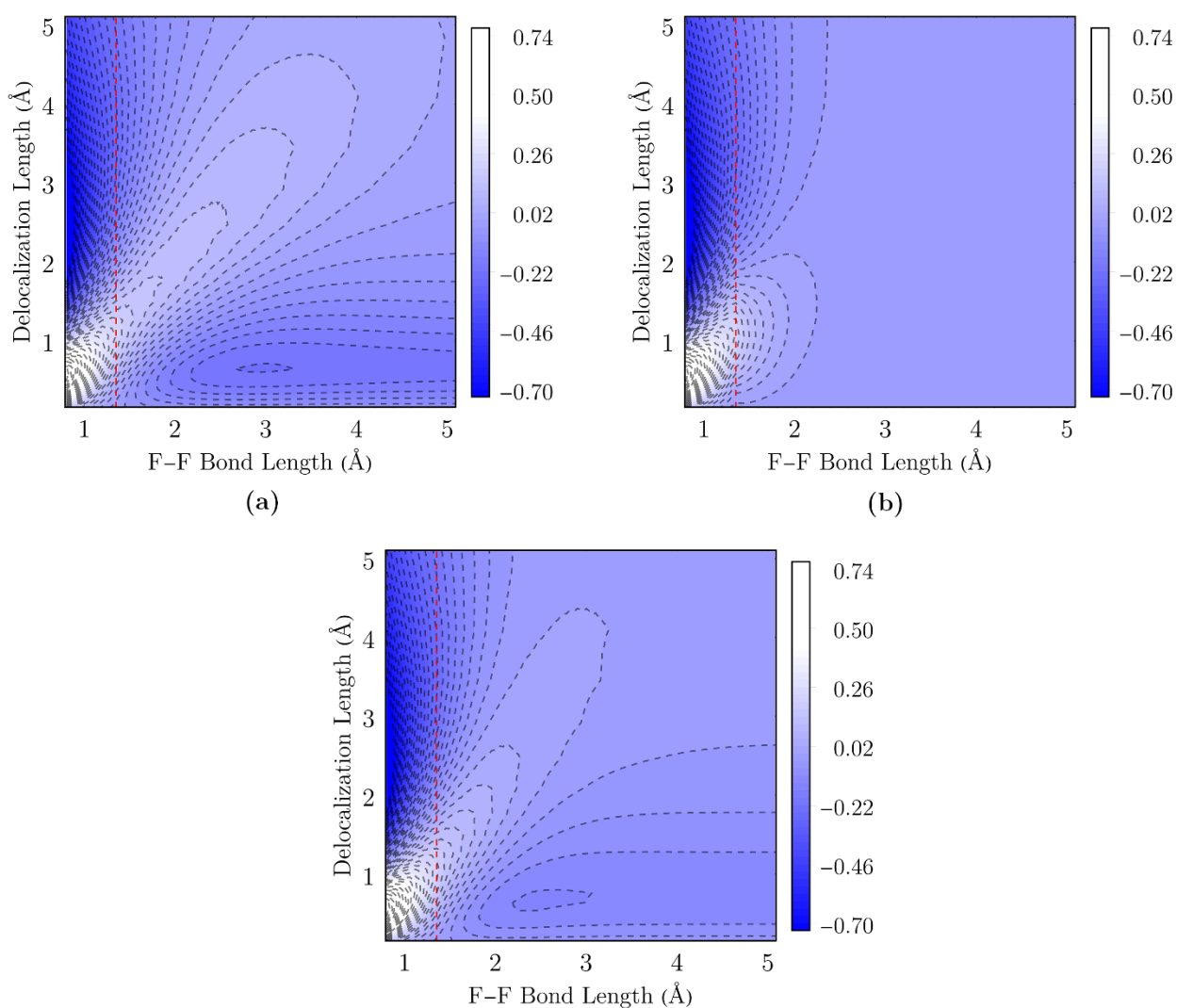


Figure 2.11 Bond delocalization shift $\overline{\Delta\text{EDR}(\text{F}_2; d)}$ of F_2 molecule, plotted *vs.* delocalization distance d and F–F bond length. (a) RHF, (b) UHF, (c) CCSD. Dotted line denotes the equilibrium bond length.

dissociation curve constructed from UHF calculations represents that the molecule is unbound, and the Coulson-Fischer point lies in the vicinity of the equilibrium bond length. As in the HF molecule, this is visible in the UHF bond delocalization shift, $\overline{\Delta\text{EDR}}(\text{F}_2; d)$ shown in Fig. 2.11, which smoothly converges to the isolated-atom limit. The D_{max} curve in Fig. 2.10(c) obtained from UHF calculations converges seamlessly to the isolated-atom limit

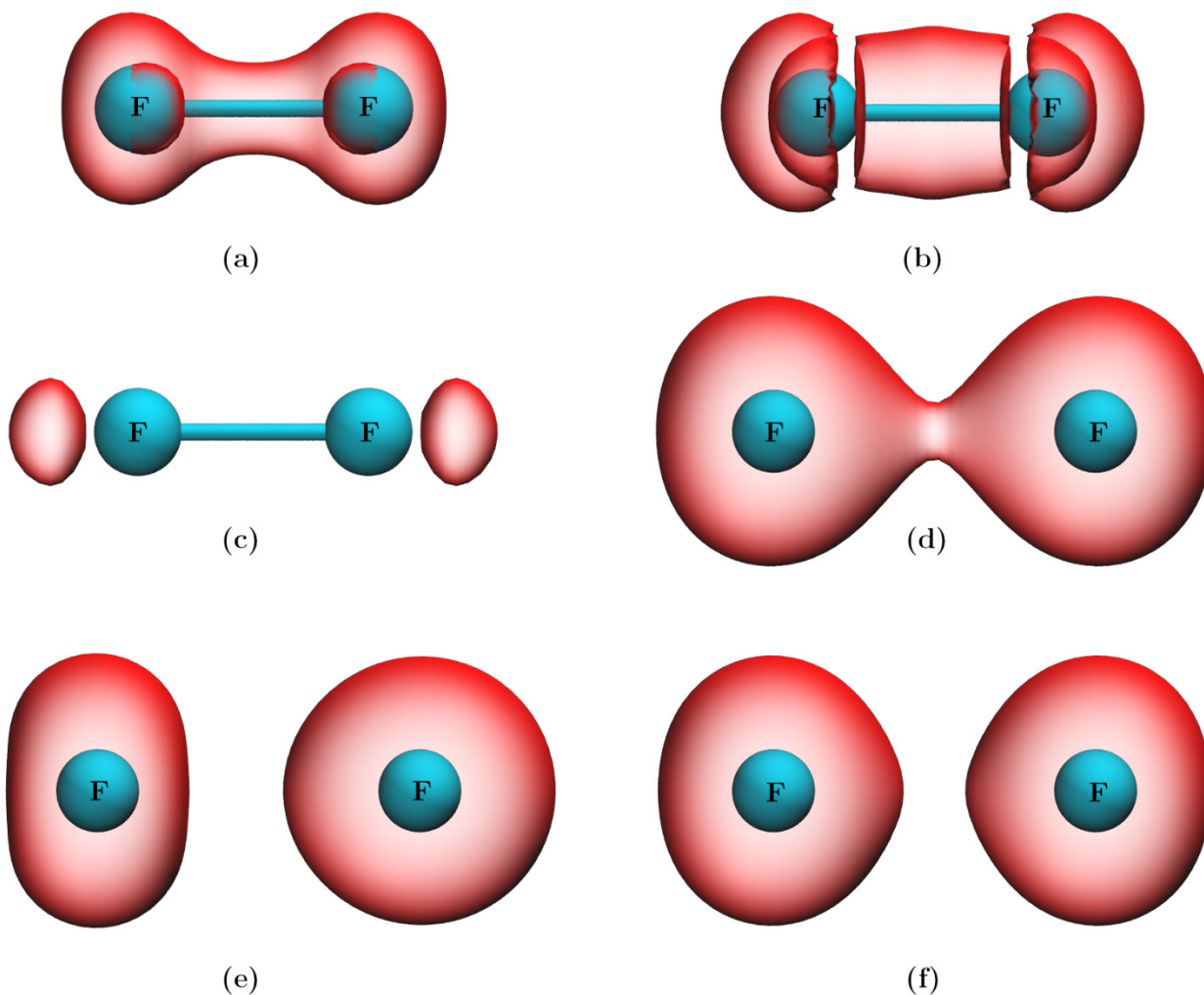


Figure 2.12 Isosurfaces of the $\text{EDR}(\vec{r}; d)$ in F_2 molecule shown using red surface at two different F–F bond lengths. (a) CCSD $\text{EDR}(\vec{r}; d = 1.0 \text{ bohr}) = 0.80$ at RHF minima of 1.3 \AA , (b) CCSD $\text{EDR}(\vec{r}; d = 1.5 \text{ bohr}) = 0.75$ at RHF minima, (c) CCSD $\text{EDR}(\vec{r}; d = 3.0 \text{ bohr}) = 0.45$ at RHF minima, (d) RHF $\text{EDR}(\vec{r}; d = 1.0 \text{ bohr}) = 0.60$ at bond length of 2.0 \AA , (e) UHF $\text{EDR}(\vec{r}; d = 1.0 \text{ bohr}) = 0.60$ at same stretched bond length of 2.0 \AA , (f) CCSD $\text{EDR}(\vec{r}; d = 1.0 \text{ bohr}) = 0.60$ at bond length of 2.0 \AA .

past the Coulson-Fischer point, while the UHF KE curve shown in Fig. 2.10(b) exhibits a small local maximum. The RHF and CCSD bond delocalization shifts again highlight the fractional spin of the dissociating atoms, with a negative peak at small d and large bond length. It is important to note that in Fig. 2.10, the CCSD dissociation limit is above the UHF dissociation limit. It is because the dissociation limit is always evaluated spin unrestricted at the current level of theory (UHF dissociation energy *vs.* UHF F atom, RCCSD dissociation energy *vs.* RCCSD F atom). The dynamical correlation (RCCSD(T) on F_2 and UCCSD(T) on F atoms) recovers a stable F–F bond. Fig. 2.12 shows the real-space plots of $EDR(\vec{r}; d)$ in F_2 near the equilibrium bond length. Like the ELF, the $EDR(\vec{r}; d)$ at small d is significantly small in the bonding region, with an “hourglass” shape that highlights the characteristic of charge-shift bonding. Stretching the bond beyond the Coulson-Fischer point exaggerates this, with the $EDR(\vec{r}; d)$ at $d = 1$ bohr almost completely converged to that of isolated fractional-spin F atoms. The $EDR(\vec{r}; d)$ at longer length scales is overall significantly smaller, corresponds to the presence of a small amount of delocalized electron density around the atoms. Finally, the \uparrow -spin UHF $EDR(\vec{r}; d)$ in Fig. 2.12 represents a small degree of symmetry-breaking, highlighting the symmetry-broken solution.

2.6 Ionic Interaction: LiH

The chemical bonding in LiH has long been a test case for quantum chemistry.¹⁴⁶⁻¹⁴⁸ The adiabatic ground state $X^1\Sigma^+$ of LiH is mostly ionic at the equilibrium bond length and has increasing covalent character as the bond is stretched.¹⁴⁶ This bonding has been studied by various descriptors^{126, 146}, and is associated with a “*harpoon*” mechanism.

The calculated ΔE_{bond} , KE, and D_{max} , as well as the Hirshfeld charge on Li atom as functions of bond length of LiH, are given in Fig. 2.13. Following the trends of other studies systems, D_{max} mirror trends in KE. Accurate CCSD calculations show that the Hirshfeld

charge drops to zero between the atomic distance of 2.5Å to 4.0Å, qualitatively reproducing the behavior observed using other descriptors.¹⁴⁶ In contrast to the CCSD results, the RHF singlet state gives an excessive charge transfer on stretching the bonds. KE obtained using the CCSD method goes through a minimum in this region, and D_{\max} goes through a maximum, qualitatively consistent with the corresponding maximum in the shared-electron distribution index.¹⁴⁶ The UHF solution shows the familiar discontinuities in KE and D_{\max} .

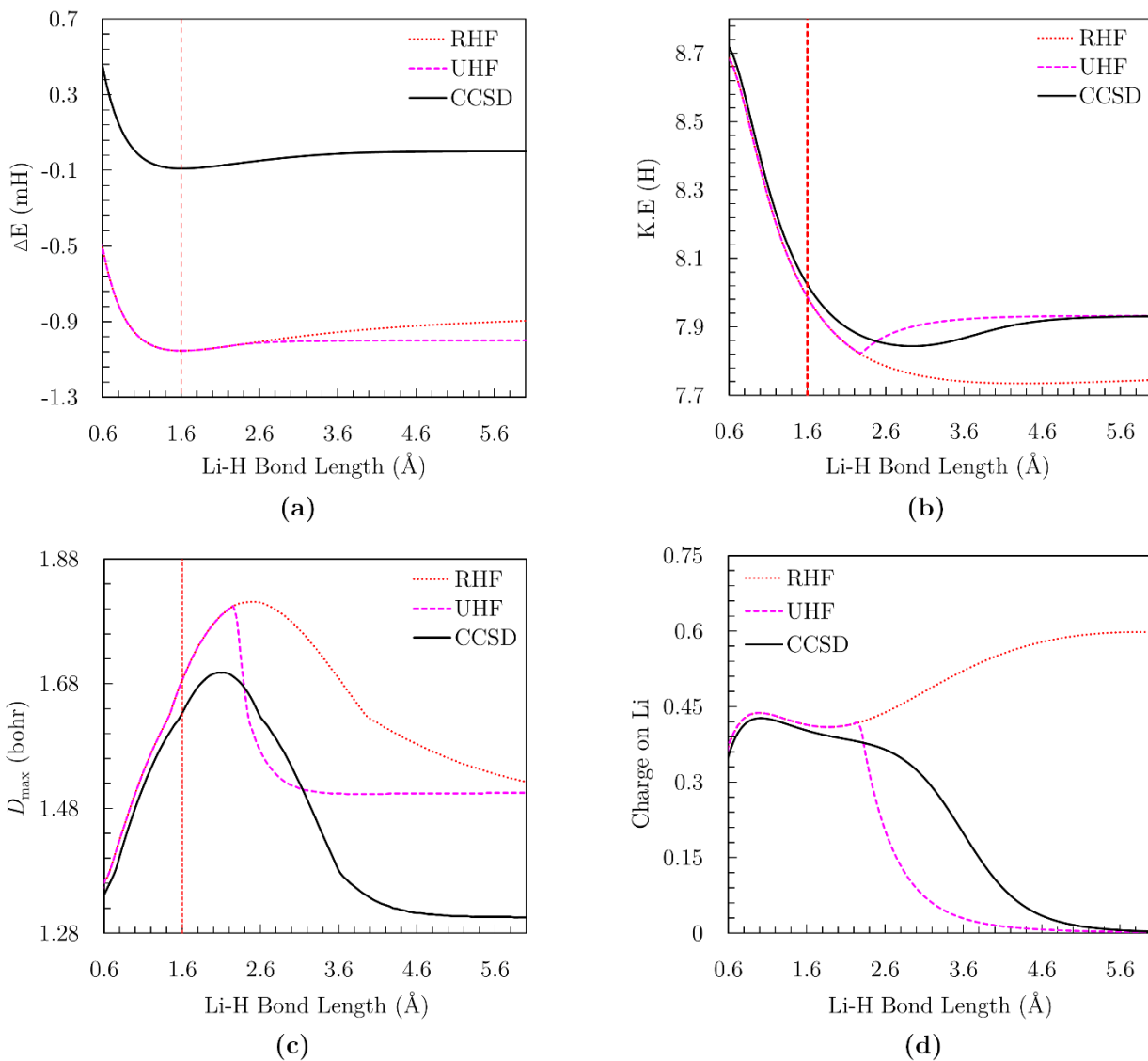


Figure 2.13 Li–H bond length of LiH molecule plotted *vs.* bond dissociation energy ΔE_{bond} (a), Expectation value of KE (b), System-averaged D_{\max} (c) and Hirshfeld charge on Li atom (d). The vertical dotted line shows equilibrium bond length.

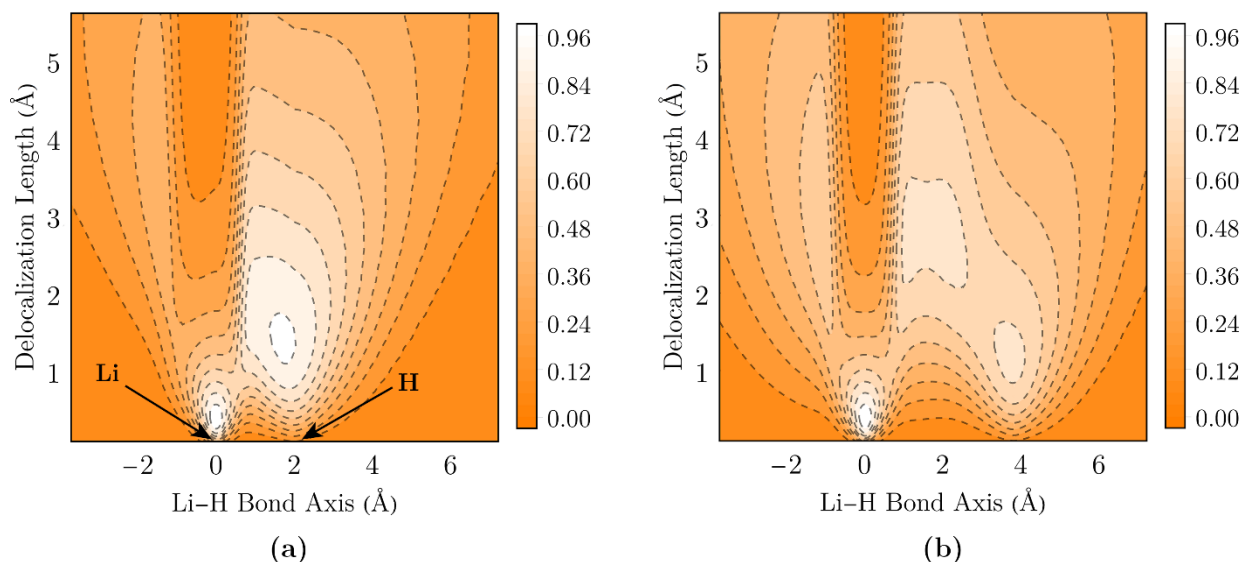


Figure 2.14 CCSD EDR($x;d$) of spin-up electrons in stretched LiH at $R = 2.0 \text{ \AA}$ (a) and at $R = 3.8 \text{ \AA}$ (b).

Figure 2.14 provides a different perspective on this system, showing how the EDR($\vec{r};d$) can highlight the back-transfer of electrons from H to Li as the bond is stretched. Stretching the bond to the length of $R = 2 \text{ \AA}$, EDR($\vec{r};d$) shows a peak in the Li core region at small d , highlighting the localized Li core electrons, and a second peak near the H atom at larger d , highlighting the delocalized valence electrons transferred to hydrogen. For further bond stretching to $R = 3.8 \text{ \AA}$, this peak bifurcates into a more localized peak on H, and a more delocalized peak on Li, highlighting the transfer of electrons into the valence region of the Li atom. This trend of bifurcation has also been reported for the ELF plots,¹⁴⁶; however, the present study further adds information that the peak near Li is less localized and more diffuse than the peak near H. The $\overline{\Delta\text{EDR}}(\text{LiH};d)$ plots for LiH in Fig. 2.15 shows that similar to the other molecules studied, the bond delocalization shift has a positive peak at small d and a negative peak at large d , highlighting how the bond formation makes the electrons more localized and more tightly bound. The RHF in Fig. 2.15(a) and the CCSD

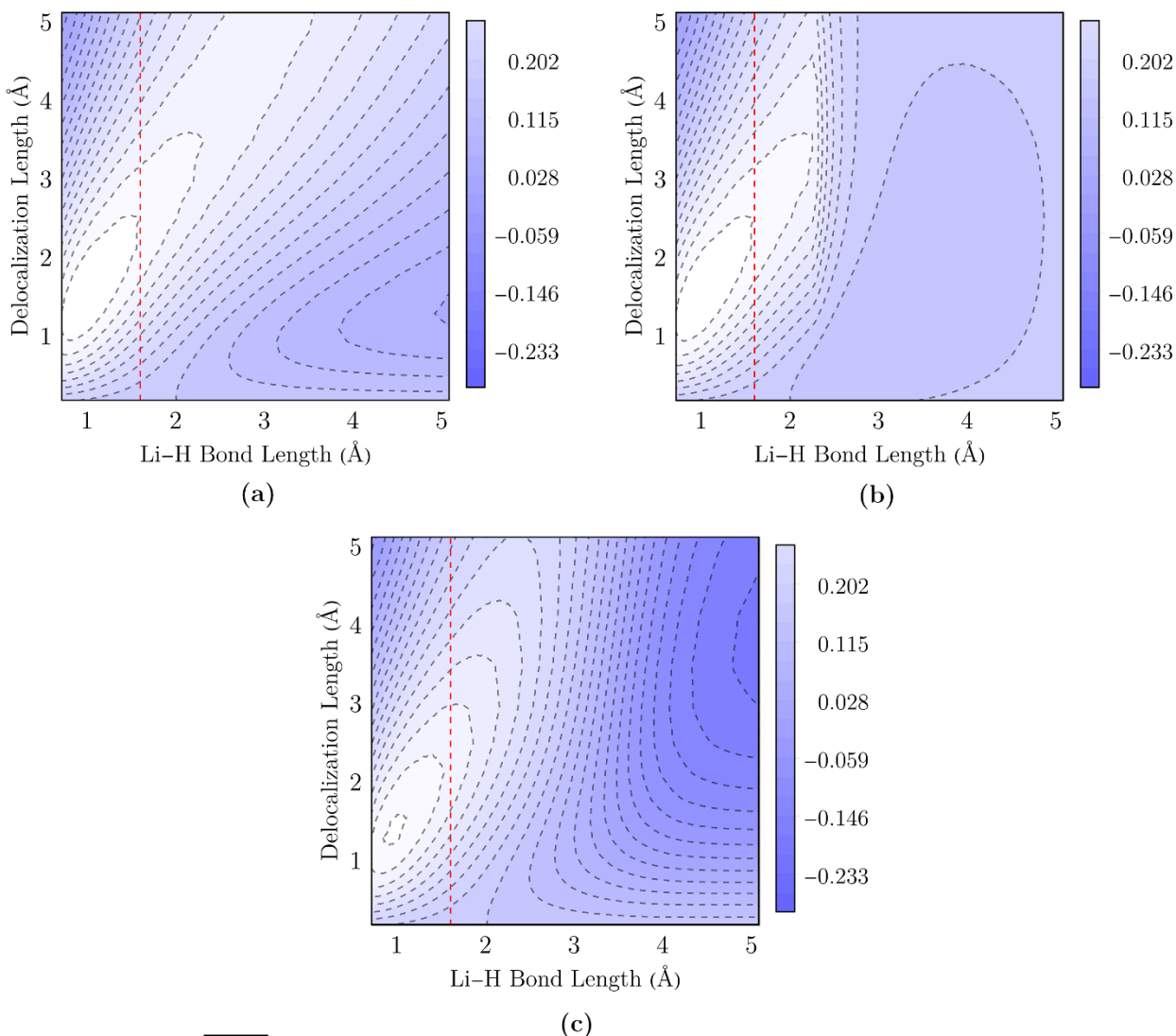


Figure 2.15 $\overline{\Delta\text{EDR}}(\text{LiH};d)$ of LiH molecule, plotted *vs.* delocalization distance d and Li–H bond length. (a) RHF, (b) UHF, (c) CCSD. Red line shows the equilibrium bond length.

in Fig. 2.15(c) bond delocalization shifts show fractional occupancy effects at large bond lengths. The UHF bond delocalization shifts Fig. 2.15(b) clearly indicates the abrupt changes at the Coulson-Fischer point and shows the expected smooth convergence to the isolated-atom limit upon further bond stretching.

2.7 Concluding Remarks

Based on the results from the studied systems mentioned in this chapter, it is concluded that $\text{EDR}(\vec{r};d)$ and its derived tools, can give insight into the bond dissociation and

confidently complement the results obtained from other contemporary tools. The D_{\max} plots largely mirror trends in the system-averaged kinetic energy for each study system. $\overline{\Delta\text{EDR}(AB;d)}$ quantifies effects of delocalization and fractional occupancy in stretched bonds, providing a more detailed picture of delocalized electrons at various bond lengths. Isosurfaces of the $\text{EDR}(\vec{r};d)$ plotted at different d highlight chemically interesting regions of space at different bond lengths. These findings help to conclude that these tools provide a novel perspective on chemical bonding and strengthen the theoretical grounds to explore the process of bond formation and breaking.

2.8 Computational Details

All calculations use the development version of the Gaussian suite of programs.¹⁴⁹ For all studies systems, calculations use restricted Hartree-Fock (RHF) theory, unrestricted Hartree-Fock (UHF), restricted coupled-cluster theory (RCCSD), and Kohn-Sham density functional theory (DFT) with the B3LYP exchange-correlation functional.¹⁵⁰⁻¹⁵⁵ Full configuration interaction (FCI) providing the exact ground state in a given basis set for H_2 is an RCCSD calculation. Stability analysis for unrestricted calculations was performed to locate stable wavefunctions using the `Stable=Opt` option of Gaussian.¹⁵⁶ CCSD density matrices are evaluated using the Z-vector approach.^{157, 158} Molecular orbitals are expanded in the aug-*cc*-pVTZ^{159, 160} basis set unless noted otherwise in the description above without the corrections for basis set superposition error. $\text{EDR}(\vec{r};d)$ and derived tools were evaluated using the methodologies detailed in [section 1.3](#). SCF calculations were performed using quadratically convergent procedures.¹⁶¹ Wolfram Mathematica version 10 was used for graphing and analysis.

Chapter 3

Quantifying the Reactivity of Atoms in Molecules

3.1 Background

The atomic partial charges (see [Appendix C](#)) obtained from the calculated wavefunctions are regularly used in organic chemistry and material sciences to rationalize the chemical reactivity.¹⁶²⁻¹⁶⁶ Among various molecular and atomic descriptors, obtained from quantum mechanical calculations, partial atomic charges, and their derived properties, e.g., Fukui reactivity indices,¹⁶⁷ are the most prominent to quantify the relationship between structure and reactivity.²⁰ For example, the relative rates of chloroacetone *vs.* 3-chloropropene nucleophilic substitution are explained in terms of the substituted carbon's partial charges. However, as detailed in [chapter 1](#), the partial charge alone provides an incomplete picture of reactivity. For example, PhS⁻ is a much better nucleophile compared to PhO⁻ in S_N2 reaction with MeI, though both have similar charge of -1.²⁶ Similarly, F⁻, Br⁻ and I⁻ have different nucleophilicity but identical atomic charges.²⁶ Many nucleophiles preferentially attack α,β -unsaturated ketones at the softer β carbon, not at the more positively charged carbonyl carbon.^{29, 30} Atomic charges alone fail to capture the presence of both positive and

negative electrostatic potential regions on the same atom in a molecule and cannot predict the σ -hole bonding between like atoms.¹⁶⁸ These limitations of partial atomic charge are consistent with chemists' "two-dimensional" pictures of reactivity: charge-controlled *vs.* orbital-controlled reactions, ionic *vs.* covalent bonds, electronegativity (Lewis acidity/basicity) *vs.* chemical hardness, and so on. Partial charge often captures the charge-controlled, ionic, and electronegativity dimensions of reactivity, but typically does not capture the orbital-controlled, covalent, hardness/softness dimensions of reactivity. These observations are based on the fact that the two-dimensional pictures of reactivity are simplifications, omitting potentially critical factors including but not limited to the role of solvents, sterics, temperature, pressure, resonance, and the physical state of reactants, *etc.* It is important to mention that a single chemical theory cannot be perfect enough to account for all these factors but any conceptual framework must find some starting grounds.

There have also been many efforts to quantify the aspects of reactivity that are missing from partial atomic charges. Atomic radii,⁶² atomic kinetic energies,⁶³ atomic-condensed Fukui functions^{40, 41}, and other tools⁷⁰⁻⁷² capture some of these aspects. Therefore, in chemical sciences literature, the terms, such as effects of atomic sizes, polarity induced by electronegativity difference, hybridization differences, the polarization of non-bonding electron pairs, formal charges, non-covalent interactions, softness-hardness, and resonance appear regularly to rationalize the missing aspects of reactivity.^{62, 163, 166} However, most of these theories and the corresponding rationalizations are less-developed and less generalizable than the atomic partial charges. For instance, close-packed surfaces of different transition metals having similar covalent radii and nearly zero partial atomic charges exhibit different chemisorption behavior.³¹ Adsorbates such as oxygen atoms can have nearly identical charges, but very different adsorption energies, on different transition metal surfaces.³² This suggests that a chemically intuitive and readily computed measure of the

“missing piece” of information could be a valuable addition to practical attempts to predict and rationalize the chemical reactivities comprehensively.

We hypothesized that the atomic average overlap distance, D_A (Eq. 1.7), provides the orbital information “missing” from calculated atomic partial charges, Q_A . We predict that the combination of Q_A and D_A offers a more complete and chemically intuitive method for quantifying the reactivity of atoms in the molecule. We included a vast range of organic compounds, cations, anions, aromatic systems, and nanomaterials in our studies to get a versatile and global picture of the capabilities of this combination. Applications are further extended to distinguish the reactivities of positional isomers, regioselectivity, and site-dependent reactivity of gold nanoclusters. [Table G.9 of Appendix G](#) provides the list of all studied systems with corresponding Hirshfeld atomic charges, Q_A , and atomic average overlap distance, D_A , values of systems mentioned in this chapter.

3.2 The Relation Between Q_A and D_A

Applying the atomic average overlap distance, D_A , to the examples in the first paragraph of [section 3.1](#), introduces its power as a partner to partial atomic charge. The sulfur of soft PhS^- ($Q_S = -0.56$ e, valence $D_S = 2.02$ bohr) has an overlap distance substantially larger than the oxygen of hard PhO^- ($Q_O = -0.82$ e, valence $D_O = 1.36$ bohr), implying PhS^- is a better soft nucleophile despite its less negative charge. The nitrogen of deprotonated o-phenyl alkynyl benzamide ($Q_N = -0.36$ e, valence $D_N = 1.20$ bohr) has a larger overlap distance than the oxygen ($Q_O = -0.48$ e, $D_O = 1.10$ bohr), consistent with experimental evidence that nitrogen is the preferred nucleophile in intramolecular anionic cyclization despite its less negative charge.^{27, 28} The halide anion valence $D_{\text{F}(-)} = 1.2$, $D_{\text{Cl}(-)} = 1.9$, $D_{\text{Br}(-)} = 2.1$, $D_{\text{I}(-)} = 2.4$ bohr and alkali cation $D_{\text{H}(+)} = 0.0$, $D_{\text{Li}(+)} = 1.0$ bohr distinguish small, hard, compact anions and cations from the larger, softer species further down the periodic table.

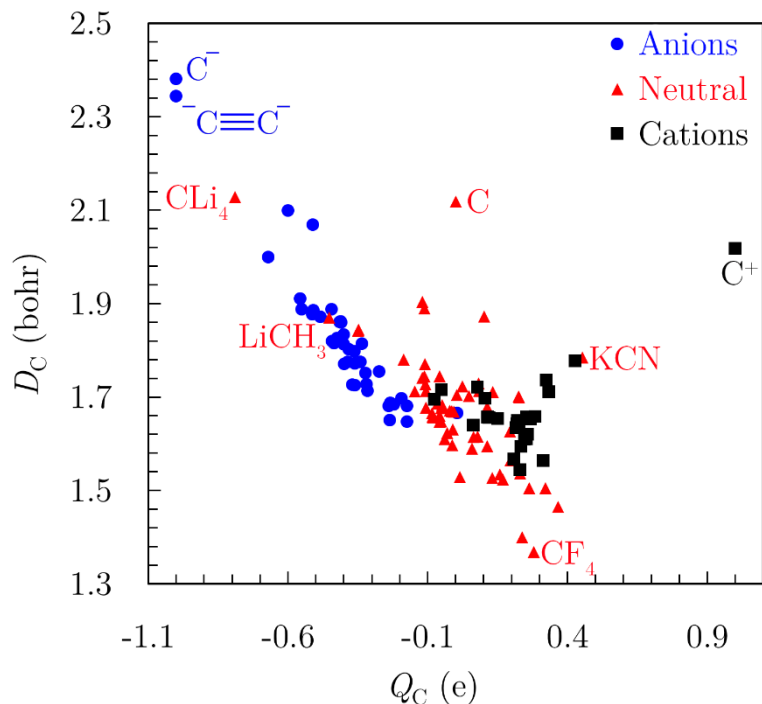


Figure 3.1 Relation between D_C and Q_C for molecules used in this study and are given in [Appendix G](#). Chemically interesting outliers are labeled.

The butenone β carbon ($Q_{C\beta} = -0.07$ e, $D_{C\beta} = 1.30$ bohr) is less positively charged than the carbonyl carbon ($Q_{CO} = 0.17$ e, $D_{CO} = 1.18$ bohr); however, the β carbon's larger overlap distance is consistent with improved orbital overlap with soft nucleophiles.

[Figure 3.1](#) establishes a general relation between Q_C and D_C computed for carbon atoms in 200 organic molecules. All values used in [Fig. 3.1](#) and corresponding names of molecules are tabulated in [Appendix G](#). This relation of [Fig. 3.1](#) shows that carbon atoms in all typical organic molecules have small values of D_C than the corresponding isolated carbon atom. Chemically, this is exactly what is expected based on the reactivity of isolated carbon atom. [Fig. 3.1](#) highlights that the D_C of most of the cationic molecules is smaller than that of the neutral molecules. In contrast, D_C of most of the anionic molecules is larger than that of the neutral molecules. This is due to the tight binding of the remaining electron density in cations, more than neutral atoms, which gives smaller orbital lobes and smaller

overlap distance. On the contrary, anionic carbon atoms must carry their electron density in diffuse, weakly bound orbitals, giving larger overlap distance. From these observations, it can be inferred that in general, Q_C and D_C show an inverse relationship but in many other situations, the atomic overlap distance distinguishes carbons with a similar charge but different chemistry. For instance, [Appendix G](#) indicates that isolated atoms C^+ , C^\bullet , C^- ($Q_C = +1, 0, -1$ e respectively) have huge $D_C > 2$ bohr consistent with their reactivity. Carbonium CH_5^+ ($D_C = 1.72$ bohr) and neopentane ($D_C = 1.58$ bohr) have nearly neutral central carbons, but D_C highlights carbonium's reactivity. 1,3,5-triazine has $Q_C = 0.11$ e nearly identical to formaldehyde, but formaldehyde's higher D_C 1.68 *vs* 1.59 bohr highlights triazine's stability. C=N carbons of acetonitrile and methyl isocyanide have modest differences in partial charge Q_C 0.08 e and -0.11 e, but large differences in D_C 1.62 bohr *vs* 1.90 bohr, highlighting methyl isocyanide's reactivity. The large overlap distance of fulminic acid ($Q_C = -0.11$ e, $D_C = 1.89$ bohr) distinguishes it from cyclopropene ($Q_C = -0.11$ e, $D_C = 1.70$ bohr). Similarly, [Fig. 3.1](#) highlights the chemistry of chemically distinct outliers. Due to the electropositive lithium atoms in CLi_4 , the electrons on carbon are held by large and diffuse orbitals giving a large value of D_A . The substitution of lithium with hydrogens in $LiCH_3$, though, gives a small reduction in negative charge but gives a comparatively large reduction on the overlap distance. Similarly, due to the higher electronegativity of fluorine atoms in CF_4 the electrons on carbon are occupying compact orbitals, hence giving a small value of D_C but carbon atom in KCN , though have a similar charge as the carbon of CF_4 but clearly have a large value of D_C .

3.3 Quantifying the Effects of Substituents

Starting with a simple description of atomic average overlap distance, D_A , characterizing the effects of substituents on the central carbon of CH_nR_{4-n} , [Fig. 3.2](#) shows a systematic

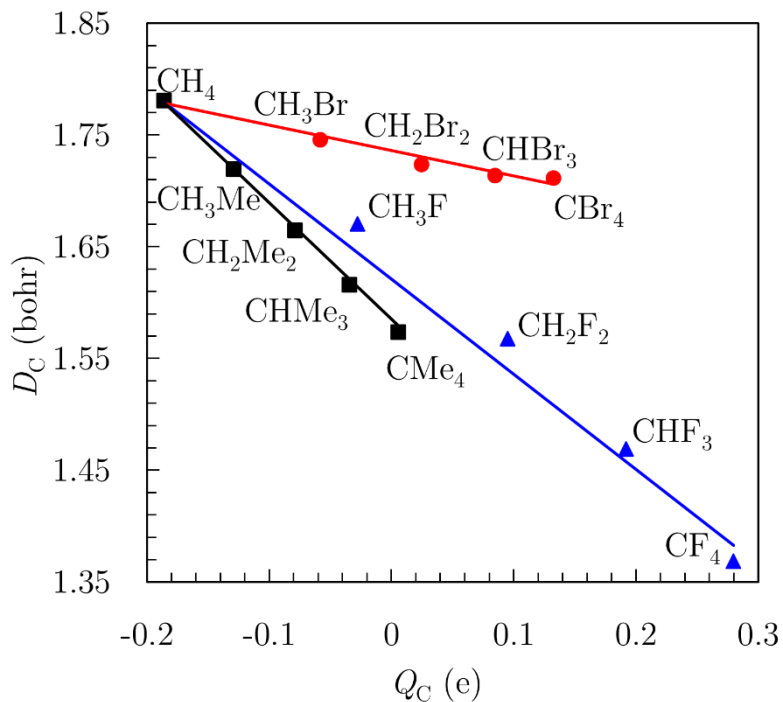


Figure 3.2 Partial charge Q_C and overlap distance D_C of the central carbon in $\text{CH}_n\text{R}_{4-n}$, $\text{R} = \text{Me}, \text{F}, \text{Br}$.

decrease in D_C and Q_C of the central carbon atom when each hydrogen of methane is substituted with a methyl group. This trend quantifies the reduction of charge on central carbon atom per each methyl group and complements the notion of higher stability of branched-chain alkanes as compared to their linear isomers.¹⁶⁹ The reduction in Q_C and D_C induced by phenyl substituents (not shown) is comparable to the methyl substituents; however, it enhances slightly at *bi*- and *tri*- substituted methane. This effect of charge reduction by substituents is much pronounced in F^- and Br^- substituted methane. The relative decrease of Q_C and D_C by successive substitution of hydrogens with fluorine shows a linear trend. However, the delocalized C–Br bond makes CH_3Br substantially more delocalized than CH_3F , and the stability imparted by further Br- substituents is very small as compared to F- substituents, which highlight the ability of D_C to detect the effect of atomic sizes and electronegative differences. It can be further elaborated by comparing the relative nature of orbitals on halogen atoms. The C–F and C–Br bonds can be thought of

as overlap between sp^3 orbital on carbon and p orbitals on the halide. The p orbital of Br atom is more diffuse than that of F atom. Thus the C–Br bond orbital is more diffuse (and the bond itself is longer) than that of the C–F bond. The shallow slope of D_C vs. Q_C for Br vs. F substitution shows this effect clearly. While the relation between Q_C and D_C is nearly linear within a substituent class, different substituents have different trends. For example, CHBr_3 has D_C larger than CH_2F_2 despite almost identical atomic charges, consistent with bromine's leaving group ability.

Figure 3.3 show similar trends for $[\text{CH}_n\text{R}_{3-n}]^-$ and $[\text{CH}_n\text{R}_{3-n}]^+$ carbon centers. As stated earlier, for anions, the more negative Q_C means larger D_C ; therefore, an increase in negative charge also increases D_C for these anionic centers but follows the same pattern as neutral molecules with each substituent has its distinct trend. A similar pattern can also be noticed for $[\text{CH}_n\text{R}_{3-n}]^+$ systems where the trend is reversed for Br and CN substituents. This indicates that both Q_C and D_C become smaller with each substitution of H with Br or CN. The most pronounced effects of substitution can be noticed for F substitutions, which again establishes the ability of this combination to capture the electronegativity effects.

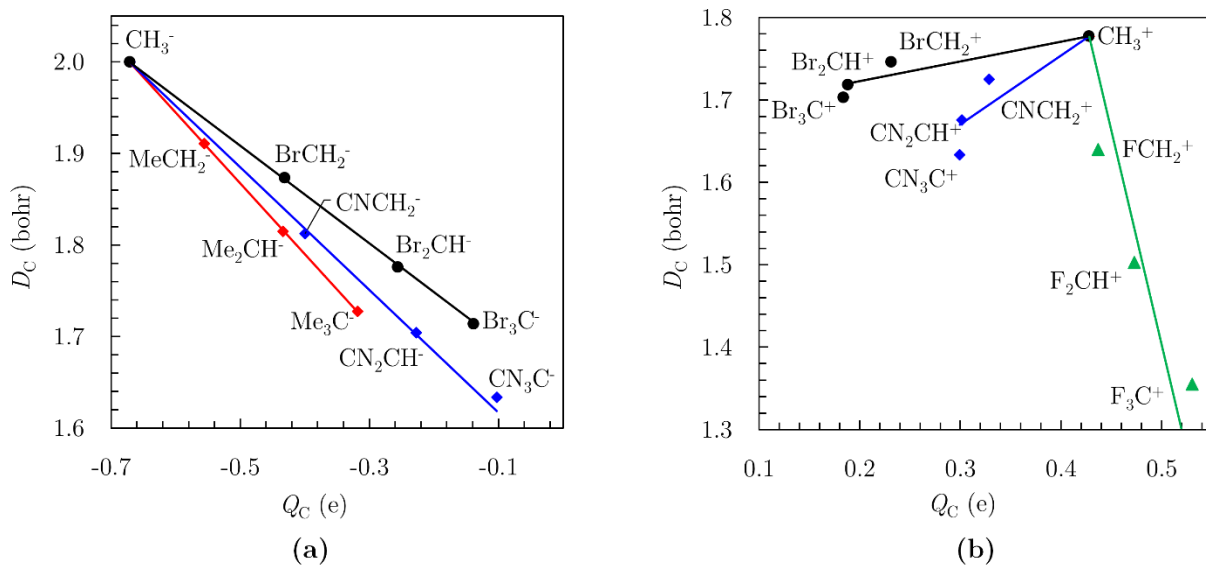


Figure 3.3 Partial charge Q_C and overlap distance D_C of the central carbon in (a) $[\text{CH}_n\text{R}_{3-n}]^-$, R = Me, Br, CN and (b) $[\text{CH}_n\text{R}_{3-n}]^+$, R = F, Br, CN

To conclude this section, the combination of Q_C and D_C is applied to captures the experimental reactivities of a diverse set of 30 monosubstituted benzenes. Experimental reactivities of meta and para positions are distilled in Hammett's σ_m and σ_p electronic substituents parameters.¹⁷⁰ The combination of Q_C and D_C of meta and para carbon atoms are used to fit their experimental σ_m and σ_p parameters using Eq. 3.1:

$$\sigma = \alpha Q_C + \beta D_C + \gamma \quad (3.1)$$

The names of substituents and their corresponding calculated and experimental parameters are given in [Appendix G](#). The fit reproduces experiment, with $R^2 = 0.956$, RMS error of 0.075, $\alpha = 20.99/e$, $\beta = 79.73/\text{bohr}$, $\gamma = 133.56$. [Fig. 3.4](#) represents the relation between experimental σ and σ predicted using Eq. 3.1. Fitting Q_C alone ($\beta = 0$) degrades the fit to $R^2 = 0.880$ and increases the RMS error by 50% to 0.122. It can be inferred that,

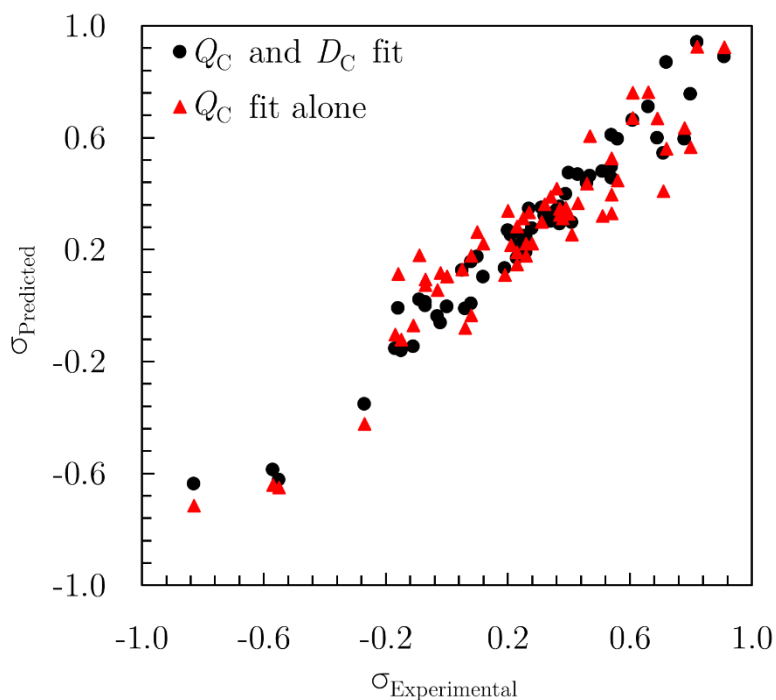


Figure 3.4 Correlation between experimental Hammett substituent effects at meta and para positions of 30 monosubstituted benzenes, and values fit to Eq. 3.1 (black circles) and fitting to Q_C alone (red triangles).

chemically, Q_C captures the broad outlines of substituent effects, and D_C adds useful information.

3.4 D_A and Aromaticity

Atomic average overlap distance measures the size of *orbital lobes*, a property that is *distinct* from the delocalization of orbitals, charge, or spin over multiple centers. To illustrate, Fig. 3.5 shows D_H for the 1s, 2s, and 2p states of H atom. D_H is modest for the single large lobe of the 1s orbital, smaller for the two lobes of the 2p orbital, and dominated by the diffuse outer lobe of the 2s orbital. This indicates that D_A gives information about hybridization; because atoms with more 2p character tend to have smaller D_A , while atoms with more 2s character tend to have larger D_A . The combination of atomic partial charges and overlap distance can distinguish the aromatics from non-aromatic and anti-aromatic systems. Fig. 3.6 plots D_C vs. Q_C for carbon atoms in representative neutral conjugated π -systems. For the heterocyclic systems, Fig. 3.6 considers the carbon furthest from the heteroatom. While aromatic benzene, non-aromatic hexatriene, and anti-aromatic cyclobutadiene have nearly

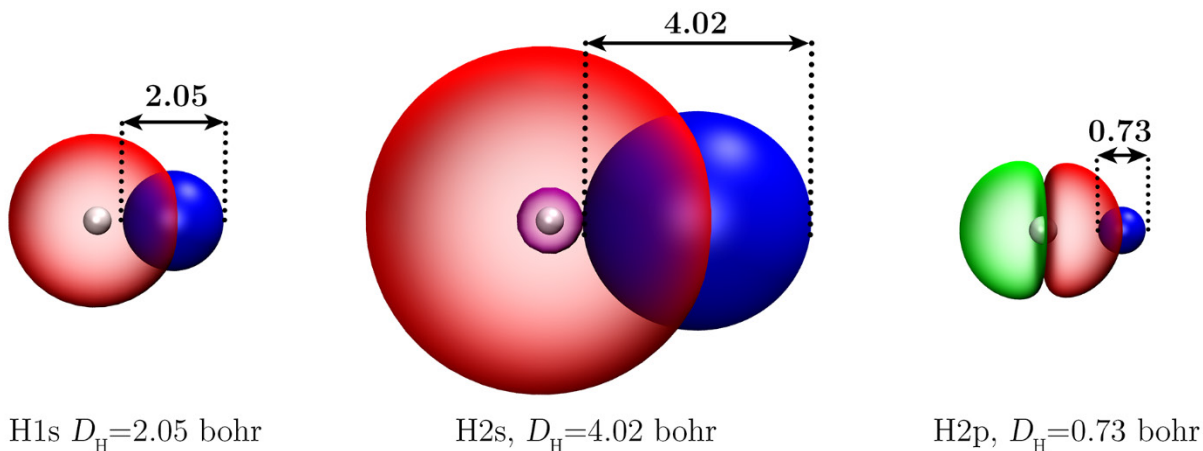


Figure 3.5 Atomic average overlap distance calculated for H atom's 1s (left), 2s (middle) and 2p (right) orbitals. The α -spin orbitals are shown in red and green. The $\text{EDR}(\vec{r};d)$ test function shown in blue. The width of test function which maximizes overlap with orbitals to give D_H is highlighted for each orbital.

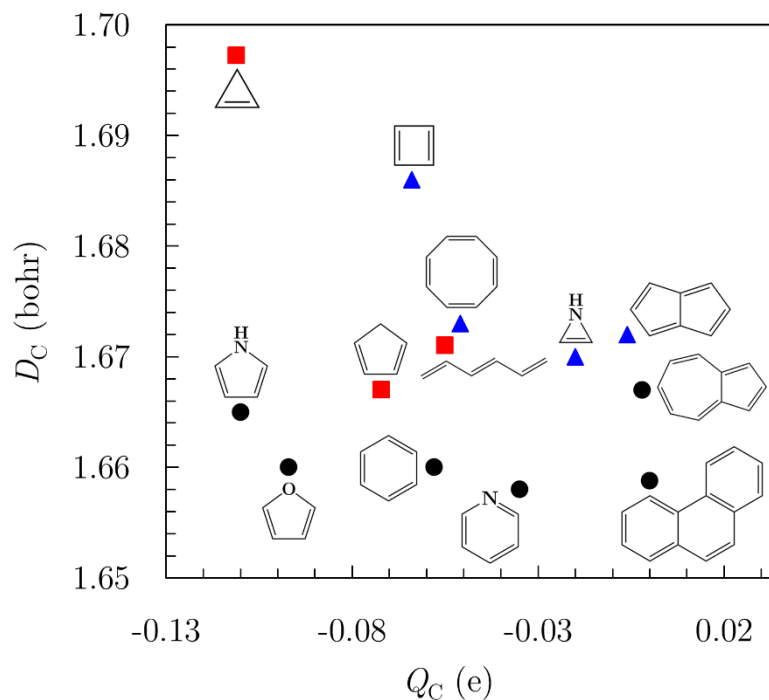


Figure 3.6 Relation between Q_C and D_C of carbon atoms in aromatic (black dots), nonaromatic (red boxes), and antiaromatic (blue triangles) conjugated molecules.

identical Q_C and have formally the same sp^2 hybridization, their computed D_C clearly distinguish the relatively unstable, weakly bound, diffuse carbons of cyclobutadiene, and the stable carbons of benzene from hexatriene. This indicates that the difference in their D_C captures the relative stability but not just changed hybridization. In contrast, heterocyclic aromatics pyridine, pyrrole, and furan give varying Q_C but similar D_C , highlighting the heteroatoms' donor-acceptor effects. The aromaticity and hence stability of fused systems are also captured by D_C . Anthracene, being aromatic, has smaller D_C and is more stable than the anti-aromatic pentalene though both of these systems have nearly the same charge. Among both of 7 ($D_C = 1.66$ bohr) and 5 ($D_C = 1.67$ bohr) membered ring in azulene, the former has a smaller value of D_C than the later, which complements the experimental¹⁷¹ and theoretical¹⁷² findings of higher reactivity of 5-membered ring towards electrophilic reagents.

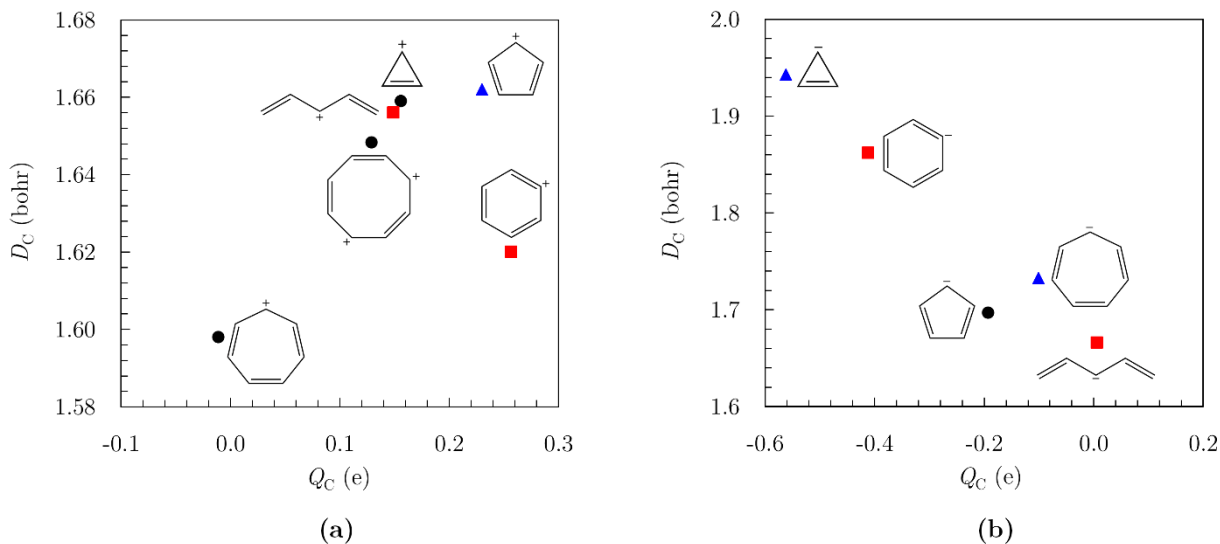


Figure 3.7 Relation between Q_C and D_C of carbon atoms in aromatic (black dots), nonaromatic (red boxes), and antiaromatic (blue triangles) (a) cationic (b) anionic charged conjugated systems.

The trends in Fig. 3.6 are also seen for charged conjugated systems. As exhibited in Fig. 3.7(a), anti-aromatic cyclopentadienyl cation has $D_C = 1.66$ bohr, substantially larger than aromatic cyclopropenyl cation ($D_C = 1.65$ bohr), aromatic cycloheptatetrylium ($D_C = 1.60$ bohr), or Huckel-nonaromatic benzene cation ($D_C = 1.62$ bohr). Aromatic cyclopentadienyl anion in Fig. 3.7(b) has $D_C = 1.70$ bohr, smaller than anti-aromatic cyclopropenyl anion ($D_C = 1.94$ bohr) or cycloheptatrienyl anion ($D_C = 1.73$ bohr), and consistent with the former's experimentally demonstrated high basicity and reactivity.^{166, 173} The beta carbon of pyrrole ($Q_C = -0.11$ e, $D_C = 1.67$ bohr) has partial charge nearly identical to acetylene ($D_C = 1.77$ bohr), but a smaller D_C highlighting pyrrole's aromatic stabilization.

3.5 Quantifying the Reactivity of Isomers

The atomic average overlap distance can distinguish the different reactivity of the same atom in different positional isomers. Fig. 3.8 plots Q_C vs. D_C of carbon atom (highlighted in red) in different positional isomers. The carbons of methyl cyanide and methylisocyanide have a modest difference in their charges; however, their D_C is dramatically different and

clearly highlights the isocyanide's reactive carbon. This trend can also be observed in four different positional isomers of methyl isocyanate. The carbons of these isomers have a slight difference in their charges, but (isocyanooxy)methane, has a very large value of D_C compared to methyl isocyanate. Whereas, the D_C and Q_C and hence the stability for the other two isomers, cyanatomethane and 3-methyl-1,2-oxazirine are nearly equal to that of methyl isocyanate. The underlying carbons of Isothiocyanatomethane and thiocyanatomethane have nearly similar charges and D_C ; however, the presence of soft sulfur atom reduces the positive charge on carbon and increases their D_C as compared to their counterparts containing hard oxygen atoms. The applications of D_C can be equally extended to distinguish the reactivity of other types of isomers. For example, among the two isomers of 5-norbornenyl anions (Fig. 3.9), D_C confirms the higher stability of endo-5H-norborbornenyl anionic center, and hence its higher acidity than the anionic carbon of exo-5H-

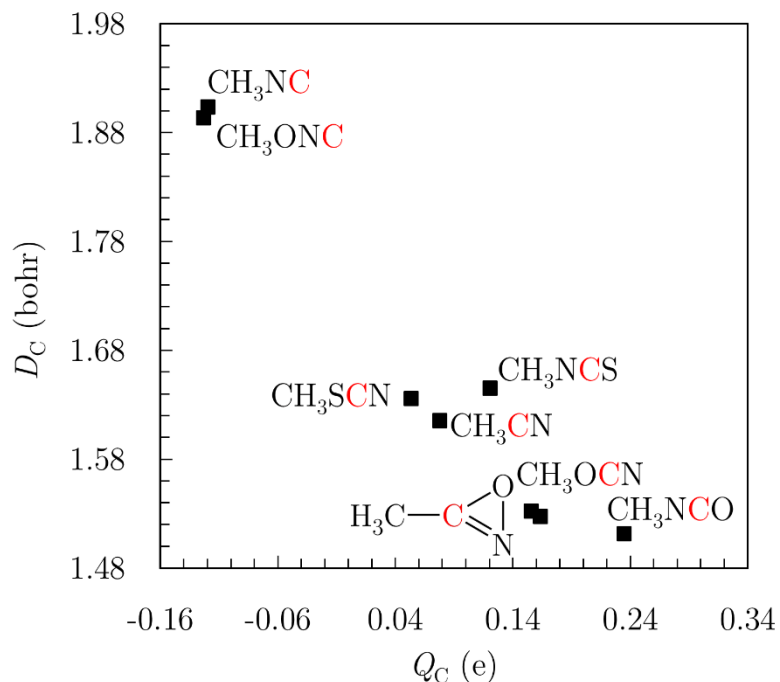


Figure 3.8 Trend in Q_C and D_C of carbon atom in different positional isomers highlighting their relative stability and reactivity.

norborborneide. This relative difference in the acidity of these anions has been attributed to the change in bond order and partial bonding to the double bond.¹⁷⁴⁻¹⁷⁶

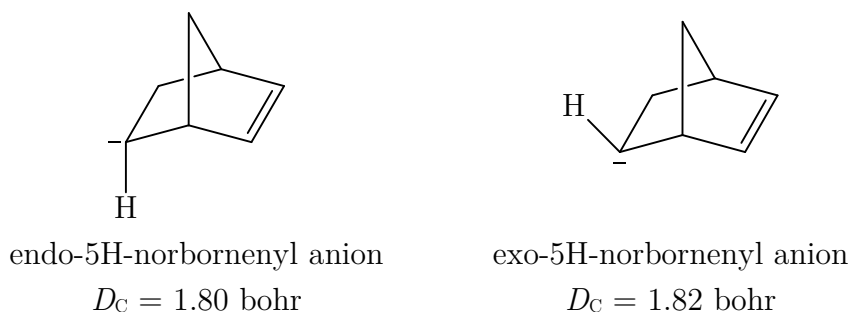


Figure 3.9 Chemical structures and atomic overlap distance of 5-norbornenyl anions isomers

This section is concluded with an example where the atomic average overlap distance provides new insights into the chemical reactivity. The *o*-alkynyl benzamide cyclization Z-5-exo *vs.* E-5-exo selectivity is predicted to depend on the alkenyl anion intermediate in Fig. 3.10.¹⁷⁷⁻¹⁷⁹ While the intermediate's anionic carbon has $Q_C = -0.30$ e, $D_C = 1.70$ bohr nearly identical in Z and E forms, the R = CH₃ group's D_H increases 1.94 bohr (Z) to 1.99 bohr (E). The atomic average overlap distance predicts that the R group C–H bonds are *just the right size, and at just the right distance*, to stabilize the E carbanion. This non-trivial extension of R=NH₂ stabilization¹⁷⁸ is consistent with the lack of E-5-exo products seen for alkynoyls that lack a stabilizing R.²⁷ Simulations predict that additional C–H bond polarization (R = CHF₂) further stabilizes the E-5-exo intermediate, while bulky R = CH₂tBu destabilizes Z-5-exo species. The R = CH₂CH₂NEt₂ group's experimentally demonstrated unusual selectivity to E-5-exo cyclization in CuI/L-proline-catalyzed domino reaction of 2-bromobenzamides and terminal alkynes¹⁷⁹ is rationalized as stabilization of the E-5-exo alkenyl anion intermediate by the R group's many polarized C–H bonds. Though details are sensitive to the simulation conditions, the suggestion that a *Lewis base* stabilizes an *adjacent carbanion* is non-trivial.

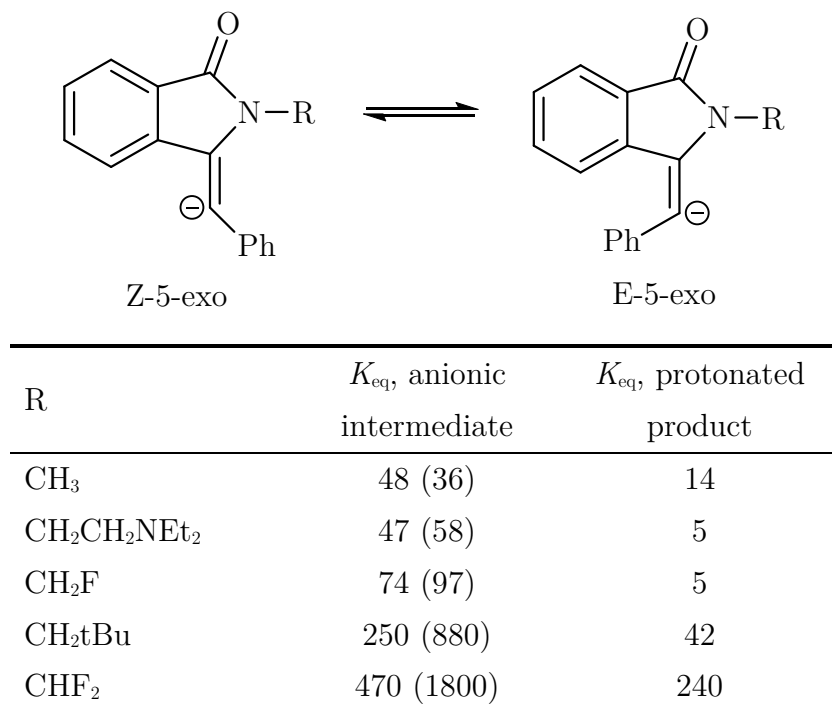


Figure 3.10 (Top) Z:E tautomerization of an alkenyl anion intermediate. (Bottom) Tautomerization equilibrium constants K_{eq} predicted for anionic intermediate and protonated product. Results in parenthesis are computed without continuum solvation.

3.6 Quantifying the Site-dependent Reactivity

The atomic average overlap distance nicely complements the atomic partial charges in capturing the site-dependent reactivity. This can be illustrated by taking the example of gold nanoparticles. Such a particle's catalytic activity¹⁸⁰ is a sensitive function of cluster size and shape, low-coordinated atoms, and support effects.^{102, 181-184} Partial charges alone provides limited insight into which parts of a cluster are most reactive.¹⁸⁵ Fig. 3.11 plots Q_{Au} vs. D_{Au} for 581 Au atoms in 60 cationic gold clusters Au₃⁺-Au₂₀⁺.¹⁸⁶ Small D_{Au} are characteristic of stable Au₁₉⁺ and Au₂₀⁺.¹⁸⁴ Au₅Zn⁺ (triangles), an experimentally observed and theoretically proved all-metal aromatic cluster,¹⁰² has small D_{Au} given the cluster size.

Figure 3.11 provides a nontrivial prediction of site-dependent reactivity in Au_7^+ . Ion mobility experiments confirm the hexagonal structure shown in Fig. 3.11.¹⁸⁶ The atomic average overlap distance predicts that the outer Au atoms have unusually small D_{Au} , while the central atom has an unusually large D_{Au} . Planar Au_9^+ and Au_{10}^+ show similar trends, as does neutral hexagonal Au_7 ($Q_{\text{edge}} = 1.47$ e, $D_{\text{edge}} = 1.07$ bohr, $Q_{\text{center}} = 0.12$ e, $D_{\text{center}} = 1.09$ bohr). Remarkably, this result rationalizes a huge body of experimental and theoretical work on MAu_6 hexagons, in which the central atom is replaced with dopant M. Experimental electron detachment energies and DFT simulations confirm this structure for TiAu_6^- , VAu_6^- , and CrAu_6^- .¹⁸² Infrared photodissociation experiments and simulations confirmed a Jahn-Teller-distorted hexagonal structure for YAu_6 .¹⁸⁷ DFT simulations predict this structure as the global minimum of neutral MAu_6 with $M = \text{Ni}, \text{Pd},$ ¹⁸⁸⁻¹⁹⁰ $\text{Mg},$ ¹⁹¹ $\text{V}^{190, 192}$, $\text{Sc}, \text{Ti}, \text{Cr}^{190}$, and $\text{Mn}^{190, 193}$; near the global minimum of $\text{Ag}_6\text{Fe}^{194}$; and at or near the global minimum of TiAu_6^+ ,

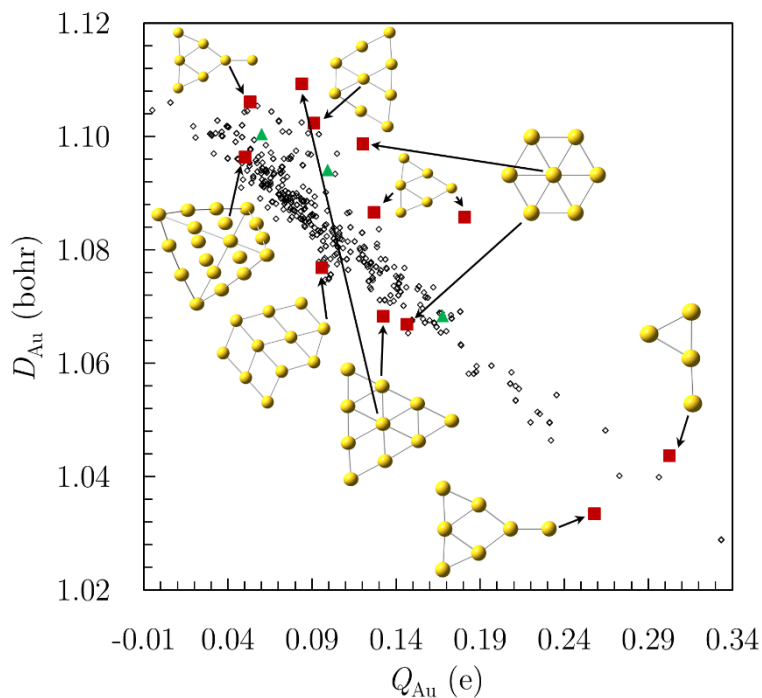


Figure 3.11 Au atom charge *vs.* overlap distance in 60 cationic gold clusters. Chemically interesting outliers are highlighted.

VAu_6^+ , CrAu_6^+ , MnAu_6^+ , and FeAu_6^+ .¹⁹⁵ Simulations also predict that doping to hexagonal TiAu_6^+ or FeAu_6^+ activates the edge atoms to O_2 binding.¹⁹⁶

3.7 Quantifying the Angle Strain Effects

The atomic average overlap distance also detects strain effects. As an illustration, Fig. 3.12 plots Q_C and D_C of propane's central carbon as functions of the C–C–C bond angle. During the calculations, the C–C–C angle was constrained, and the molecule was optimized with all other degrees of freedom. While Q_C gives little indication of strain, D_C is minimized near the equilibrium angle (open diamond) and increases with bond bending. The inset in Fig. 3.12 further confirms that cyclopropane (1), cyclobutene (2), cyclopentane (3), and cyclohexane (4) have D_C increases with ring strain.

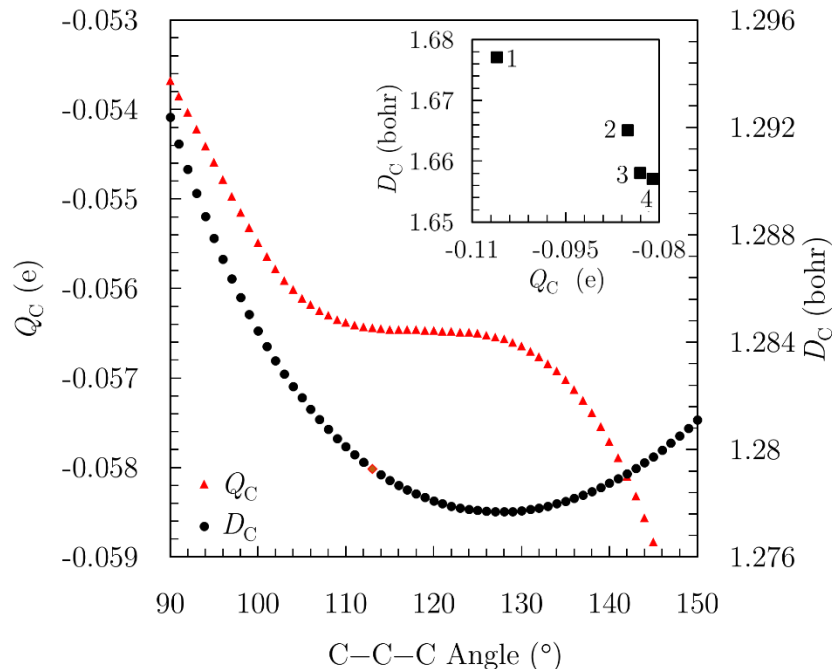


Figure 3.12 Propane's central carbon Q_C (red triangles) and D_C (black circles) plotted vs. C–C–C bond angle. The inset shows the Q_C vs., D_C plot for cyclopropane (1), cyclobutene (2), cyclopentane (3), and cyclohexane (4).

3.8 Concluding Remarks

This work illustrates the applications of atomic average overlap distance to fill the “missing piece” of partial atomic charges and provide a complete picture of the stability and reactivity of different sites in molecules, solids, and nanoparticles. The atomic average overlap distance and partial charges can classify the relative stability of different carbocations and carbanions and can highlight the effects of heteroatoms, substituents, and conjugation in organic compounds. This combination can quantify the reactivity difference between positional isomers and can also distinguish the aromatic compounds from non-aromatic and anti-aromatic system. Analysis of different substituents shows how this combination can be used to fit the experimental Hammett parameters.

3.9 Computational Details

Calculations use the development version of the Gaussian suite of programs.¹⁹⁷ Calculations on organic molecules use density functional theory (DFT) with the 6-31+G(d,p) atom-centred basis set and the long-range-corrected Becke-Lee-Yang-Parr (LC-BLYP) functional appropriate for anions.^{152, 198-200} Calculations on alkenyl anions use a continuum model²⁰¹ for 2-propanol solvent. The table in [Fig. 3.10](#) shows $K_{\text{eq}}=\exp(-\Delta E/RT)$ computed directly from quantum mechanical calculations results using the same level of theory. Calculations on gold clusters use the Perdew-Wang 1991 (PW91)²⁰² GGA, the LANL2DZ relativistic effective core potential, and the associated basis sets^{203, 204} Large molecules including diamond, graphene, and C_{60} are simulated with the 6-31G basis set.

The [table G.7](#) and [G.8](#) of [Appendix G](#) show the methods and basis sets dependence of D_C and Q_C . [Fig. G.1](#) shows the results of [Fig. 3.2](#) obtained using different basis sets. Each basis set produces a global shift in the trends of each substituent, but the trends remain the same.

Chapter 4

Quantifying Protein-ligand Interactions

4.1 Background

Electronic structure simulations using the molecular orbital methods have been proved to be a valuable tool in biological and medicinal chemistry, as illustrated in recent applications to quantitative structure-activity relationships (QSAR),⁸¹ ligand-target interactions,⁸² mechanistic proposals for enzyme catalysis,²⁰⁵ and simulations of entire proteins.⁸⁴ However, orbitals, as a conceptual and interpretative tool, are underutilized in biological and medicinal chemistry. This can be associated with multiple reasons, specifically, the high computational cost for the simulation of macromolecules, the limited information provided by the available orbital based interpretative tools, and the complexity of the obtained results. The common methodology of analyzing one orbital at a time (e.g., frontier orbitals analysis⁴²), which is extensively used for small molecules, though useful in some studies,^{81, 206} (e.g., appropriate in QSAR contexts⁸¹) can be inefficient for large, low-symmetry ligands and active sites. The majority of contemporary computer-aided drug discovery methods, from hit identification, *de novo* design to lead-optimization, rely on computed charges, and force-field parameters obtained mostly from molecular mechanics simulations. However, these methods have shown questionable accuracy in some recent studies^{207, 208} while treating

the non-classical binding effects,²⁰⁹ proton transfer²¹⁰, or metal coordination²¹⁰. For example, the placement of a drug molecule in an active site will necessarily depend heavily on the non-covalent interactions²⁰⁹, which can be poorly described in modern docking engines and scoring functions^{209, 211-214}, especially the aromatic interactions²¹¹. The medicinal chemists often focus on electrostatic and hydrophobic interactions visualized across a biomolecule's entire surface.^{85, 215-217} This has been illustrated in a recent study of 17 α -hydroxylase-17,20-lyase inhibition, where sophisticated density functional theory (DFT) molecular orbital calculations were analyzed solely in terms of computed electrostatic potentials (ESP).²¹⁸ The plots of ESP constructed from electron density obtained from experimental X-ray diffraction based data have also been used extensively for high-throughput screening.²¹⁹⁻²²¹ Many investigators have explored orbital-based conceptual DFT descriptors in biochemistry.²²² Recent examples include the applications of condensed Fukui functions²²³, chemical hardness & softness,^{224, 225} and the electron localization function (ELF).²⁰⁶ However, based on the above-mentioned reasons, these tools are mostly unfamiliar to many experimentalists and remained underutilized as compared to their applications for small molecules.⁷³

The extension of orbital overlap distance as a complement to calculated ESP can provide a valuable addition to these interpretative tools. Combining the molecular density surface plots of ESP and $D(\vec{r})$, and quantitative analysis of these surfaces provides both qualitatively and quantitatively, an easy to use methods of calculations and interpretation of results in terms of the classical hard-soft acid-base (HSAB) concept of chemistry. This chapter demonstrates the applications of this combination to representative problems in biological and medicinal chemistry, including metal-proteins and ligand-proteins interactions. The end of the chapter provides an illustration of the previous medicinal chemistry study of drug candidate electrostatic potentials^{85, 215}, where the overlap distance provides a novel and non-trivial prediction for improving *in vivo* activity.

4.2 Combination of ESP and Overlap Distance – An Illustration

To demonstrate how the combination of ESP and $D(\vec{r})$ distinguishes coordination sites on a single molecule, Fig. 4.1 provides a novel and biologically relevant illustration. Cysteine molecule has three chemically distinct Lewis base sites O, N, S, and can form chelates in many different ways.²²⁶ Fig. 4.1 shows the optimized structure, molecular electron density surface plot of ESP, and $D(\vec{r})$ of a representative conformation of deprotonated cysteine, evaluated in a continuum water solvent. The ESP plot clearly distinguishes the Lewis base sites from the surrounding molecule; however, it cannot much distinguish N (highlighted using letter “A”) from S (highlighted using letter “B”). In contrast, the $D(\vec{r})$ plot clearly distinguishes the large orbital lobes of the chemically “soft” S Lewis base from the “harder” O (highlighted using letter “X”) and N Lewis bases. The quantitative analysis of these surfaces shows how the maximum values of ESP and $D(\vec{r})$ on highlighted regions of O (ESP = -0.25 au, $D(\vec{r})$ = 3.00 bohr), N (ESP = -0.18 au, $D(\vec{r})$ = 3.15 bohr) and S (ESP = -0.15 au, $D(\vec{r})$ = 3.45 bohr) rationalize these differences.

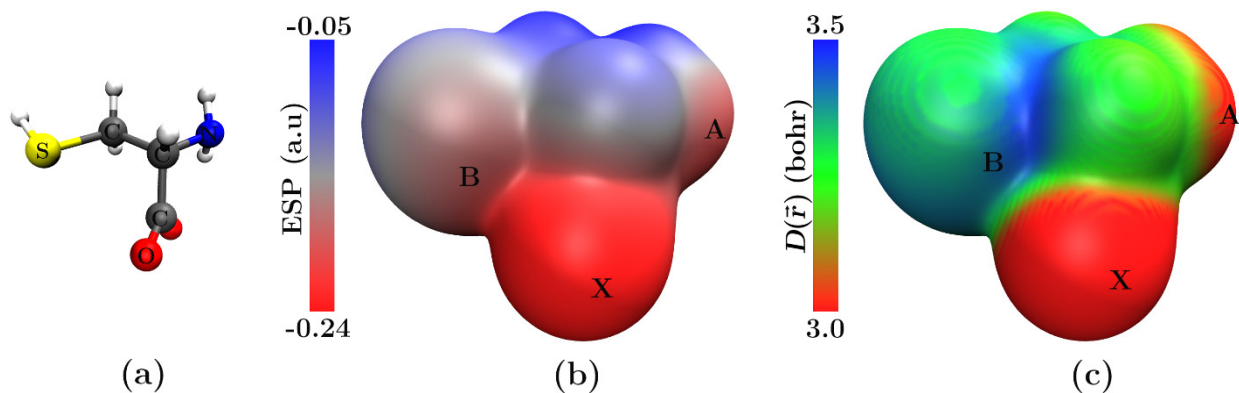


Figure 4.1 (a) Optimized structure and 0.001 e/bohr³ electron density molecular surfaces of (b) electrostatic potential and (c) overlap distance of deprotonated cysteine. The regions highlighted using letters point to positions of ESP and $D(\vec{r})$ extrema of S, N and O atoms.

As mentioned in the previous chapter (Fig. 3.1), ESP (hence atomic partial charges) and overlap distance, in general, have a chemically reasonable correlation. The addition of the electron density to a particular region on a molecule enhances the negative ESP of that region and makes orbital lobes large, *i.e.*, diffuse, which in turn makes the $D(\vec{r})$ larger. However, the differences between O, N, and S Lewis bases in Fig. 4.1 show that the $D(\vec{r})$ provides additional information beyond the electrostatic potential alone, for example, $D(\vec{r})$ highlights the diffuse lone pairs of S atom.

4.3 Visualizing Protein-ligand Interactions

This section describes the rationalization of protein-ligand interactions using the ESP and $D(\vec{r})$ combination. It details how this combination can capture the non-covalent interactions between binding-pockets of protein and ligands in terms of the HSAB concept. Two diverse protein model systems are considered in this section, which involves a variety of chemically hard and soft atoms.

4.3.1 Avidin-Biotin Binding

The avidin family proteins have been used for many decades as an essential biotechnological tool for analysis²²⁷ and drug development²²⁸ due to their extraordinarily high affinity^{229, 230} for biotin through noncovalent interactions and ultrahigh stability of avidin-biotin complex^{230, 231}. The binding site of avidin consists of an array of polar and aromatic residues providing a variety of noncovalent interactions, which are responsible for the recognition and optimization of biotin in the binding site.²³⁰ The aromatic amino acid residues Trp70, Phe72, Phe79, and Trp97, develop a hydrophobic region around the binding site and polar residues Thr35, Thr77, Ser16, Ser73, Ser75, Asn12, Asn118, and Tyr33 stabilize the complex through a network of multiple hydrogen bonds. The combination of ESP and $D(\vec{r})$ elaborates the selectivity of the binding pocket for the biotin molecule.

Figure 4.2 depicts the orientation of the biotin molecule in the binding pocket and its molecular electron density surface plots of ESP and $D(\vec{r})$. ESP surface plot (Fig. 4.2b) shows that the oxygen atoms of valeryl carboxylate moiety and ureido ring are negative regions (red color), *i.e.*, Lewis basic sites or hydrogen bond acceptors. In contrast, both ureido nitrogen atoms are positive regions (blue color), *i.e.*, Lewis acidic sites or hydrogen

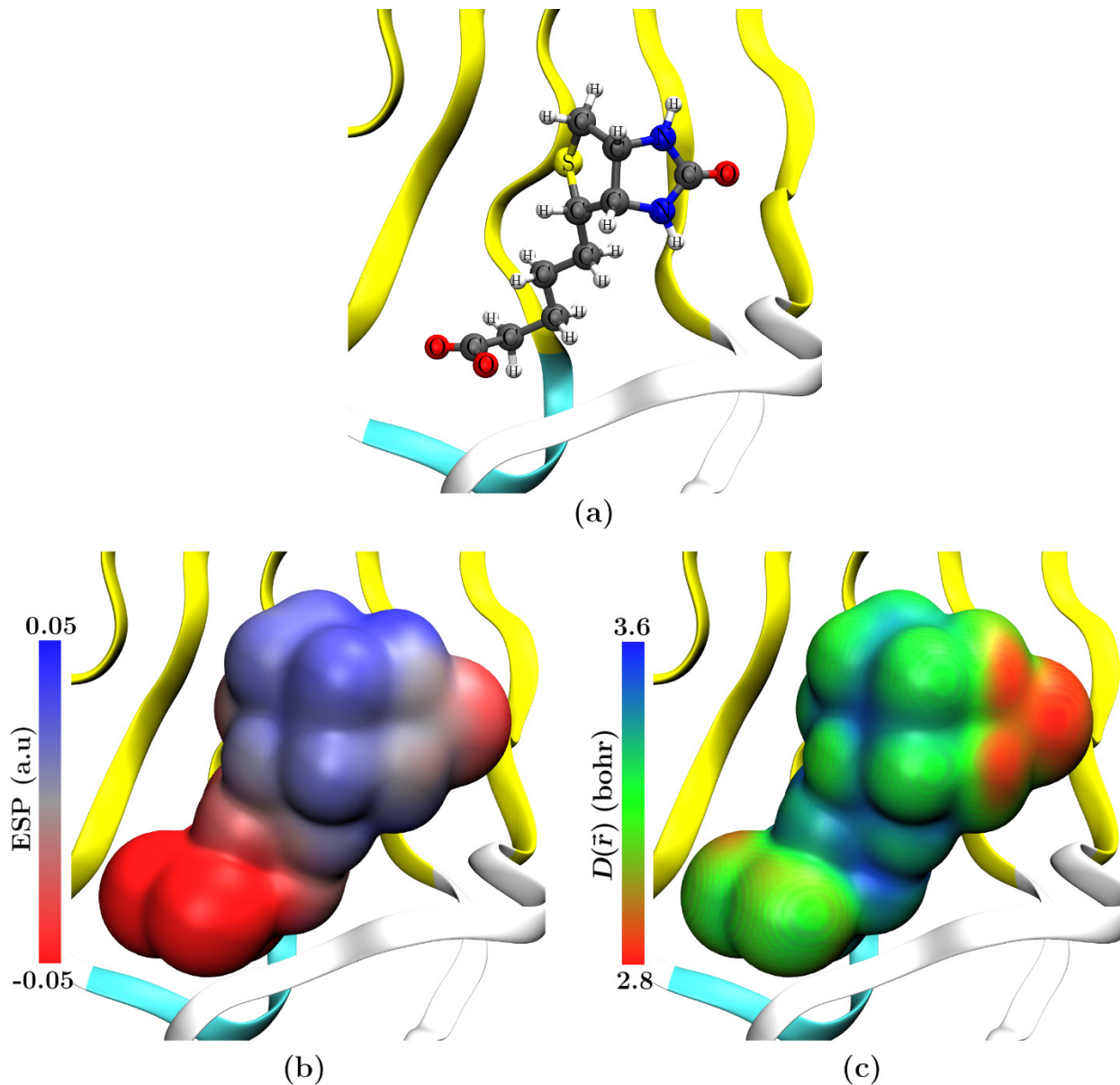


Figure 4.2 Graphic depictions of biotin molecule inside the binding pocket of streptavidin; (a) molecular geometry, and 0.001 e/bohr^3 electron density molecular surface plots (b) electrostatic potential (c) overlap distance.

bond donors. The sulfur atom of tetrahydrothiophene ring is also a relatively negative site. The $D(\vec{r})$ plot in Fig. 4.2(c) shows that the overlap distance in the Lewis acidic sites is small (red) corresponds to the compact orbitals of small lobes, whereas it is large (green) in the Lewis basic sites due to the large and diffuse orbital lobes. These observations revealed that the value (color intensity) of $D(\vec{r})$ is different on the oxygen atoms of valeryl carboxylate, ureido ring, and sulfur sites. Hence the overlap distance distinguishes the diffuse, soft Lewis basic sites from the compact, hard basic sites on the biotin molecule, which are responsible for its compact binding in avidin family proteins.

Molecular ESP and $D(\vec{r})$ plots on the active site surface of streptavidin are shown in Fig. 4.3. These plots highlight different hydrogen bond donor and acceptor regions on the surface of the binding pocket. Regions labeled as “A” and “B” in Fig. 4.3(a) shows the Lewis acidic sites (blue; positive ESP) or hydrogen bond donor $-OH$ groups of Ser73, Ser75,

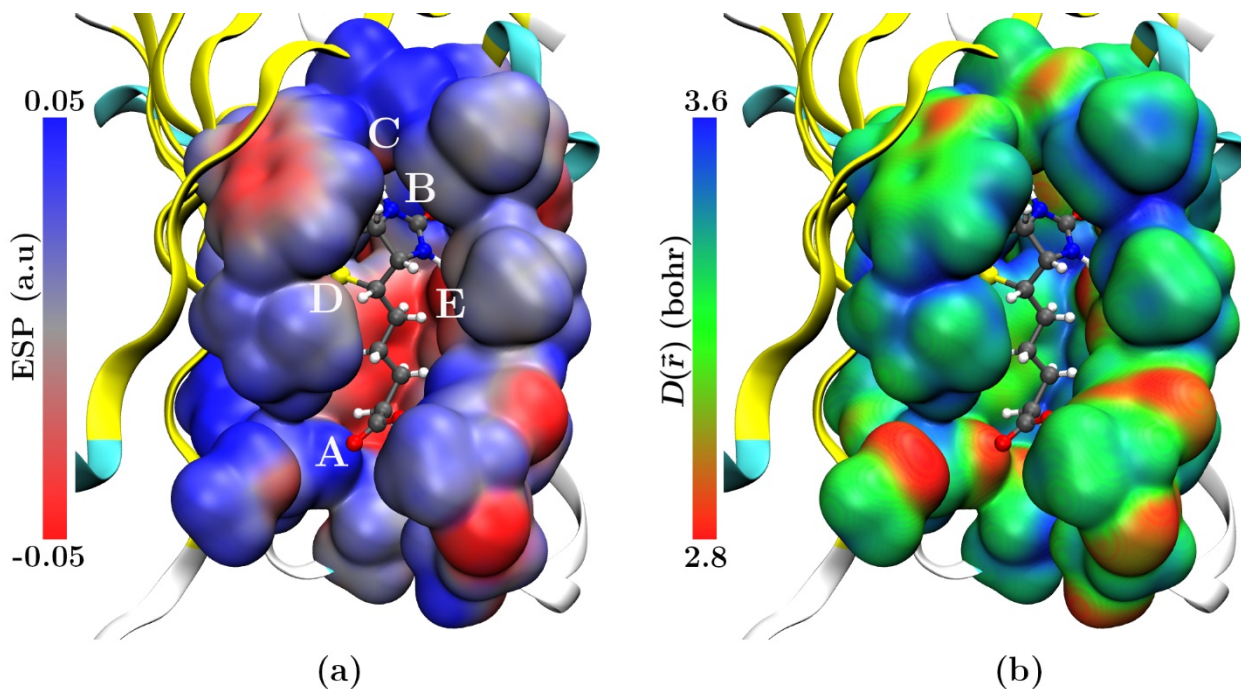


Figure 4.3 $0.001 \text{ e}/\text{bohr}^3$ molecular electron density surface plots of streptavidin binding pocket; (a) electrostatic potential (b) overlap distance. The important regions involved in binding interactions are highlighted using letters.

and Ser16, Tyr33 respectively whereas, regions labeled as “C” and “E” shows Lewis basic sites (red; negative ESP) or hydrogen bond acceptor oxygens of Tyr33, Asn118, and Thr35 respectively. The region labeled “D” represents the surface of Thr77 hydroxyl group. The active site's Lewis acidic (A and B) and basic (C and E) regions are perfectly aligned with biotin's hydrogen bond donors and acceptors. The overlap distance $D(\vec{r})$ plot in Fig. 4.3(b) shows that the localized, chemically “hard” Lewis acids and bases interacting with the uriedo ring (the region surrounding “B”) are clearly distinguished from the chemically “soft” Lewis acids interacting with the tetrahydrothiophene sulfur (region “D”). The relative comparison of $D(\vec{r})$ molecular surface plots of both ligand (Fig. 4.2) and binding pocket (Fig. 4.3) clearly distinguishes the interactions between chemically hard and soft Lewis acids and bases of biotin with corresponding regions of avidin which are responsible for selective biotin complexation. This illustrates the power of ESP and $D(\vec{r})$ surface plots to capture and distinguish each interaction involved in protein and ligand binding.

4.3.2 Thyroxine-Globulin Binding

The second example considers the thyroxine-binding globulin (TBG) complex. Thyroxine is the major hormone controlling mammalian activity, cellular development, regulating cellular oxygen consumption and the metabolism of body and brain.^{232, 233} The concentrations of thyroxine in the tissues and its control release is significantly important because its higher concentration leads to hyperactivity and its deficiency develops dormancy.^{232, 234} In the blood, thyroxine is carried by thyroxine-binding globulin (TBG) enzyme, which exhibits very strong binding affinity for this molecule.²³⁵ Similar to the biotin, the thyroxine molecule contains various hydrogen bond donors and acceptors atoms, but its distinguishable characteristic is the four iodo groups present in different chemical environment on the molecule. The thyroxine ligand combines a chemically hard peptide, a relatively soft and weak Lewis base on the phenyl groups, a soft and strong Lewis basic iodine lone pairs, and

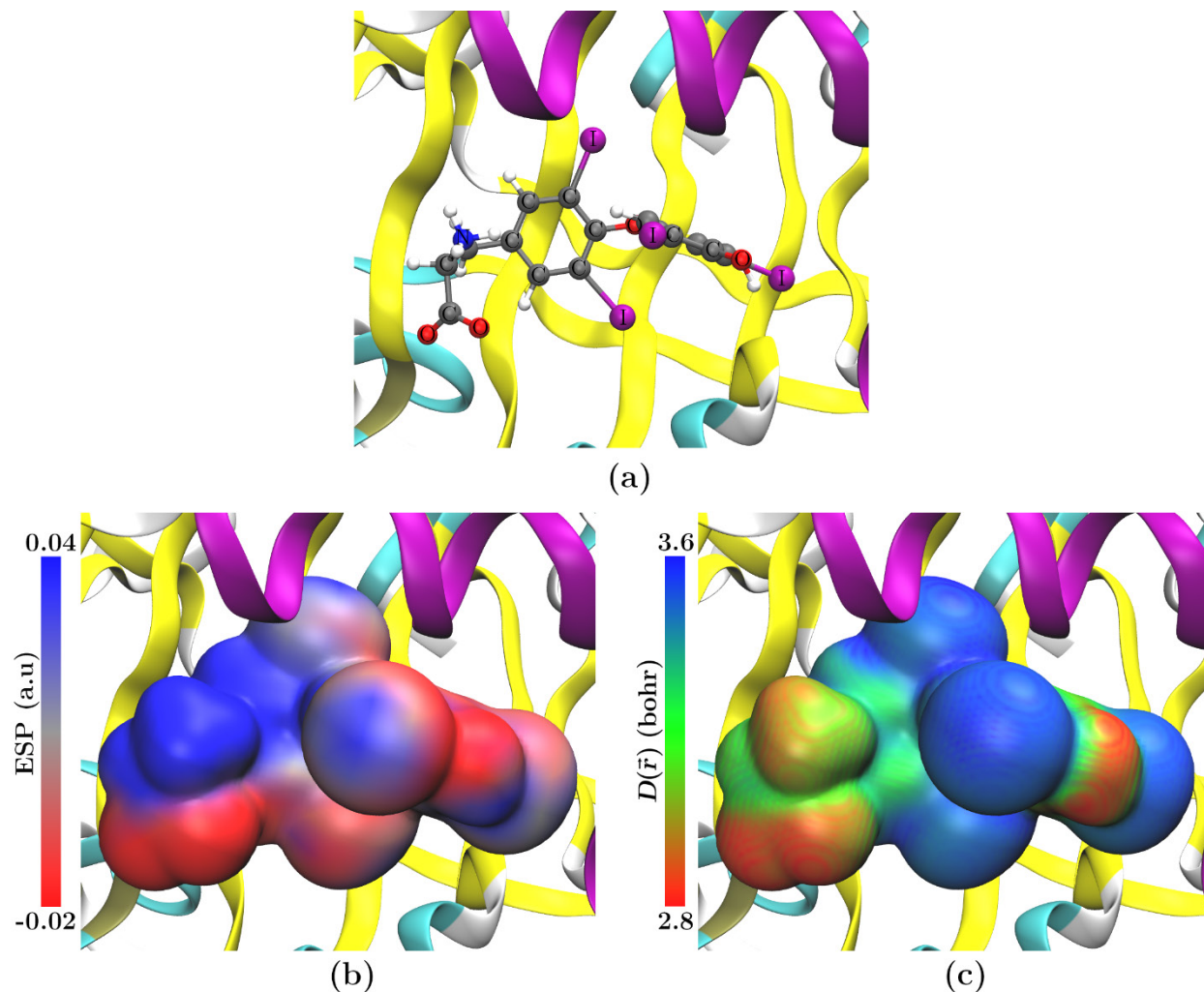


Figure 4.4 Graphic depictions of thyroxine molecule inside the binding pocket of TBG; (a) molecular geometry, and 0.001 e/bohr^3 electron density molecular surface plots (b) electrostatic potential (c) overlap distance.

a soft and moderately strong Lewis acid as the iodine σ -holes¹⁰³ visible in Fig. 4.4. The amino propionate, phenolic group, and carboxylic group are negative regions, *i.e.*, Lewis-basic sites of the molecule. The molecular surface plots show that $D(\vec{r})$ on the four iodine sites is large, highlighting their chemically soft nature due to their diffuse orbitals. The overlap distance of oxygen atoms surface is small and shows that electrons are more localized in compact orbitals and highlight their chemically hard characteristics. It is interesting to note that the amino propionate group ($\text{ESP} = -0.047 \text{ au}$, $D(\vec{r}) = 3.00 \text{ bohr}$) and carboxylic

oxygen (ESP = -0.047 au, $D(\vec{r}) = 2.76$ bohr) have an equal charge but different overlap distance which distinguishes former as a soft Lewis-basic site as compared to latter. The oxygen atom (ESP = -0.025 au, $D(\vec{r}) = 2.89$ bohr) bridging the tyrosine and phenolic groups is less negative compared to phenolic oxygen (ESP = -0.042 au, $D(\vec{r}) = 2.79$ bohr) but its large overlap distance shows that it is more diffuse and is a soft Lewis basic site.

Figure 4.5 shows the molecular ESP and $D(\vec{r})$ plots of the thyroxine-binding site in TBG and highlights the different hydrogen bond donor and acceptor regions. As expected, the regions with negative ESP have relatively large overlap distance (chemically soft). Generally, the binding pocket has a large $D(\vec{r})$, while the outside of the pocket has a small $D(\vec{r})$, which indicates that the overall binding pocket is mostly chemically soft. Specifically, the Lewis acidic groups of active sites labeled as “A”, “C” and “E” and Lewis basic groups highlighted as “B”, and “D” are aligned with thyroxine's hydrogen bond donors and acceptors respectively. Region “A” shows the hydrogen bond donor-acceptor interaction of carboxylic oxygen and nitrogen of Arg378. Regions “C” and “D” show that soft iodine of

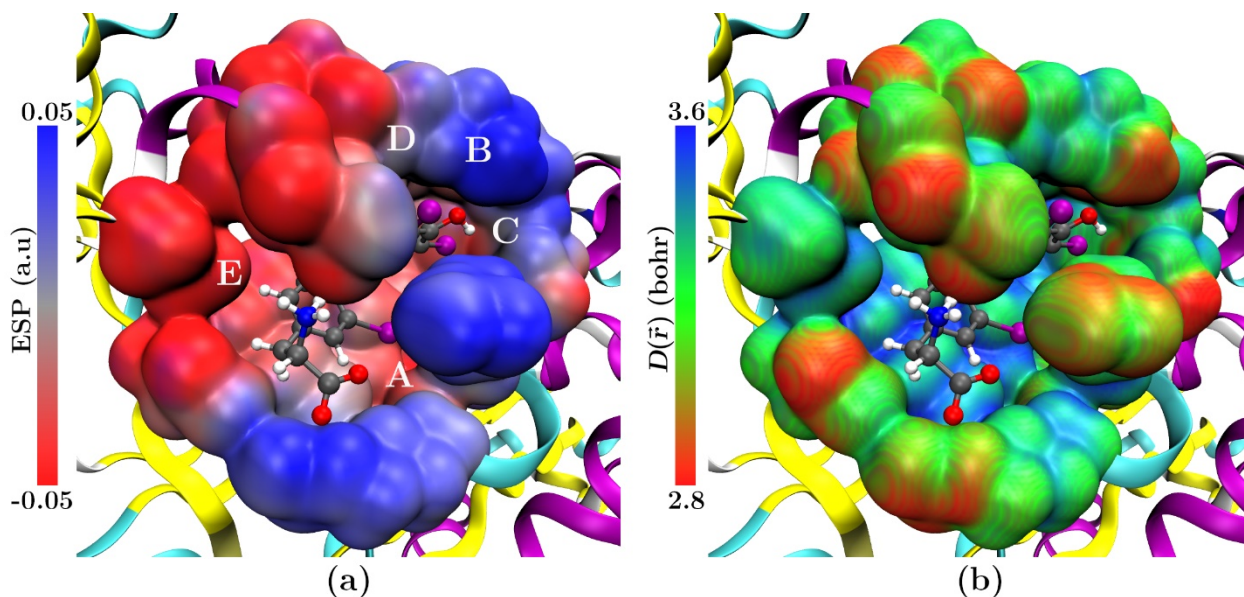


Figure 4.5 0.001 e/bohr³ molecular electron density surface plots of TBG binding pocket; (a) electrostatic potential (b) overlap distance. The important regions involved in binding interactions are highlighted using letters.

thyroxine interacts with soft regions of active sites, which mostly involves the backbone carbon and hydrogen atoms. Region “E” indicates the relatively soft backbone carbon atoms of Leu276 interacting with soft carbon and hydrogen of the amino propionate group. These results again establish that the combination of ESP and $D(\vec{r})$ form a unique tool to rationalize the binding of ligands in proteins and provide an opportunity to interpret these binding interactions in terms of classical concepts of chemistry.

4.4 Quantifying Protein-metal Interactions

This section extends the applications of overlap distance to elaborate the selective binding of metal ions to metalloproteins. Two examples are considered, first involves the protein which has binding pockets for a single metal atom type, and the second includes the proteins which have binding pockets selective for two different types of metal ions.

4.4.1 Gold–GolB Binding

Some bacteria such as *Salmonella typhimurium*, *Salmonella enterica* and *Cupriavidus Metallidurans* use gold selective MerR-type transcriptional regulators and metallochaperones to detect the presence of toxic gold ions, even at very low concentrations.²³⁶⁻²³⁹ These metalloregulatory proteins can distinguish Au^+ from Cu^+ or Ag^+ and competitively binds to toxic gold ions.^{237, 238} This high selectivity for Au^+ ions disable them to affect the functioning of other metalloregulatory proteins, especially the Cu^+ trafficking proteins²³⁶. The putative gold-chaperone, GolB from *Salmonella typhimurium* is a typical example that selectively binds the soft Lewis acid Au^+ with much higher affinity as compared to those metals which are even moderately soft Lewis acid such as Cu^+ .²⁴⁰ It uses a conserved binding site involving the thiolates of Cys10 and Cys13, making it an ideal system where hard-soft acid-base interactions are essential. Though the rupture forces for Cu–S bond in GolB binding pocket, estimated using AFM-based SMFS methods, are

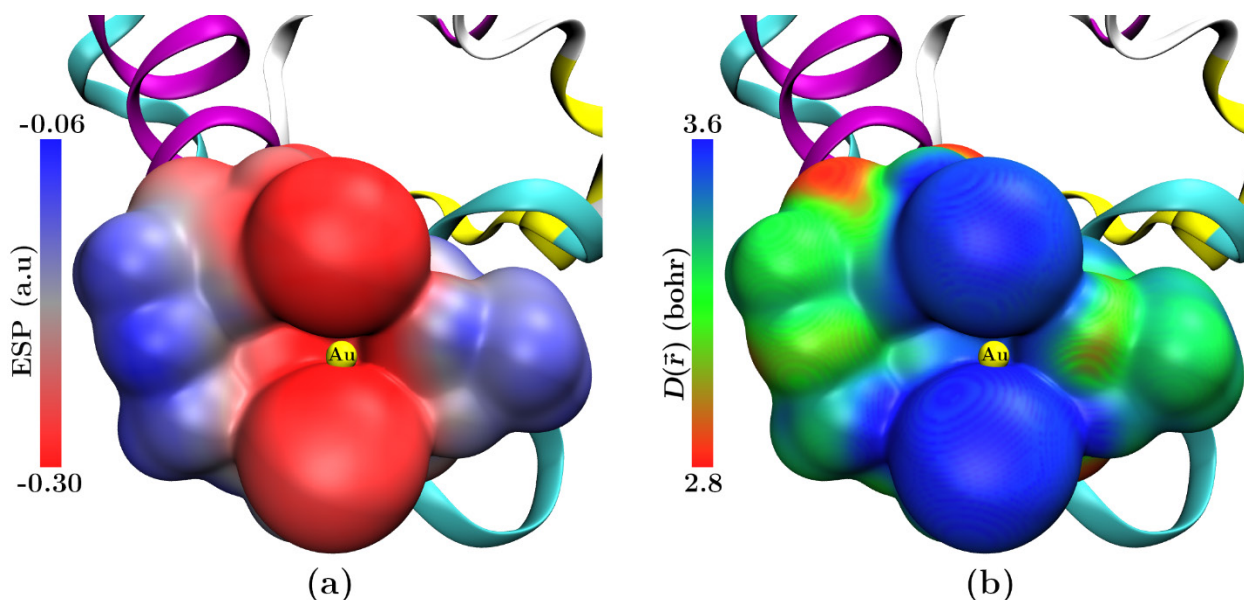


Figure 4.6 0.001 e/bohr³ molecular electron density surface plots of GolB binding pocket holding Au⁺ atom; (a) electrostatic potential (b) overlap distance. Au⁺ ion in the pocket is shown using a yellow sphere.

comparable to those of the Au–S bond, but there is a significant difference in the binding affinities of Au⁺ and Cu⁺.²³⁶ The combination of the surface ESP and $D(\vec{r})$ plots captures these experimental observations of selective binding in GolB.

Figure 4.6 shows that the surface ESP plots of thiolates in the binding pocket of GolB are mostly negative, making the binding site a Lewis base. The value of minimum surface ESP in the region of Au⁺ binding is calculated to be -0.293 au. The surface $D(\vec{r})$ plots show that the thiolates of binding pocket have a large overlap distance compared to the other regions of the surface with maximum surface $D(\vec{r})$ calculated to be 3.692 bohr. The combinations of surface ESP and $D(\vec{r})$ plots establish that the binding pocket is a chemically soft Lewis basic site. Gas-phase calculations of isolated Au⁺ and Cu⁺ ions at ω B97X-D/cc-pVDZ level of theory using effective core potential, complement the experimental findings. Though Cu⁺ (ESP = 0.304 au, $D(\vec{r})$ = 1.789 bohr) is more positive compared to Au⁺ (ESP = 0.270 au, $D(\vec{r})$ = 2.030 bohr), but small overlap distance makes

it a probably harder Lewis acid as compared to Au^+ which is a preferred candidate for this binding site due to its large overlap distance, *i.e.*, soft Lewis acidic character. These findings of $D(\vec{r})$ further complement the absolute hardness (η) of ions ($\text{Cu}^+ = 6.28 \text{ eV}$ *vs.* $\text{Au}^+ = 5.6 \text{ eV}$)²⁴¹ calculated using their experimental ionization potentials and electron affinities.

4.4.2 Selective Binding in Formylglycine-Generating Enzyme

The second example provides an insight into the selectivity of two binding pockets on the same protein. Formylglycine-Generating Enzyme (FGE), recognized as a powerful tool in protein engineering²⁴²⁻²⁴⁷ is a unique copper protein which catalyzes the oxygen-dependent conversion of specific cysteine residues of arylsulfatases and alkaline phosphatases on client proteins to formylglycine.^{244, 248} Insufficiency of FGE in human cells causes multiple sulfatase deficiencies, which is a rare but fatal disease.^{249, 250} Cu^+ is an integral cofactor of this enzyme²⁵¹ with very high binding affinity²⁴⁴ and has been reported to increase the *in vitro* activity of FGE up to 20 fold.²⁴⁸ Cu^+ binding pocket constitutes the sulfhydryl groups of two cysteines Cys269 and Cys274.²⁴⁴ This binding pocket can also bind Ag^+ ions with nearly equal selectivity, but the binding of Cd^{2+} on the same pocket involves some specific conformational changes at the active site.²⁴⁴ The crystal structure used in the present studies, reported by Meury *et al.*,²⁴⁴ was crystallized using Ag^+ , a redox-stable Cu^+ mimic. FGE also contains binding sites for two Ca^{2+} ²⁴⁴ ions labeled as Ca1 and Ca2 in Fig. 4.7. The binding site of Ca1 consists of a carboxylate group of Asp202 and hydroxyl groups of Ile189, Asn188, and Tyr204 in addition to a coordinated water molecule, whereas the hydroxyl groups of Asn222, Val223, Gly225, and Val227 constitute the binding site for Ca2. Surface ESP and $D(\vec{r})$ plots distinguish the hard-soft acid-base selectivity of binding pockets for relatively hard Lewis acid Cu^+ , Ag^+ , and Cd^{2+} from the relatively soft Lewis acid Ca^{2+} .

Figure 4.7 (a and b) plots the molecular ESP surfaces of Cu^+ and Ca^{2+} binding pockets. The two Ca^{2+} binding sites have a high concentration of negative charge due to

the involvement of carboxylate and hydroxyl groups. This high concentration of negative charge is visible as bright-red regions in the ESP plot, clearly distinct from the other regions of the enzyme surface. Hence, the surface ESP provides an opportunity to visibly locate the Ca^{2+} binding sites. The binding pocket of Cu^+ is less negative, *i.e.*, weak Lewis basic site as compared to the binding pockets of Ca^{2+} due to the involvement of less electronegative sulfur atoms of cysteine residue and is not visible on the ESP surface as a distinct bright-

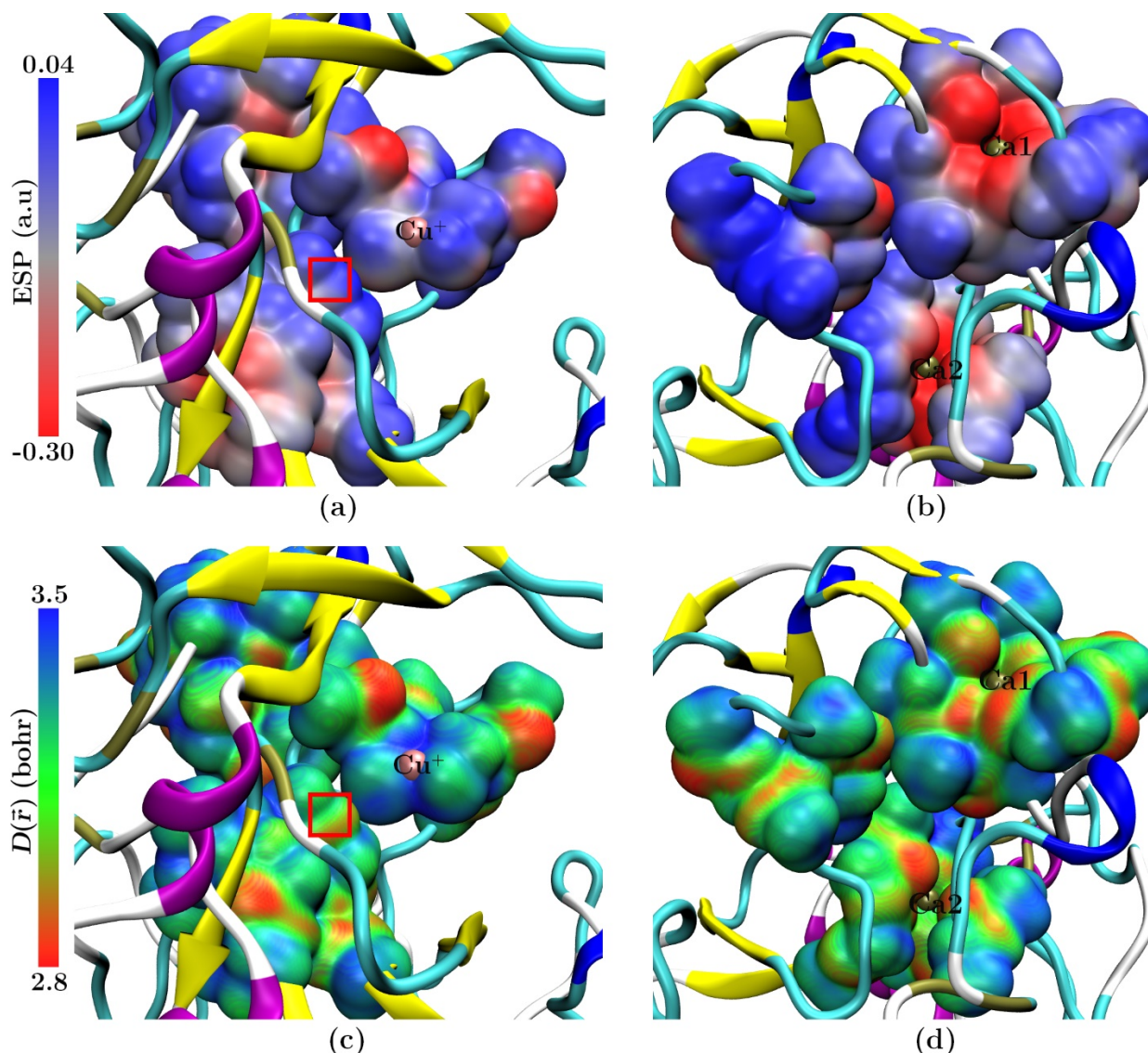


Figure 4.7 0.001 e/bohr^3 molecular electron density surface plots of FGE binding pocket; (a) ESP of Cu^+ binding pocket, (b) ESP of Ca1 and Ca2 binding pockets, (c) $D(\vec{r})$ of Cu^+ binding pocket and (d) $D(\vec{r})$ of Ca1 and Ca2 binding pockets. Red box indicates representative regions with similar ESP but different $D(\vec{r})$.

red region. Therefore, the binding pocket of Ca^{2+} ions is a more Lewis basic site as compared to the binding pocket of Cu^+ . The minimum surface ESP values were calculated to be -0.009 au and -0.410 au for Cu^+ and for both Ca^{2+} binding pockets, respectively. The $D(\vec{r})$ surface plots of both Cu^+ and Ca^{2+} binding pockets in Fig. 4.7 (c and d) exhibit that the binding pocket of the former, though, is less negative but chemically soft site due to its large overlap distance (3.461 bohr) compared to that of the latter (2.853 bohr and 2.916 bohr for Ca1 and Ca2 binding pockets respectively). These plots of orbital overlap distance show the chemically “soft” cysteine Lewis bases in the high-affinity Cu^+ binding site as a bright-blue region and the “harder” Ca^{2+} binding sites as bright-red regions. This distinguishes the region that binds Cu^+ , which was not possible with ESP plots alone. Given both the ESP and $D(\vec{r})$ plots, it would be more straightforward to distinguish the locations of all three binding sites visibly.

The gas-phase calculations performed on isolated metal ions show that both Cu^+ (ESP = 0.304 au, $D(\vec{r}) = 1.789$ bohr) and Ag^+ (ESP = 0.283 au, $D(\vec{r}) = 1.893$ bohr) have nearly similar surface charge and overlap distance which explains how these two metal ions compete for this binding sites and also complements the experimental findings that Ag^+ is an excellent mimic of Cu^+ in copper transporting ATPases,^{252, 253} copper sensing transcription factors,²⁵⁴⁻²⁵⁶ and copper chaperones^{257, 258}. The bivalent Cd^{2+} (ESP = 0.625 au, $D(\vec{r}) = 1.778$ bohr) though has a higher surface charge compared to both Ag^+ and Cu^+ , but its nearly same value of $D(\vec{r})$ makes it a competitor for this binding site which has also been reported experimentally²⁴⁴. The calculations on isolated Ca^{2+} ion demonstrate that its higher surface charge and just the right size of $D(\vec{r})$ agrees well with the binding pocket, highlighting its selective binding to this particular binding pocket.

4.5 Applications for Structure-based Drug Design

Previous sections have demonstrated the power of ESP and $D(\vec{r})$ to capture and distinguish the selectivity of binding pockets in enzyme and corresponding distinction in the chemistry of various interactions sites on the surface of the ligand. These findings encourage to extend the applications of this combination for drug design. This section provides two examples explaining how this combination can provide the nontrivial predictions in structure-based drug design.

4.5.1 Promiscuous Binding

It has been identified that rhodanines are problematic “promiscuous hitters” that interact nonspecifically with many targets.^{259, 260} However, other studies suggest that rhodanines are “privileged scaffolds” useful in drug design.^{206, 261} A recent experimental and computational study suggested that rhodanines' HOMO orbital and negative ESP are strongly localized at the exocyclic sulfur, and attributed this to rhodanine's distinct intermolecular interaction profile.²⁰⁶

Figure 4.8 shows the HOMO-1 orbitals, ESP, and $D(\vec{r})$ surfaces of the benzylidene-substituted rhodanine derivative studied previously.²⁰⁶ The surface ESP minimum (Fig. 4.8b) occurs on the exocyclic oxygen, not on the less electronegative exocyclic sulfur. On the contrary, the $D(\vec{r})$ is largest (Fig. 4.8c) on the exocyclic sulfur, consistent with the HOMO-

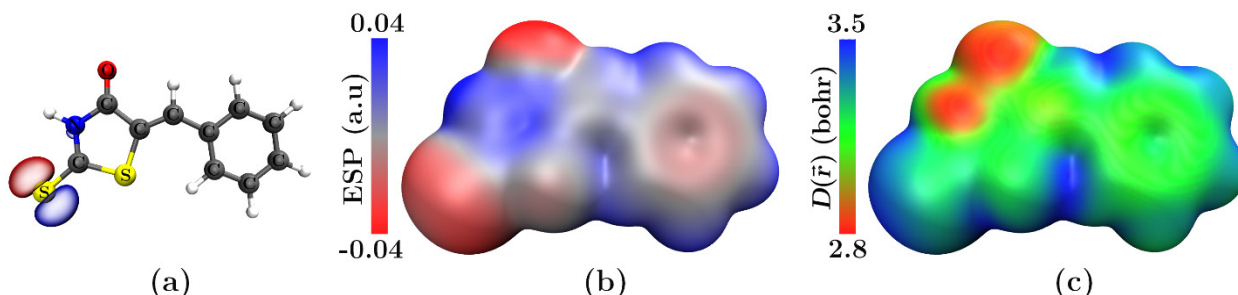


Figure 4.8 (a) Optimized geometry and HOMO-1 and 0.001 e/bohr³ molecular electron density surface plots of (b) ESP, and (c) $D(\vec{r})$ of benzylidene-substituted rhodanine.

1 orbital. The overlap distance is relatively large (blue) on the exocyclic sulfur, distinguishing it from the more compact exocyclic oxygen (red) and aromatic sulfur (green). Quantitatively, Hirshfeld charges analysis shows that the exocyclic sulfur has atomic $Q_s = -0.22e$ and valence $D_s = 1.94$ bohr, substantially larger than the ring sulfur ($Q_s = +0.04e$, $D_s = 1.85$ bohr) and less charged but more diffuse than the exocyclic oxygen ($Q_o = -0.28e$, $D_o = 1.32$ bohr). Chemically, it can be suggested that rhodanines' exocyclic oxygen and sulfur have reactivity qualitatively similar to deprotonated amides. Deprotonated amides perform a nucleophilic attack by the less negative nitrogen atom, rather than the more negative oxygen atom, consistent with the nitrogen atom's substantially larger orbital overlap distance.⁸⁸ Therefore, based on these findings, it can be suggested that rhodanine's promiscuous binding arises due to the presence of both hard and soft anionic regions, involving the less negative exocyclic sulfur, rather than just the more negative exocyclic oxygen, consistent with the former's substantially larger orbital overlap distance.

4.5.2 Designing of CENP-E Inhibitor

The second example adopts the pattern of structure-activity relationship studies guided by molecular orbital calculations. This example revisits a series of studies by Hirayama *et al.*, developing centromere-associated protein-E (CENP-E) inhibitors.^{85, 215} CENP-E is a mitotic spindle motor protein and a promising target for cancer therapies. A combination of high-throughput screening, structure-activity relationship measurements, and homology model docking identified lead compound 6a shown in Fig. 4.9 (numbering is taken from the experimental references). The structure-activity relationship (SAR) analysis in these reported studies was performed by visual inspection of the computed ESP maps. Based on these inspections, it was suggested that *in vitro* activity was correlated with a neutral ESP on the aromatic ring moiety, the region highlighted with black boxes in Fig. 4.9. However, compound 6a possessed insufficient cellular activity despite its neutral aromatic ring. This

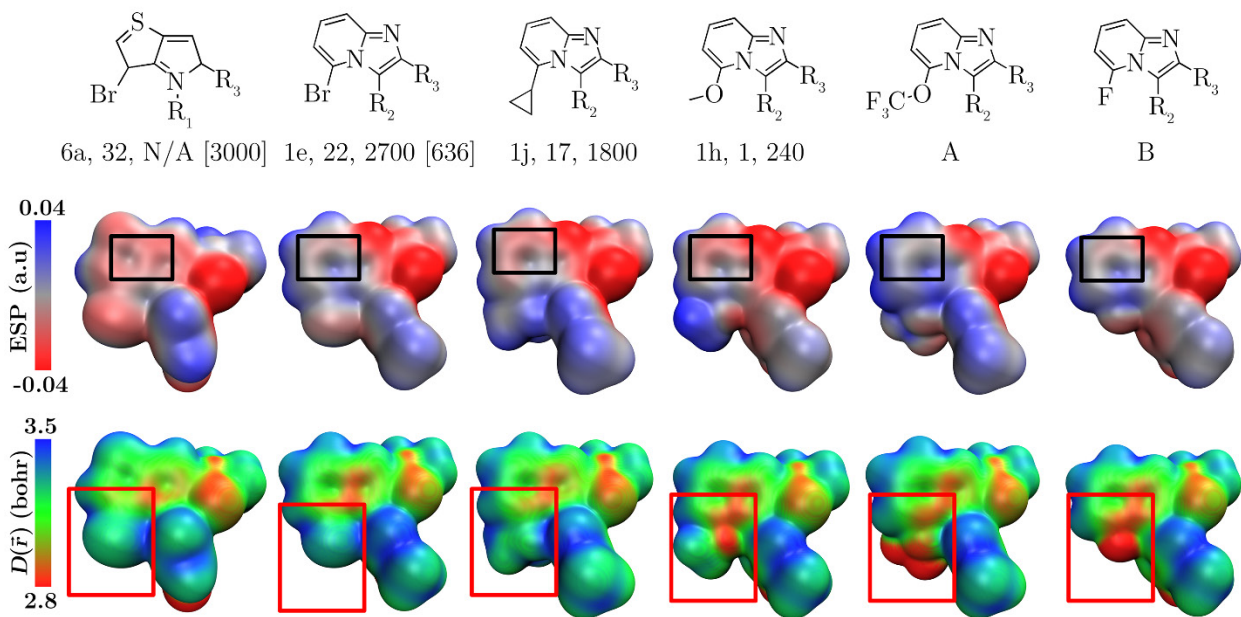


Figure 4.9 (top) Structures, *in vitro* CENP-E IC_{50} values (in nM), and *in vivo* HeLa cell proliferation values (in nM) [p-HH3 EC_{50} (nM)] of CENP-E inhibitors 6a, 1e, 1j, and 1h and inhibitors A and B proposed here. R_1 = *p*-fluorobenzene; R_2 = *m*-methyl-*p*-fluorobenzene; R_3 = C(=O)N(C₂H₄NMe₂)PhCl₂. 0.001 e/bohr³ molecular electron density surface plots of (middle) predicted ESP and (bottom) $D(\vec{r})$ of the fused-ring regions. The neutral fused-ring ESP (black boxes) was previously shown to be correlated with the *in vitro* activity.

motivated the synthesis of new lead 1e, whose neutral aromatic region was combined with higher *in vivo* activity. Subsequent derivatization produced improved species 1j and 1h, leading to the eventual identification of a potent 5-methoxy imidazo[1,2-*a*]pyridine derivative.

Figure 4.9 shows the structures, measured *in vivo* and *in vitro* activities, and computed surface ESP and $D(\vec{r})$ of 6a, 1e, 1j, and 1h. Fig. 4.9 also adds the computed structure, ESP, and $D(\vec{r})$ of two new compounds A and B proposed in this work. The computed ESP plots follow the previously reported trends²¹⁵, *i.e.*, all of these compounds having high *in vitro* activity have relatively neutral ESP on the fused-ring system represented using black boxes. The $D(\vec{r})$ surface plots provide a new and nontrivial

prediction that *compact substituents with small overlap distance in the aromatic ring region improve in vivo activity*. Substitution 6a to 1e replaces the relatively large $D(\vec{r})$ of the thiophene S with the smaller $D(\vec{r})$ of the imidazole group. Substitution 1e to 1j and to 1h further replaces the relatively large $D(\vec{r})$ of the bromo substituent with the smaller $D(\vec{r})$ of the cyclopropyl and methoxy groups. This smaller $D(\vec{r})$ is visible in Fig. 4.9 as green for compound 1j and red for compound 1h. Compounds with high *in vivo* activity appear to have a small $D(\vec{r})$ in this region.

Based on this analysis, it is predicted that replacing methoxy with a trifluoromethyl ether or a fluoro substituent, a strategy increasingly adopted in medicinal chemistry and drug discovery,²⁶² gives novel compound A and B respectively which will exhibit improved *in vivo* activity. Both of these compounds have not been previously proposed as a CENP-E inhibitor. Fig. 4.9 shows that both A and B combine a relatively neutral ESP in the aromatic ring moiety with a small $D(\vec{r})$ in the region of the aromatic ring substituents. On this basis,

it is predicted that these compounds will exhibit higher activities than 1h. It is therefore further predicted that replacing the corresponding methoxy with a trifluoromethyl ether or fluoro substituent in the final reported⁸⁵ imidazo[1,2-a]pyridine derivative (+)-12 could provide additional increases in the activity. Fig. 4.10 shows the full chemical structure of (+)-12 and of these proposed CENP-E inhibitors.

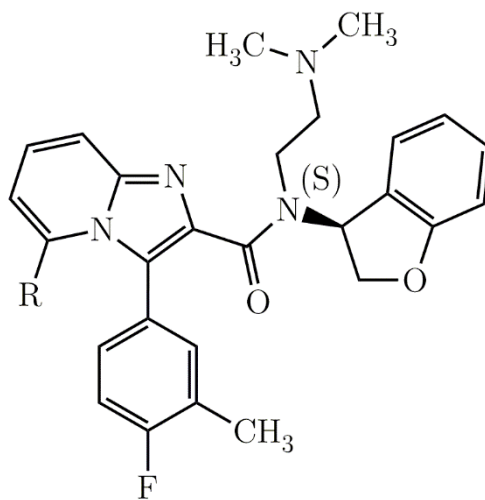


Figure 4.10 Full chemical structure of proposed CENP-E inhibitor. R = -O-CF₃ and R = -F are the new inhibitors based on Fig. 4.9 molecule A and B respectively proposed here.

4.6 Concluding Remarks

The work presented in this chapter show how $D(\vec{r})$ can complement ESP maps in biological and medicinal chemistry, providing a clearer picture of orbital overlap effects in large biochemical systems. The surface plots of overlap distance distinguish the diffuse and polarizable parts of a biomolecule surface from compact and hard parts. The combination of $D(\vec{r})$ and ESP rationalized the binding pattern of biotin and thyroxine in terms of the hard-soft acid-base concept. This combination quantified the binding of Au^+ to the GolB protein and the different experimental coordination chemistry of pairs of ions with similar size and charge, distinguishes the binding sites of soft Cu^+ and hard Ca^{2+} cations on formylglycine generating enzyme, highlights the orbital-driven aspects of rhodanine's promiscuous binding, and provides new nontrivial predictions in structure-based drug design. These results pave the way for applying the $D(\vec{r})$ and ESP in interpreting molecular orbital calculations in biochemistry and medicinal chemistry.

4.7 Computational Details

The coordinates of protein macromolecules mentioned in the above studies were invoked from Protein Data Bank (PDB). The obtained coordinates correspond to the crystal structures, which can be significantly different from the actual structure of the protein in aqueous solutions under physiological conditions. To get a realistic geometry before the molecular orbital calculations, the structure of each protein underwent molecular dynamics (MD) simulations in water. The procedures of these calculations are detailed below.

4.7.1 Preparation of Systems for MD Simulations

Structures of studied systems, Avidin-Biotin complex (PDB ID: 2AVI), Thyroxine-binding globulin complex (PDB ID: 2CEO), gold-binding protein GolB (PDB ID: 4Y2I) and

Formylglycine-generating enzyme (PDB ID: 5NXL) were acquired from the Protein Databank. The crystallographic asymmetric unit of the Avidin-biotin complex contains two distinguishable avidin macromolecules that were separated using the CCDC Mercury²⁶³ program before simulations, and only one avidin-biotin complex was used for further studies. Explicit hydrogen atoms were added to all initial PDB structures using the *reduce* flag of the *pdb4amber* module of AmberTools²⁶⁴ after removing the crystallographic waters using the *dry* flag of *pdb4amber*. From the avidin-biotin complex, the reduced coordinates of biotin ligand were extracted using CCDC Mercury. They were used as initial geometry for calculation of NPA charges using the Gaussian 09 suite of programs²⁶⁵. For calculations of NPA charges, biotin geometry was optimized at B3LYP/6-31g(d,p)²⁶⁶⁻²⁶⁹ level of theory using dichloromethane as a solvent in SCRF^{201, 270} implicit solvent model as implemented in Gaussian 09. The obtained NPA charges were used in the mol2 file of biotin ligand, which was generated using the *antechamber* module of AmberTools. The covalent bonds parameters (bonds, angles, and dihedrals) of biotin were generated using the *parmchk* module and were used as input along with mol2 file to obtain the force field library of biotin using the *xleap* module and GAFF atom types. The thyroxine-binding globulin protein contains thyroxine ligand and a glycerol molecule as non-standard residues. The above-mentioned procedure was adopted for thyroxine ligand to calculate NPA charges and force field library, whereas for glycerol residue AM1-BCC charge method was used to generate the charges using the *antechamber* module.

For force field parametrization of Au⁺ in GolB and Cu⁺ and Ca²⁺ in the Formylglycine-generating enzyme, the bonded model strategy involving the RESP charge fitting was adopted using version 3.0 *MCPB.py* program.²⁷¹ The metal atoms were separated from protein using CCDC Mercury, and their mol2 files were generated using the *antechamber* module. The oxidation state of metal ions was inserted by modifying its charge information

in the mol2 file. The quantum mechanical single point energy calculations on both small and large models were carried out using the Gaussian 09 at B3LYP/6-31g(d) level of theory by involving ECP for Au atom. The *Seminario* method²⁷¹ was adopted to generate the force field parameters, which involves the determination of bond and angle force constants from the sub-matrices of the cartesian Hessian matrix. The *ChgModB* algorithm²⁷¹ was used to perform the RESP charge fitting and to generate the final mol2 files for all the metal site residues.

The calculated force field parameters for ligands and metal ions were used along with *dry* and *reduced* PDB files of proteins to obtain the topology and coordinate files for MD simulation using the *xLEaP* module of AmberTools. For standard residues of all systems, the ff14SB force field parameters²⁷² were used. Each system was neutralized with either Na⁺ or Cl⁻ counter ions and was solvated with a truncated octahedron TIP3P²⁷³ water molecules box using an 8 Å solvent buffer between the solute and the closest edge of the unit cell.

4.7.2 Initial Energy Minimization

All initial coordinates of the studied systems underwent a two-step minimization procedure with the *sander* module of AmberTools. In the first step, protein and ligand (or metals ions) were held fixed using positional restraints of 20 kcal/mol Å² while the surrounding solvent water and counterions were minimized with the steepest descent method for the first 250 steps and then the conjugate gradient method for rest of 250 steps. Constant volume periodic boundary dynamics with a nonbonded cutoff of 10 Å were used. In the second step, the whole system was minimized with the steepest descent method for the first 2500 steps and then the conjugate gradient method for the rest of 2500 steps with a 10 Å cutoff for nonbonded interactions. The final minimized structures were used for MD simulations.

4.7.3 MD Simulations

The MD simulations on all the studied systems were carried out in two steps using the *sander* module with eight parallel processors. In the first step of equilibration protocol, all the systems were heated up from 0 K to 300 K by gradually increasing the temperature at constant volume periodic conditions using Langevin dynamics²⁷⁴ with a collision frequency of 1/ps. During this step, positional restraints were held constant at 10 kcal/mol Å² on the protein and ligand (or metals), and long-range interactions were treated with the Particle Mesh Ewald (PME) method for periodic boundaries using a cutoff of 10 Å. During the equilibration, bonds involving hydrogen atoms were constrained with the SHAKE²⁷⁵ algorithm. A total of 10,000 molecular dynamics steps were carried out with a time step of 2 fs per step to give a total simulation time of 20 ps.

The second step involves the MD equilibration on the whole unrestrained system. The density of the system was relaxed using the constant pressure of 1 atm using a Berendsen thermostat with isotropic position scaling, and constant temperature of 300 K maintained with a Langevin thermostat using periodic boundary conditions at a relaxation time of 2 ps. Like the previous run, the bonds involving hydrogen atoms were constrained with the SHAKE algorithm²⁷⁵, and the long-range interactions were treated with the PME method for periodic boundaries using a cutoff of 10 Å. This equilibration run consists of 50,000 molecular dynamics steps to give a total simulation time of 100 ps. During both equilibration steps, the trajectory file was updated after every 100 steps.

The final frame of the equilibrated MD trajectories was assumed as a model configuration of the proteins and was used to isolate the protein-ligand/metal coordinates for solvent molecule and counter ions using the *CPPTRAJ* module of the AmberTools for further molecular orbital calculations.

4.7.4 Molecular Orbital Calculations and Analysis

Two-layer ONIOM²⁷⁶ calculations were carried out for each equilibrated protein system using the Gaussian 09²⁶⁵ suite of programs. Long-range corrected hybrid density functional ω B97X-D²⁷⁷, which includes empirical dispersion, was employed to describe the higher quantum mechanics (QM) layer in combination with the 6-311G(d,p) basis set involving ECP for Iodine atom. In contrast, the AMBER²⁷⁸ molecular mechanics were used to treat the low-level layer of the protein molecules. The missing atom type parameters for molecular mechanics were incorporated using *amber=hardfirst* keyword in Gaussian ONIOM calculations. For avidin-biotin and thyroxine-binding globulin complexes, the calculations were carried out in two steps. In the first step, the high-level layer only included the ligand atoms, and the rest of the protein residues were treated as a low-level layer, whereas in the second step, the binding pocket of the protein was treated as a high-level layer and the remainder constitutes the low-level layer including the ligand molecule. For GolB and formylglycine-generating enzyme, only the second step involving the binding pocket at the high-level layer was performed for which, initially, all the atoms from the residues within a 6 Å sphere of the metal or the ligand were included in the high-level layer, and then the residues beyond 6 Å were truncated at chemically reasonable positions. The Gaussian formatted checkpoint files were used to obtain electron density, ESP, and $D(\vec{r})$ in Gaussian cube file format using Multiwfn program⁹⁵. For the calculations of $D(\vec{r})$, an even-tempered grid of 50 exponents was used starting from 2.50 Bohr⁻² and with an increment of 1.50 Bohr⁻². For the studied systems, the calculated ESP and $D(\vec{r})$ cube files were projected over 0.001 e/bohr³ molecular electron density surface. In the molecular geometry and density isosurface plots of all systems, the low-level layer of protein is depicted as a ribbon diagram coloured by secondary structure using VMD²⁷⁹ version 1.9.3, and the same program was used to plot the ESP and $D(\vec{r})$ surfaces.

Chapter 5

Quantifying Solvent Softness

5.1 Background

The Lewis concept of acids as electron-pair acceptors and bases as electron pair donors²⁸⁰,²⁸¹ can explain aspects of solvation, as solvent and solute both may act as donors and/or acceptors.²⁸² Pearson's concept of hard and soft acids and bases (HSAB)^{98, 283} can help rationalize such donor-acceptor interactions and can be extended to solvation.²⁸² HSAB theory suggests that, for acids and bases of comparable strength, chemically "hard" and nonpolarizable acids prefer to interact with hard bases and *vice versa*. Extension of this concept to solution implies that chemically hard solvents tend to dissolve hard solutes, and soft solvents dissolve soft solutes.^{101, 284}

Several aspects of solution chemistry have been attributed to solvent hardness and softness. In aqueous-organic solvent mixtures, the sulfates of "soft" Cd^{2+} tend to become less soluble with increasing water content, whereas sulfates of harder 3d cations like Cu^{2+} and Co^{2+} show the opposite trend.²⁸⁵ The relatively hard chloride salts of Ni^{2+} and Co^{2+} show higher solubility with increasing water content, whereas the softer bromide salts show the opposite trend.²⁸⁶ Metal cation complexes of N-phenylaza-15-crown-5 show stability

order $\text{Ca}^{2+} > \text{Cd}^{2+} > \text{Mg}^{2+} > \text{Ag}^+$ in soft acetonitrile (Marcus $\mu = 0.35$; see [next section](#) for definition of μ scale), but the opposite order in harder methanol (Marcus $\mu = 0.02$).²⁸⁷ Phenol alkylation by 3-bromopropene in the presence of potassium carbonate via Williamson ether synthesis produces mostly allyl phenyl ether in “harder” acetone (Marcus $\mu = 0.03$) and mostly *o*-allyl phenol in “softer” benzene or toluene (Marcus $\mu = 0.3-0.4$), illustrating solvent effects on *O/C* alkylation.^{284, 288} Sodium phenolate alkylation by 3-chloropropene gives near 100% *O*-alkylation in ethanol and only 22% *O*-alkylation in phenol.^{289, 290} Similar solvent effects are found for nucleophilic substitution and elimination reactions.²⁹¹⁻²⁹³ The Wittig reaction proceeds much rapidly in DMSO than in other solvents.²⁹⁴ In DMSO, the oxygen reduction and evolution reactions of Li-Air batteries follow reversible one-electron O_2/O_2^- pathway whereas the same reaction in acetonitrile or dimethyl ether yields reduction to O_2^{2-} and O^{2-} .²⁹⁵ Nonlinearities in the measured Marcus μ values of water-acetonitrile mixtures quantify the degree of microscopic heterogeneity.²⁹⁶ Similar solvent dependence is seen in ionic liquids (ILs).²⁹⁷ In addition, the substitutions of soft/hard groups on ILs impart a drastic change of viscosity, enthalpy of vaporization, and the ion conductivities of those ILs²⁹⁸; also, the hardness/softness of ions of ILs directly controls the solubility of materials like polymers in them.^{299, 300}

5.2 Empirical Solvent Softness Scales

Several groups have proposed empirical scales of solvent softness. These are based on measured Gibbs energy of transfer of metal ions³⁰¹, infrared or Raman spectral shifts^{302, 303}, half-wave potentials³⁰⁴, reaction enthalpies^{305, 306}, second-order rate constants³⁰⁷, fluorescence shifts³⁰⁸, and so on³⁰⁹. The donor number D_N scale of Gutmann is based on the computed enthalpy for solvent coordination to soft Lewis acid antimony (V) chloride in a diluting 1,2-dichloroethane medium.³¹⁰ The D_S scale of Persson *et al.*^{311, 312}, is based on the solvent-

induced shift in the position of the Raman band for Hg-Br bond symmetric stretching in HgBr₂. D_s values are available for a large number of solvents.²⁸² The B_{hard} and B_{soft} scales of solvent hard and soft basicity³⁰³ are respectively based on infrared absorbance solvatochromic shifts of phenol O–H stretching and iodoacetylene I–C stretching. The μ -scale of solvent softness proposed by Marcus^{282, 301} is based on the difference between Gibbs energies of transfer for “soft” Ag⁺ *vs.* “hard” Na⁺ and K⁺ ions.³⁰¹

5.3 Quantifying Softness Using Electronic Structure

The continued development of new solvent systems motivates the extension of solvent scales. Electronic structure simulations enable such extensions. The connection between electronic structure and chemical hardness is well-established in the realm of conceptual density functional theory (DFT).³⁷ These connections and definitions are detailed in [Appendix E](#). As stated in [chapter 1](#), the absolute hardness and softness calculated using the conceptual DFT have been extensively applied in areas including organic reactivity⁴³⁻⁴⁶, aromaticity⁴⁷, coordination complexes⁴⁸⁻⁵⁰, surface chemistry⁵¹, biological systems⁵², and so on.^{37, 51, 53, 54} However, systematic applications to solvent hardness and softness are scarce.

In this chapter, the applications of the molecular surface plots of $D(\vec{r})$ are extended to model empirical solvent softness scales. The results of the quantitative analysis of $D(\vec{r})$ molecular surfaces are used to fit the Marcus μ values of solvent softness. The obtained results are compared with the results obtained from computed global softness (Eq. E.2 and E.3 of [Appendix E](#)). A key result of this work is the extension of the Marcus μ -scale to ionic liquid (IL) solvents. ILs, composed of organic cations and anions combinations, have led to applications including capacitors, fuel-cell, batteries, lubricants, dye-sensitized solar cells, and sensor technologies³¹³⁻³¹⁷. Cosolvents such as H₂O or DMSO can lower IL viscosity

and improve their performance ³¹⁸. The hard/soft nature of IL counter ions and cosolvents ²⁹⁷⁻³⁰⁰ motivates the quantitative characterization of their chemical softness/hardness.

5.4 Predicting Marcus Softness Scale Using Overlap

Distance

We begin by correlating solvent molecules' computed $D(\bar{r})$, global softness ($1/\eta$; see Eq. E.2 of [Appendix E](#)), and HOMO-LUMO gap (Eq. E.3) to their measured empirical Marcus μ -scale values. The 34 solvents are considered from Table 1 of Ref. ^[301] and are given in [Table G.2](#) of [Appendix G](#). [Fig. 5.1](#) plots the solvents' μ -values *vs.* the surface-averaged $D(\bar{r})$, or global softness $1/\eta$ (Eq. E.2). [Table 5.1](#) reports linear fits of μ to these data. Additionally, [Fig. 5.2\(a\)](#) shows the corresponding plot of μ *vs.* $1/Gap$, with trends matching $1/\eta$. [Fig. 5.2\(b\)](#) shows the relation between $D(\bar{r})$ and $1/Gap$. All of these calculated parameters are also given in [Appendix G](#).

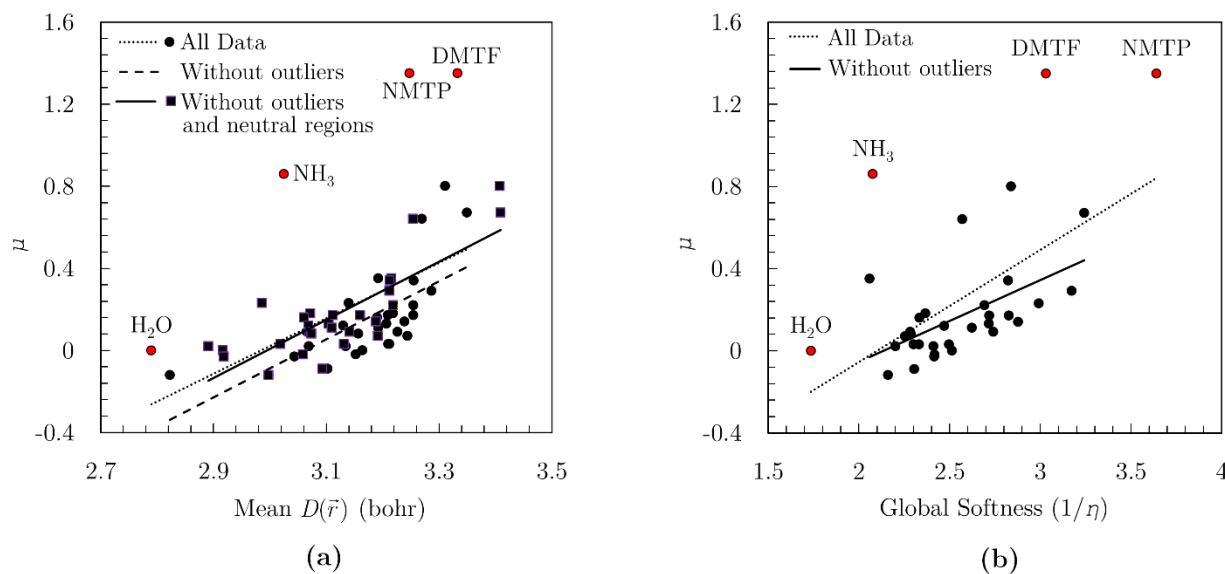


Figure 5.1 Measured Marcus μ parameters plotted *vs.* computed mean $D(\bar{r})$ (a) and computed global softness $1/\eta$ (b). Important outliers are highlighted.

Table 5.1 Linear fits of experimental Marcus μ parameter to computed $D(\bar{r})$, global softness $1/\eta$ (Eq. E.2), or HOMO-LUMO Gap (Eq. E.3). Fits are performed for the 34 solvents in Table I of Ref. [301]. A = All data, B = Without outliers, C = Without outliers, $D(\bar{r})$ on charged areas only. MAE = Mean absolute error, ME = Mean error, RMSD = root-mean-square deviation.

| Method | Data | Equation | R ² | MAE | ME | RMSD |
|------------------------|------|----------------------------------------|----------------|-------|--------|-------|
| $D(\bar{r})$ (bohr) | A | $\mu = 1.349 D(\bar{r}) - 4.026$ (5.1) | 0.209 | 0.230 | 0.000 | 0.321 |
| | B | $\mu = 1.413 D(\bar{r}) - 4.325$ (5.2) | 0.445 | 0.126 | 0.000 | 0.159 |
| | C | $\mu = 1.418 D(\bar{r}) - 4.249$ (5.3) | 0.659 | 0.244 | -0.147 | 0.804 |
| $1/\eta$ (a.u) | A | $\mu = 0.397(1/\eta) - 0.848$ (5.4) | 0.292 | 0.194 | -0.082 | 0.312 |
| | B | $\mu = 0.547(1/\eta) - 1.150$ (5.5) | 0.331 | 0.170 | 0.082 | 0.203 |
| $1/Gap$ (a.u) | A | $\mu = 0.277(1/Gap) - 0.891$ (5.6) | 0.531 | 0.176 | 0.000 | 0.247 |
| | B | $\mu = 0.214(1/Gap) - 0.687$ (5.7) | 0.294 | 0.123 | 0.000 | 0.180 |

Figure 5.1 shows a broadly consistent relation between computed and experimental values; solvents that are “soft” by the Marcus scale have large computed average surface $D(\bar{r})$ and large computed global softness $1/\eta$. Chemically, the “softness” measured by the Marcus μ -scale is broadly consistent with “softness” as envisioned by conceptual DFT. Moreover, this softness is an intrinsic property of the molecules in question, such that the global softness $1/\eta$ computed for an isolated solvent molecule is broadly predictive of its Marcus μ in the condensed phase.

Additional chemical insight comes from the four outliers in Fig. 5.1; ammonia, water, N-methylthiopyrrolidinone (NMTP), and N,N-dimethylthioformamide (DMTF). These are by the Marcus scale softer than expected, given their global hardness and surface average $D(\bar{r})$. These outliers are not an error in the computed values; rather, they are an important indication of these specific solvents' special coordination chemistry, *i.e.*, Ag^+ , Na^+ , and K^+ may undergo coordination with these solvents in addition to dissolution. Sandstrom and

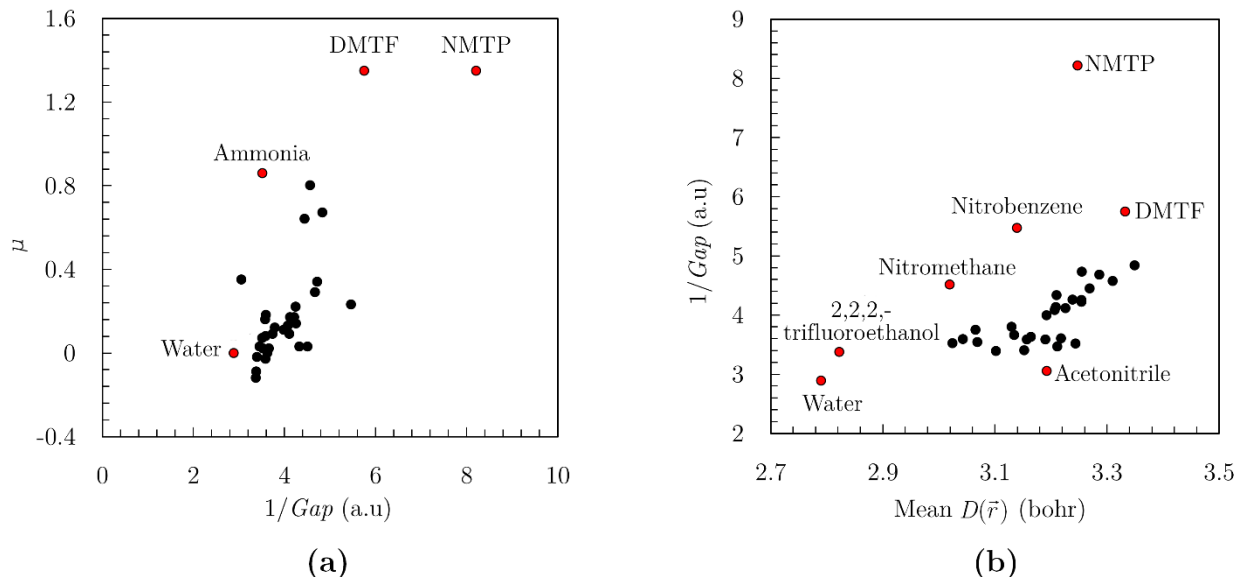


Figure 5.2 (a) Correlation between Marcus’s μ -scale and $1/Gap$ and (b) Correlation between $1/Gap$ and mean $D(\bar{r})$ of solvents. The important outliers are highlighted.

coworkers³¹² found that ammonia, NMTP, DMTF, and water were major outliers in an otherwise reasonably linear relation between μ and D_s scales. These are visible as labeled points 70, 73, and 76 in Ref. [312] Figure 6c. These authors rationalized the results for water in terms of its coordination to the Marcus probe ions. Experimentally, aqueous solutions of Ag^+ show four loosely coordinated water molecules, whereas aqueous solutions of Na^+ and K^+ show higher coordination numbers.^{312, 319} While those authors did not explain the chemistry behind the other outliers, the fact that the calculations reported here reproduce the special experimental behavior of these solvents is encouraging. Omitting these four outliers significantly improves the correlation between measured and computed values. The best fit to μ comes from averaging the $D(\bar{r})$ over the charged regions of the molecule surface, *i.e.*, those points \bar{r} on the surface, possessing molecular electrostatic potential $|ESP(\bar{r})| > 0.04$ a.u. This technique reduces contributions from neutral alkyl chains, which are likely not much involved in the differential coordination of Ag^+ *vs.* Na^+ , K^+ .

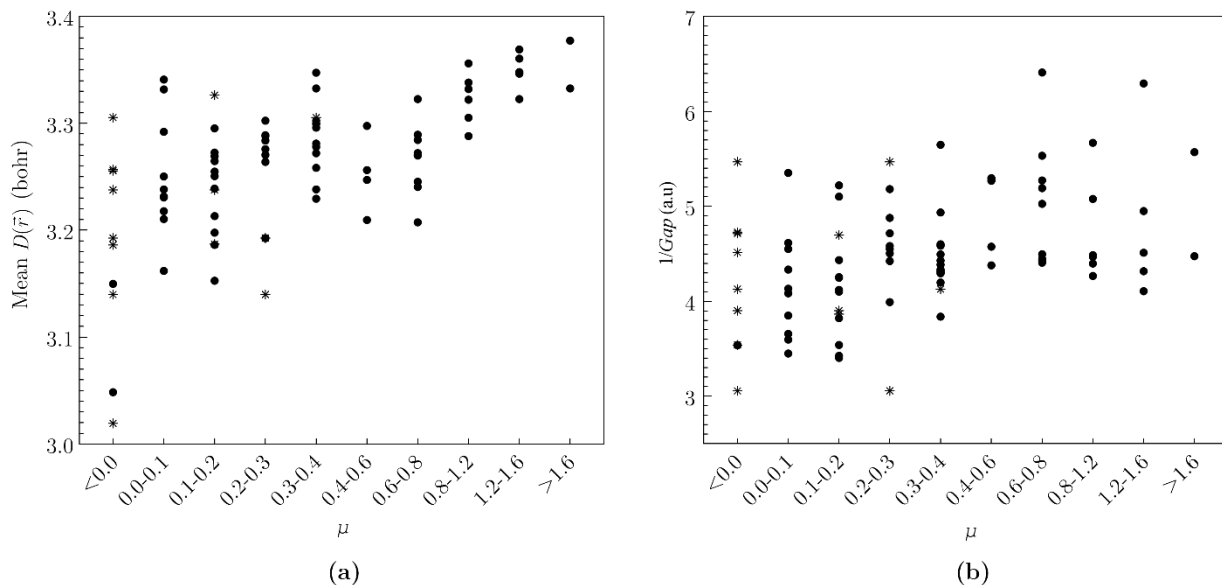


Figure 5.3 Correlation between Marcus’s μ -scale and mean $D(\bar{r})$ (a) and $1/Gap$ (b) of solvents mentioned in Table 2 of Ref. [301]. Asterisks show those data points where the two spectroscopic measures of μ “grossly disagree”.

Next, the estimated Marcus μ -values of 60 additional solvents, reported in Table 2 of Ref. [301] are considered and evaluated from either a linear fit to D_s or the difference between B_{hard} and B_{soft} measures of hard and soft basicity. Fig. 5.3(a) plots μ vs. the computed surface-averaged $D(\bar{r})$. Cases where the two spectroscopic measures of μ “grossly disagree” are plotted as asterisks. Fig. 5.3(a) provides additional insight into the chemistry of the relation between $D(\bar{r})$ and Marcus μ . Solvents with large experimental μ values invariably possess large $D(\bar{r})$. For example, every solvent with $D(\bar{r}) < 3.20$ bohr has $\mu < 0.3$, and every solvent with $D(\bar{r}) < 3.27$ bohr has $\mu < 0.8$. Fig. 5.3(b) shows that this trend does not hold as well for global softness $1/Gap$, which proves to be somewhat worse than $D(\bar{r})$ at predicting these μ values. Chemically, solvents with small experimental μ values tend to have smaller $D(\bar{r})$, consistent with compact regions of small orbital overlap distance. Solvents that combine a small Marcus μ with a large $D(\bar{r})$ tend to be weakly coordinating. For example, benzene, tetrahydrofuran, acetonitrile, and

benzonitrile have one of the two spectroscopic measures assign $\mu < 0$, and all have relatively large $D(\bar{r}) > 3.2$ bohr.

5.5 Extension to Other Solvent Softness Scales

It is next considered whether the computed electronegativity and global softness or computed $D(\bar{r})$ and surface-averaged electrostatic potential, ESP, can be predictive for other solvent scales. Table 5.2 shows the fits of the empirical μ , D_s , and DN scales. Fits are to 26 different solvents for which μ , D_s , and DN are well-known (Ref. [312]). All computed and experimental values are provided as Table G.3 of Appendix G. The results in Table 5.2 are again instructive. The combination of $D(\bar{r})$ and ESP does a better job of modeling the Marcus μ scale, giving an RMSD lower than the corresponding fit to electronegativity and global softness. In contrast, electronegativity and global softness give somewhat smaller RMSD for the D_s and DN scales. Hardness and orbital-overlap descriptors are relatively more important for modeling the μ scale. Considering first the fits to ESP and $D(\bar{r})$, the best-fit coefficient of ESP is 40-150 (CR) times that of $D(\bar{r})$ for the D_s and

Table 5.2 Linear fits of μ , D_s and DN solvent scales to computed mean $D(\bar{r})$ (bohr), mean ESP and global softness $1/\eta$ (a.u) and electronegativity χ (a.u) of 26 solvents.

| Formula | RMS%D | CR* |
|-------------------------------------------------------|-------|------|
| $\mu = 1.95 D(\bar{r}) - 7.17 \text{ ESP} - 6.02$ | 62.2 | 4 |
| $D_s = 65.0 D(\bar{r}) - 2651 \text{ ESP} - 177$ | 27.6 | 40 |
| $\text{DN} = 21.5 D(\bar{r}) - 3328 \text{ ESP} - 33$ | 41.7 | 154 |
| $\mu = 0.26 (1/\eta) - 0.48 \chi - 0.41$ | 70.7 | 2 |
| $D_s = -0.11 (1/\eta) - 313 \chi + 71.9$ | 24.5 | 2800 |
| $\text{DN} = -15.3 (1/\eta) - 413 \chi + 130$ | 36.6 | 27 |

* Coefficient Ratio between first and second coefficient

DN scales, but only 4 times that of $D(\vec{r})$ for the μ scale. Similarly, for the fits to electronegativity and global softness, the best-fit coefficient of electronegativity is 20-2800 times that of global softness for D_s and DN scales, but only two times that of global softness for the μ scale. This is consistent with the suggestion that D_s and DN quantify a solvent's "soft donor ability", *i.e.*, these scales are based on the soft acceptor molecules HgBr_2 and SbCl_5 respectively ³¹², whereas, μ quantifies a solvent's relative soft *vs.* hard donation.

5.6 Development of Solvent Versatility Scale

Figure 5.1 shows how the orbital overlap distance effectively differentiates regions of a molecule surface dominated by compact *vs.* diffuse orbitals. Not every property of a solvent can be condensed into one number. Experiments suggest that "good" solvents and detergents are versatile, with chemical functionality enabling them to interact with multiple molecules of different kinds. It is not possible to quantify this behaviour using a single global hardness/softness. However, variations in the orbital overlap distance across a surface (RMSD $D(\vec{r})$) should quantify this behaviour and provide information about the variety of solvating interactions available. Fig. 5.4 plots mean $D(\vec{r})$ *vs.* RMSD $D(\vec{r})$ of 34 solvents in Table I of Ref.^[301].

Molecules that have both hard and soft regions on the molecular surface exhibit a large value of RMSD $D(\vec{r})$. Appendix G shows the calculated RMSD $D(\vec{r})$ for several solvents. Solvents like mercaptoethanol, DMSO, and N-methylformamide have a large value of RMSD $D(\vec{r})$, which complements their ability to dissolve a variety of hard or soft substances. Similarly, 2,2,2-trifluoroethanol, propylene carbonate, and 1,2-ethanediol also show large values of RMSD $D(\vec{r})$, which explains their versatile solvating ability. The solvents like water, ammonia, tetrahydrothiophene, acetonitrile, and 1,1-Dichloroethane have relatively small values of RMSD $D(\vec{r})$ which is in accordance with their ability to

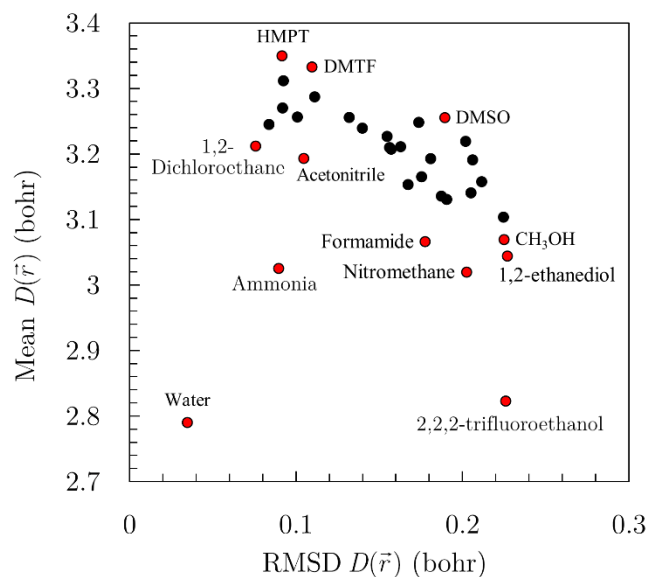


Figure 5.4 Correlation between mean $D(\bar{r})$ and RMSD $D(\bar{r})$ of solvents elaborating the versatility of solvents. The outliers are highlighted using red spots.

dissolve only limited substances of specific hard/soft nature. Water, having a hard oxygen atom with little variations on $D(\bar{r})$, has a small value of RMSD $D(\bar{r})$ whereas, alcohols have a higher value compared to water, and RMSD $D(\bar{r})$ increases with an increase in the number of carbon atoms. Both acetone and 1,2-Dichloroethane have the same value of μ and nearly equal value of the mean $D(\bar{r})$, but large RMSD $D(\bar{r})$ of the former explains its considerable dissolving ability compared to later.

5.7 Applications to Ionic Liquids

The obtained best linear fitting model (Eq. 5.6 of Table 5.1) was used to predict the μ values for selected 20 ionic liquids (ILs). Table G.4 of Appendix G lists the full names of these ILs. Table 5.3 shows the predicted values along with mean $D(\bar{r})$ and RMSD $D(\bar{r})$ of each ionic liquid system. The table indicates that the anionic part plays a fundamental role in controlling the softness of ionic liquid. Ionic liquids having [Br] and [Cl] as anions have

a large value of μ indicating their chemical softness, whereas those ILs which combines hard anions $[\text{CF}_3\text{SO}_3]$ and $[\text{PF}_6]$ have small μ values owing to their chemical hardness. Similarly, ILs with $[\text{MeSO}_4]$ anion shows an intermediate value of μ . For the same anion, the cations $[\text{N}_{1116}]$ and $[\text{C}_2\text{py}]$ imparts large μ values to ionic liquids compared to the $[\text{emim}]$ and $[\text{mPhim}]$ cations. [Table 5.3](#) shows that RMSD $D(\bar{r})$ increases with a decrease in Mean $D(\bar{r})$ where ionic liquids having hard anions and small μ values show large RMSD $D(\bar{r})$. This exhibits that hard ILs have substantial solvating abilities.

Table 5.3 Predicted μ values for selected ionic liquids.

| Ionic Liquid | Mean $D(\bar{r})$ (bohr) | RMSD $D(\bar{r})$ (bohr) | Predicted μ |
|-------------------------------------------------|--------------------------|--------------------------|-----------------|
| $[\text{N}_{1116}][\text{Br}]$ | 3.373 | 0.123 | 0.536 |
| $[\text{C}_2\text{py}][\text{Br}]$ | 3.350 | 0.157 | 0.503 |
| $[\text{N}_{1116}][\text{Cl}]$ | 3.338 | 0.082 | 0.486 |
| $[\text{emim}][\text{Br}]$ | 3.337 | 0.178 | 0.484 |
| $[\text{mPhim}][\text{Br}]$ | 3.332 | 0.168 | 0.478 |
| $[\text{C}_2\text{py}][\text{Cl}]$ | 3.302 | 0.106 | 0.436 |
| $[\text{mPhim}][\text{Cl}]$ | 3.292 | 0.126 | 0.421 |
| $[\text{emim}][\text{Cl}]$ | 3.290 | 0.133 | 0.419 |
| $[\text{N}_{1116}][\text{MeSO}_4]$ | 3.221 | 0.178 | 0.321 |
| $[\text{mPhim}][\text{MeSO}_4]$ | 3.175 | 0.176 | 0.255 |
| $[\text{C}_2\text{py}][\text{MeSO}_4]$ | 3.164 | 0.171 | 0.239 |
| $[\text{emim}][\text{MeSO}_4]$ | 3.157 | 0.178 | 0.230 |
| $[\text{N}_{1116}][\text{CF}_3\text{SO}_3]$ | 3.143 | 0.252 | 0.209 |
| $[\text{N}_{1116}][\text{PF}_6]$ | 3.112 | 0.301 | 0.166 |
| $[\text{mPhim}][\text{CF}_3\text{SO}_3]$ | 3.092 | 0.238 | 0.137 |
| $[\text{C}_2\text{py}][\text{CF}_3\text{SO}_3]$ | 3.067 | 0.236 | 0.101 |
| $[\text{emim}][\text{CF}_3\text{SO}_3]$ | 3.063 | 0.238 | 0.096 |
| $[\text{mPhim}][\text{PF}_6]$ | 3.056 | 0.286 | 0.086 |
| $[\text{C}_2\text{py}][\text{PF}_6]$ | 3.022 | 0.288 | 0.038 |
| $[\text{emim}][\text{PF}_6]$ | 3.019 | 0.288 | 0.034 |

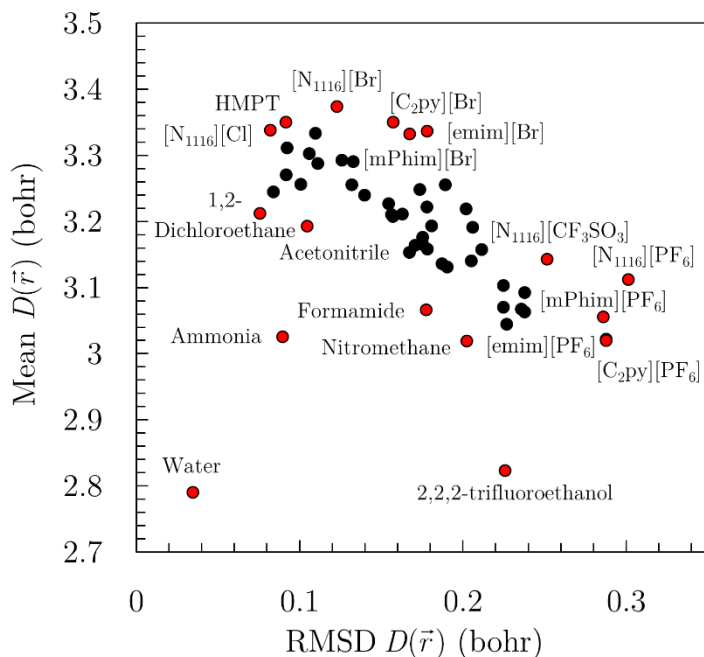


Figure 5.5 Correlation between mean $D(\bar{r})$ and RMSD $D(\bar{r})$ of conventional solvents and ILs elaborating the dissolution versatility. The outliers are highlighted using red spots.

Figure 5.5 extends the data of Fig. 5.4 by including the calculated parameters of ILs mentioned in Table 5.3. The trend between mean $D(\bar{r})$ and RMSD $D(\bar{r})$ is mostly linear, with RMSD $D(\bar{r})$ decreases with an increase in the mean $D(\bar{r})$. However, the ILs generally show large RMSD $D(\bar{r})$ as compared to the conventional solvent molecules indicating their dissolution versatility. Also, the RMSD $D(\bar{r})$ of ILs is mostly controlled by the nature of their anionic constituents. The ILs containing comparatively soft anions such as [Br] exhibit higher mean $D(\bar{r})$ and an intermediate value of RMSD $D(\bar{r})$. On the contrary, the ILs containing [PF₆] anions have large values of RMSD $D(\bar{r})$ followed by those consisting of [CF₃SO₃] anion, though both types have intermediate values of the mean $D(\bar{r})$. It can be concluded by combining the predicted μ and RMSD $D(\bar{r})$ values, that ILs containing [PF₆] anions are chemically hard but are more versatile and can dissolve a variety of substances, complementing the various experimental findings.³²⁰

Both theory and experiments suggest that ions of ILs can exist in multiple conformations.^{321, 322} To quantify the variations in mean $D(\bar{r})$ and RMSD $D(\bar{r})$ due to different conformations, these quantities were calculated for two conformations, *trans-trans* (TT) and *gauche-trans* (GT) of 1-butyl-3-methylimidazolium³²³, as an illustration. Fig. 5.6 shows that the mean $D(\bar{r})$ is the same for both the conformations, which suggests that conformational changes do not have the profound effect of the chemical softness of ILs. Similarly, RMSD $D(\bar{r})$ also shows an insignificant variation with conformational changes, which establish that the solvating ability is not significantly affected by conformational equilibria. It can be inferred from these results that the reported method to estimate μ is equally valid for all the adopted conformations of solvent molecules, and the optimized geometry of a single conformation gives a reliable estimate of μ for all other conformations.

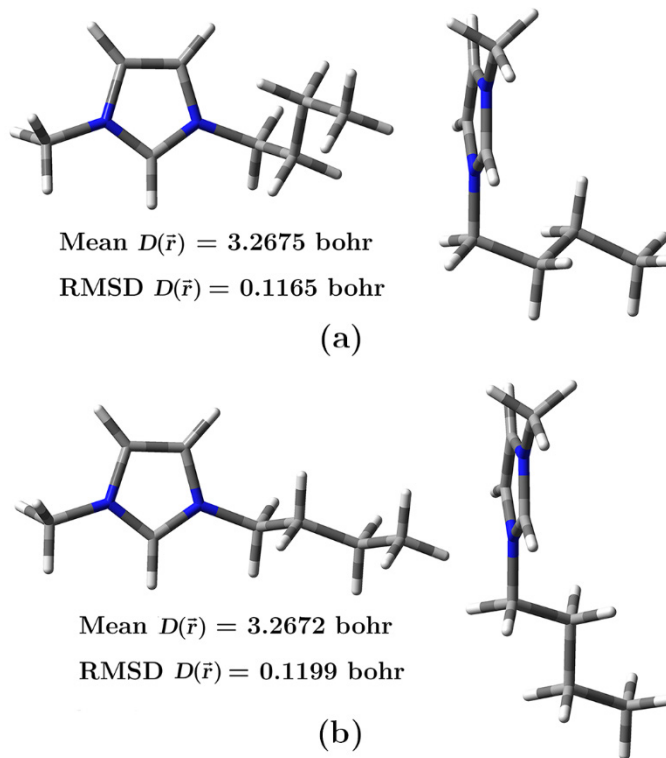


Figure 5.6 Optimized geometries and calculated mean $D(\bar{r})$ and RMSD $D(\bar{r})$ of two 1-butyl-3-methylimidazolium (a) Trans – trans (b) Gauche – trans conformations.

5.8 Applications to Ionic Liquids/co-solvents

The chapter is ended by predicting the μ values for binary ILs/cosolvents systems by using water and DMSO as cosolvents for 25 ionic liquids systems. [Table 5.4](#) presents the calculated

Table 5.4 Predicted μ values for selected ionic liquids and ionic liquids/cosolvents along with mean and RMSD $D(\bar{r})$ (bohr).

| Ionic Liquid | Without cosolvent | | | Water as cosolvent | | | DMSO as cosolvent | | |
|-------------------------------------------|-------------------|-------------------|--------|--------------------|-------------------|--------|-------------------|-------------------|-------|
| | Mean $D(\bar{r})$ | RMSD $D(\bar{r})$ | μ | Mean $D(\bar{r})$ | RMSD $D(\bar{r})$ | μ | Mean $D(\bar{r})$ | RMSD $D(\bar{r})$ | μ |
| [P ₄₄₄][Ac] | 3.284 | 0.122 | 0.409 | 3.241 | 0.182 | 0.349 | 3.278 | 0.138 | 0.401 |
| [P ₄₄₄][DCA] | 3.279 | 0.121 | 0.402 | 3.237 | 0.179 | 0.343 | 3.274 | 0.138 | 0.396 |
| [C ₈ mim][Ac] | 3.260 | 0.147 | 0.376 | 3.212 | 0.200 | 0.307 | 3.259 | 0.158 | 0.374 |
| [C ₈ mim][DCA] | 3.254 | 0.144 | 0.368 | 3.207 | 0.196 | 0.300 | 3.255 | 0.156 | 0.368 |
| [bpy][Ac] | 3.239 | 0.136 | 0.345 | 3.180 | 0.198 | 0.262 | 3.243 | 0.153 | 0.352 |
| [P ₄₄₄][NO ₃] | 3.237 | 0.186 | 0.343 | 3.197 | 0.219 | 0.286 | 3.241 | 0.187 | 0.348 |
| [C ₄ mim][Ac] | 3.231 | 0.149 | 0.335 | 3.175 | 0.203 | 0.255 | 3.238 | 0.161 | 0.344 |
| [bpy][DCA] | 3.231 | 0.132 | 0.335 | 3.175 | 0.193 | 0.255 | 3.238 | 0.150 | 0.344 |
| [C ₄ mim][DCA] | 3.225 | 0.145 | 0.325 | 3.170 | 0.198 | 0.248 | 3.233 | 0.159 | 0.337 |
| [C ₈ mim][NO ₃] | 3.201 | 0.206 | 0.292 | 3.157 | 0.233 | 0.229 | 3.214 | 0.204 | 0.310 |
| [P ₄₄₄][BF ₄] | 3.198 | 0.252 | 0.287 | 3.162 | 0.267 | 0.236 | 3.209 | 0.242 | 0.303 |
| [N ₁₁₁₂ OH][Ac] | 3.193 | 0.189 | 0.280 | 3.132 | 0.227 | 0.194 | 3.212 | 0.191 | 0.308 |
| [N ₁₁₁₂ OH][DCA] | 3.186 | 0.183 | 0.270 | 3.128 | 0.220 | 0.188 | 3.207 | 0.187 | 0.300 |
| [bpy][NO ₃] | 3.159 | 0.202 | 0.233 | 3.108 | 0.227 | 0.160 | 3.187 | 0.203 | 0.272 |
| [C ₈ mim][BF ₄] | 3.154 | 0.272 | 0.225 | 3.115 | 0.281 | 0.170 | 3.177 | 0.259 | 0.258 |
| [C ₄ mim][NO ₃] | 3.154 | 0.208 | 0.225 | 3.105 | 0.230 | 0.155 | 3.183 | 0.208 | 0.266 |
| [P ₄₄₄][NTf ₂] | 3.138 | 0.263 | 0.203 | 3.113 | 0.269 | 0.168 | 3.158 | 0.256 | 0.230 |
| [bpy][BF ₄] | 3.098 | 0.277 | 0.145 | 3.056 | 0.278 | 0.086 | 3.143 | 0.265 | 0.209 |
| [N ₁₁₁₂ OH][NO ₃] | 3.095 | 0.230 | 0.142 | 3.047 | 0.239 | 0.073 | 3.148 | 0.230 | 0.216 |
| [C ₈ mim][NTf ₂] | 3.094 | 0.271 | 0.140 | 3.069 | 0.273 | 0.104 | 3.125 | 0.265 | 0.184 |
| [C ₄ mim][BF ₄] | 3.094 | 0.278 | 0.140 | 3.054 | 0.279 | 0.083 | 3.139 | 0.267 | 0.204 |
| [bpy][NTf ₂] | 3.041 | 0.262 | 0.064 | 3.015 | 0.260 | 0.029 | 3.088 | 0.264 | 0.132 |
| [C ₄ mim][NTf ₂] | 3.039 | 0.263 | 0.062 | 3.014 | 0.261 | 0.027 | 3.086 | 0.264 | 0.129 |
| [N ₁₁₁₂ OH][BF ₄] | 3.024 | 0.292 | 0.041 | 2.988 | 0.281 | -0.011 | 3.098 | 0.284 | 0.146 |
| [N ₁₁₁₂ OH][NTf ₂] | 2.984 | 0.261 | -0.016 | 2.962 | 0.253 | -0.047 | 3.050 | 0.271 | 0.077 |

μ values for pure ILs, ILs/water, and ILs/DMSO binary systems. For all ILs, the addition of water results in a decrease in the μ values, and for ILs $[\text{N}_{1112}\text{OH}][\text{BF}_4]$ and $[\text{N}_{1112}\text{OH}][\text{NTf}_2]$ it becomes negative. In contrast, the addition of DMSO results in an increase in the μ values for most of ILs. In some cases, the addition of DMSO as cosolvent imparts insignificant variations to the predicted μ values, which can be attributed to the combined mean $D(\vec{r})$ of IL components being comparable to that of DMSO. These results complement the experimental findings of the dissolution of cellulose in some ILs, which state that the addition of DMSO to ILs/cellulose system, enhances the solubility of cellulose, while the addition of water or ethanol precipitate cellulose from these systems ³²⁴⁻³²⁶.

5.9 Concluding Remarks

The orbital overlap distance, $D(\vec{r})$, distinguishes the chemically hard and soft regions on the surface of a molecule hence mean $D(\vec{r})$ can be related to the chemical softness/hardness of solvent molecules. A method is presented to estimate Marcus's μ values of solvents softness by fitting empirical μ with calculated mean $D(\vec{r})$. It is shown that both mean $D(\vec{r})$ and global softness provides a reasonable estimate of solvent softness. The surface variation of $D(\vec{r})$, *i.e.*, RMSD $D(\vec{r})$ is related to the solvation ability of solvent where large RMSD $D(\vec{r})$ shows that the solvent can dissolve both hard and soft solutes. The extension to some other scales of "solvent soft basicity" is also reported. The proposed method was used to predict Marcus μ values for ILs and IL/cosolvent systems.

5.10 Computational Details

The μ values of solvents used in the present study were taken from Ref.^[301] and are given as [Appendix G](#). All calculations were performed with the Gaussian 09²⁶⁵ suite of programs.

All calculations were carried out in gas-phase using the three-parameter hybrid exchange functional developed by Becke³²⁷ in conjunction with the exchange-correlation potential, corrected via a gradient developed by Lee *et al.* (B3LYP).²⁶⁷ All calculations use 6-31+g(d,p) basis set³²⁸⁻³³²; however, the results of basis set dependence are given in [Table G.5](#) of [Appendix G](#). For all systems, the values of $D(\vec{r})$, the HOMO-LUMO energy gap and the global softness were calculated at geometries optimized to a global minimum using tight convergence criteria. For the calculation of global softness, vertical ionization potentials and electron affinities were used. Quantitative analysis of $D(\vec{r})$ on 0.001 e/bohr³ electron density molecular surfaces was performed using a modified version of Multiwfn V3.6(dev)^{95, 333} to get mean $D(\vec{r})$ and RMSD $D(\vec{r})$.

Chapter 6

Quantifying the Reactivity of Graphene Defects

6.1 Background

Structural defects in graphene open the bandgap and allow catalysts and intermediates to bind to the surface.³³⁴⁻³³⁸ These defects alter graphene's chemical reactivity^{33, 334, 339} and electronic structure,³⁴⁰⁻³⁴³ induce magnetism³⁴⁴⁻³⁴⁷ and reduce electron mobility^{348, 349}, Young's Modulus^{350, 351} and Poisson ratio³⁵². These defects can appear during production and growth or can be incorporated by post-processing particle (electron and ion beam) irradiation and chemical methods termed as chemical functionalization.^{334, 341, 353-355} Foreign adatoms, which interact with graphene either by van der Waals interactions (physisorption), chemical bonds (chemisorption), or as substitutional impurities, have received considerable attention due to their ability to act as catalysts (e.g. transition metals) or due to the controlled alterations in electrical conductivity and electronic structure of graphene (e.g. boron or nitrogen doping).^{334, 355, 356} Adatoms often bind to graphene at defects, particularly at the vacant sites of vacancy defects.³⁵⁷ The control of the location of Stone – Wales (SW) and vacancy defects, type of dopant, and adatoms pave the way towards the preparation of new graphene-based

materials with novel physical and chemical properties.^{341, 358, 359} Chemically, the doping can enhance its reactivity as a catalyst, as diene or dienophile in Diels-Alder, in aerobic oxidations, oxidative dehydrogenations, and cycloaddition reactions.^{355, 360-364} The transition metal atoms adsorbed on vacancy defects having high spatial selectivity can turn the defect site into a single atom catalyst.^{337, 365-367}

Understanding the physical and chemical consequences of graphene defects and their interactions with dopants requires an understanding of the defect's atomic and electronic structure.³⁶⁸ Computed descriptors of electronic structure can often provide such understanding from relatively simple calculations. However, as illustrated in the previous chapter for other selective systems, molecular ESP and atomic partial charges (Q_A) are insufficient for materials like carbon allotropes as well. For example, as given in [Table 1.1](#) of [Chapter 1](#), the pristine graphene, diamond, and C_{60} all have a partial atomic charge of zero but possess different reactivities and heat of formations.⁸⁸

Intrinsic defects in graphene often combine relatively large variations in chemical reactivity with relatively insignificant variations in ESP or atomic partial charges. Chemically, all of the atoms in an intrinsic defect have the same electronegativity. To illustrate, a single vacancy (V_1), double vacancy (V_2), and Stone-Wales (SW) defects are considered, as shown in [Fig. 6.1](#). Both [Table 6.1](#) and [Fig. 6.1](#) show that these defects have relatively small variations in ESP and atomic charges. However, previous studies have demonstrated that these different defects have different chemistry. These defects show markedly different binding energies to H_2OH , H_2OCO , NO , $-H$, $-F$, and $-Ph$ groups.^{33, 34} These defects also show different adsorption energies for transition metal atoms, even atoms with similar charge and ionic radius.^{366, 369} The pentagons of V_2 and SW are more prone to oxidation, while the octagons prefer reduction and provide favourable sites for radical attacks.³⁵ Extrinsic defects in graphene can also combine significant variations in chemical

reactivity with small differences in electrostatics. Nitrogen and phosphorus dopants both give comparable changes to graphene's computed ESP; however, phosphorus lowers the activation energy for cycloaddition and favors [4+2] over [2+2] cycloadditions.³⁶

There have been many efforts to quantify aspects of graphene reactivity missing from partial atomic charges and ESP. Frontier orbitals analysis³⁷⁰ and conceptual density functional theory (DFT)³⁷ based descriptors such as reactivity indices^{37, 59, 371}, and Fukui functions^{35, 372-375}, *etc.*, have been used to complement the atomic partial charges. However, as mentioned in [Appendix E](#), these methods are strongly dependent on the basis set and exchange-correlation potential used in DFT calculations.^{37, 58} In addition, frontier orbitals and conceptual DFT quantifies global properties only, and these methods struggle to distinguish the local chemistry of different sites on a single molecule.^{37, 59, 60}

The findings of the previous chapters suggest that the orbital overlap distance could be particularly well-suited to understand the chemistry of graphene intrinsic and extrinsic defects. As established in [section 3.6](#) of [Chapter 3](#), the differences in hybridization and diffuseness at defect sites⁸⁸ correlate with the relative reactivity of individual atoms at defect sites. The overlap distance thus provides a useful new perspective on the site-dependent reactivity of graphene defects.

6.2 Quantifying the Reactivity of Intrinsic Defects

We start by considering the defect-free/pristine graphene surface and the surface containing vacancy and the Stone-Wales intrinsic defects. [Fig. 6.1](#) compares the ESP and $D(\vec{r})$ evaluated on the 0.001 electrons/bohr³ density isosurface. [Table 6.1](#) shows the corresponding atom-averaged quantities. [Fig. 6.2](#) shows the computed HOMO and LUMO plots. As discussed above, the ESP at the defect sites differs little from the surrounding graphene.

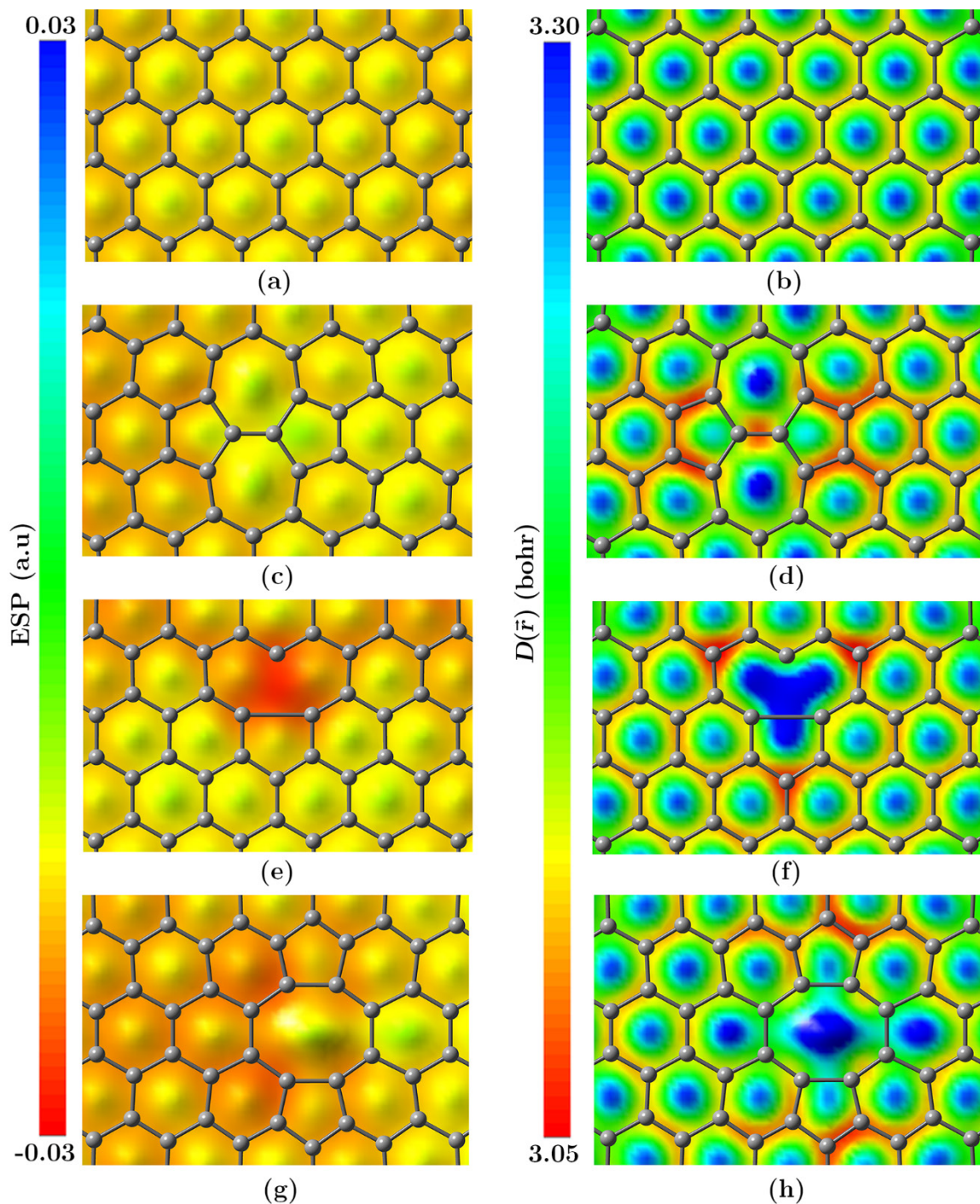


Figure 6.1 $0.001 \text{ e}/\text{bohr}^3$ density isosurface plots of ESP on left for (a) pristine (c) SW (e) reconstructed V_1 and (g) reconstructed V_2 defects. The right of figure represents similar density isosurface plots of $D(\vec{r})$ for (b) pristine (d) SW (f) reconstructed V_1 and (h) reconstructed V_2 defects. The plots on right distinguish the regions on surface with compact orbitals of small $D(\vec{r})$ (red) from the regions which have more diffuse orbitals showing large values of $D(\vec{r})$ (blue).

Inspection of the $D(\vec{r})$ plots in Fig. 6.1 shows much richer chemistry. $D(\vec{r})$ is relatively small in the π system, consistent with the p -orbital character of the π orbitals, and is relatively large in the aromatic ring centers matching the previous results of chapter 3.⁸⁸ More importantly, the orbital overlap distance clearly distinguishes the carbon atoms of SW pentagons *vs.* heptagons (Fig. 6.1d). The pentagons possess smaller orbital lobes consistent with chemically “harder” behavior. Similarly, the hollow site of heptagons has a large value of $D(\vec{r})$ as compared to the hollow site of pentagons, and the junction of these pentagons has relatively small $D(\vec{r})$.

The computed ESP of V_1 defect (Fig. 6.1e), shows that the hollow site of the nine-member ring has negative ESP, making it a relatively *basic* region on the graphene surface. The most basic site is the radical/unsaturated carbon atom. The corresponding $D(\vec{r})$ (Fig. 6.1f) shows that the occupied orbital lobes around this site are relatively large and diffuse, with a large $D(\vec{r})$. A combination of these results suggests that the V_1 defect has a *soft*

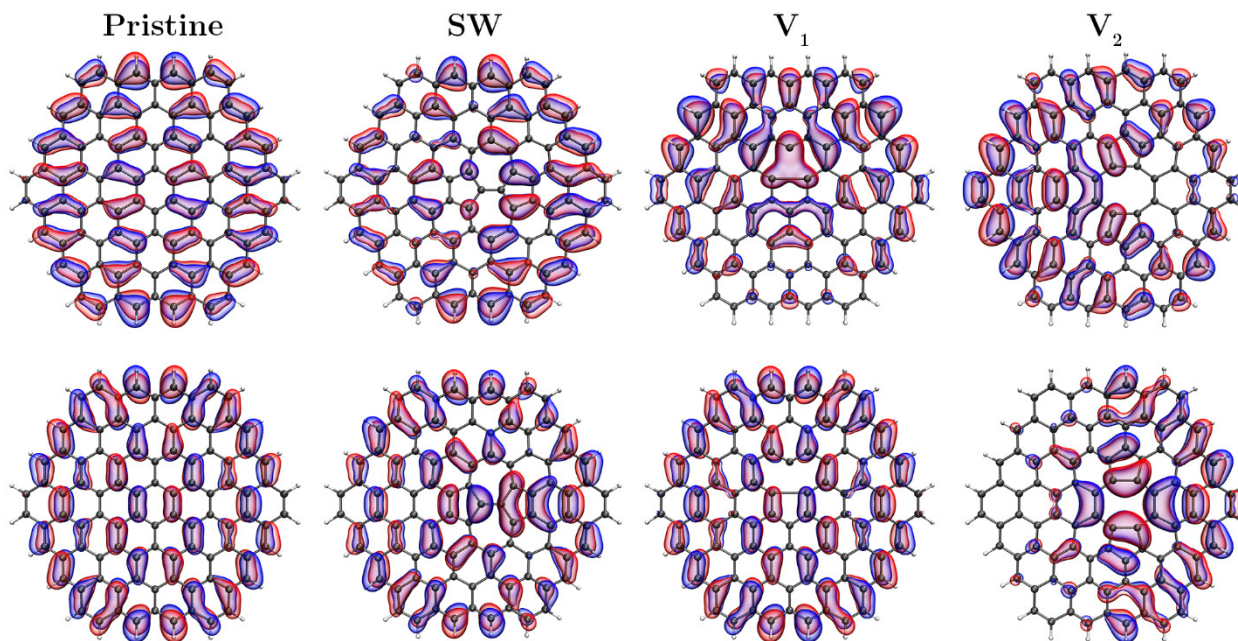
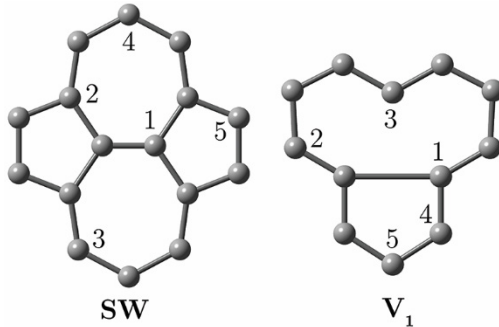


Figure 6.2 0.01 e/bohr³ alpha electron density surface plots of frontier orbital plots (top) HOMO and (bottom) LUMO for optimized geometries of pristine, Stone-Wales (SW), reconstructed single vacancy (V_1) and double vacancy (V_2) defects.

basic character. The ESP of V_2 defects (Fig. 6.1g) shows that the octagonal hollow site has a more positive ESP, making it a relatively acidic site on the graphene surface. The corresponding $D(\vec{r})$ (Fig. 6.1h) is again rather large, suggesting that the V_2 defect has a *soft acidic* character. These predictions proved to be consistent with the literature. Chemically soft transition metal cations show relatively strong adsorption to the graphene V_1 defect.³⁷⁶ Relatively soft transition metals such as Ag, Au, and Pt show four times enhanced stability on V_2 *vs.* on pristine graphene. In contrast, relatively hard metals such as Li show already strong binding to pristine graphene and insignificant enhancement in the stability of V_2 *vs.* pristine graphene.³⁷⁷ Note that the defect HOMO and LUMO (Fig. 6.2) only provides a global picture and cannot distinguish the site-dependent reactivity. We next demonstrate how combining atom-averaged charges and overlap distance D_A distinguishes the reactivity of each carbon atom at defect sites. Table 6.1 presents calculated Hirshfeld charges Q_C , and D_C of selected carbon atoms of SW and V_1 defects.

Table 6.1 Hirshfeld charges Q_C (e) and atomic overlap distance D_C (bohr) for selected atoms (labelled in the figure) of defected graphene systems relative to the central carbon atom of pristine graphene.



| Atom | SW | | V_1 | |
|------|--------|-------|--------|-------|
| | Q_C | D_C | Q_C | D_C |
| C1 | 0.021 | 1.000 | 0.024 | 1.062 |
| C2 | -0.016 | 1.002 | -0.006 | 1.005 |
| C3 | 0.016 | 1.017 | 0.021 | 1.060 |
| C4 | -0.006 | 1.016 | -0.007 | 1.004 |
| C5 | -0.017 | 0.981 | -0.023 | 0.996 |

First, consider the Stone-Wales defect. Atom C4 is slightly negative and has a relatively large value of D_C , consistent with the *soft basic* character. Atom C5 has the most negative charge and lowest value of D_C , consistent with the *hard basic* character. Similarly, atom C1 is a “*hard acidic*” while atom C3 is a “*soft acidic*” site. These findings suggest that soft and hard acidic reagents will prefer sites C4 and C5, respectively. Similarly, hard and soft basic species will prefer SW sites C1 and C3, respectively. These predictions for Stone-Wales defect reactivity concur with other quantum mechanical descriptors³⁵ and are consistent with the literature. Chemically *hard* radicals such as F, Ph, and COOH prefer SW site C1 for chemisorption.³³⁻³⁵ Metal atoms preferentially adsorb to SW heptagons (C2) over pentagons (C5) despite their similar charges.³⁷⁸ Next, consider the V_1 defect. Here atom C1 has the most positive charge and largest D_C , consistent with the soft acidic character. Atom C5 has the most negative charge and lowest D_C , consistent with the hard basic character. Atom C3 has a dangling bond giving a relatively large D_C . This is broadly consistent with the literature; the V_1 reactivity is dominated by the dangling bond of C3.³⁷⁹

6.3 Quantifying the Reactivity of Extrinsic Defects

Next, consider the orbital overlap distance for extrinsic substitutional defects. [Fig. 6.3](#) compares the ESP and $D(\vec{r})$ evaluated on the 0.001 electrons/bohr³ density isosurface for defects where two carbon atoms are substituted with nitrogen, phosphorus, boron, or silicon respectively. For these systems, the dopant atoms lie in the graphene plane. These extrinsic defects yield relatively larger charge polarization and larger variations in the surface ESP. Nitrogen is electron-withdrawing and gives a net positive charge in the graphene π system ([Fig. 6.3a](#), Mulliken charges -0.9 e on nitrogen, ~0.4 e on adjacent carbon atoms). Phosphorus and boron are electron-donating, consistent with their electronegativities lower than carbon, and give a net negative charge in the graphene π system. Similar effects were

previously seen for phosphorus dopants.³⁸⁰ Phosphorus doping gives Mulliken charges +1.3 e on phosphorus, -0.5 e to -0.8 e on adjacent carbon atoms. The orbital overlap distance

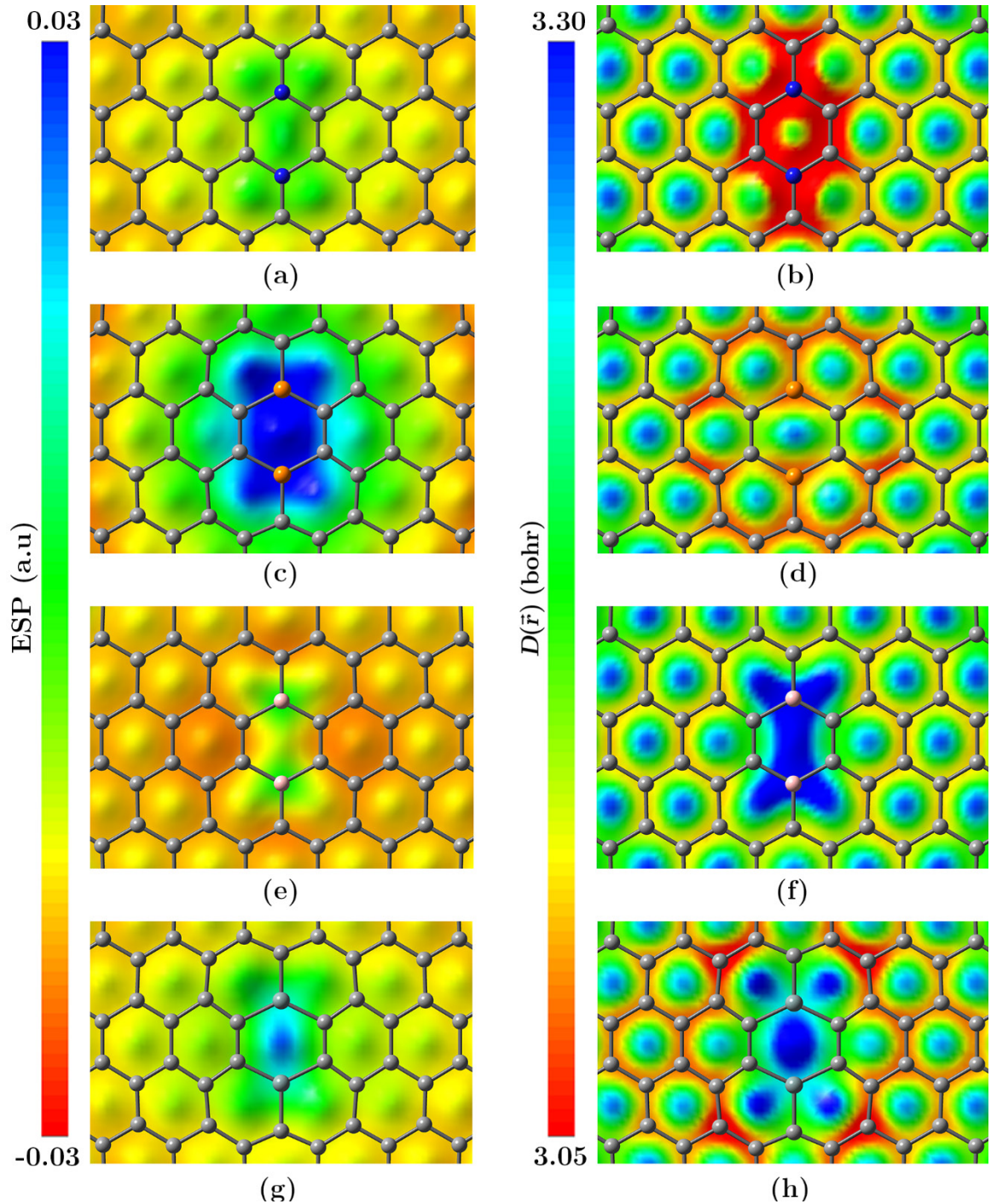


Figure 6.3 0.001 e/bohr³ density isosurface plots of ESP on left for (a) 2N (c) 2P (e) 2B and (g) 2Si doped graphene. The right of figure represents similar density isosurface plots of $D(\vec{r})$ for (b) 2N (d) 2P (f) 2B and (h) 2Si doping.

also shows large differences between nitrogen, phosphorus, and boron dopants. The compact and electron-withdrawing nitrogen dopants make the $D(\vec{r})$ relatively small both at nitrogen and at adjacent carbon atoms (Fig. 6.3b). Physically, as stated in chapter 3, charge and overlap distance often show an inverse relation. When electron density is removed from an atom increasing its partial charge, the remaining electrons are held relatively tightly, reducing the overlap distance. Carbon atoms near an N dopant are relatively “hard” compared to pristine graphene. The electron-donating phosphorus dopants also make the overlap distance slightly smaller near the defect, consistent with the more positive charge (Fig. 6.3d). In contrast, boron dopants dramatically increase the overlap distance, despite the overall positive ESP (Fig. 6.3f). Similar trends occur for silicon dopants (Fig. 6.3h). Broadly speaking, nitrogen doping gives a “hard” basic site, phosphorous doping gives a relatively strong acidic site with intermediate “hardness”, while boron and silicon doping generate relatively “soft” acidic sites due to the large value of $D(\vec{r})$ around the doping atoms. These results complement the literature, which finds that [2+2] cycloaddition of hard reagents like benzene is preferred for 2N doped over 2B and 2Si doped graphene.³⁶

6.4 Quantifying the Adsorption of Metal Atoms

The chapter is concluded by considering transition metal adsorption to vacancy defects. Previous computational studies have shown rather complex trends, with binding to V_1 defects generally more favorable than the formation of bulk metal.³⁸¹ Table 6.2 illustrates that orbital effects are particularly important for binding. Pairs of transition metal atoms possessing similar atomic radius and surface electrostatic potential can have very different V_1 binding energies. Examples include Ni and Co, Fe and Cu, or Pt and Au. Remarkably, in most cases, atoms with a larger value of the surface overlap distance tend to bind stronger to V_1 . This nontrivial prediction allows predicting V_1 binding from a simulation of only the

isolated metal atom. Fig. 6.4 rationalizes why the surface $D(\vec{r})$ is useful. The surface $D(\vec{r})$ in Fig. 6.4 form two trendlines, corresponding to “ s -valent” and “ d -valent” metals. The “ s -valent” metals with the larger surface $D(\vec{r})$ have an s -type highest occupied atomic orbital. Examples include isolated spin quintet Fe with electronic configuration $[\text{Ar}]3d^64s^2$, and isolated spin-doublet Au with electronic configuration $[\text{Xe}]4f^{14}5d^{10}6s^1$.

The “ d -valent” metals with the smaller surface $D(\vec{r})$ have a d -type highest occupied atomic orbital. Examples include isolated spin-singlet nickel atom with electronic configuration $[\text{Ar}]3d^84s^2$. Within these groups, atoms with a relatively large surface $D(\vec{r})$ give relatively large binding to V_1 . For example, “ d -valent” Pd, Pt, and Rh have surface $D(\vec{r})$ increase 2.18, 2.25, 2.49 bohr, and have V_1 binding increase -160, -187, -254 kJ/mol. Similarly, “ s -valent” Mo, Ir, Fe have $D(\vec{r})$ increase 5.20, 5.73, 5.89 bohr and have V_1 binding increase -112, -201, -235 kJ/mol respectively.

Table 6.2 Trends in transition metal binding. The first column shows the atomic radius³⁸², the second and third columns represent surface ESP and surface $D(\vec{r})$ of isolated neutral transition metal atoms calculated at 0.001 e/bohr³ density isosurface. The fourth column shows the computed binding energies to V_1 defects relative to bulk metal taken from Ref. [381].

| Metal | Atomic Radius (Å) | Surface ESP (a.u) | Surface $D(\vec{r})$ (bohr) | V_1 B.E (kJ/mol) |
|-------|-------------------|-------------------|-----------------------------|--------------------|
| Ni | 1.24 | 0.007 | 2.096 | -201 |
| Co | 1.26 | 0.015 | 5.976 | -267 |
| Fe | 1.32 | 0.018 | 5.890 | -235 |
| Cu | 1.32 | 0.009 | 5.588 | -267 |
| Pt | 1.36 | 0.005 | 2.256 | -187 |
| Au | 1.36 | 0.006 | 4.161 | 54 |
| Cr | 1.39 | 0.013 | 6.092 | -221 |
| Pd | 1.39 | 0.005 | 2.186 | -160 |
| Ir | 1.41 | 0.018 | 5.731 | -201 |
| Rh | 1.42 | 0.012 | 2.497 | -254 |

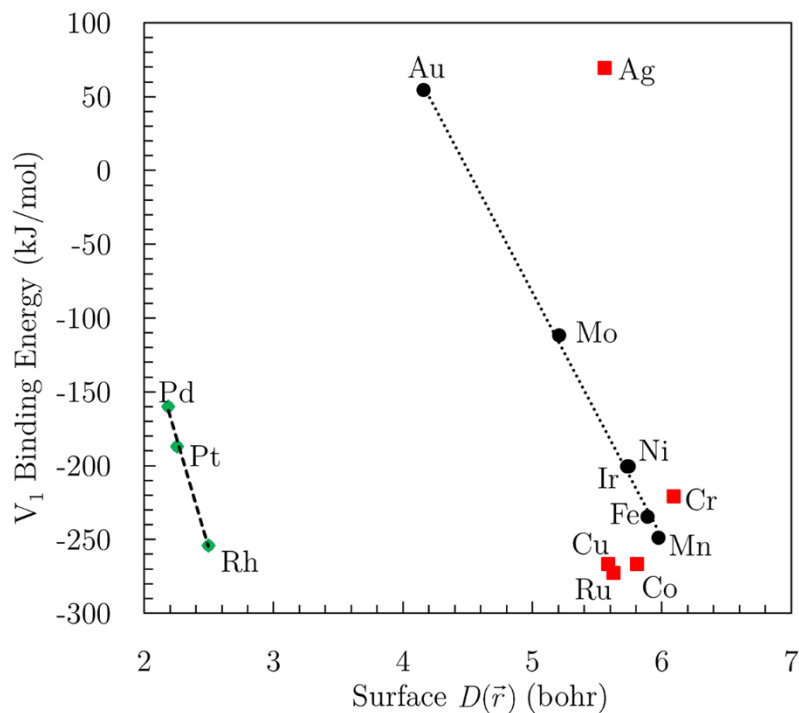


Figure 6.4 Relation between binding energies of some selected transition metals atoms on V_1 defect and surface $D(\bar{r})$ calculated at 0.001 e/bohr^3 density isosurface. The outliers are shown using red squares.

The chapter is closed by demonstrating the $D(\bar{r})$ for an adsorbed metal. Fig. 6.5 shows the surface $D(\bar{r})$ for cobalt, iron, and manganese adsorbed to a V_1 vacancy defect. The $D(\bar{r})$ is relatively large on the cobalt atom and smaller on iron and manganese. Similar trends occur for the carbons near the transition metal. In terms of electrostatics, the calculated charges of the bound metal are 0.02 e for cobalt, 0.32 e for iron, and 0.39 e for manganese. Overall, adsorbed cobalt provides a comparatively “*soft*” weak acid site. Iron and manganese provide “*harder*” and more acidic sites. These results are consistent with the observation that cobalt single-atom catalysts preferentially bind “*soft*” H_2 , whereas manganese shows higher selectivity for binding “*harder*” CO .^{366, 383}

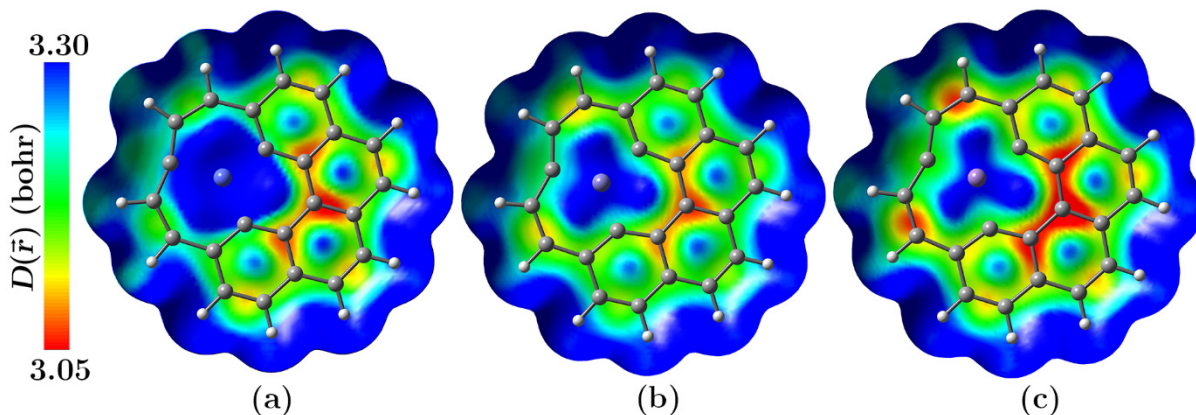


Figure 6.5 Plots of $D(\vec{r})$ on 0.001 e/bohr³ electron density isosurface for chemisorbed transition metal atoms (a) Co (b) Fe (c) Mn at the V₁ defect site of graphene flakes.

6.5 Concluding Remarks

The orbital overlap distance provides a useful complement to electrostatic potentials for visualizing and interpreting the reactivity of graphene defects. The $D(\vec{r})$ is particularly useful for intrinsic defects, whose large variations in reactivity generally do not produce large variations in electrostatics. Combining the $D(\vec{r})$ with ESP gives a richer picture of reactivity in extrinsic defects. The computed $D(\vec{r})$ of isolated metal atoms also prove to give insights into their adsorption to graphene defects. Overall, these results motivate further applications of the $D(\vec{r})$ to understand defect chemistry.

6.6 Computational Details

All defects are modelled as finite zero-dimensional hydrogen-capped graphene flakes. Most of the calculations introduce defects into a polybenzenoid hydrocarbon C₉₆H₂₄ containing 37 fused benzene rings. Previous studies have validated this as a model for local defects.⁸² For transition metal adatoms, a smaller graphene flake was selected for which the adsorption energies have been reported.¹⁶ Electronic structure calculations use the Gaussian 09²⁶⁵ suite

of programs. Geometries were optimized with density functional theory (DFT) using the (U)M06-2X³⁸⁴ level of theory with the 6-31G(d) basis set. Single-point energy calculations were subsequently carried on the optimized structures at the (U)M06-2X level with the larger basis set 6-311G(d,p). For transition metal atoms, the calculations were performed using def2-TZVP³⁸⁵ basis set. The obtained formatted check-point files of Gaussian were used as input for the Multiwfn⁹⁵ program to calculate, density, $D(\vec{r})$ and ESP Gaussian cube file format. The same program was used to calculate both D_A and Q_A using the Hirshfeld partitioning scheme.

Chapter 7

Visualizing the σ -hole Using Orbital Overlap Distance

7.1 Background

In 1992, Brinck *et al.* reported that the molecular electrostatic potential (ESP) around the halogen atom in haloalkanes is not isotropic but shows regions of positive and negative values.³⁸⁶ The positive region is localized in the elongation of the C–X (X = Cl, Br, I) covalent bond while the negative ESP is found as a concentric belt around the C–X bond

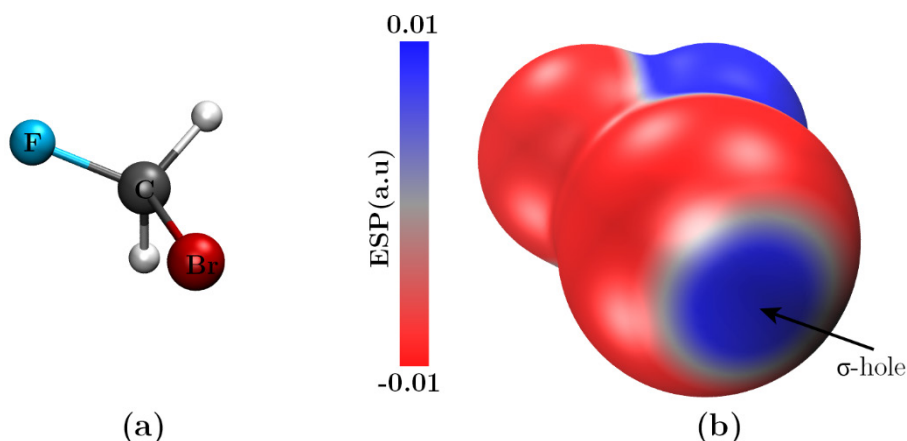


Figure 7.1 (a) Optimized geometry of bromofluoromethane at ω B97-XD/6-311G(d,p) level. (b) Molecular ESP plots on 0.001 e/bohr^3 electron density surface. The blue disc highlighted using an arrow indicates the location of σ -hole.

as shown in Fig. 7.1.^{6, 386} The maxima in the surface plots of ESP along the lateral extension of the C–X covalent bond is called σ -hole.^{6, 387} These regions are typically associated with lower electronic density³⁸⁸, and the σ -holes are formed due to the anisotropy in the distribution of the atoms' charges.¹⁰³ These positive regions of ESP allow the halogens to develop non-covalent interactions with the negative site, e.g., a lone pair of a Lewis base or an anion, and these interactions are termed as halogen bonding or σ -hole interactions.¹⁰³ These interactions are highly directional and have been known experimentally (using infrared analysis and crystallography) for around 50 years.^{6, 389-391}

The origin of σ -hole can be explained using the concept of atomic orbitals.⁶ The valence shell of halogens, e.g., Br, has an electronic configuration of $3d^{10}, 4s^2, 4p_x^2, 4p_y^2, 4p_z^1$ with halogen bound to a partner along the z -axis, as shown in Fig. 7.2. The electron of p_z orbital is localized in the C–X bond, which results in a deficiency of electron density in the outer non-bonding lobe of p_z orbital along the lateral extension of C–X covalent bond, hence the formation of σ -hole. The electron pairs of remaining p_x and p_y orbitals in combination with s orbital concentrate the electron density as a concentric belt around the C–X bond and produce an electrostatically negative region. This indicates that the halogen

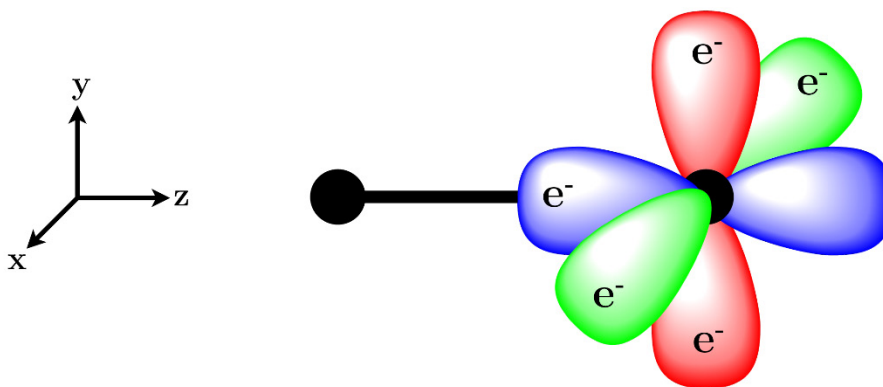


Figure 7.2 Valence p orbital arrangement on halogen atom in C–X bond. The lobes of p_x orbital are shown using green, p_y orbital using red and p_z orbital using blue colors. Both C and X atoms are represented using black dots. The electron deficient outer lobe of p_z orbital expresses itself as a σ -hole.

atom can interact non-covalently with both nucleophiles (along the extensions of the C–X bond, *i.e.*, $\sim 180^\circ$) and electrophilic sites ($\sim 90^\circ$ – 120° relative to the C–X bond).^{168, 392, 393} Experimentally, these interactions have been observed as a close contact in crystalline halides.^{394–396} Desiraju *et al.*,³⁹⁷ classified the crystalline A–X \cdots X–B interactions as type I (symmetrical interactions where $\angle AXX = \angle XXB$) and type II (bent interactions where $\angle AXX \approx 180^\circ$ and $\angle XXB \approx 90^\circ$). In crystalline solids, halogens can also have “like attracting like” interactions where a halogen atom in one molecule interacts through its σ -hole the negative electrostatic region around the σ -hole of the same halogen in another identical molecule.^{168, 398, 399} For example, in 4-bromo-3-chlorophenol, Cl \cdots Cl, and Br \cdots O form type I and type II contacts respectively, while in solid Cl₂, Cl \cdots Cl interactions of each Cl atom are both of type I and type II.

As stated earlier, σ -hole are formed due to the polarization of the electronic charge of an atom imparted by its covalent bond formation, so any factor that enhances this polarization strengthens the magnitude of σ -hole¹⁰³ which is represented as the value of ESP maxima.⁶ A higher magnitude of σ -hole indicates atom's higher polarizability and less electronegativity relative to the rest of molecule.^{6, 168} Therefore, the magnitude of σ -hole in the methyl halides increases with the order of F < Cl < Br < I with an increase in their polarizability and decrease in electronegativity down the group.¹⁶⁸ The most electronegative and least polarizable covalently bonded fluorine often do not have significant anisotropy in the charge to develop σ -hole.^{390, 400} Therefore, the halogen bonding or σ -hole interactions of fluorides are less common.⁴⁰⁰ The magnitude of σ -hole also increases as the R portion of R–X becomes more electron-withdrawing.⁴⁰⁰ For example, if R is strongly electron-withdrawing such as NC– or F₃C– etc., then all or nearly all of the halogen surface may have a positive ESP.^{392, 401, 402} These groups can also induce σ -hole on F atom.⁴⁰³

Since the formation of the covalent bond between any two atoms can affect the distribution of electron density on each of them, therefore the anisotropies of surface ESP can also be expected on atoms other than halogens.^{6, 404} Based on this reason, the σ -holes have also been reported on atoms of groups IV to VI elements and even on noble gases along the lateral extension of their covalent bonds.^{6, 404-410} Recent studies also report the existence of σ -hole and σ -hole interactions on transition metals nanoclusters as well.^{411, 412} Based on their occupation numbers and deficiencies in the valence s, p, and d orbitals of these elements, their σ -holes are characterized as σ_s , σ_p and, σ_d respectively.⁴¹¹ Depending upon the nature of corresponding orbitals, it is observed that σ_s are diffuse and non-directional, while σ_p and σ_d are localized and directional.^{411, 413}

Though molecular ESP plots define σ -holes, however in many cases, these plots provide an incomplete description of σ -hole. For example, as detailed in the [next section](#), the magnitude of ESP cannot distinguish the σ -hole of Br in CHFBr₂ from the σ -hole of I in CH₂FI. Similarly, Duarte *et al.*,⁴¹⁴ reported that the ESP plots are insufficient to explain the nature F–Br · · · X–R interactions (with X = F, Cl, Br, I and R = –H, –F) and information about the molecular polarizabilities are required to explain all features of these interactions. Clark *et al.*,⁴¹⁵ reported that without the inclusion of polarization effects, purely electrostatic interpretations of interactions are inadequate. To overcome these deficiencies of ESP, other tools have been used to quantify the σ -hole interactions. These tools include the lowest local ionization energies, $\bar{I}_{s,\min}$, local surface electron attachment energy, $E_s(\vec{r})$, natural bond orbital (NBO) analysis, quantum theory of atoms in molecules (QTAIM), and conceptual DFT based tools *etc.*^{390, 411, 416-418} In addition to the shortcomings of conceptual DFT tools mentioned in the previous chapter, other tools such as $\bar{I}_{s,\min}$ also depends on the electronic density and energy of orbital,⁴¹⁹ thus sensitive to the method and level of theory used for calculations. NBO cannot distinguish between polarization and charge-transfer

interactions⁴¹⁵ and bond critical points in QTAIM cannot correctly identify the type of interactions between the atoms connected by the bond paths.⁴²⁰

Based on these motivations, we used orbital overlap distance, $D(\vec{r})$ plots to quantify the σ -holes on various covalently bonded small molecules of groups IV-VII elements. Since $D(\vec{r})$ distinguishes the compact and diffuse orbitals, so it can provide valuable additions to the characterization of the relative nature of σ -hole as diffuse or compact and can also rationalize the corresponding σ -hole interactions. We, therefore, used these plots to predict the variations in binding energies of F-Cl \cdots CN-R and F-Cl \cdots SiN-R types of halogen bonded complexes. We extended the applications of surface plots of $D(\vec{r})$ to distinguish the relative nature of σ -holes on various transition metals' nanoclusters. The results of this chapter complement the findings of surface ESP plots and establish $D(\vec{r})$ as a substitute for other tools, such as $\bar{I}_{s,\min}$ to quantify the σ -hole interactions.

7.2 σ -holes on p-Block Elements

We start by showing how the combination of ESP and $D(\vec{r})$ surface plots capture the location and relative nature of σ_p -holes by taking the example of p-block elements. [Fig. 7.3](#) shows the optimized structures and calculated ESP and $D(\vec{r})$ surface plots of trifluorohalomethanes. The formation of σ_p -holes on halogen atoms of these molecules has been detailed in the [previous section](#). [Fig. 7.3](#) confirms that the magnitude of σ_p -holes, *i.e.*, ESP maxima, increases with an increased atomic number down the group. The $D(\vec{r})$ surface plots show that σ_p -hole regions of halogens have large values of $D(\vec{r})$ and are more diffuse relative to the other regions of the atom. With a decrease in electronegativity and an increase in polarizability, the values of $D(\vec{r})$ increase down the group with more diffuse σ_p -hole of trifluoroiodomethane have a region with the largest value of $D(\vec{r})$ while σ_p -hole of

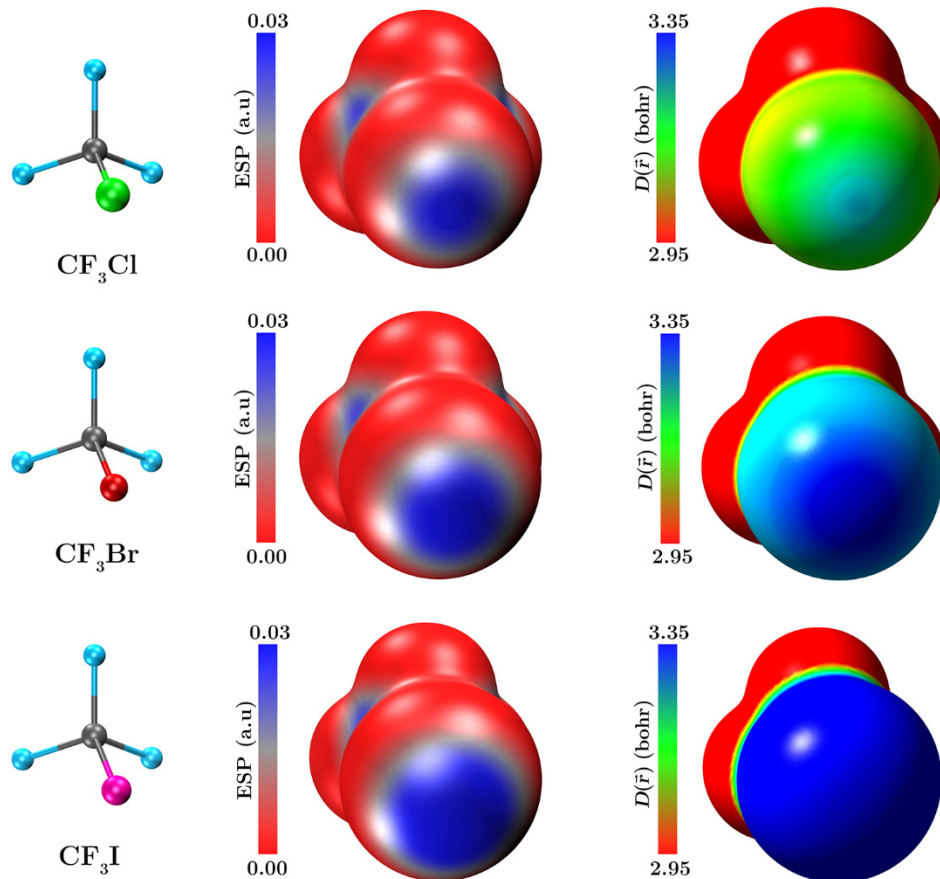


Figure 7.3 σ_p -holes on representative trifluorohalomethanes. (Left) molecule structure (Middle-Right) molecular ESP and $D(\vec{r})$ plotted on the and $0.001 \text{ e}/\text{bohr}^3$ electron density isosurface.

trifluorochloromethane has a localized disc shape region with a relatively small value of $D(\vec{r})$. Besides, for all halomethanes, the negative ESP, *i.e.*, nucleophilic regions surrounding the σ -holes, are relatively compact indicated by their small $D(\vec{r})$ relative to the σ -hole, which suggests that these regions are relatively hard-basic sites. The hardness of these regions decreases down the group with an increase in the magnitude and size of σ -holes.

We extend the discussion of Fig. 7.3 by indicating how the $D(\vec{r})$ plots are unique to characterize the σ -holes. As mentioned in the previous chapters, for a typical case, an increase in positive charge in a particular region of a molecule results in a corresponding

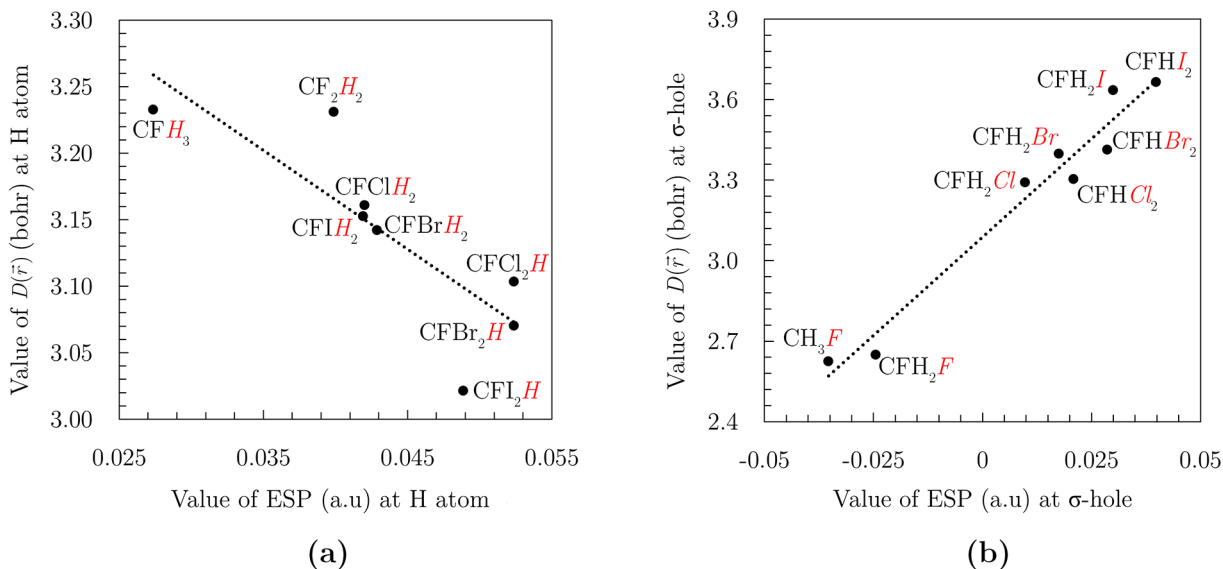


Figure 7.4 Relation between molecular ESP and $D(\vec{r})$ evaluated on the and $0.001e/\text{bohr}^3$ electron density isosurface of halomethanes (a) on H atom along the extension of C–H bond and (b) at the center of σ -hole of halogen atom shown in red (*italic*).

decrease in the value of $D(\vec{r})$ in that regions because the remaining electron density is held by the compact orbitals. This is elaborated in Fig. 7.4(a) which plots surface ESP *vs* $D(\vec{r})$ evaluated on the H atom along the extension of the C–H bond in a series of halometahnes. An increase in halogen substituents increases surface ESP on the H atom and decreases $D(\vec{r})$ so that the plot exhibits a negative slope. On the contrary, Fig. 7.4(b) shows that $D(\vec{r})$ increases with an increase in the value of ESP at the centre of σ -hole evaluated on halogen atoms. The plot indicates that both $D(\vec{r})$ and ESP are linearly related ($R^2 = 0.96$), exhibiting a positive slope and complementing Fig. 7.3. These findings highlight that the formation of σ -holes not only involves the polarization of electronic charges but is also associated with variations in orbitals characteristics such as hybridization, *etc.*, which are nicely captured by $D(\vec{r})$ plots.

To further extend, how $D(\vec{r})$ complements ESP, Fig. 7.5 shows the surface plots of these quantities for CHFBr_2 and CH_2FI molecules. For both molecules, the magnitude of σ -

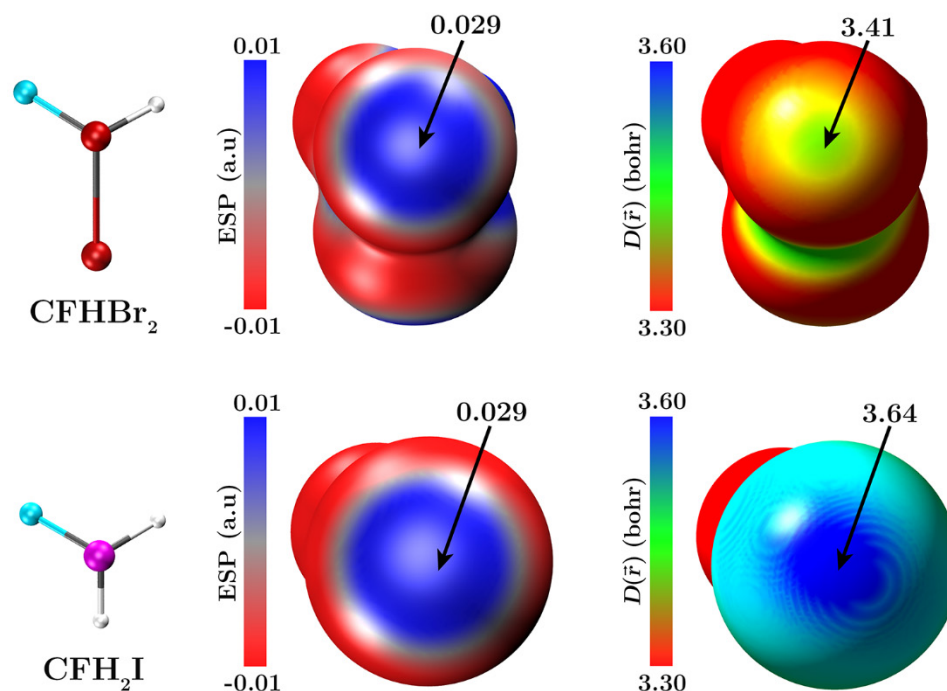


Figure 7.5 σ_p -holes on CFHBr_2 and CFH_2I molecules. (Left) molecule structure (Middle-Right) molecular ESP and $D(\vec{r})$ plotted on the $0.001 \text{ e}/\text{bohr}^3$ electron density isosurface.

holes (*i.e.*, surface ESP maxima) is the same that 0.029 a.u. , which indicates that ESP plots alone cannot distinguish the relative nature of the σ -holes of both molecules. However, surface $D(\vec{r})$ plots clearly distinguish the compact σ -hole of Br in CFHBr_2 from the relatively diffuse σ -hole of I in CFH_2I .

Figure 7.6 illustrates the location and relative nature of σ -holes in terms of molecular ESP and $D(\vec{r})$ surface plots, respectively, of some molecules containing group IV-VI elements. These atoms can have a number of σ -holes equal to the number of covalent bonds they form. In the molecule of GeH_3F , the triangular σ_p -hole is located along the extension of the F–Ge bond and at the interaction of three H–Ge bonds, as shown by its ESP plot. The σ -holes formed due to the H–Ge bonds are also along the extension of these bonds, however due to the selected orientation of the molecule, only one of these σ -holes is partially visible in the Fig. 7.6. The σ_p -hole on Ge atom is not surrounded by the region of negative

ESP as demonstrated by halogen, but it just represents the region on the surface, which has positive ESP. The $D(\vec{r})$ plots nicely complement the ESP findings by capturing the location of σ_p -holes, which appears as a triangular region and as a green ribbon with a large value of $D(\vec{r})$ representing their diffuse nature. Similarly, in the PH_2F molecule, the σ -hole is visible in the ESP surface plot along the extension of the F–P bond. However, σ -holes formed by the two H–P bonds are not visible due to the dominant-negative ESP on P lone

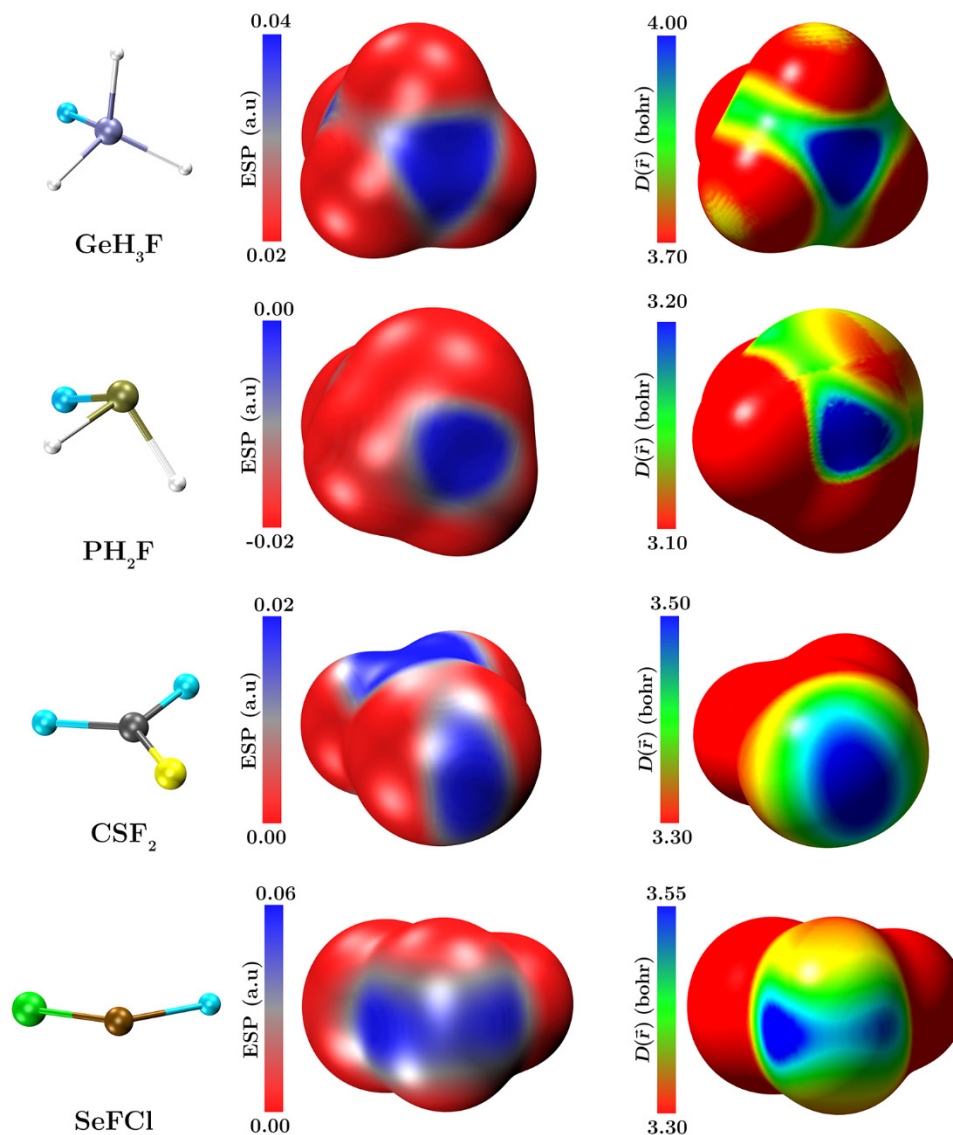


Figure 7.6 σ_p -holes on group IV-VI elements in representative molecules. (Left) molecule structure (Middle-Right) molecular ESP and $D(\vec{r})$ plotted on the and $0.001 \text{ e}/\text{bohr}^3$ electron density isosurface.

pairs region. The $D(\vec{r})$ surface plot also captures the location of the σ -hole as a diffuse triangular region with an associated large value of $D(\vec{r})$. In the molecule of CS_2F , the S is divalent, but it forms a double bond with C due to which there is only one oval-shaped σ -hole located on S atom, as illustrated by the ESP surface plot. Similar to the previous example, this σ -hole is also the most diffuse part of the molecule due to the large value of $D(\vec{r})$. There are two σ -holes on the Se atom of SeFCl molecule, which are formed along the extension of the F–Se and Cl–Se bonds. The effects of electronegativity difference between F and Cl atoms on the magnitude and size of σ -holes are clearly visible where the σ -hole induced by F atom is large in size and magnitude as compared to the one formed by Cl atom. This difference is more clearly captured in the $D(\vec{r})$ surface plot where σ -hole due to F atom is more diffuse as compared to that of Cl. These results indicate that σ -holes are not limited to halogen only but are also present on other elements of normal groups. These results also suggest that, in general, σ_p -holes are associated with relatively large $D(\vec{r})$ regions, which shows that these regions provide soft-acidic sites in σ_p -hole interactions. ESP plots can identify the location of σ -holes, but $D(\vec{r})$ surface plots complement the finding of ESP by distinguishing the relative diffuse or compact nature of these σ -holes.

7.3 σ -holes on Transition Metal Nanoclusters

We extend the applications of the combination of molecular ESP and $D(\vec{r})$ to visualize the σ -holes on transition metals (TM) nanoclusters. The valence configuration of the group 11 noble metals, *i.e.* (Cu group), is $d^{10}s^1$ with singly occupied s orbital similar to hydrogen. Upon the formation of the Au_2 cluster, these singly occupied s orbital combine, and their electrons are mainly localized in the bonding region, which creates a positive ESP over the end region along the extension of Au–Au bond as mentioned by Stenlid *et al.*⁴¹² and shown in Fig. 7.7. Since the deficiencies of valence s orbitals induce these positive regions in Cu

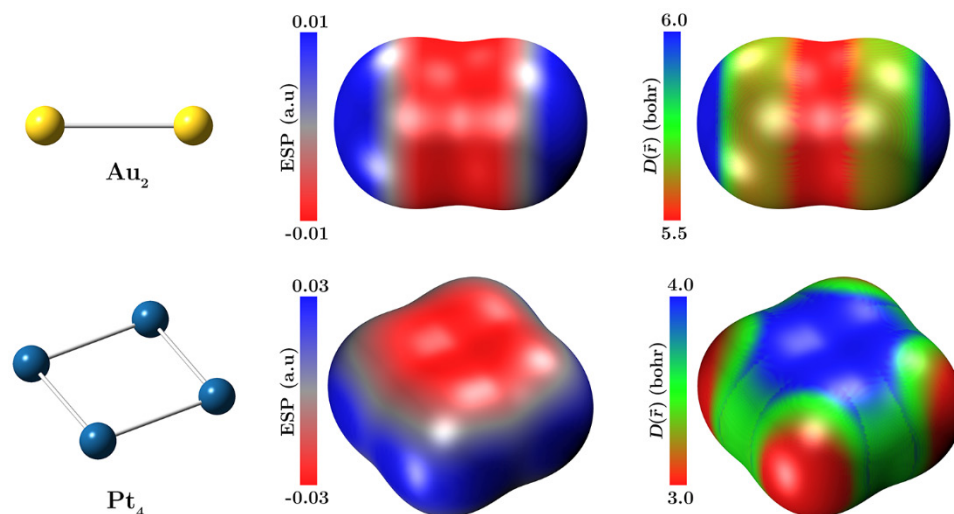


Figure 7.7 Representative examples of σ_s and σ_d on transition metal nano clusters Au_2 and Pt_4 respectively. The left side of figure shows the gas phase optimized geometry.

group metals, therefore, these can be categorized as σ_s -holes. Fig. 7.7 shows that $D(\vec{r})$ in the σ_s -holes regions of Au_2 are distinct from the rest of the molecule, which indicates that $D(\vec{r})$ can capture the σ -holes on transition metals as well. Additionally, the σ_s -holes of Au_2 have large values of $D(\vec{r})$ while the bonding region, which is associated with negative ESP, has small $D(\vec{r})$, implying the former regions are comparatively diffuse while the later are compact. Next, consider the example of the Pt_4 cluster. The valence electron configuration of Pt is $5d^96s^1$. As reported by Stenlid *et al.*,⁴¹¹ the formation of Pt_4 creates two types of local ESP positive regions due to the deficiencies of electrons in valence s and d orbitals, induced by the concentration of electrons from these orbitals to the bonding regions between Pt atoms. The deficiencies in valence s orbitals create regions of positive ESP on the corners of Pt_4 , which are visible in Fig. 7.7. However, these regions are not associated with ESP maxima. The overlap of $5dz^2$ and $5dx^2-y^2$ creates the deficiencies in d orbitals along the extension of the Pt–Pt bonds, which show the local maxima in ESP. These regions thus from σ_d -holes at each side of the corner of Pt_4 square planer structure, as can be seen in Fig. 7.7. In contrast to the Au_2 molecule, the $D(\vec{r})$ plots of Pt_4 cluster are compact at σ_d -holes regions and are diffuse in the hallowed site of the cluster. The compact nature of σ_d -holes

can be associated with the compact nature of d orbitals relative to the s orbitals. However, $D(\vec{r})$ the plot nicely distinguishes the σ -holes from the rest of the molecules.

To further elaborate the types and nature of σ -holes on TM nanoclusters, Fig. 7.8 shows the surface plots of ESP and $D(\vec{r})$ for TM_8 clusters of Pt, Ir and Au. The surface ESP plots of these nanoclusters follow the previously reported trends of Stenlid *et al.*⁴¹¹. For Pt_8 cluster, the ESP maxima are located at three points at the side of each corner Pt atom

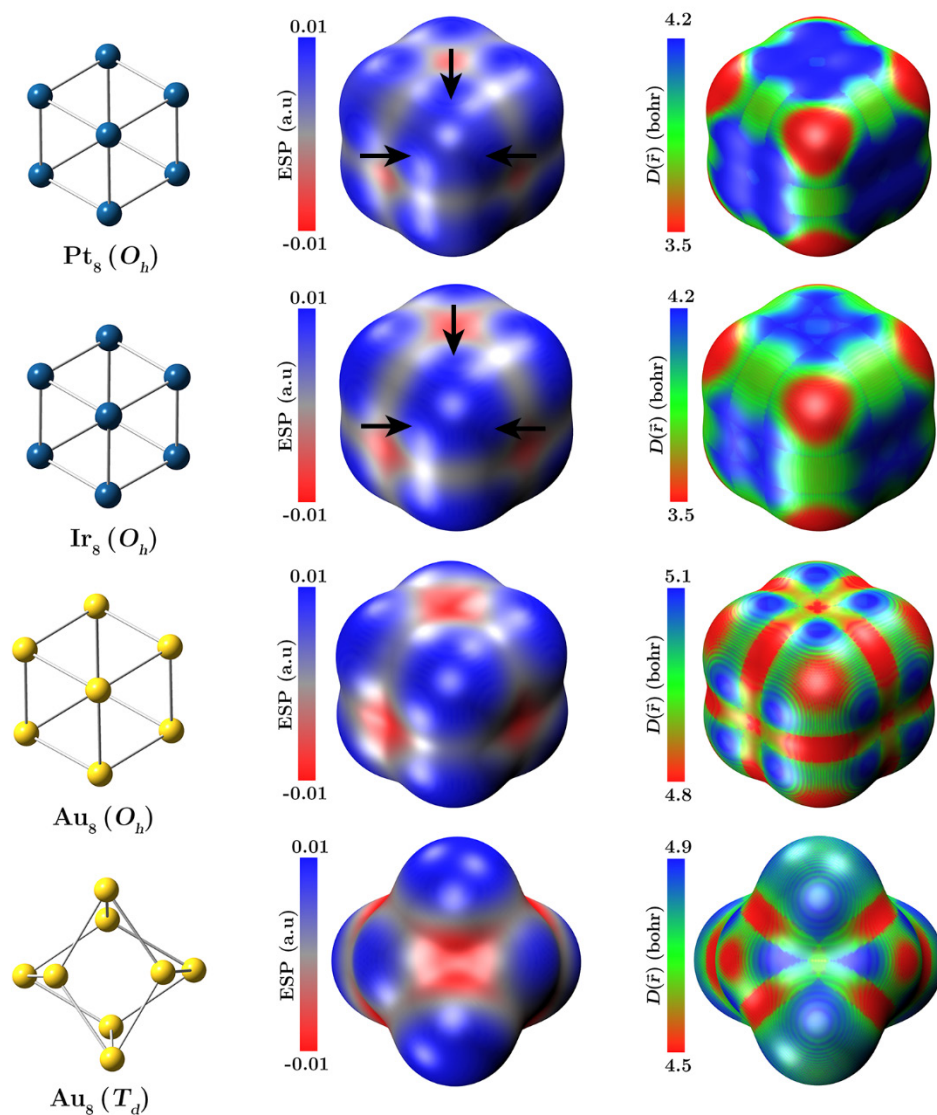


Figure 7.8 ESP and $D(\vec{r})$ of transition metals Au, Pt and Ir TM_8 nanoclusters in O_h and T_d symmetry. The left side of figure shows the gas phase geometries.

highlighted using arrows. These points correspond to the extension of each Pt–Pt bond formed by the overlap of $5d_{x^2-y^2}$ and $5d_{z^2}$ (NBO occupation: $5d_{xy}^{1.97} 5d_{xz}^{1.97} 5d_{yz}^{1.97} 5d_{x^2-y^2}^{1.56} 5d_{z^2}^{1.56} 6s^{0.75} 6p^{0.21}$)⁴¹¹ orbitals, which creates the d orbital electron deficiency at these points and hence provides the examples of σ_d -holes. The $D(\vec{r})$ surface plot of Pt₈ shows maxima in negative ESP regions, which are located at the interatomic hollow sites. Similar to the Pt₄ clusters, the σ_d -holes regions of Pt₈ are compact compared to the rest of the molecule, as revealed by the small value of $D(\vec{r})$ on these regions. On the other hand, the ESP maxima of Ir₈ are created by the overlap of compact $5d_{x^2-y^2}$ and $5d_{z^2}$ orbitals and relatively diffuse and partially filled remaining $5d$ orbitals (NBO occupation: $5d_{xy}^{1.65} 5d_{xz}^{1.65} 5d_{yz}^{1.65} 5d_{x^2-y^2}^{1.51} 5d_{z^2}^{1.51} 6s^{0.75} 6p^{0.29}$).⁴¹¹ This overlap results in a triangular-shaped ESP maximum, *i.e.*, σ_d -holes at each corner of the Ir₈ cluster. The corners of triangular ESP regions are highlighted using arrows in Fig. 7.8. Like the Pt₈ cluster, the $D(\vec{r})$ surface plot is compact at the σ_d -holes sites; however, the magnitude of $D(\vec{r})$ (red color intensity) is smaller as compared to that for Pt₈ cluster. This indicated that $D(\vec{r})$ captures the mixing of relatively diffuse $5d$ orbitals, which was absent in the Pt₈ cluster. For both, O_h and T_d Au₈ clusters, the ESP maxima is located at the corner sites and not along the extension of the Au–Au bond, which contradicts the classical definition of σ -hole. This anomaly is also captured by $D(\vec{r})$ surface plot, which exhibits different behaviors for Au₂ (Fig. 7.7) and Au₈ clusters, e.g., ESP maxima regions for Au₂ and Au₈ (T_d) have a large value of $D(\vec{r})$. In contrast, for Au₈ (O_h), these regions are compact with smaller values of $D(\vec{r})$. To get further insight into the nature of ESP maxima on gold nanoclusters, we extended the study to include large-sized nanoclusters of Au₁₃ and Au₅₅.

Figure 7.9 shows the surface ESP and $D(\vec{r})$ plots of low energy, icosahedral and cuboctahedra Au₁₃, and cuboctahedra Au₅₅ nanoclusters. The ESP maxima of these clusters

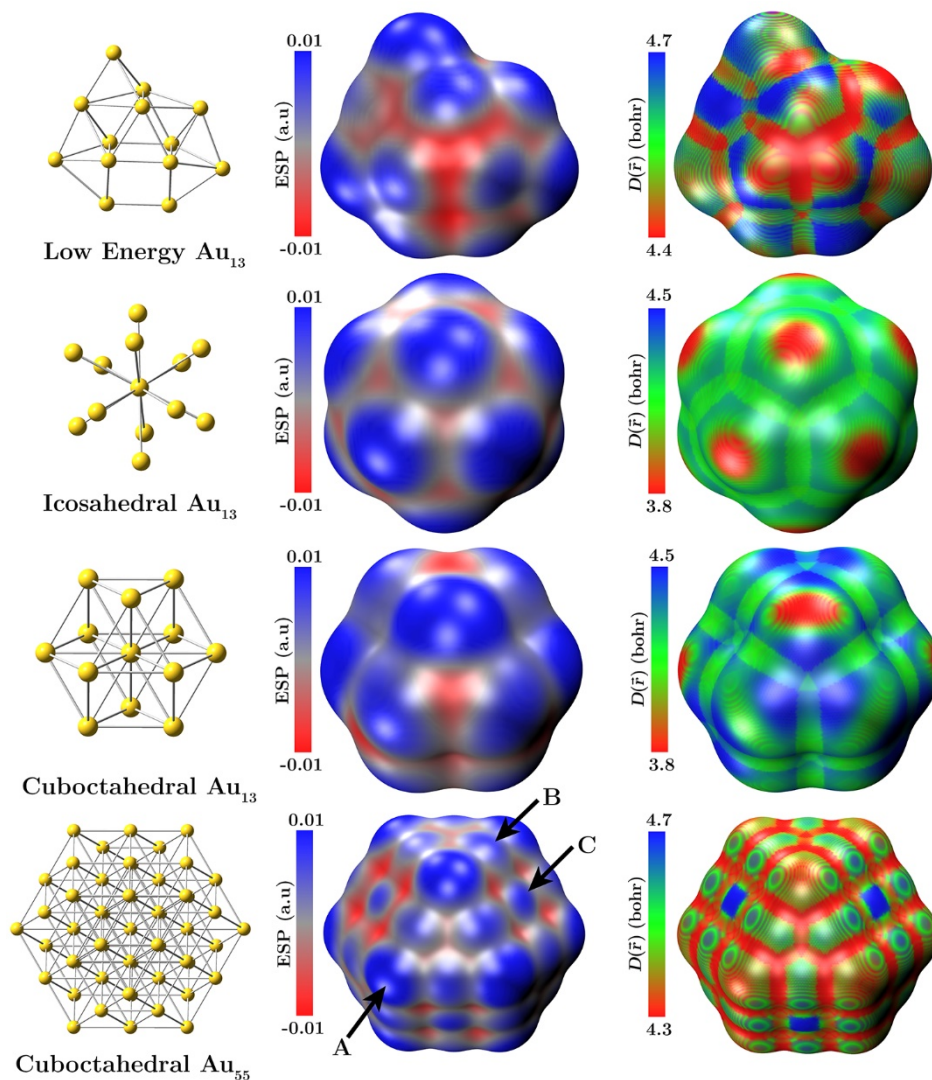


Figure 7.9 Surface plots of ESP and $D(\vec{r})$ of Au_{13} and Au_{55} nanoclusters. The left side of figure shows the gas phase geometries.

are located at low coordinated atoms.⁴¹¹ For the low energy Au_{13} cluster, this maximum is positioned at the capping atom, whereas for other Au_{13} clusters, the maxima are located at each corner atom. For Au_{55} cluster the ESP positive values follow the previously reported trend⁴¹² of corners (A) > edges (B) > facets (C) which complement their catalytic activity order.⁴¹² Similar to the Au_8 clusters these ESP maxima are not positioned along the extension of Au–Au bond but are located at the tips, *i.e.*, on top sites of Au atoms contradicting the definition of a true σ -hole. The $D(\vec{r})$ plots show the top atom of low

energy Au₁₃ cluster, which has a maximum value of ESP, is relatively more diffuse as compared to edge atoms which have lower values of ESP. The corner atoms of other Au₁₃ clusters, which are associated with ESP maxima, have the smallest values of $D(\vec{r})$, following the trends of other TM nanoclusters of Figs. 7.7, and 7.8. This trend is also followed in the Au₅₅ cluster; however, the facet central atoms (highlighted using letter “C” in Fig. 7.9), which have positive ESP, have the largest values of the surface $D(\vec{r})$, making them relatively the most diffuse atoms in the cluster. Only these regions of Au₅₅ can be categorized as true σ -holes. Based on these observations, we suggest that the regions of ESP maxima on gold clusters are not σ -holes but show a local polarization in ESP induced by the bond formation. These anomalies of gold clusters have also been reported by Stenlid *et al.*, who used the term pseudo- σ -holes for these regions.⁴¹¹

These studies establish that the combination of ESP and $D(\vec{r})$ surface plots provides a valuable tool to capture the location and rationalize the relative nature of various types of σ -holes on TM clusters.

7.4 Quantifying σ -holes Interactions

As stated in section 7.1, a typical halogen bonding or σ -hole interaction has R–X · · · B (X = halogen, B = Lewis base) angle nearly 180°, with binding energy for neutral B being less than 8 kcal/mol.³⁹⁰ Besides, the R–X bond in the halogen bonded complex can be longer or shorter than in the free R–X molecule, but usually by no more than 0.03Å, and X · · · B separation is generally 5–30% less than the sum of the respective van der Waals radii.^{390, 392.}

⁴²¹ But the halogen bonded complexes of type F–Cl · · · CN–R where R ranges from strong electron-withdrawing (R = CN, NO₂) to strong electron-donating (R = Li, Na) show deviations from some of these criteria like decrease in the Cl–C separation, lengthening of the F–Cl bond and drastic increase in binding energy.^{390, 422} Politzer *et al.*,³⁹⁰ have attributed

these anomalies in terms of a highly positive σ -hole on chlorine, which exerts a strongly polarizing electric field upon the CN–R carbons and imparts some degree of coordinate covalent character in these halogen bonded complexes. These authors quantified the variations in binding energies of these complexes using most negative ESP (represented as V_{\min} kcal/mol) and lowest local ionization energies $\bar{I}_{s,\min}$ on the surface of halogen bond or σ -hole acceptor base B (CN–R or SiN–R):³⁹⁰

$$\text{B.E} = -4.018\bar{I}_{s,\min} - 0.2768V_{\min} + 39.56 \quad (7.1)$$

where local ionization energy (in eV) is defined as:

$$\bar{I}(\vec{r}) = \frac{\sum_i \rho_i(\vec{r}) |\varepsilon_i|}{\rho_i(\vec{r})} \quad (7.2)$$

In Eq. 7.1, $\rho_i(\vec{r})$ is the electronic density of orbital i with energy ε_i at a point \vec{r} . The quantity $\bar{I}_{s,\min}$ depends on the electronic density and energy of orbital,⁴¹⁹ thus sensitive to the method and level of theory used for calculations. Since $D(\vec{r})$ is based on the one-particle density matrix and does not depend on the energy of orbitals, so it can provide the same predictions but without any ad-hoc orbital-energy-dependent corrections. We used the maximum value of $D(\vec{r})_{\max}$ as a substitute of $\bar{I}_{s,\min}$ to quantify the variations in the Politzer *et al.*³⁹⁰ reported binding energies of F–Cl · · · CN–R and F–Cl · · · SiN–R types of σ -hole bonded complexes. The calculations were performed on all free CN–R and SiN–R molecules listed in [Table G.6](#) of [Appendix G](#). For each σ -hole acceptor B, V_{\min} was located on the surface of C or Si atom along the extension of the N–C (Si) bonds.

Equation 7.3 fits the binding energies from Ref.^[390] of all studies 22 complexes listed in [Appendix G](#) taken together using double regression model in terms of V_{\min} and $D(\vec{r})_{\max}$:

$$\text{B.E} = \alpha D(\bar{r})_{\max} - \beta V_{\min} - \gamma \quad (7.3)$$

The fit reproduces the reported binding energies with $\alpha = 13 \pm 1 \text{ kcal.mol}^{-1}.\text{bohr}^{-1}$, $\beta = 0.51 \pm 0.02$ and $\gamma = 52 \pm 4 \text{ kcal.mol}^{-1}$. [Table 7.1](#) compares the fitting parameters of Eq. 7.3 with the reported³⁹⁰ parameters of Eq. 7.1.

Table 7.1 Correlation coefficients and RMS errors in reported and predicted binding energies

| Model | R ² | RMS Error |
|---------|----------------|-----------|
| Eq. 7.1 | 0.987 | 1.020 |
| Eq. 7.3 | 0.978 | 1.307 |

The results of [Table 7.1](#) indicates that substituting $\bar{I}_{s,\min}$ with $D(\bar{r})_{\max}$ not only removes the factor of orbital energy dependence in the calculations but also provides a highly comparable

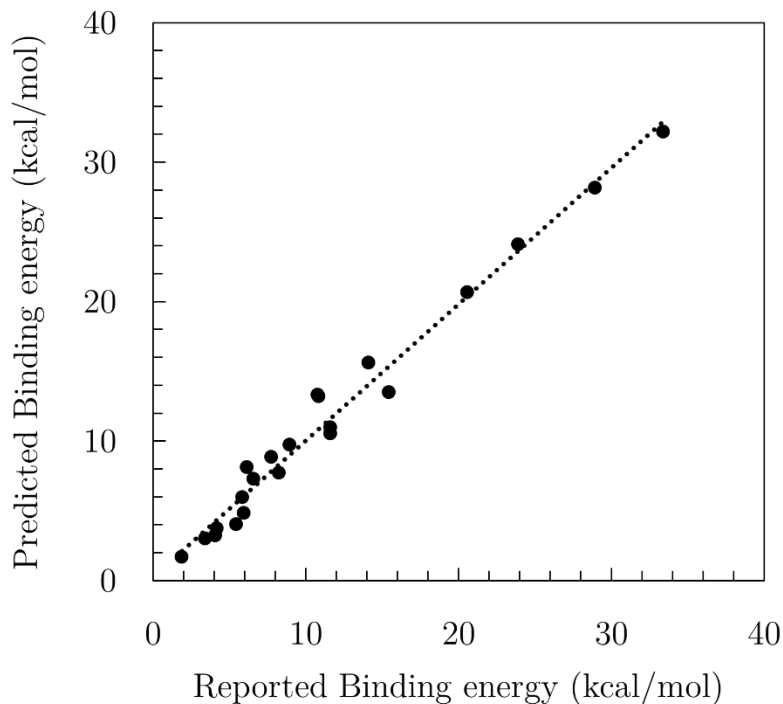


Figure 7.10 Relation between reported and predicted binding energies using Eq. 7.3 for F–Cl complexes with CN–R and SiN–R acceptors given in Appendix G.

correlation between predicted and calculated binding energies with a straightforward method of calculations. Fig. 7.10 shows the relation between reported binding energies and the binding energies predicted using Eq. 7.3. The figure confirms that there exists a strong correlation between the reported and predicted binding energies. The regression fit of Eq. 7.3 also highlights that the diffuse or compact nature of halogen bond or σ -hole acceptors plays a significant role in holding the components together, which is nicely captured by the $D(\vec{r})$ surface plots.

7.5 Concluding Remarks

The halogen bonding and other σ -hole interactions are fundamental for crystal engineering and the development of multicomponent pharmaceutical co-crystals. The understanding of the relative hard or soft nature of σ -holes is essential to interpret their interactions in crystalline materials. The results of this chapter indicated that the combination of ESP and $D(\vec{r})$ surface plots capture the location and relative nature of σ -holes on the normal groups and TM elements. The $D(\vec{r})$ surface plots specifically complement ESP plots for those systems which have the same magnitude of σ_s -holes. These plots highlighted that σ_s -hole are more diffuse, σ_p -holes are relatively compact and σ_d -hole are most compact *i.e.*, chemically hard in nature which corresponds to the relative nature of σ -holes forming orbitals. The $D(\vec{r})$ surface plots can distinguish each σ_p -hole formed on group IV-VI elements resulted from their covalent bonds in the molecule. These plots also distinguished the soft σ_s -hole types of positive ESP regions of Au and Cu nanoclusters from σ_d -holes of other TM elements. The binding energies of complexes $F-Cl \cdots CN-R$ and $F-Cl \cdots SiN-R$ can be predicted using the minimum of ESP, V_{\min} , and maximum of overlap distance $D(\vec{r})_{\max}$ of acceptor base with high correlations between calculated and predicted values.

7.6 Computational Details

All the calculations use the Gaussian 09²⁶⁵ suite of programs. The calculations for Figs. 7.1, 7.3 to 7.6 use B3LYP functional and Def2-QZVP basis set for gas-phase geometry optimization. The coordinates of TM nanoclusters used in Figs. 7.7-7.9 were obtained from Ref. [411] and Ref. [412]. The calculations for these clusters were carried out at PW91PW91/Def2-SV(P) level with effective core potential using the spin states mentioned in those references. The calculations for section 7.4 use the B3PW91 functional and 6-31G(d,p) basis set following the method of Ref. [390]. The Gaussian formatted checkpoint files were used to obtain electron density, ESP, and $D(\vec{r})$ grid data in the Gaussian cube file format using Multiwfn program⁹⁵. For the calculations of $D(\vec{r})$, an even-tempered grid of 50 exponents was used starting from 2.50 Bohr⁻² and with an increment of 1.50 Bohr⁻². For the studied systems, the calculated ESP and $D(\vec{r})$ cube files were projected over 0.001 e/bohr³ molecular electron density surface. The molecular graphics were created using VMD²⁷⁹ version 1.9.3 and GaussView 5 package.

Chapter 8

Assessment, Implications, and Outlook

8.1 Discussion

The comprehensive understandings about the chemical reactivities of atoms, ions, molecules, and nanomaterials require the knowledge of orbitals since their reactions involve the synergy between electrostatic and orbital interactions. The relative importance of electrostatics and orbital contributions varies as a function of the nature of reacting species. For instance, the former dominates in reactions that are charge-controlled, ionic, or driven by electronegativity differences. At the same time, the latter becomes a significant player in orbital-controlled, covalent, and chemical-softness provoked interactions. Interpretations of chemical reactivity using electrostatics only may provide answers in specific reactions but can drastically fail in several others. The motivation of this dissertation was to use the orbital overlap distance, and its atomic average quantities to complement the electrostatic potential and calculated partial charges to get a full spectrum of chemical reactivity. Our studies indicated that the role of these tools is aggrandized in those cases where species having similar charges show different reactivities. This includes the distinction between the relative stability of allotropes, aromaticity *vs.* anti/non-aromaticity, the selectivity of metal ions to a protein binding pocket, and reactivities of atoms in nanomaterials and graphene

sheets. In other cases, these tools combine with calculated charges or ESP to predict the reactivities qualitatively or quantitatively in terms of any experimental or computed parameter. This category includes the quantitative structure–property investigations to predict the substituents' effects, *i.e.*, Hammett parameters, binding energies in non-covalent interactions, acid–base binding affinities, stability constants, solvent softness, and interactions of metal ions to graphene defects, *etc.* The qualitative aspect of this category includes the analysis of reactivity based on chemical reasoning of hard and soft acids and bases (HSAB), e.g., predictions in structure-based drug design, protein–ligand interactions, interactions of small molecules with graphene defects, and relative nature of σ -holes, *etc.* Finally, the mother tool $\text{EDR}(\vec{r}; d)$ provided insights into the ubiquitous problem of bond stretching and highlighted the associated limitations of electronic structure methods.

8.2 Broader Impacts of the Tools

The results of the studies mentioned in this dissertation and associated publications will provide valuable assistance to the experimental and theoretical community to quantify and predict the chemical reactivity by using fast, reliable, and feasible $\text{EDR}(\vec{r}; d)$ based tools. This dissertation introduces the applications of these tools in all major fields including, organic chemistry, nanochemistry, materials sciences, medicinal chemistry, solution chemistry, and surface sciences, which will pave the way towards their utilization in a broad spectrum of research. Our implementations of these tools to one of the leading open-source electronic wavefunction analysis code, Multiwfn, will make them accessible to a vast scientific community. In addition, we have prepared the technical notes containing working examples, which are also part of the Multiwfn official manual. These notes will help to make this toolkit accessible to the non-specialist users who have a basic working knowledge of computational chemistry.

8.3 Limitations of the Tools

- Since $\text{EDR}(\vec{r}; d)$ is based on orbitals, so it cannot be evaluated using experimental electron density obtained from X-ray or electron diffraction. This limitation puts these tools at a disadvantage over ESP, atoms in molecules (AIM), and non-covalent interactions (NCI) based descriptors, which are extensively used by the community working in experimental charge density analysis despite their well-established limitations.
- Due to the same reason mentioned above, $\text{EDR}(\vec{r}; d)$ based tools cannot be evaluated as well for force-field based methods such as molecular dynamics simulations. These tools cannot interpret the molecular mechanics calculations of macromolecules, which is the leading research area of chemical physics, materials science, and biophysics. The availability of these tools was repeatedly inquired by the community working in molecular mechanics when the results of this dissertation were presented at conferences and workshops.
- Presently, $\text{EDR}(\vec{r}; d)$ and its derived tools are implemented only for atomic and molecular gas-phase calculations and not available for plane-wave methods. This limitation restricts these tools to address the problems of a vast community of physics and material sciences working in solid-state chemistry using plane-wave electronic structure codes.

8.4 Future Directions

We plan to undertake the following studies in the future.

- Some of our initial studies on individual transition metal ions in the gas phase indicated that the values of their surface $D(\vec{r})$ are correlated to their experimental

coordination behaviors and follow the trends of Irving–Williams series. These studies suggested that the combination of $D(\vec{r})$, ESP and radius of metal ions can predict the experimental stability constants with excellent correlations. These findings will be extended by performing systematic analysis on the coordination of metal ions, especially to the cyclic ligands such as crown ethers, *etc.*

- Implement $\text{EDR}(\vec{r}; d)$ and derived tools to plane-wave codes such as Quantum ESPRESSO and a hybrid Gaussian and plane waves (GPW) code CP2K. These implementations and corresponding representative studies will invite a vast community to use these tools for solid-state, liquid, periodic, material, crystal, and biological systems.
- Develop the second generation of these tools by replacing the one-particle density matrix with other types of density matrices, such as the response density matrix. The substitution with the response density matrix will provide insights into the variation of local polarizabilities and visualization of reactive regions during a chemical reaction.

Appendix A

The Electronic Structure Methods

A.1 Fundamentals

Any problem in the electronic structure of matter is covered by the Schrödinger's equation⁴²³⁻⁴²⁵, which, for an isolated N -electron atomic or molecular system is given by:

$$\hat{H}\Psi = E\Psi \quad (\text{A.1})$$

where E is the electronic energy of the system, $\Psi = \Psi(\mathbf{x}_1, \mathbf{x}_2, \dots, \mathbf{x}_n)$ is the wavefunction and \hat{H} is the non-relativistic Hamiltonian operator for N electrons and M nuclei (in atomic units)⁴²⁶:

$$\begin{aligned} \hat{H} &= -\frac{1}{2} \sum_{i=1}^N \nabla_i^2 - \frac{1}{2} \sum_{A=1}^M \frac{1}{m_A} \nabla_A^2 - \sum_{i=1}^N \sum_{A=1}^M \frac{Z_A}{r_{iA}} + \sum_{i=1}^N \sum_{j>i}^N \frac{1}{r_{ij}} + \sum_{A=1}^M \sum_{B>A}^M \frac{Z_A Z_B}{R_{AB}} \\ &= \hat{T}_e + \hat{T}_n + \hat{V}_{ne} + \hat{V}_{ee} + \hat{V}_{nn} \end{aligned} \quad (\text{A.2})$$

The solution of Eq. A.1 depends on the positions of electrons, \mathbf{r} , and nuclei, \mathbf{R} with nuclear charges Z_A and Z_B for A and B respectively having mass m in atomic units.⁴²⁶ With exception to hydrogen-like atoms, Schrödinger's equation cannot be solved analytically, and approximations are introduced to reduce the complexity of the calculations.⁴²⁶ The Born-Oppenheimer approximation⁴²⁷ considers the electrons in a molecule to be moving in the field of fixed nuclei due to their large mass differences. This approximation eliminates the kinetic energy of nuclei, *i.e.*, term \hat{T}_n in Eq. A.2 and considers the last term, \hat{V}_{nn} that is,

the repulsion between nuclei to be constant. The remaining terms in Eq. A.2 are called electronic Hamiltonian⁴²⁶ describing the motion of N electrons in the field of M point charges:

$$\hat{H}_{ele} = \hat{T}_e + \hat{V}_{ne} + \hat{V}_{ee} \quad (\text{A.3})$$

This leads to the solution of the *electronic* Schrödinger equation:

$$\hat{H}_{ele} \Psi(\mathbf{r}; \mathbf{R}) = E_{ele}(\mathbf{R}) \Psi(\mathbf{r}; \mathbf{R}) \quad (\text{A.4})$$

The electronic structure methods in quantum chemistry aim to find the solutions of Eq. A.4 by either approximating the wavefunction or the Hamiltonian.

Henceforth, the subscript *ele* of the electronic Hamiltonian in Eq. A.4 will be ignored for simplicity. The Dirac or *bra-ket* notation⁴²⁸ will be used to represent the integrals of many-electron or one-electron wavefunction, *i.e.*:

$$\langle \Psi | \Psi \rangle = \int d\mathbf{r} \Psi^*(\mathbf{r}) \Psi(\mathbf{r}) \quad (\text{A.5})$$

Similarly, the one- and two-electron integrals in Dirac notation will be represented as:⁴²⁶

$$\langle i | \hat{h} | j \rangle = \langle \psi_i | \hat{h} | \psi_j \rangle = \int d\mathbf{r}_1 \psi_i^*(\mathbf{r}_1) \hat{h}(\mathbf{r}_1) \psi_j(\mathbf{r}_1) \quad (\text{A.6})$$

$$\langle ij | ij \rangle = \langle \psi_i \psi_j | \psi_i \psi_j \rangle = \int \int d\mathbf{r}_1 d\mathbf{r}_2 \psi_i^*(\mathbf{r}_1) \psi_j^*(\mathbf{r}_2) r_{12}^{-1} \psi_i(\mathbf{r}_1) \psi_j(\mathbf{r}_2) \quad (\text{A.7})$$

A.2 The Hartree-Fock (HF) Approximation

The simplest approximation to solve the electronic problem of Eq. A.4 is to assume that the system consists of non-interacting electrons, *i.e.*, $\hat{V}_{ee} = 0$ in Eq. A.3. This makes the electronic Hamiltonian a sum of one-electron Hamiltonians and the molecular wavefunction a product of independent one-particle wavefunctions, termed as the Hartree product (HP).⁴²⁹

$$\Psi(\mathbf{r}_1, \mathbf{r}_2, \dots, \mathbf{r}_N) = \psi_1(\mathbf{r}_1) \cdot \psi_2(\mathbf{r}_2) \cdot \psi_3(\mathbf{r}_3) \cdot \dots \cdot \psi_N(\mathbf{r}_N) = \prod_{i=1}^N \psi_i(\mathbf{r}_i) \quad (\text{A.8})$$

The electronic energy thus becomes:

$$E_{\text{HP}} = \sum_{i=1}^N \int d\mathbf{r}_i \psi_i^*(\mathbf{r}_i) \hat{h}_i \psi_i(\mathbf{r}_i) + \sum_{i=1}^N \sum_{j>i}^N \iint d\mathbf{r}_i d\mathbf{r}_j \frac{|\psi_i(\mathbf{r}_i)|^2 \cdot |\psi_j(\mathbf{r}_j)|^2}{r_{ij}} \quad (\text{A.9})$$

where \hat{h} is the core-Hamiltonian⁴³⁰ which can be given as:

$$\hat{h}_i = -\frac{1}{2} \nabla_i^2 - \sum_{A=1}^M \frac{Z_A}{r_{iA}} \quad (\text{A.10})$$

This then gives a set of N eigenvalue equations known as Hartree equations:^{431, 432}

$$\left[\hat{h}_i + \sum_{j>i}^N \int d\mathbf{r}_j \frac{\psi_j^*(\mathbf{r}_j) \psi_j(\mathbf{r}_j)}{r_{ij}} \right] \psi_i = \varepsilon_i \psi_i \quad (\text{A.11})$$

The second term in Eq. A.11 represents the Coulomb repulsion to all other electrons.

Suppose now that Φ is approximated as an antisymmetrized wavefunction obeying the Pauli exclusion principle and is obtained by a linear combination of Hartree products.

This wavefunction can be expressed in the form of Slater determinant.^{433, 434}

$$\Phi(\mathbf{r}_1, \mathbf{r}_2, \dots, \mathbf{r}_N) = \frac{1}{\sqrt{N!}} \begin{vmatrix} \psi_1(\mathbf{r}_1) & \psi_2(\mathbf{r}_1) & \dots & \psi_N(\mathbf{r}_1) \\ \psi_1(\mathbf{r}_2) & \psi_2(\mathbf{r}_2) & \dots & \psi_N(\mathbf{r}_2) \\ \vdots & \vdots & & \vdots \\ \psi_1(\mathbf{r}_N) & \psi_2(\mathbf{r}_N) & \dots & \psi_N(\mathbf{r}_N) \end{vmatrix} \quad (\text{A.12})$$

where $1/\sqrt{N!}$ is the normalization factor and $\langle \Phi | \Phi \rangle$ equal to 1. Solving Eq. A.4 using

Slater determinant gives the energy expectation values as:⁴²⁶

$$\begin{aligned}
E_{\text{HF}} &= \langle \Phi | \hat{H} | \Phi \rangle \\
&= \sum_{i=1}^N \langle i | \hat{h} | i \rangle + \sum_{i=1}^N \sum_{j>i}^N \langle ij | ij \rangle - \sum_{i=1}^N \sum_{j>i}^N \langle ij | ji \rangle \\
&= \sum_{i=1}^N \langle i | \hat{h} | i \rangle + \frac{1}{2} \sum_{i,j=1}^N (J_{ij} - K_{ij})
\end{aligned} \tag{A.13}$$

where

$$\hat{J}_{ij} = \sum_{i=1}^N \sum_{j>i}^N \langle ij | ij \rangle = \iint d\mathbf{r}_i d\mathbf{r}_j \psi_i(\mathbf{r}_i) \psi_i^*(\mathbf{r}_i) \frac{1}{r_{ij}} \psi_j^*(\mathbf{r}_j) \psi_j(\mathbf{r}_j) \tag{A.14}$$

$$\hat{K}_{ij} = \sum_{i=1}^N \sum_{j>i}^N \langle ij | ji \rangle = \iint d\mathbf{r}_i d\mathbf{r}_j \psi_i^*(\mathbf{r}_i) \psi_j(\mathbf{r}_i) \frac{1}{r_{ij}} \psi_i(\mathbf{r}_j) \psi_j^*(\mathbf{r}_j) \tag{A.15}$$

The \hat{J} are the Coulomb integrals and \hat{K} are called the exchange integrals. The *Hartree-Fock approximation* is the method whereby the orbitals ψ_i are found that minimize Eq. A.13 for the Slater determinantal form of Φ .⁴³⁵ The minimization of Eq. A.13 subject to the orthonormalization conditions:⁴²⁶

$$\int d\mathbf{r} \psi_i^*(\mathbf{r}) \psi_j(\mathbf{r}) = \delta_{ij} \tag{A.16}$$

Operators in Eqs. A.10, A.14, and A.15 can be combined into an effective one-electron operator termed Fock operator:⁴³⁰

$$\hat{F} = \hat{h} + \sum_j \hat{J}_j - \hat{K}_j \tag{A.17}$$

So that the Hartree-Fock equation for orbitals ψ_i in many electrons wavefunction Φ becomes:

$$\hat{F} |\psi_i\rangle = \varepsilon_i |\psi_i\rangle \tag{A.18}$$

The solution of Eq. A.18 is a difficult task mathematically. The widely used strategy is to use Roothaan-Hall procedure^{435, 436} to expand the molecular orbitals (MOs) in simple one-electron basis functions, which are also known as the atomic orbitals (see section A.5). Each molecular orbital, ψ_i is expanded as a linear combination of atomic orbitals (LCAO), χ_μ :⁴³⁵

$$\psi_i(\mathbf{r}) = \sum_{\mu}^K C_{\mu i} \chi_{\mu}(\mathbf{r}) \quad (\text{A.19})$$

This yields a set of Hartree-Fock equations of type Eq. A.18 in the atomic orbital basis, which can be expressed in matrix notations as:

$$\mathbf{FC} = \mathbf{SC}\epsilon \quad (\text{A.20})$$

Where \mathbf{F} is the Fock matrix given as:

$$F_{\mu\nu} = \langle \mu | \hat{F} | \nu \rangle = \int d\mathbf{r}_1 \chi_{\mu}^*(\mathbf{r}_1) \hat{F} \chi_{\nu}(\mathbf{r}_1) \quad (\text{A.21})$$

and \mathbf{S} the overlap matrix:

$$S_{\mu\nu} = \langle \mu | \nu \rangle = \int d\mathbf{r}_1 \chi_{\mu}^*(\mathbf{r}_1) \chi_{\nu}(\mathbf{r}_1) \quad (\text{A.22})$$

Diagonalization of the overlap matrix results:

$$\mathbf{S}\mathbf{L}_S = \mathbf{L}_S\mathbf{\Lambda}_S \quad (\text{A.23})$$

where \mathbf{L}_S is the matrix of eigenvectors and $\mathbf{\Lambda}_S$ is the diagonal matrix of corresponding eigenvalues which can be used to build the symmetric orthogonalization matrix:

$$\mathbf{S}^{-1/2} \equiv \mathbf{L}_S \mathbf{\Lambda}_S^{-1/2} \mathbf{L}_S^{\dagger} \quad (\text{A.24})$$

where \mathbf{L}_S^{\dagger} denotes the matrix transpose. Diagonalization of the Fock matrix and transformation of the obtained eigenvectors into the atomic orbitals basis will result:

$$\mathbf{C} = \mathbf{S}^{-1/2} \mathbf{C}' \quad (\text{A.25})$$

Inserting Eq. A.25 into Eq. A.20 and diagonalization results:

$$\mathbf{F}' \mathbf{C}' = \mathbf{C}' \boldsymbol{\varepsilon} \quad (\text{A.26})$$

The eigenvalue problem can then be solved for \mathbf{C}' by diagonalization of \mathbf{F}' . This indicates that the Roothaan-Hall equations^{435, 436} can be solved by simply diagonalizing the Fock matrix to get the eigenvalues $\boldsymbol{\varepsilon}$.⁴²⁶

The HF method providing an average treatment to electron-electron interaction usually recovers 99% of the total experimental energy.⁴³⁷ The remaining 1% energy, which is called the correlation energy, is generally of the order of 0.04 Hartree per electron pair. This is equivalent to about 1 eV or 100 kJ/mol, the same order of magnitude as electron excitations and molecular binding energies.⁴³⁷ This correlation energy is vital to explain chemical phenomena such as dispersion interactions, *etc.* In addition, as detailed in Chapter 2, the restricted HF method cannot describe the dissociation of molecules into open-shell fragments. Similarly, the unrestricted HF method, though, mostly gives the qualitatively correct picture of bond dissociations, but the resulting potential energy curves are not accurate. Most of the post-HF electronic structure methods focus on improving HF approximation.

A.3 Correlated Ab Initio Methods

The post HF-methods focus in obtaining the correlation energy (E_{corr}) which is defined as the difference between the exact nonrelativistic energy of the system (ξ_0) and the Hartree-Fock energy (E_{HF}) obtained in the limit of complete basis set.⁴²⁶

$$E_{corr} = \xi_0 - E_{HF} \quad (\text{A.27})$$

The E_{corr} is negative because the E_{HF} is an upper bound to the exact energy. The main correlated ab initio methods are configuration interaction (CI), Møller-Plesset (MP) perturbation theory, and the coupled-cluster methods, which are summarized below.

A.3.1 Configuration Interaction (CI)

Among all the post-HF correlated ab initio methods, configuration interaction is conceptually the most straightforward method.⁴²⁶ In this method the wavefunction is constructed using the linear combinations of the HF determinant and its corresponding excited determinants:⁴³⁸

$$\begin{aligned} |\Psi_{CI}\rangle &= c_0 |\Phi\rangle + \sum_{ai} c_a^i |\Phi_a^i\rangle + \sum_{\substack{a<b \\ i<j}} c_{ab}^{ij} |\Phi_{ab}^{ij}\rangle + \sum_{\substack{a<b<c \\ i<j<k}} c_{abc}^{ijk} |\Phi_{abc}^{ijk}\rangle + \sum_{\substack{a<b<c<d \\ i<j<k<l}} c_{abcd}^{ijkl} |\Phi_{abcd}^{ijkl}\rangle + \dots \\ &= \sum_{\mu} \hat{\tau}_{\mu} |\Phi\rangle \end{aligned} \quad (\text{A.28})$$

where $|\Phi_a^i\rangle$ is the singly excited determinant corresponds to the excitation from occupied orbital a to virtual orbital i , $|\Phi_{ab}^{ij}\rangle$ is the doubly excited determinant, *etc.*, up to and including N -tuply excited determinants.⁴²⁶ The coefficient c represents the contribution of the corresponding term to the Ψ_{CI} wavefunction. The restriction on the summation indices (*e.g.*, $a<b$ or $i<j$, *etc.*) ensures that a given excited state is counted only once.

Considering all possible excited determinants in the wavefunction expansion defines the Full Configuration Interaction (FCI) method. Solving the FCI problem corresponds to solving the Schrödinger equation precisely within the space spanned by the basis set $\{\chi_{\mu}\}$. In principle, though FCI provides an exact solution of the many-electron problem, practically only a finite set of N -electron trial wavefunctions can be handled as the number of determinants increases exponentially with the number of electrons and molecular orbitals.

For example, for some arbitrary set of $2K$ one-electron spin orbitals, $\binom{2K}{N}$ different N -electron Slater determinants can be constructed.⁴²⁶ Even for small molecules with a finite one-electron basis, the trial wavefunction must be truncated to use only a fraction of all possible N -electron wavefunctions. Consequently, CI provides an upper bound to the exact energy.⁴³⁹ The commonly employed truncation scheme considers the single and double excitations relative to the reference state and is termed as configuration interaction singles doubles (CISD) method.⁴⁴⁰ The truncation of CI provides a hierarchy, where the accuracy of a given model is systematically improved by considering higher excited determinants. However, the truncated CI method is associated with the shortcoming of lacking the size-consistency. For a system of non-interacting fragments, truncated CI cannot reproduce the total energy as a sum of the energies of the individual fragments. The size-consistency is only achieved when all possible excitations are included in the trial wavefunction, *i.e.*, FCI.⁴⁴¹

A.3.2 Møller-Plesset Perturbation Theory

The perturbation theory provides a systematic procedure of finding the correlation energy while remaining size-consistent at each level.⁴⁴² In this approach, the total Hamiltonian of the system is partitioned into a zeroth-order unperturbed part, \hat{H}_0 which has known eigenfunctions and eigenvalues and a perturbation \hat{V} :⁴²⁶

$$\hat{H}^\lambda = \hat{H}_0 + \lambda \hat{V} \tag{A.29}$$

Where λ is called the ordering parameter, which eventually becomes unity. This approach is called the Rayleigh-Schrödinger perturbation theory (RSPT).^{426, 443} If it is assumed that all perturbed quantities are functions of λ then the exact eigenfunctions and eigenvalues can be expanded in a Taylor series in λ :⁴⁴³

$$E = \sum_{k=0}^{\infty} \lambda^k E^{(k)} \quad (\text{A.30})$$

$$|\Psi\rangle = \sum_{k=0}^{\infty} \lambda^k |\Psi^{(k)}\rangle \quad (\text{A.31})$$

The total energy of Eq. A.30 concerning Hamiltonian of Eq. A.29 and wavefunction A.31 can now be expressed as:

$$(\hat{H}_0 + \hat{V}) \sum_{k=0}^{\infty} |\Psi^{(k)}\rangle = \sum_{k=0}^{\infty} E^{(k)} \sum_{k=0}^{\infty} |\Psi^{(k)}\rangle \quad (\text{A.32})$$

Considering the n terms in λ , it can be simplified as:⁴⁴³

$$(\hat{H}_0 - E^{(0)}) |\Psi^{(n)}\rangle = -\hat{V} |\Psi^{(n-1)}\rangle + \sum_{k=1}^n E^{(k)} |\Psi^{(n-k)}\rangle \quad (\text{A.33})$$

The corresponding energy can be obtained as:

$$E^{(n)} = \langle \Psi^{(0)} | \hat{V} | \Psi^{(n-1)} \rangle; \quad n > 0 \quad (\text{A.34})$$

The Møller-Plesset perturbation theory⁴⁴⁴ considers the zeroth-order Hamiltonian and wavefunction as the Fock operator and the corresponding HF Slater determinant respectively, *i.e.*:

$$\hat{H}_0 = \hat{F} \quad (\text{A.35})$$

$$|\Psi^{(0)}\rangle = |\Phi\rangle \quad (\text{A.36})$$

The calculation of first-order energy correction requires the first order wavefunction, according to Eq. A.34, which can be expressed as:

$$|\Psi^{(1)}\rangle = -\sum_{\mu>0} \frac{|\Phi_{\mu}\rangle \langle \Phi_{\mu} | \hat{V} | \Phi \rangle}{E_{\mu}^{(0)} - E^{(0)}} = \frac{1}{4} \sum_{ijab} t_{ij}^{ab} |\Phi_{ij}^{ab}\rangle \quad (\text{A.37})$$

Where t_{ij}^{ab} represents the first order double excitation amplitude, given as:

$$t_{ij}^{ab} = -\frac{\langle ab || ij \rangle}{\varepsilon_a + \varepsilon_b - \varepsilon_i - \varepsilon_j} \quad (\text{A.38})$$

The total MP2 energy can be expressed as:

$$\begin{aligned} E_{\text{MP2}} &= \sum_i \varepsilon_i + \frac{1}{2} \sum_i \langle ij || ij \rangle + \frac{1}{4} \sum_{ijab} t_{ij}^{ab} \langle \Phi_{ij}^{ab} \rangle \\ &= E_{\text{HF}} + \frac{1}{4} \sum_{ijab} t_{ij}^{ab} \langle \Phi_{ij}^{ab} \rangle \end{aligned} \quad (\text{A.39})$$

MP2 method recovers 80 - 90% of the correlation energy with computational requirements scale as $O(M^5)$ (where M is the number of basis functions).⁴⁴⁵⁻⁴⁴⁷ It is one of the extensively used electronic structure methods because it includes the long-range correlation effects such as dispersion interactions, *etc.*⁴⁴⁸

A.3.3 Coupled-Cluster Methods

The coupled-cluster approach^{449, 450} is one of the most accurate and reliable electronic structure methods for calculating the correlation energy. It is based on the HF wavefunction; however, instead of the linear expansion of the wavefunction used by configuration interaction (CI), the coupled-cluster uses an exponential expansion:⁴⁵⁰

$$\begin{aligned} |\Psi_{\text{CC}}\rangle &= e^{\hat{T}} |\Phi\rangle \\ &= (1 + \hat{T} + \frac{1}{2} \hat{T}^2 + \frac{1}{3!} \hat{T}^3 + \dots) |\Phi\rangle \end{aligned} \quad (\text{A.40})$$

where \hat{T} is the cluster operator written as a sum of operators that generate singly-excited, doubly-excited, triply-excited,..., N -excited determinants as $\hat{T} = \sum_{i=1}^N \hat{T}_i$ with:⁴⁵⁰

$$\hat{T}_1 |\Phi\rangle = \sum_{ai} t_a^i |\Phi_a^i\rangle \quad (\text{A.41})$$

$$\hat{T}_2 |\Phi\rangle = \sum_{\substack{a<b \\ i<j}} t_{ab}^{ij} |\Phi_{ab}^{ij}\rangle \quad (\text{A.42})$$

$$\hat{T}_2^2 |\Phi\rangle = \sum_{\substack{a<b \\ i<j}} \sum_{\substack{c>d \\ k>l}} t_{ab}^{ij} t_{cd}^{kl} |\Phi_{abcd}^{ijkl}\rangle \quad (\text{A.43})$$

Like in the CI method, the expansion must be truncated to include only a few excited determinants. The popular coupled-cluster singles and doubles (CCSD)⁴⁴⁹ model truncates the expansion at $\hat{T} = \hat{T}_1 + \hat{T}_2$. This model has the same number of parameters as configuration interaction singles and doubles (CISD) but improves upon it by approximately accounting for higher-order terms using products of lower-order terms. The inclusion of such products makes CC methods size extensive so that the quality of the computation is not affected for the larger molecules. The computational cost for CCSD scales as $O(o^2v^4)$, where o is the number of occupied orbitals and v is the number of virtual orbitals.⁴⁵¹

CCSD method can be improved by the inclusion of \hat{T}_3 operator, and it is termed as CCSD(T) method.⁴⁵² This additional term increases the computational cost which scales now as $O(o^3v^4)$ making it expensive for large molecules so that it becomes impractical for systems containing transition metals.⁴⁵¹

A.4 Density Functional Theory (DFT)

The density functional theory (DFT) has become a standard electronic structure method for diverse materials modelling problems in physics, chemistry, material sciences and multiple branches of engineering.³ DFT predict properties of many-electron systems without recourse to the wavefunction, using only the information contained in the ground state electron density.³

The electron density represents the probability of finding electron 1 in a volume element $d\mathbf{r}_1$, which is obtained by integrating over all spin and spatial coordinates of \mathbf{x}_i ($i = 2, 3, \dots, N$) electrons and the spin coordinate s of electron 1. Due to the indistinguishability of electrons, the probability of finding any electron in $d\mathbf{r}_1$ is N times the probability for one electron:³

$$\rho(\mathbf{r}) = N \int \dots \int ds_1 d\mathbf{r}_2 \dots d\mathbf{r}_N |\Psi(\mathbf{r}_1, \mathbf{r}_2, \dots, \mathbf{r}_N)|^2 \quad (\text{A.44})$$

This indicates that the normalization of electron density corresponds to the total number of electrons in the system.

$$\int d\mathbf{r} \rho(\mathbf{r}) = N \langle \Psi | \Psi \rangle = N \quad (\text{A.45})$$

The entire field of DFT rests on two fundamental mathematical theorems proved by Kohn and Hohenberg¹⁵⁰ and the derivation of a set of equations by Kohn and Sham.¹⁵¹ The first theorem establishes that the ground state energy from Schrödinger's equation is a unique functional of the electron density.¹⁵⁰ The operator of Eq. A.2 that describes the interaction of electrons and nuclei can be expressed in terms of the external potential, $v_{ext}(\mathbf{r})$ in which the electrons move. For atoms, molecules and solids, $v_{ext}(\mathbf{r})$ is the Coulombic potential of nuclei with charge Z_A at position \mathbf{R}_A :¹

$$\begin{aligned} \hat{V}_{ne} &= \sum_i^N \left(- \sum_A^M \frac{Z_A}{|\mathbf{r}_i - \mathbf{R}_A|} \right) \\ &= \int d\mathbf{r} v_{ext}(\mathbf{r}) \hat{\rho}(\mathbf{r}) \end{aligned} \quad (\text{A.46})$$

where $\hat{\rho}(\mathbf{r})$ is the density operator. The expectation value of \hat{V}_{ne} can then be expressed as a density functional:

$$\langle \Psi | \hat{V}_{ne} | \Psi \rangle = \int d\mathbf{r} v_{ext}(\mathbf{r}) \rho(\mathbf{r}) = V_{ne}[\rho] \quad (\text{A.47})$$

The relations established by the first theorem allow writing the ground state energy in terms of electron density functionals as:⁴⁵³

$$E[\rho] = T[\rho] + V_{ee}[\rho] + V_{ne}[\rho] \quad (\text{A.48})$$

The kinetic energy of electrons can be expressed as:⁴⁵⁴

$$T[\rho] = -\frac{1}{2} \int d\mathbf{r} \left[\nabla^2 \gamma(\mathbf{r}, \mathbf{r}') \right]_{\mathbf{r}'=\mathbf{r}} \quad (\text{A.49})$$

where $\gamma(\mathbf{r}, \mathbf{r}')$ represents the one-particle reduced density matrix (see [Appendix B](#)). The electron-electron repulsion interaction can be given as:⁴⁵⁴

$$V_{ee}[\rho] = \iint d\mathbf{r}_1 d\mathbf{r}_2 \frac{P_2(\mathbf{r}_1, \mathbf{r}_2)}{r_{12}} \quad (\text{A.50})$$

where $P_2(\mathbf{r}_1, \mathbf{r}_2)$ is the pair density, which includes the classical Coulomb repulsion and quantum-mechanical exchange-correlation effects. The classical and quantum-mechanical effects can be separated explicitly as:⁴⁵⁴

$$P_2(\mathbf{r}_1, \mathbf{r}_2) = \frac{1}{2} \rho(\mathbf{r}_1) [\rho(\mathbf{r}_2) + h_{xc}(\mathbf{r}_1, \mathbf{r}_2)] \quad (\text{A.51})$$

which effectively defines the *exchange-correlation hole*, $h_{xc}(\mathbf{r}_1, \mathbf{r}_2)$ of the electron at \mathbf{r}_1 . Eq.

A.50 can now be rewritten as:

$$V_{ee}[\rho] = J[\rho] + E_{xc} \quad (\text{A.52})$$

where $J[\rho]$ is the classical Coulomb repulsion energy which can be given as:

$$J[\rho] = \frac{1}{2} \iint d\mathbf{r}_1 d\mathbf{r}_2 \frac{\rho(\mathbf{r}_1)\rho(\mathbf{r}_2)}{r_{12}} \quad (\text{A.53})$$

and E_{xc} is the exchange-correlation energy:

$$E_{\text{xc}}[\rho] = \frac{1}{2} \int \int d\mathbf{r}_1 d\mathbf{r}_2 \frac{\rho(\mathbf{r}_1)h_{\text{xc}}(\mathbf{r}_1, \mathbf{r}_2)}{r_{12}} \quad (\text{A.54})$$

Eq. A.48 can now be written as:⁴⁵⁴

$$E[\rho] = T[\rho] + V_{ne}[\rho] + J[\rho] + E_{\text{xc}}[\rho] \quad (\text{A.55})$$

The kinetic energy and electron-electron interaction terms can be combined to introduce a new functional, the Hohenberg-Kohn (HK) functional¹⁵⁰:

$$F_{\text{HK}}[\rho] = T[\rho] + J[\rho] + E_{\text{xc}}[\rho] \quad (\text{A.56})$$

The HK theorem assures that $F_{\text{HK}}[\rho]$ exists, but the actual form of $F_{\text{HK}}[\rho]$ is unknown (except for $J[\rho]$) and is approximated. For a fixed number of electrons, the Hamiltonian operators for any two systems differ only by external potential v_{ext} . Hence HK functional is universal:⁴⁵⁴

$$E[\rho] = \underbrace{F_{\text{HK}}[\rho]}_{\text{universal}} + \underbrace{\int d\mathbf{r} v_{\text{ext}}(\mathbf{r})\rho(\mathbf{r})}_{\text{system-dependent}} \quad (\text{A.57})$$

The second HK theorem¹⁵⁰ defines that the electron density, which minimizes the energy of the overall functional is the true electron density corresponding to the full solution of Schrödinger's equation. The trial density $\tilde{\rho}(\mathbf{r})$ will determine its own external potential and wavefunction $\tilde{\Psi}(\mathbf{r}_1, \mathbf{r}_2, \dots, \mathbf{r}_N)$. Applying the variation principle for this wavefunction:

$$\langle \tilde{\Psi} | \hat{H} | \tilde{\Psi} \rangle = F_{\text{HK}}[\tilde{\rho}] + \int d\mathbf{r} v_{\text{ext}}(\mathbf{r})\tilde{\rho}(\mathbf{r}) = E_v[\tilde{\rho}] \geq E_v[\rho] \quad (\text{A.58})$$

The equality in Eq. A.58 is achieved if the exact density is used. If true functional form were known, then the minimum in energy could be obtained by varying the electron density.² This variational principle is used in practice with approximate forms of the DFT functionals.²

The exchange-correlation functional ($E_{\text{xc}}[\rho]$) approximate a small but essential part of total energy (exchange-correlation energy). The problem of finding the accurate approximations to $E_{\text{xc}}[\rho]$ is the biggest challenge in DFT.³ Whereas, the accuracy of correlated wavefunction methods, such as configuration interaction, can be improved systematically; no comparable procedure is available to improve density functional approximations.³ The improvements in the functionals are carried out by knowing the deficiencies of existing functionals, benchmarking to the experiments, or to the results of high-level correlated wavefunction methods.³ A brief description of the properties of different types of density functionals is presented below.

- 1. The Local Density Approximation (LDA):** The central idea of the model system, on which virtually all approximate exchange-correlation functionals are based, is a hypothetical uniform electron gas (UEG). This is a system in which electrons move on a positive background charge distribution such that the entire ensemble is electrically neutral. The infinite UEG system is physically interpreted as a model for an idealized metal. The local density approximations (LDA) functionals are exact UEG systems as they only depend on the local values of $\rho[\mathbf{r}]$.⁴⁵⁴

$$E_{\text{xc}}^{\text{LDA}}[\rho] = \int d\mathbf{r} \rho(\mathbf{r}) \varepsilon_{\text{xc}}(\rho) \quad (\text{A.59})$$

where $\varepsilon_{\text{xc}}(\rho) = \varepsilon_{\text{x}}(\rho) + \varepsilon_{\text{c}}(\rho)$ is the exchange-correlation energy per particle of the electron gas, which is the function of the density only. The LDA exchange is given as:

$$E_{\text{x}}^{\text{LDA}}[\rho] = -\frac{3}{4} \left(\frac{3}{\pi} \right)^{1/3} \int d\mathbf{r} \rho^{4/3}(\mathbf{r}) \quad (\text{A.60})$$

These functionals have frequently been employed in solid-state physics to study the bulk transition metals. However, as molecular systems are finite and exhibit rapidly varying charge densities, therefore LDA are associated with insufficient accuracy for chemical applications. Examples of these functionals are SVWN5, and XAVWN5. $E_C^{\text{LDA}}[\rho]$ of these functionals are developed by Vosko, Wilk, and Nusair (VWN).²⁶⁸

- 2. The Generalized Gradient Approximation (GGA):** To account for the non-uniformity of the electron density, the generalized gradient approximation (GGA) extends the information in a given point \mathbf{r} by the gradient of the density.³

$$E_{\text{XC}}^{\text{GGA}}[\rho] = \int d\mathbf{r} f(\rho, \nabla\rho) \quad (\text{A.61})$$

Usually, the functionals are formulated in terms of one of the following dimensionless quantities instead of expressing explicitly in terms of $\nabla\rho(\mathbf{r})$:

$$x(\mathbf{r}) = \frac{|\nabla\rho(\mathbf{r})|}{\rho^{4/3}(\mathbf{r})} \quad (\text{A.62})$$

$$s(\mathbf{r}) = \frac{x(\mathbf{r})}{2(3\pi^2)^{1/3}} \quad (\text{A.63})$$

The quantity $s(\mathbf{r})$ is called reduced density gradient⁴⁵⁴ and can be interpreted as a parameter of local inhomogeneity in charge density. For instance, $s(\mathbf{r})$ adopts large values near the nucleus (large gradient) and far from nuclei, and smaller values in a bonding region and region of large density while the uniform electron gas would yield $s(\mathbf{r}) = 0$. The exchange part of $E_{\text{XC}}^{\text{GGA}}[\rho]$ in terms of function F having reduced density gradient argument can be expressed as:⁴²⁹

$$E_{\text{X}}^{\text{GGA}}[\rho] = E_{\text{X}}^{\text{LDA}}[\rho] - \int d\mathbf{r} F(s)\rho^{4/3}(\mathbf{r}) \quad (\text{A.64})$$

where function F has two main classes of realization, the first one is based on exchange functional developed by Becke in 1988, abbreviated as B.

$$F^{\text{B}} = \frac{\beta s^2(\mathbf{r})}{1 + 6\beta s(\mathbf{r}) \sinh^{-1} s(\mathbf{r})} \quad (\text{A.65})$$

where β is an empirical parameter that was determined to be 0.0042 by a least-square fit to the exactly known exchange energies of the rare gas atoms He through Rn.³ Functionals which are related to this approach include FT97⁴⁵⁵, PW91^{456, 457}, CAM(A) and CAM(B).³

The second class of GGA exchange functionals uses for F a rational function of the reduced density gradient. Representative functionals of this class are B86,¹⁵² P86,⁴⁵⁸ LG³ and PBE⁴⁵⁹. For example, F of P86 functional can be written as:^{3, 454}

$$F^{\text{P86}} = \left(1 + 1.296 \left(\frac{s(\mathbf{r})}{(24\pi^2)^{1/3}} \right)^2 + 14 \left(\frac{s(\mathbf{r})}{(24\pi^2)^{1/3}} \right)^4 + 0.2 \left(\frac{s(\mathbf{r})}{(24\pi^2)^{1/3}} \right)^6 \right)^{1/15} \quad (\text{A.66})$$

- 3. *meta*-GGA:** Following the strategy of GGA, the next step involves the inclusion of higher derivatives of the density, such as the Laplacian $\nabla^2 \rho(\mathbf{r})$ and/or the Kohn-Sham kinetic energy density given as:

$$\tau(\mathbf{r}) = \sum_i^N |\nabla \psi(\mathbf{r})|^2 \quad (\text{A.67})$$

A density functional approximation of this type is referred to as *meta*-GGA.

$$E_{\text{XC}}^{m\text{-GGA}}[\rho] = \int d\mathbf{r} f(\rho, \nabla \rho, \nabla^2 \rho, \tau) \quad (\text{A.68})$$

Examples for *meta*-GGAs include TPSS⁴⁶⁰, SCAN⁴⁶¹, or B97M-rV⁴⁶².

4. Hybrid Functionals: Typically, the exchange contributions are significantly more significant in absolute numbers than the corresponding correlation effects. Therefore, the exchange contribution constitutes a suitable starting point for further improvement of the accuracy. However, the exchange energy of the Slater determinant can be computed exactly. The hybrid functionals³²⁷ add a fraction of exact exchange $E_x[\psi_i]$ from HF theory evaluated with KS orbitals and rely on approximate functionals only for the part missing in the HF picture, *i.e.*, electron correlation:^{3, 454}

$$E_{\text{XC}}[\rho] = c_{\text{HF}} E_{\text{X}}^{\text{HF}}[\psi_i] + (1 - c_{\text{HF}}) E_{\text{X}}^{\text{DFT}}[\rho] + E_{\text{C}}^{\text{DFT}}[\rho] \quad (\text{A.69})$$

Hybrid functionals typically exhibit excellent performance for properties that can be attributed to short-range electron-electron interactions; however, these functionals are less successful for describing the long-range interactions.³ For example, charge-transfer excitations are significantly underestimated due to an insufficient amount of exact exchange. The recent approach to handle this deficiency is to split the exchange contribution into a short-range and long-range component. The smooth transition between the two is achieved by employing a sigmoidal switching function, typically the error function (erf):⁴⁶³⁻⁴⁶⁵

$$\frac{1}{r_{12}} = \underbrace{\frac{1 - \text{erf}(\mu r_{12})}{r_{12}}}_{\text{short-range}} + \underbrace{\frac{\text{erf}(\mu r_{12})}{r_{12}}}_{\text{long-range}} \quad (\text{A.70})$$

where μ is an adjustable parameter which controls the attenuation of the short-range contribution. The examples of hybrid functionals are M06⁴⁶⁶, PBE0^{467, 468}, B3LYP²⁶⁶⁻²⁶⁸, and M06-2x⁴⁶⁶. Examples for the range-separated counterparts are CAM-B3LYP⁴⁶⁹, LC- ω PBE⁴⁷⁰, and ω B97X⁴⁷¹, *etc.*

Double hybrid functionals not only include occupied KS orbitals to evaluate exact exchange, but also virtual orbitals to incorporate a fraction of correlation energy derived from wavefunctions. Notable examples are Furche's functional⁴⁷² and Grimme's B2-PLYP functional⁴⁷³.

A.5 Basis Sets

Generically, a basis set is a collection of vectors which defines a space in which a problem is solved. In quantum chemistry, the “basis set” refers to the set of (non-orthogonal) one-particle functions used for the generation of the many-electrons wavefunctions⁴²⁶ (Slater determinants or a linear combination of Slater determinants) as defined by Eq. A.19. Expanding a molecular orbital, in a set of known functions is not an approximation if the basis is complete. However, a complete basis means that an infinite number of functions must be used, which is impossible in actual calculations. Hence, practical electronic structure calculations use finite basis sets. It has long been recognized that very large basis sets are needed if high-quality wavefunction that also takes into account the electron correlation are the target. These large basis set requirements lead to computationally very demanding procedures. The type of basis functions used also influences accuracy.⁴⁴³ The better a single basis function is able to reproduce the unknown function, the fewer basis functions necessary for achieving a given level of accuracy. As stated earlier that the computational effort of ab initio methods scales formally at least as M^4 , it is fundamental to make the basis set as small as possible without compromising the accuracy. On the other hand, in the DFT scheme, the orbitals play an indirect role and are introduced only as a tool to construct the charge density. Therefore, it is expected that the basis set requirements in DFT calculations are less severe than in wavefunction based methods.³

In conventional wavefunction based approaches, the atomic orbitals are universally chosen to consist of *Gaussian-type-orbitals*, GTO of general form:^{474, 475}

$$\chi_{abc}^{\text{GTO}}(x, y, z) = Nx^a y^b z^c e^{-\alpha r^2} \quad (\text{A.71})$$

where N is a normalization constant, which ensures $\langle \chi_\mu | \chi_\mu \rangle = 1$. α represents the orbital exponent, which controls the width of the orbital (large α gives tight function, small α gives diffuse function). $L = a + b + c$ is used to classify the GTO as s -function ($L = 0$), p -function ($L = 1$), d -function ($L = 2$), *etc.* However, for $L > 1$ the number of cartesian GTO functions exceeds the number of $(2l + 1)$ physical functions of angular momentum l . The GTO basis functions provide computational advantages over other types of functions because very efficient algorithms exist for analytical calculations of four-centre-two-electron integrals occurring in Coulomb and HF exchange terms.³

Slater-type-orbitals (STO) were used in the early days of computational quantum chemistry. A typical STO is expressed as:⁴⁷⁶

$$\chi_{abc}^{\text{STO}}(x, y, z) = Nx^a y^b z^c e^{-\alpha r} \quad (\text{A.72})$$

STOs have several advantages over GTOs, however, many-centre integrals are notoriously difficult to compute with STO basis set since no analytical techniques are available, and only numerical methods can be used.³ This explains why these functions do not play any role in modern wavefunction based quantum chemical programs. STO's are more accurate than GTO's but are slower computationally. The standard solution adopted by many electronic structure codes is to use a linear combination of enough GTO's to mimic an STO. These basis sets are called *contracted Gaussian-type orbitals* (CGTO) and can be generally expressed as:³

$$\chi_{abc}^{\text{CGTO}}(x, y, z) = N \sum_{i=1}^n c_i x^a y^b z^c e^{-\alpha_i r^2} \quad (\text{A.73})$$

The electronic structure codes which provide both DFT and wavefunctions based methods, such as Gaussian which is used for all calculations mentioned in this dissertation, use CGTO basis sets. It is also important to say that basis sets which do not comply with LCAO schemes are used in the *plane-wave* based DFT electronic structure codes. Plane waves are not centred at nuclei but extend throughout the entire space. The plane-wave basis sets are extensively used in solid-state physics.

Appendix B

The One-particle Density Matrix

As described in [Appendix A](#), all properties of an N-fermions system can be obtained from its wavefunction $\Psi(\mathbf{r}_1, \mathbf{r}_2 \dots \mathbf{r}_N)$ where \mathbf{r} denotes the coordinates of N fermions, and spin dependence has been suppressed for simplicity. For a pure state, the quantity, $\Psi(\mathbf{r}_1, \mathbf{r}_2 \dots \mathbf{r}_N) \Psi^*(\mathbf{r}'_1, \mathbf{r}'_2 \dots \mathbf{r}'_N)$ is called von Neumann Nth-order density matrix⁴⁷⁷, where the asterisk denotes the complex conjugate of the wavefunction. In 1928-1930 Dirac showed that density matrix provides more elegant results if integrated over coordinates of all but one fermion which defines one-particle density matrix (1-RDM): ^{477, 478}

$$\gamma(\mathbf{r}, \mathbf{r}') \equiv N \int d^3 \mathbf{r}_2 \dots d^3 \mathbf{r}_N \Psi(\mathbf{r}_1, \mathbf{r}_2 \dots \mathbf{r}_N) \Psi^*(\mathbf{r}'_1, \mathbf{r}'_2 \dots \mathbf{r}'_N) \quad (\text{B.1})$$

For spin-orbitals with occupancies n_i :

$$\gamma(\mathbf{r}, \mathbf{r}') = \sum_i n_i \phi_i(\mathbf{r}) \phi_i^*(\mathbf{r}') \quad (\text{B.2})$$

The diagonal 1-RDM elements, $\rho(\mathbf{r}) = \lim_{\mathbf{r}' \rightarrow \mathbf{r}} \gamma(\mathbf{r}, \mathbf{r}')$ provide the probability density for finding an electron at a point \mathbf{r} . The off-diagonal 1-RDM elements, $\mathbf{r} \neq \mathbf{r}'$, though are not quantum-mechanical observables but can provide insight into the chemical bonding.^{128, 479} The interference effects of atomic orbitals may be more apparent in the 1-RDM than in the diagonal charge density.^{479, 480} 1-RDM also provides the expectation value of the electronic kinetic energy.^{481, 482} The 1-RDM contributes to the electron pair density through the Fermi hole, $(\propto |\gamma(\mathbf{r}, \mathbf{r}')|^2)$.^{483, 484} The off-diagonal parts of the 1-RDM show positive and negative peaks and saddle points which arise from chemical bonds and do not occur in the

promolecular 1-RDM.^{479, 485} Various definitions of covalent bond orders have been established using the off-diagonal elements of the 1-RDM in Hilbert space.⁴⁸⁶⁻⁴⁸⁸ The off-diagonal elements are indirectly linked to the momentum-space description of the chemical system and provide information about the velocity and overlap of electrons.⁴⁷⁹

1-RDM is associated with an inherent problem of being six variables function not possible to be visualized all at once. Some methods have been developed to extract useful information about bonding out of the full 1-RDM. Two-dimensional plots of the 1-RDM along symmetry axes have been used to characterize and classify the various off-diagonal regions.^{128, 479} Such analyses are particularly useful for transition density matrices.⁴⁸⁹⁻⁴⁹¹ Orbital and basis-set independent bond orders^{126, 483, 484, 492-495} have been obtained by the integration of the 1-RDM, its square root, or the Fermi hole over atomic domains.⁶⁴ The domain-averaged Fermi holes, which provide the quantitative assessment of electron delocalization, location and degree of electrons pairing, energy ordering of resonance structures, and finer details of electron-electron interactions, are obtained by partial integration over atomic domains.^{127, 483, 496} Direct partitioning of the 1-RDM into pairs of atomic domains provides useful information about covalent bond orders, bond polarization, transferability, bonding multiplicity, and contribution of individual atoms to covalent bonds which in turn quantify the dative nature of the bonds.⁴⁹⁷⁻⁴⁹⁹ The kinetic energy density⁴⁸³ in positive definite form is an explicit function of the 1-RDM, provides the electron localization function (ELF),^{69, 500-502} the localization and delocalization indices quantifying electron pair distributions between atoms,⁵⁰³ the non-covalent interaction index (NCI),⁵⁰⁴ the source function,⁵⁰⁵ electron population analysis based electron delocalization index⁵⁰⁶ and electron localizability indicator.⁵⁰⁷ Electron sharing indices from different partition schemes based on density matrices have highlighted the effect of correlation in polar, non-polar, and aromatic systems.⁵⁰⁸ The localized orbital locator (LOL), reciprocal form factor, and parity function

obtained by projecting the off-diagonal 1-RDM onto the subspaces of internal or external coordinates, provide complementary analysis of molecular electronic structure.⁵⁰⁹⁻⁵¹¹ Analyses of the projected Fermi hole provide insight into the interplay of exchange hole delocalization and strong correlation in dissociating bonds.⁵¹²⁻⁵¹⁵

Like all of the tools mentioned above, the electron delocalization range function, $\text{EDR}(\mathbf{r}; d)$ is designed to extract information from six variable 1-RDM and complements these tools by focusing on the distance between points \mathbf{r} and \mathbf{r}' in $\gamma(\mathbf{r}, \mathbf{r}')$.⁹¹

Appendix C

The Atomic Partial Charges

A fundamental concept in chemistry is that in most of the molecules, some atoms are relatively electron-rich (*i.e.*, negative), and correspondingly others have a deficiency of electron (*i.e.*, positive). Atomic partial (or point) charges are the non-integer values measured in elementary charge units, which are assigned to the atoms in a molecule due to the asymmetric distribution of electrons. Partial charges are one of the basic chemical concepts for rationalizing, modelling, and predicting molecular interactions.

Partial charges are associated with the inherent problem of lacking a rigorous physical basis. They are arbitrary defined quantities that cannot be measured experimentally and cannot be unambiguously determined by quantum mechanical methods. Therefore, there exist about 30 different approaches for obtaining atomic partial charges.⁵¹⁶ Some methods of charges assignment show functional correlations and exhibit a significant degree of statistical commonality.⁵¹⁷ However, severe contradictions and unrealistic charge assignments are also common. For example, six different methods assign charge to the carbon atom in CH_3NO_2 in the range of -0.478 to 0.564.⁵¹⁷ A particular method may be useful for a specific purpose. Still, none method is best for all purposes.⁵¹⁷

Our Multiwfn implementation of EDR($\mathbf{r};d$) based toolkit allows estimating atomic average overlap distance, D_A , and corresponding atomic partial charges using Hirshfeld, Hirshfeld-I, Voronoi deformation density (VDD), AIM, and Becke partitioning methods. However, this dissertation entirely uses Hirshfeld charges. A brief description of these methods is given below.

Hirshfeld charge is defined as:⁵¹⁸

$$Q_A = Z_A - \int d\mathbf{r} w_A^{\text{Hirsh}}(\mathbf{r}) \rho^{\text{def}}(\mathbf{r}) \quad (\text{C.1})$$

where the molecular deformation density, defined as the density difference between the molecule and the promolecule is given as:

$$\rho^{\text{def}}(\mathbf{r}) = \rho(\mathbf{r}) - \rho^{\text{pro}}(\mathbf{r}) \quad (\text{C.2})$$

Algebraically, the promolecule density at point \mathbf{r} is defined as:

$$\rho^{\text{pro}}(\mathbf{r}) = \sum_A \rho_A^{\text{free}}(\mathbf{r} - \mathbf{R}_A) \quad (\text{C.3})$$

where the functions ρ^{free} are suitably positioned, spherically averaged ground-state atomic densities. For each atom, a sharing function or Hirshfeld weight is given as:

$$w_A^{\text{Hirsh}}(\mathbf{r}) = \frac{\rho_A^{\text{free}}(\mathbf{r} - \mathbf{R}_A)}{\rho^{\text{pro}}(\mathbf{r})} \quad (\text{C.4})$$

The Hirshfeld charges are qualitatively consistent with general chemical concepts such as electronegativity, inductive effects, and resonance effects.⁵¹⁹ They are insensitive to the quality of wavefunction and are highly efficient due to the use of grid-based integration schemes.⁵²⁰ These charges only reflect the amount of electron density transferred during molecule formation and ignore the density which is not transferred, hence suffer minimum information loss.⁵¹⁹ However, since the Hirshfeld scheme completely ignores the contributions of atomic dipole moments, these charges poorly reproduce quantities such as molecular dipole moment and electrostatic potential, *etc.*⁵²⁰ They are typically underestimated as compared to other charge schemes. However, in general, Hirshfeld charges are considered reliable for a broader class of molecules.⁵¹⁹

In the Hirshfeld method, there is no unique way to construct the promolecular densities.⁵²¹ For example, the LiF promolecular density can be built using either of Li^0F^0 , Li^+F^- , or Li^-F^+ .⁵²¹ Also, for charged systems, the choice of appropriate reference is not clearly defined. In the Hirshfeld-I method,⁵²¹ these ambiguities are eliminated by gradually refining the atomic spaces using the self-consistent procedure. The weighting function of atom A at iteration n is given as:^{521, 522}

$$w_A^{(n)}(\mathbf{r} - \mathbf{R}_A) \equiv \frac{\rho_A^{(n-1)}(\mathbf{r} - \mathbf{R}_A)}{\rho_{\text{pro}}^{(n-1)}(\mathbf{r})} \quad (\text{C.5})$$

The first iteration of the Hirshfeld-I method uses the neutral atomic densities (following the original Hirshfeld scheme), and the self-consistent procedure is continued until all atomic charges are converged to a given criterion.⁵²¹

Similarly, the other partitioning based charge methods differ from the Hirshfeld method in terms of weighting function w . For example, in the Voronoi deformation density (VDD) charge method, the Voronoi cell-like partitioning is used, where each cell corresponds to an atom.⁵²³ Generally, VDD charges are similar to the Hirshfeld charges.⁵²³ AIM (Atoms in molecules) charge method, which is also known as Bader charge, represents the charge integrated into the AIM basin.⁶⁴ The AIM method mostly gives chemically reasonable charges and are extensively used for charge density data obtained from diffraction experiments.⁵²⁴ Becke charge method uses Becke's weighting function,⁵²⁵ which is based on the conversion of whole space integral into multiple single-centre spherical integrals. This method provides reasonable charges for typical organic molecules but assigns unrealistic charges to ionic systems.⁵²⁶

Appendix D

The Electrostatic Potential

In 1973 Scrocco and Tomasi⁵²⁷ introduced the electrostatic potential (ESP), $V_{\text{ESP}}(\mathbf{r})$, to avoid the problems of arbitrariness associated with atomic partial charges detailed in [Appendix C](#). ESP is based on Coulomb's law and can be expressed in atomic units as:^{527, 528}

$$V_{\text{ESP}}(\mathbf{r}) = V_{\text{nuc}}(\mathbf{r}) + V_{\text{ele}}(\mathbf{r}) = \sum_A \frac{Z_A}{|\mathbf{r} - \mathbf{R}_A|} - \int d\mathbf{r}' \frac{\rho(\mathbf{r}')}{|\mathbf{r} - \mathbf{r}'|} \quad (\text{D.1})$$

where Z_A is the charge on the nucleus A , located at \mathbf{R}_A ; $|\mathbf{r} - \mathbf{R}_A|$ represents the distance of nucleus A from \mathbf{r} and $|\mathbf{r} - \mathbf{r}'|$ is the distance of each electronic charge increment $d\mathbf{r}'\rho(\mathbf{r}')$ from \mathbf{r} . If pseudo-potential is used, then Z_A represents the number of explicitly described electrons. ESP quantifies the electrostatic interaction between a unit point charge placed at point \mathbf{r} and the system under study. A positive or negative value of ESP represents that the position of point \mathbf{r} is dominated by nuclear or electronic charges, respectively. The atomic unit of ESP is energy/charge, *i.e.*, Hartree/e, where e represents the elementary charge. However, eV/e and kcal/mol.e are other common units used for ESP.

ESP is a three-dimensional local property that has a rigorous physical definition and can also be determined from the experiment using the diffraction data.^{529, 530} This means that the true values of ESP can be obtained from the exact wavefunction. ESP can be evaluated at any or all points \mathbf{r} in the space of the system, and results can be presented at a point, in a line, or in a two-dimensional plane. However, the commonly adopted procedure was suggested by Bader *et al.*⁹⁶ is to show ESP as a closely spaced grid covering the entire

three-dimensional outer electron density $\rho(\mathbf{r})$ surface of the molecule. The electron density isosurface of 0.001 e/bohr³ is commonly adopted because, according to Bader *et al.*,⁹⁶ it encompasses approximately 96% of the electronic charge of the system. This representation method particularly highlights the chemically significant regions of molecules such as lone pairs and π electrons, *etc.*⁵³¹

ESP surface plots have been widely used for the rationalization of protein-ligand interactions and the prediction of nucleophilic and electrophilic sites for a chemical reaction.⁵³⁰ For enzymatic studies, these plots are used to distinguish the positive or negative regions which can enhance or inhibit the particular type of enzymatic activity.^{530, 532, 533} These characterizations can provide insight into the drug-receptor or enzyme-substrate interactions where interacting species recognize each other using their surface ESP.^{530, 532-534} ESP has been a workhorse for studying hydrogen bonds, molecular recognition, and intermolecular interactions.⁵³⁰ The surface ESP plots find applications to predict and rationalize interactions of small molecules with transition metal and oxide surfaces.^{535, 536} Quantitative analysis of the molecular ESP surfaces in terms of the statistical features such as variance, maximum, minimum, and average values are correlated to the condensed phase properties such as heats of phase transitions, solvation energies, critical constants, boiling points, solubilities, partition coefficients, surface tension, and viscosities, *etc.*, which depends on the non-covalent interactions.^{537, 538} ESP forms the basis of halogen bonds and other σ -hole interactions, and its statistical features are used to quantify the magnitude, size, linearity, and range of a σ -hole.⁶

In certain cases, the use of ESP surface plots requires careful consideration. For example, the ESP of a neutral spherically-symmetrical ground-state atom is positive everywhere though the number of electrons and the nuclear charge is the same.⁵³⁹ Similarly, the bond regions of molecules usually show positive ESP though these regions are mostly assumed to

be associated with buildups of electron density.^{530, 540-544} These anomalies have been attributed to the fact that the nuclear charges are concentrated while the electrons are dispersed, due to which the former are sometimes unexpectedly dominant.³⁸⁸ Also, the ESP of a molecule is generally calculated in its unperturbed ground states, which does not include the effects of charge polarization induced by the other interacting atom, ion, or molecule in its vicinity.^{414, 415, 545-548} As the interacting molecules come close to each other, their ground state ESP becomes irreverent, and only strong Lewis acid and basic sites maintain their importance.^{388, 415, 547} Due to this deficiency of ground state ESP, there are several favourable interactions that are stabilized by the charge polarization but appeared to be prohibited on the basis of ESP. For example, the ESP in the π region of 1,4-difluorobenzene is weakly negative, but it interacts attractively with the lone pair of the nitrogen in the HCN molecule.⁵⁴⁹ Similarly, the π region of 1,3,5-trifluorobenzene is associated with weak positive ESP, but it interacts attractively with the hydrogen of HCN.⁵⁴⁹

Appendix E

The Chemical Softness in Conceptual DFT

The connection between electronic structure and chemical hardness/softness is well-established in the realm of conceptual density functional theory (DFT).³⁷ Parr and Pearson⁵⁵⁰ defined an isolated system's global hardness as the second derivative of energy with respect to the number of electrons when the external potential is held fixed.³⁸

$$\eta = \left(\frac{\partial^2 E}{\partial N^2} \right)_{v(r)} \quad (\text{E.1})$$

The global softness is the inverse of hardness $S = 1 / \eta$.³⁹ One may approximate η in terms of the computed vertical ionization potential I and electron affinity A .⁵⁵⁰

$$\eta \approx I - A \quad (\text{E.2})$$

One may also approximate η in terms of the computed highest occupied orbital (HOMO) and lowest unoccupied orbital (LUMO) energies.³⁷

$$Gap = \varepsilon_{\text{LUMO}} - \varepsilon_{\text{HOMO}} \quad (\text{E.3})$$

Previous studies have demonstrated that the chemical hardness calculated from Eq. E.3 provides sufficiently accurate results at Hartree Fock (HF) level.⁵⁵⁻⁵⁷ Beyond HF and at DFT level, this method becomes strongly dependent on the basis set and exchange-correlation potential used in DFT calculations.^{37, 58}

Appendix F

Multiwfn Implementations

The $\text{EDR}(\mathbf{r};d)$ and $D(\mathbf{r})$ were implemented to an open-source wavefunction analysis package Multiwfn, initially in version 3.4 (release date: 13-June-2017), and are available in all the subsequent releases. Multiwfn is FORTRAN 90 based program that uses Math Kernel Library (MKL) and DISLIN graphical library and is compiled using Intel FORTRAN compiler (ifort). However, an unofficial and non-standard version is also available on GitHub, which can be compiled using GNU FORTRAN without graphical support. The pre-compiled binary files are also available from the official website (<http://sobereva.com/multiwfn/>). Multiwfn is a free of charge, highly-efficient, user-friendly, and flexible analysis package which supports the wavefunction and output files generated by nearly all molecular quantum chemistry programs. It generates the grid files of electron and spin densities, $\text{EDR}(\mathbf{r};d)$, $D(\mathbf{r})$, ESP and the other real-space functions in the Gaussian cube file format, which can be plotted using standard visualization programs such as VMD. It also has the built-in tools to perform the quantitative analysis of molecular surfaces, which are useful to get minimum, maximum, average, and RMSD of $D(\mathbf{r})$ and ESP surfaces, *etc.*

The $\text{EDR}(\mathbf{r};d)$ and $D(\mathbf{r})$ were added to the main functions routines as function 20 (`ifunc==20`) representing $\text{EDR}(\mathbf{r};d)$ and function 21 (`ifunc==21`) representing $D(\mathbf{r})$ in `function.f90` source file. The implementations involve the addition of two new subroutines and two new functions, which are given below. Besides, the standard user interface subroutine `selfunc_interface` was significantly modified to get user input about the length scale, d to evaluate $\text{EDR}(\mathbf{r};d)$, or to get the number of $\text{EDR}(\mathbf{r};d)$ exponents, the

start value, and corresponding increments to evaluate $D(\mathbf{r})$ using even-tempered exponents set between 1 to 50. The main working subroutine **EDRcal** calculates $\text{EDR}(\mathbf{r};d)$ at a point \mathbf{r} by using electron density at that point obtained from **fdens** function of Multiwfn. It loops over all atomic orbital primitives and finds the value of atomic orbital and its overlap with the EDR test function at the point by considering the x , y , and z contributions separately. For the occupied orbitals, these pieces of information are stored in the intermediate arrays **psi** and **Bint**, respectively. The values of these arrays are then combined to get the final value of $\text{EDR}(\mathbf{r};d)$ at a point \mathbf{r} . The procedure is repeated for the number of lengths scales d , given as **nedr**, which is one for **ifunc==20** and varies for **ifunc==21** maximum up to 50 depending upon the input given by the user. Function **edr(x,y,z)** converts the user-inputted length-scale d into the $\text{EDR}(\mathbf{r};d)$ exponent (Eq. 1.4 of chapter 1) as $\alpha = 1/d^2$ and calls this subroutine to evaluate $\text{EDR}(\mathbf{r};d)$ at all points with electron density greater than 10^{-10} e/bohr³ using the **nedr=1**.

For calculations of $D(\mathbf{r})$, *i.e.*, **ifunc==21**, subroutine **EDRcal** uses the second implemented subroutine **three_point_interpolation** and performs the three-point numerical fit to evaluate $D(\mathbf{r})$. Function **edrdmax(x,y,z)** uses the user-inputted number of $\text{EDR}(\mathbf{r};d)$ exponents (**nedr**), start value (**edrastart**), and increments (**edrainc**) to generate even-tempered exponents set, $\alpha_i = 1/d_i^2$ ($i = 1,2,3,\dots,\text{nedr}$). The **edrastart** is the largest exponent α_1 , and subsequent exponents are incremented by $\alpha_i / \alpha_{\text{edrainc}}$.

In Multiwfn, $\text{EDR}(\mathbf{r};d)$ and $D(\mathbf{r})$ grid files can be generated using option 5 of the main menu and then selecting options 20 or 21, respectively, from the submenu. Option 3 and 4 of the main menu allows evaluating these quantities on a line or on a plane. The quantitative analysis of $D(\mathbf{r})$ molecular surface on the electron or spin density isosurface can be carried out by using option 12 of the main menu.

```

!*****
!
!           Standard user interface to get input for EDR(r;d) and D(r)
!
!*****

subroutine selfunc_interface(itype,ifunc)
integer,parameter :: max_edr_exponents=50
integer :: ifunc,edrmxpara,wrtnumedr,nedr
real*8 :: dedr,edrastart,edrainc
real*8 :: wrtexpo(max_edr_exponents)
real*8 :: wrtstart
call funclist
read(*,*) ifunc

! Read length scale to evaluate EDR(r;d)
if (ifunc==20) then
    write(*,*) "Input length scale d (Bohr) e.g. 0.85"
    read(*,*) dedr
! Read EDR(r;d) exponents to evaluate D(r)
else if (ifunc==21) then
    write(*,*) "1 Manually input total number, start and increment in EDR exponents"
    write(*,*) "2 Use default values i.e. 20,2.50,1.50"
    read(*,*) edrmxpara
    if (edrmxpara==1) then
        write(*,*) "Please input in order: exponents start increment e.g. 20 2.5
        1.5"
        write(*,*) "Note: Max. allowed exponents are 50 and min. allowed increment
        is 1.01"
        read(*,*) nedr,edrastart,edrainc
        if (nedr<1) then
            write(*,*) "Error: Bad Number of EDR exponents. Should be between 1
            to 50"
            write(*,*) "Press ENTER button to exit"
            read(*,*)
            stop
        else if (nedr>50) then
            write(*,*) "Error: Bad Number of EDR exponents. Should be between 1
            to 50"
            write(*,*) "Press ENTER button to exit"
            read(*,*)
            stop
        end if
        if (edrainc<1.01d0) then
            write(*,*) "Error: Bad increment in EDR exponents. Should not be
            less than 1.01"
            write(*,*) "Press ENTER button to exit"
            read(*,*)
            stop
        end if
    else if (edrmxpara==2) then
        nedr=20
        edrastart=2.5D0
        edrainc=1.5D0
    end if
    write(*,*) "The following EDR exponents will be used in calculation:"
    wrtstart=edrastart
    do wrtnumedr=1,nedr

```

```

        wrtexpo(wrtnumedr)=wrtstart
        wrtstart=wrtstart/edrainc
        write(*,"(E13.5)") wrtexpo(wrtnumedr)
    end do
    write(*,*)
end if
end subroutine

!*****
!
!           Main Working Subroutine used to evaluate EDR(r;d) and D(r)
!
!*****

subroutine EDRcal(runtype,x,y,z,nedr,ed,edrval,edrdmaxval)
real*8, intent(in) :: x,y,z,ed(max_edr_exponents)
integer, intent(in) :: nedr
real*8, intent(out):: edrdmaxval,edrval(max_edr_exponents)
real*8 :: rho,dmaxdummy
real*8 :: psi(nmo),AMUVal(max_edr_exponents),Bint(nmo,max_edr_exponents)
real*8 :: xamu(3,max_edr_exponents),amu0(max_edr_exponents)
integer :: j,ixyz,i,iedr,runtype

edrval = 0D0
! If calculation use ifunc==21 that is runtype==2 i.e., evaluate D(r)
if (runtype==2) then
    edrdmaxval = 0D0
end if

! First evaluate the density at point x,y,z
rho=fdens(x,y,z)

if(rho.gt.1D-10) then
    ! Initialize the intermediate arrays
    psi = 0d0
    Bint=0d0
    ! Loop over all of the atomic orbital (AO) primitives
    do j=1,nprims
        ! Find the angular momentum type of AO j
        ix=type2ix(b(j)%type)
        iy=type2iy(b(j)%type)
        iz=type2iz(b(j)%type)
        ! Find the exponent of AO j
        ep=b(j)%exp
        ! Get the distance from the current point to AO j center
        sftx=x-a(b(j)%center)%x
        sfty=y-a(b(j)%center)%y
        sftz=z-a(b(j)%center)%z
        sftx2=sftx*sftx
        sfty2=sfty*sfty
        sftz2=sftz*sftz
        rr=sftx2+sfty2+sftz2
        ! At point r evaluate the value of AO j and its overlap with the EDR test
        function ignoring very distant contributions
        expterm=0.0
        amu0 = 0d0
        if (expcutoff>0.or.-ep*rr>expcutoff) then
            expterm=exp(-ep*rr)

```

```

do iedr=1,nedr
    amu0(iedr)=(2d0*ed(iedr)/pi)**(3d0/4d0)
    *(pi/(ep+ed(iedr)))**(3d0/2d0)&
    * exp(-ep*ed(iedr)/(ep+ed(iedr))*rr)
end do
end if

if (expterm==0D0) cycle
! Add the prefactors for different angular momentum cases to the A0 value
GTFval=sftx**ix *sfty**iy *sftz**iz *expterm
! Loop over ixyz to evaluate the x, y, and z contributions separately
do iedr=1,nedr
    do ixyz=1,3
        ival=ix
        sftval=sftx
        if (ixyz.eq.2) then
            ival=iy
            sftval=sfty
        else if (ixyz.eq.3) then
            ival=iz
            sftval=sftz
        end if
        If (ival.eq.0) then
            xamu(ixyz,iedr)=1d0
        else if (ival.eq.1) then
            xamu(ixyz,iedr)=sftval*ed(iedr)/(ed(iedr)+ep)
        else If (ival.eq.2) then
            xamu(ixyz,iedr)=(sftval*ed(iedr)/(ed(iedr)+ep))**2d0 +
            1d0/(2d0*(ed(iedr)+ep))
        else If (ival.eq.3) then
            xamu(ixyz,iedr)=(sftval*ed(iedr)/(ed(iedr)+ep))**3d0 +
            sftval*3d0*ed(iedr)/(2d0*(ed(iedr)+ep)**2d0)
        else If (ival.eq.4) then
            xamu(ixyz,iedr)=sftval**4d0*
            (ed(iedr)/(ed(iedr)+ep))**4d0 + sftval**2d0
            *3d0*ed(iedr)**2d0/(ed(iedr)+ep)**3d0 &
            + 3d0/(4d0*(ed(iedr)+ep)**2d0)
        else If (ival.eq.5) then
            xamu(ixyz,iedr)=sftval**5d0*
            ed(iedr)**5d0/(ed(iedr)+ep)**5d0 + sftval**3d0*
            5d0*ed(iedr)**3d0/(ed(iedr)+ep)**4d0 &
            + sftval *15d0*ed(iedr)/(4d0*(ed(iedr)+ep)**3d0)
        else
            write(*,*) "Angular momentum out of range"
            Call EXIT()
        end if
    end do
end do
do iedr=1,nedr
    AMUVal(iedr)=amu0(iedr)*xamu(1,iedr)*xamu(2,iedr)*xamu(3,iedr)
end do
! Fill the arrays psi and Bint with values of A0 and overlap contributions,
respectively by including the occupied orbitals only
do i=1,nmo
    if (nint(MOocc(i)) .GE. 1D0) then
        psi(i)=psi(i)+co(i,j)*GTFval
    end if
end do
end do

```

```

        do iedr=1,nedr
            do i=1,nmo
                if (nint(MOocc(i)) .GE. 1D0) then
                    Bint(i,iedr)=Bint(i,iedr)+co(i,j)*AMUVal(iedr)
                end if
            end do
        end do
    end do

    ! Combine psi and Bint to get the final value of edr
    edrval = 0d0
    do i=1,nmo
        do iedr=1,nedr
            edrval(iedr)=edrval(iedr)+psi(i)*Bint(i,iedr)
        end do
    end do
    ! If calculation use ifunc==21 that is runtime==2 i.e., evaluate D(r)
    if (runtime==2) then
        call three_point_interpolation(nedr,ed,edrval,edmax,dmaxdummy)
        edrdmaxval=edmax
    ! If calculation use ifunc==20 that is runtime==1 i.e., evaluate EDR(r;d)
    else if (runtime==1) then
        do iedr=1,nedr
            edrval(iedr)=edrval(iedr)*rho**(-0.5D0)
        end do
    else
        write(*,*) "EDRcal runtime out of range"
        call EXIT()
    end if
end if
end subroutine

!*****
!
!           Subroutine for three-point numerical fit to evaluate D(r)
!
!*****

subroutine three_point_interpolation(n,x,y,xmax,ymax)
integer, intent(in) :: n
real*8, intent(in) :: x(max_edr_exponents),y(max_edr_exponents)
real*8, intent(out) :: xmax,ymax
integer :: i,imax
real*8 :: x1,x2,x3,y1,y2,y3,a,b
100 format ('XXX ',3F9.5)
ymax = -1.0d0
imax = -1
do i=1,n
    if (y(i) .gt. ymax) then
        ymax = y(i)
        imax = i
    end if
end do
if (imax < 1 .or. imax > n) then
    write(*,*) "Error: Bad imax"
    call EXIT()
end if
end if

```

```

if (imax .eq. 1 .or. imax .eq. n) then
  xmax = x(imax)**(-0.5d0)
  return
end if
x1 = x(imax-1)**(-0.5d0)
x2 = x(imax)**(-0.5d0)
x3 = x(imax+1)**(-0.5d0)
y1 = y(imax-1)
y2 = y(imax)
y3 = y(imax+1)
a = ((y3-y2)/(x3-x2)-(y2-y1)/(x2-x1))/(x3-x1)
b = ((y3-y2)/(x3-x2)*(x2-x1)+(y2-y1)/(x2-x1)*(x3-x2))&
  /(x3-x1)
xmax = x2-b/(2d0*a)
ymax = y2-b**(2d0)/(4d0*a)
end subroutine

!*****
!
!                               Function to calculate EDR(r,d)
!
!*****

real*8 function edr(x,y,z)
real*8 :: ed(max_edr_exponents),edrval(max_edr_exponents)
nedr=1
ed(1)=dedr**(-2.0d0)
call EDRcal(1,x,y,z,nedr,ed,edrval,edrdmaxval)
edr=edrval(1)
end function

!*****
!
!                               Function to calculate D(r)
!
!*****

real*8 function edrdmax(x,y,z)
real*8 :: ed(max_edr_exponents),edrdmaxval,edrval(max_edr_exponents)
real*8 :: edrexponent
integer iedr
! Create an even tempered exponents set
edrexponent = edrastart
do iedr=1,nedr
  ed(iedr)=edrexponent
  edrexponent=edrexponent/edrainc
end do
call EDRcal(2,x,y,z,nedr,ed,edrval,edrdmaxval)
edrdmax=edrdmaxval
end function

```

Appendix G

Supplementary Computational Data

Table G.1 D_C , Q_C , and experimental Hammett σ parameters for selected benzene derivatives used in [Chapter 3](#).

| No. | Substituent | Position | Q_C (e) | D_C (bohr) | σ value |
|-----|-------------------|----------|-----------|--------------|----------------|
| 1 | Br | Meta | -0.0495 | 1.6572 | 0.39 |
| | | Para | -0.0550 | 1.6581 | 0.23 |
| 2 | Cl | Meta | -0.0496 | 1.6577 | 0.37 |
| | | Para | -0.0565 | 1.6582 | 0.23 |
| 3 | F | Meta | -0.0481 | 1.6588 | 0.34 |
| | | Para | -0.0644 | 1.6584 | 0.06 |
| 4 | SO ₂ F | Meta | -0.0420 | 1.6547 | 0.80 |
| | | Para | -0.0296 | 1.6563 | 0.91 |
| 5 | SiF ₃ | Meta | -0.0502 | 1.6563 | 0.54 |
| | | Para | -0.0384 | 1.6576 | 0.69 |
| 6 | NO ₂ | Meta | -0.0474 | 1.6559 | 0.71 |
| | | Para | -0.0396 | 1.6573 | 0.78 |
| 7 | N ₃ | Meta | -0.0504 | 1.6583 | 0.37 |
| | | Para | -0.0628 | 1.6586 | 0.08 |
| 8 | H | Meta | -0.0580 | 1.6600 | 0.00 |
| | | Para | -0.0580 | 1.6600 | 0.00 |
| 9 | NHNH ₂ | Meta | -0.0575 | 1.6608 | -0.02 |
| | | Para | -0.0842 | 1.6609 | -0.55 |
| 10 | SiH ₃ | Meta | -0.0571 | 1.6586 | 0.05 |
| | | Para | -0.0525 | 1.6592 | 0.10 |
| 11 | COCl | Meta | -0.0505 | 1.6559 | 0.51 |
| | | Para | -0.0352 | 1.6576 | 0.61 |
| 12 | CCl ₃ | Meta | -0.0503 | 1.6560 | 0.40 |
| | | Para | -0.0465 | 1.6575 | 0.46 |
| 13 | CF ₃ | Meta | -0.0489 | 1.6565 | 0.43 |
| | | Para | -0.0434 | 1.6576 | 0.54 |
| 14 | CN | Meta | -0.0461 | 1.6556 | 0.56 |

| | | | | | |
|----|------------------------------------|------|---------|--------|-------|
| | | Para | -0.0351 | 1.6571 | 0.66 |
| 15 | NCO | Meta | -0.0501 | 1.6577 | 0.27 |
| | | Para | -0.0578 | 1.6583 | 0.19 |
| 16 | C(NO ₂) ₃ | Meta | -0.0422 | 1.6532 | 0.72 |
| | | Para | -0.0295 | 1.6556 | 0.82 |
| 17 | CHCl ₂ | Meta | -0.0512 | 1.6574 | 0.31 |
| | | Para | -0.0491 | 1.6583 | 0.32 |
| 18 | OCHCl ₂ | Meta | -0.0508 | 1.6578 | 0.38 |
| | | Para | -0.0554 | 1.6582 | 0.26 |
| 19 | CHO | Meta | -0.0528 | 1.6576 | 0.41 |
| | | Para | -0.0406 | 1.6587 | 0.47 |
| 20 | OCH ₂ Cl | Meta | -0.0508 | 1.6587 | 0.25 |
| | | Para | -0.0554 | 1.6586 | 0.08 |
| 21 | CONH ₂ | Meta | -0.0539 | 1.6575 | 0.28 |
| | | Para | -0.0471 | 1.6585 | 0.36 |
| 22 | Me | Meta | -0.0584 | 1.6597 | -0.07 |
| | | Para | -0.0652 | 1.6600 | -0.17 |
| 23 | OMe | Meta | -0.0539 | 1.6597 | 0.12 |
| | | Para | -0.0763 | 1.6596 | -0.27 |
| 24 | CH ₂ NH ₂ | Meta | -0.0597 | 1.6600 | -0.03 |
| | | Para | -0.0641 | 1.6602 | -0.11 |
| 25 | CF ₂ CF ₃ | Meta | -0.0494 | 1.6641 | 0.47 |
| | | Para | -0.0438 | 1.6648 | 0.52 |
| 26 | CCH | Meta | -0.0541 | 1.6578 | 0.21 |
| | | Para | -0.0518 | 1.6590 | 0.23 |
| 27 | CH ₂ CF ₃ | Meta | -0.0534 | 1.6657 | 0.12 |
| | | Para | -0.0538 | 1.6660 | 0.09 |
| 28 | CMe(NO ₂) ₂ | Meta | -0.0479 | 1.6550 | 0.54 |
| | | Para | -0.0384 | 1.6568 | 0.61 |
| 29 | SCHCH ₂ | Meta | -0.0539 | 1.6579 | 0.26 |
| | | Para | -0.0499 | 1.6587 | 0.20 |
| 30 | Et | Meta | -0.0591 | 1.6597 | -0.07 |
| | | Para | -0.0658 | 1.6599 | -0.15 |
| 31 | N(Me) ₂ | Meta | -0.0577 | 1.6602 | -0.16 |
| | | Para | -0.0864 | 1.6605 | -0.83 |
| 32 | CH(CN) ₂ | Meta | -0.0456 | 1.6640 | 0.53 |
| | | Para | -0.0458 | 1.6642 | 0.52 |
| 33 | NH ₂ | Meta | -0.0554 | 1.6604 | -0.09 |
| | | Para | -0.0838 | 1.6605 | -0.57 |

Table G.2 Calculated values of solvents mentioned in Table 1 of Ref.[³⁰¹]

| Solvent | μ | Mean $D(\mathbf{r})$ (bohr) | RMSD $D(\mathbf{r})$ (bohr) | With cut off | | 1/Gap | 1/(I-A) |
|------------------------------------|-------|--------------------------------|--------------------------------|--------------------------------|----------------------|-------|---------|
| | | | | Mean $D(\mathbf{r})$ (bohr) | RMSD $D(\mathbf{r})$ | | |
| N-methylthiopyrrolidinone-2 | 1.35 | 3.248 | 0.174 | 3.248 | 0.174 | 8.213 | 3.641 |
| N,N-dimethylthioformamide | 1.35 | 3.333 | 0.110 | 3.343 | 0.096 | 5.749 | 3.031 |
| Ammonia | 0.86 | 3.025 | 0.090 | 3.025 | 0.090 | 3.517 | 2.077 |
| Tetrahydrothiophene | 0.80 | 3.311 | 0.093 | 3.320 | 0.104 | 4.568 | 2.841 |
| Hexamethyl thiophosphoric triamide | 0.67 | 3.350 | 0.092 | 3.409 | 0.086 | 4.836 | 3.243 |
| Pyridine | 0.64 | 3.270 | 0.092 | 3.291 | 0.083 | 4.448 | 2.571 |
| Acetonitrile | 0.35 | 3.193 | 0.105 | 3.216 | 0.086 | 3.057 | 2.059 |
| Benzonitrile | 0.34 | 3.256 | 0.101 | 3.289 | 0.086 | 4.728 | 2.823 |
| Hexamethylphosphoric triamide | 0.29 | 3.287 | 0.111 | 3.233 | 0.145 | 4.677 | 3.174 |
| Nitrobenzene | 0.23 | 3.140 | 0.205 | 3.145 | 0.222 | 5.469 | 2.993 |
| Dimethyl sulfoxide | 0.22 | 3.255 | 0.190 | 3.255 | 0.189 | 4.247 | 2.693 |
| 1-Butanol | 0.18 | 3.219 | 0.202 | 3.142 | 0.241 | 3.601 | 2.368 |
| N,N-dimethylacetamide | 0.17 | 3.210 | 0.157 | 3.187 | 0.164 | 4.128 | 2.719 |
| N,N-diethylacetamide | 0.17 | 3.255 | 0.132 | 3.197 | 0.157 | 4.216 | 2.829 |
| 1-Propanol | 0.16 | 3.191 | 0.206 | 3.133 | 0.229 | 3.580 | 2.335 |
| N,N,N',N'-tetramethylurea | 0.14 | 3.239 | 0.140 | 3.188 | 0.162 | 4.255 | 2.879 |
| N-methylpyrrolidinone-1 | 0.13 | 3.207 | 0.158 | 3.140 | 0.177 | 4.078 | 2.717 |
| N-methylformamide | 0.12 | 3.130 | 0.191 | 3.142 | 0.191 | 3.794 | 2.471 |
| N,N-dimethylformamide | 0.11 | 3.193 | 0.181 | 3.186 | 0.189 | 3.992 | 2.624 |
| N,N-diethylformamide | 0.09 | 3.226 | 0.155 | 3.190 | 0.174 | 4.114 | 2.743 |
| Formamide | 0.09 | 3.066 | 0.178 | 3.070 | 0.184 | 3.748 | 2.284 |
| Ethanol | 0.08 | 3.157 | 0.212 | 3.133 | 0.219 | 3.586 | 2.289 |
| 1,1-Dichloroethane | 0.07 | 3.244 | 0.084 | 3.264 | 0.096 | 3.517 | 2.257 |
| 1,2-Dichloroethane | 0.03 | 3.212 | 0.076 | 3.252 | 0.083 | 3.461 | 2.303 |
| Acetone | 0.03 | 3.210 | 0.163 | 3.210 | 0.163 | 4.335 | 2.498 |
| Nitromethane | 0.03 | 3.019 | 0.203 | 3.019 | 0.203 | 4.516 | 2.333 |
| γ -Butyrolactone | 0.02 | 3.135 | 0.187 | 3.135 | 0.187 | 3.661 | 2.412 |
| Methanol | 0.02 | 3.069 | 0.225 | 3.069 | 0.225 | 3.536 | 2.202 |
| Water | 0.00 | 2.790 | 0.035 | 2.790 | 0.035 | 2.889 | 1.736 |
| tetramethylene-sulfone | 0.00 | 3.165 | 0.176 | 3.165 | 0.176 | 3.626 | 2.514 |
| trimethyl-phosphate | -0.02 | 3.153 | 0.168 | 3.059 | 0.190 | 3.401 | 2.419 |
| 1,2-ethanediol | -0.03 | 3.044 | 0.227 | 3.044 | 0.227 | 3.589 | 2.416 |
| Propylene carbonate | -0.09 | 3.103 | 0.225 | 3.103 | 0.225 | 3.389 | 2.306 |
| 2,2,2-trifluoroethanol | -0.12 | 2.823 | 0.226 | 2.856 | 0.234 | 3.377 | 2.163 |

Table G.3 Experimental μ , Ds, and DN values along with the calculated properties of some selected solvents.

| Solvent | μ | Ds | DN | Mean $D(\mathbf{r})$ (bohr) | Mean V_{surf} (a.u) | η (a.u) | χ (a.u) |
|-------------------------------|-------|------|------|--------------------------------|---------------------------------|--------------|--------------|
| Tetrahydrothiophene | 0.8 | 43 | 6 | 3.311 | 0.00387 | 0.2189 | -0.1079 |
| Pyridine | 0.64 | 38 | 33.1 | 3.270 | 0.00240 | 0.2248 | -0.1521 |
| Acetonitrile | 0.35 | 12 | 14.1 | 3.193 | 0.00467 | 0.3271 | -0.1737 |
| Benzonitrile | 0.34 | 12 | 11.9 | 3.256 | 0.00479 | 0.2115 | -0.1720 |
| Hexamethylphosphoric triamide | 0.29 | 34 | 38.8 | 3.287 | 0.00204 | 0.2138 | -0.1139 |
| Nitrobenzene | 0.23 | 9 | 4.4 | 3.140 | 0.00439 | 0.1828 | -0.1988 |
| Dimethyl sulfoxide | 0.22 | 27.5 | 29.8 | 3.255 | 0.00456 | 0.2354 | -0.1198 |
| 1-Butanol | 0.18 | 18 | 29 | 3.219 | 0.00279 | 0.2777 | -0.1391 |
| N,N-dimethylacetamide | 0.17 | 24 | 27.8 | 3.210 | 0.00354 | 0.2422 | -0.1248 |
| N,N-diethylacetamide | 0.17 | 24 | 32.2 | 3.255 | 0.00374 | 0.2372 | -0.1236 |
| 1-Propanol | 0.16 | 18 | 30 | 3.191 | 0.00267 | 0.2793 | -0.1386 |
| N,N,N',N'-tetramethylurea | 0.14 | 24 | 29.6 | 3.239 | 0.00225 | 0.2350 | -0.1184 |
| N-methylpyrrolidinone-1 | 0.13 | 27 | 27.3 | 3.207 | 0.00385 | 0.2452 | -0.1231 |
| N-methylformamide | 0.12 | 22 | 49 | 3.130 | 0.00522 | 0.2636 | -0.1348 |
| N,N-dimethylformamide | 0.11 | 24 | 26.6 | 3.193 | 0.00448 | 0.2505 | -0.1289 |
| N,N-diethylformamide | 0.09 | 24 | 30.9 | 3.226 | 0.00446 | 0.2430 | -0.1263 |
| Formamide | 0.09 | 21 | 36 | 3.066 | 0.00355 | 0.2668 | -0.1396 |
| Ethanol | 0.08 | 19 | 32 | 3.157 | 0.00217 | 0.2789 | -0.1391 |
| 1,2-Dichloroethane | 0.03 | 7 | 0 | 3.212 | 0.00586 | 0.2890 | -0.1686 |
| Acetone | 0.03 | 15 | 17 | 3.210 | 0.00423 | 0.2307 | -0.1427 |
| Nitromethane | 0.03 | 9 | 2.7 | 3.019 | 0.00447 | 0.2215 | -0.2019 |
| γ -Butyrolactone | 0.02 | 14 | 18 | 3.135 | 0.00501 | 0.2732 | -0.1430 |
| tetramethylene-sulfone | 0 | 15 | 14.8 | 3.165 | 0.00520 | 0.2758 | -0.1501 |
| trimethyl-phosphate | -0.02 | 23 | 23 | 3.153 | 0.00046 | 0.2940 | -0.1494 |
| 1,2-ethanediol | -0.03 | 20 | 20 | 3.044 | 0.00163 | 0.2787 | -0.1449 |
| Propylene carbonate | -0.09 | 12 | 15.1 | 3.103 | 0.00570 | 0.2950 | -0.1574 |

Table G.4 Calculated properties of ILs used in this dissertation. The full names of these ILs are given at the end of this table.

| Ion | Mean V_{surf} (a.u) | RMSD V_{surf} (a.u) | Mean $D(\mathbf{r})$ (bohr) | RMSD $D(\mathbf{r})$ (bohr) | Surface area (bohr ²) |
|---------------------------------------|---------------------------------|---------------------------------|--------------------------------|--------------------------------|--------------------------------------|
| [N ₁₁₁₆] | 0.1300 | 0.0373 | 3.3159 | 0.0808 | 831.3 |
| [C ₂ py] | 0.1555 | 0.0145 | 3.2551 | 0.0921 | 571.8 |
| [bpy] | 0.1394 | 0.0268 | 3.2759 | 0.0936 | 725.2 |
| [emim] | 0.1529 | 0.0171 | 3.2404 | 0.1270 | 598.1 |
| [mPhim] | 0.1359 | 0.0242 | 3.2527 | 0.1210 | 745.0 |
| [C ₄ mim] | 0.1373 | 0.0286 | 3.2675 | 0.1165 | 745.8 |
| [C ₈ mim] | 0.1136 | 0.0423 | 3.2935 | 0.1203 | 1057 |
| [N _{1112OH}] | 0.1571 | 0.0263 | 3.2112 | 0.1975 | 563.8 |
| [P ₄₄₄₄] | 0.1109 | 0.0222 | 3.3156 | 0.0792 | 1376 |
| [PF ₆] | -0.1786 | 0.0059 | 2.6895 | 0.0273 | 400.9 |
| [I] | -0.1971 | 0.0000 | 3.7082 | 0.0000 | 304.9 |
| [Cl] | -0.2205 | 0.0000 | 3.4145 | 0.0005 | 240.4 |
| [Br] | -0.2053 | 0.0000 | 3.5509 | 0.0004 | 269.3 |
| [CF ₃ SO ₃] | -0.1647 | 0.0233 | 2.8370 | 0.1313 | 469.9 |
| [MeSO ₄] | -0.1672 | 0.0380 | 3.0481 | 0.1775 | 453.6 |
| [FAP] | -0.1220 | 0.0144 | 2.6939 | 0.0430 | 930.9 |
| [SbF ₆] | -0.1667 | 0.0032 | 2.6736 | 0.0606 | 460.0 |
| [Pf ₂ N] | -0.1215 | 0.0249 | 2.7842 | 0.1463 | 917.7 |
| [BF ₄] | -0.1961 | 0.0052 | 2.7027 | 0.0241 | 327.3 |
| [NTf ₂] | -0.1339 | 0.0217 | 2.8124 | 0.1458 | 747.5 |
| [B(CN) ₄] | -0.1380 | 0.0106 | 3.2672 | 0.0984 | 611.6 |
| [OctOSO ₃] | -0.1054 | 0.0608 | 3.2245 | 0.1996 | 990.9 |
| [NO ₃] | -0.2013 | 0.0087 | 2.8800 | 0.0854 | 302.9 |
| [MeOSO ₃] | -0.1672 | 0.0380 | 3.0481 | 0.1775 | 453.6 |
| [EtOSO ₃] | -0.1539 | 0.0453 | 3.1074 | 0.1940 | 534.2 |
| [HexOSO ₃] | -0.1176 | 0.0586 | 3.1988 | 0.2036 | 838.8 |
| [TCM] | -0.1518 | 0.0101 | 3.1977 | 0.1221 | 499.5 |
| [BuOSO ₃] | -0.1332 | 0.0541 | 3.1615 | 0.2033 | 686.8 |
| [(EtO) ₂ PO ₂] | -0.1384 | 0.0453 | 3.2160 | 0.1618 | 717.0 |
| [DCA] | -0.1718 | 0.0097 | 3.1489 | 0.1513 | 392.1 |
| [NO ₂] | -0.2122 | 0.0077 | 3.1890 | 0.1997 | 268.6 |
| [SnCl ₃] | -0.1478 | 0.0193 | 3.4959 | 0.3409 | 558.6 |
| [SCN] | -0.1849 | 0.0090 | 3.3631 | 0.1355 | 344.1 |
| [Ac] | -0.1832 | 0.0402 | 3.1643 | 0.1717 | 365.1 |
| [MeOAc] | -0.1598 | 0.0534 | 3.1662 | 0.1922 | 482.5 |
| [F ₃ Ac] | -0.1737 | 0.0253 | 2.8330 | 0.1437 | 413.1 |

$[N_{1116}]$ = Hexyl(trimethyl)ammonium
 $[C_2py]$ = N-ethyl pyridinium
 $[bpy]$ = Butyl pyridinium
 $[emim]$ = 1-Ethyl-3-methyl imidazolium
 $[mPhim]$ = 1-Methyl-3-phenyl imidazolium
 $[C_4mim]$ = 1-Butyl-3-methylimidazolium
 $[C_8mim]$ = 3-Methyl-1-octylimidazolium
 $[N_{1112OH}]$ = 2-hydroxyethyl-trimethylammonium
 $[P_{4444}]$ = Tetrabutylphosphonium
 $[PF_6]$ = Hexafluorophosphate
 $[I]$ = Iodide
 $[Cl]$ = Chloride
 $[Br]$ = Bromide
 $[CF_3SO_3]$ = Trifluoromethanesulfonate (Triflate)
 $[MeSO_4]$ = Methylsulphate
 $[FAP]$ = Trifluorotris(pentafluoroethyl)phosphate
 $[SbF_6]$ = Hexafluoroantimonate
 $[Pf_2N]$ = bis(perfluoroethylsulfonyl)imide
 $[BF_4]$ = Tetrafluoroborate
 $[NTf_2]$ = bis(trifluoromethylsulfonyl)imide
 $[B(CN)_4]$ = Tetracyanoborate
 $[OctOSO_3]$ = Octyl sulfate
 $[NO_3]$ = Nitrate
 $[MeOSO_3]$ = Methyl sulfate
 $[EtOSO_3]$ = Ethyl sulfate
 $[HexOSO_3]$ = Hexyl sulfate
 $[TCM]$ = Tricyanomethanide
 $[BuOSO_3]$ = Butyl sulfate
 $[(EtO)_2PO_2]$ = Diethyl phosphate
 $[DCA]$ = Dicyanamide
 $[NO_2]$ = Nitrite
 $[SnCl_3]$ = Trichlorostannanide
 $[SCN]$ = Thiocyanate
 $[Ac]$ = Acetate
 $[MeOAc]$ = Methoxyacetate
 $[F_3Ac]$ = Trifluoroacetate

Table G.5 Basis set dependence of calculated mean $D(\mathbf{r})$ (bohr) and RMSD $D(\mathbf{r})$ (bohr) of selected solvents.

| Solvent | Property | 6-31+G(d,p) | 6-311++G(d,p) | aug-cc-pVDZ | aug-cc-pVTZ | aug-cc-pVQZ |
|-----------------------------|----------------------|-------------|---------------|-------------|-------------|-------------|
| N-methylthiopyrrolidinone-2 | Mean $D(\mathbf{r})$ | 3.2475 | 3.2542 | 3.2518 | 3.2531 | 3.2455 |
| | RMSD $D(\mathbf{r})$ | 0.1739 | 0.1694 | 0.1731 | 0.1688 | 0.1673 |
| Pyridine | Mean $D(\mathbf{r})$ | 3.2698 | 3.2796 | 3.2746 | 3.2742 | 3.2606 |
| | RMSD $D(\mathbf{r})$ | 0.0921 | 0.0843 | 0.0848 | 0.0840 | 0.0862 |
| Acetonitrile | Mean $D(\mathbf{r})$ | 3.1927 | 3.2043 | 3.1961 | 3.1961 | 3.1878 |
| | RMSD $D(\mathbf{r})$ | 0.1047 | 0.0952 | 0.0951 | 0.0954 | 0.0972 |
| Dimethyl sulfoxide | Mean $D(\mathbf{r})$ | 3.2550 | 3.2591 | 3.2543 | 3.2612 | 3.2557 |
| | RMSD $D(\mathbf{r})$ | 0.1896 | 0.1920 | 0.1819 | 0.1766 | 0.1742 |
| N-methyl formamide | Mean $D(\mathbf{r})$ | 3.1302 | 3.1415 | 3.1377 | 3.1385 | 3.1341 |
| | RMSD $D(\mathbf{r})$ | 0.1908 | 0.1918 | 0.1850 | 0.1873 | 0.1884 |
| Formamide | Mean $D(\mathbf{r})$ | 3.0659 | 3.0784 | 3.0784 | 3.0767 | 3.0718 |
| | RMSD $D(\mathbf{r})$ | 0.1778 | 0.1821 | 0.1769 | 0.1773 | 0.1800 |
| 1,1-Dichloroethane | Mean $D(\mathbf{r})$ | 3.2443 | 3.2430 | 3.2489 | 3.2525 | 3.2308 |
| | RMSD $D(\mathbf{r})$ | 0.0841 | 0.0791 | 0.0694 | 0.0697 | 0.0793 |
| Acetone | Mean $D(\mathbf{r})$ | 3.2104 | 3.2197 | 3.2111 | 3.2134 | 3.2063 |
| | RMSD $D(\mathbf{r})$ | 0.1631 | 0.1649 | 0.1628 | 0.1593 | 0.1586 |
| Methanol | Mean $D(\mathbf{r})$ | 3.0694 | 3.0765 | 3.0767 | 3.0753 | 3.0724 |
| | RMSD $D(\mathbf{r})$ | 0.2251 | 0.2192 | 0.2147 | 0.2089 | 0.2106 |
| Water | Mean $D(\mathbf{r})$ | 2.7898 | 2.7990 | 2.7999 | 2.8094 | 2.8076 |
| | RMSD $D(\mathbf{r})$ | 0.0349 | 0.0154 | 0.0291 | 0.0101 | 0.0112 |

Table G.6 Calculated maximum surface $D(\mathbf{r})$ and minimum ESP of σ -hole acceptors. The binding energies are adopted from Ref. [390].

| Molecule | Binding Energy (kcal/mol) | $V_{s,\min}$ (kcal/mol) | $D(\mathbf{r})_{\max}$ (bohr) |
|---------------------|------------------------------|----------------------------|----------------------------------|
| SiN-F | 1.900 | 7.334 | 4.323 |
| SiN-Cl | 3.420 | 4.953 | 4.330 |
| SiN-CCH | 4.090 | 4.359 | 4.324 |
| SiN-CCF | 4.210 | 3.467 | 4.328 |
| SiN-H | 6.610 | -2.925 | 4.350 |
| SiN-CH ₃ | 7.770 | -5.902 | 4.353 |
| SiN-Li | 20.60 | -26.24 | 4.463 |
| SiN-Na | 23.93 | -31.91 | 4.502 |
| CN-CN | 5.480 | -17.16 | 3.558 |
| CN-NC | 5.880 | -21.21 | 3.547 |
| CN-NO ₂ | 5.970 | -19.07 | 3.544 |
| CN-F | 6.180 | -25.59 | 3.542 |
| CN-CF ₃ | 8.270 | -24.23 | 3.565 |
| CN-Cl | 8.970 | -28.22 | 3.560 |
| CN-Br | 10.78 | -29.33 | 3.790 |
| CN-H | 10.86 | -34.10 | 3.596 |
| CN-CCF | 11.63 | -30.67 | 3.564 |
| CN-CCH | 11.64 | -29.78 | 3.562 |
| CN-CH ₃ | 14.13 | -39.37 | 3.576 |
| CN-SiH ₃ | 15.45 | -34.13 | 3.618 |
| CN-Li | 28.94 | -58.67 | 3.781 |
| CN-Na | 33.40 | -64.76 | 3.849 |

Table G.7 Calculated D_C (bohr) and Q_C (e) of some selected molecules using different methods with 6-31+G(d,p) basis set

| Method | Methane | | Ethylene | | Benzene | | buta-1,3-diene | |
|-----------------|---------|-------|----------|-------|---------|-------|----------------|-------|
| | Q_C | D_C | Q_C | D_C | Q_C | D_C | Q_C | D_C |
| HF | -0.147 | 1.781 | -0.094 | 1.753 | -0.050 | 1.672 | -0.099 | 1.746 |
| LSDA | -0.205 | 1.787 | -0.122 | 1.752 | -0.064 | 1.666 | -0.120 | 1.744 |
| B3LYP | -0.170 | 1.777 | -0.103 | 1.746 | -0.053 | 1.666 | -0.105 | 1.739 |
| LC-BLYP | -0.186 | 1.780 | -0.111 | 1.744 | -0.058 | 1.660 | -0.114 | 1.736 |
| B3PW91 | -0.180 | 1.774 | -0.109 | 1.743 | -0.057 | 1.663 | -0.110 | 1.736 |
| ω B97X-D | -0.178 | 1.775 | -0.108 | 1.743 | -0.057 | 1.663 | -0.110 | 1.736 |
| CCSD | -0.153 | 1.766 | -0.092 | 1.737 | -0.048 | 1.660 | -0.095 | 1.730 |

Table G.8 Calculated D_C (bohr) and Q_C (e) of some selected molecules using different basis sets at LC-BYLP level of theory

| Basis set | Methane | | Ethylene | | Benzene | | buta-1,3-diene | |
|---------------|---------|-------|----------|-------|---------|-------|----------------|-------|
| | Q_C | D_C | Q_C | D_C | Q_C | D_C | Q_C | D_C |
| 6-31++G(d,p) | -0.186 | 1.781 | -0.111 | 1.744 | -0.058 | 1.660 | -0.114 | 1.736 |
| 6-311++G(d,p) | -0.185 | 1.781 | -0.109 | 1.745 | -0.058 | 1.660 | -0.113 | 1.736 |
| aug-cc-pVDZ | -0.185 | 1.784 | -0.110 | 1.748 | -0.057 | 1.663 | -0.112 | 1.739 |
| aug-cc-pVTZ | -0.185 | 1.778 | -0.108 | 1.741 | -0.057 | 1.663 | -0.111 | 1.733 |
| aug-cc-pVQZ | -0.186 | 1.777 | -0.109 | 1.740 | -0.057 | 1.663 | -0.111 | 1.733 |

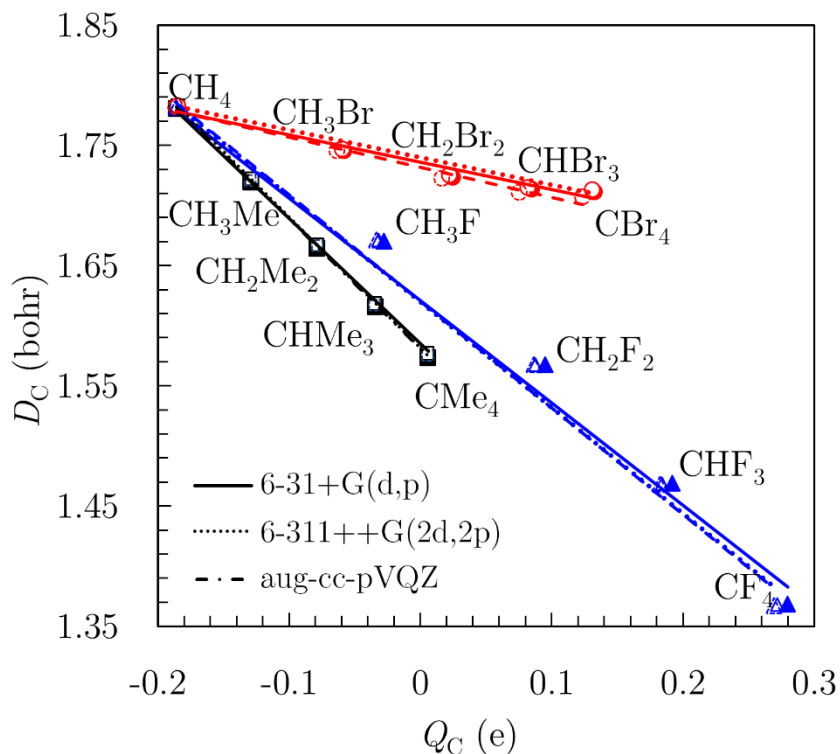
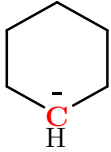
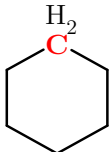
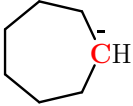
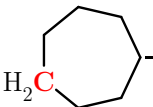
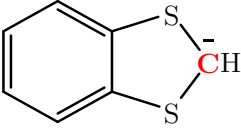
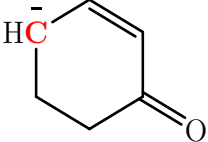
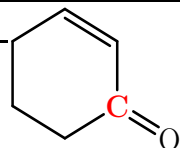
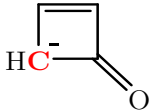
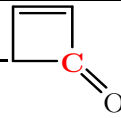
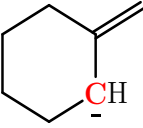
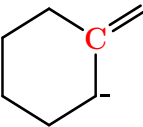


Figure G.1 Basis set dependence of relations mentioned in Fig. 3.2 of Chapter 3. The solid lines with filled data symbols corresponds to 6-31+G(d,p) results. Dotted line with empty symbols shows 6-311++G(2d,2p) results. The data with dashed line and symbols is obtained using aug-cc-pVQZ basis sets.

Table G.9 Calculated atomic partial charges Q_C (e) and atomic average overlap distance D_C (bohr) of systems mentioned in [Chapter 3](#). The listed property represents the carbon atom shown as boldfaced and red.

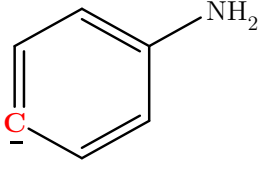
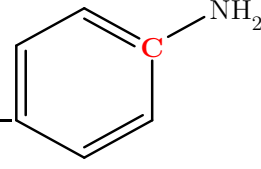
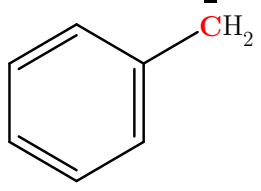
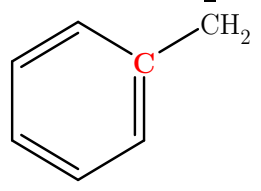
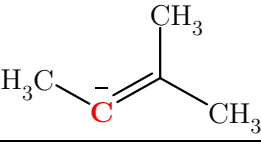
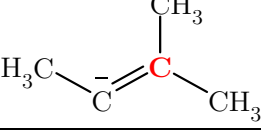
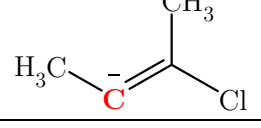
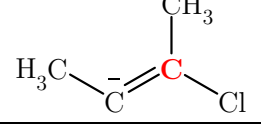
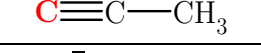
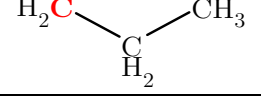
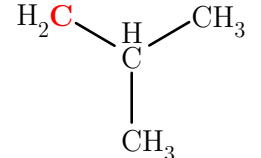
| Sr. # | Structure | Name | Q_C | D_C |
|-------|----------------------------------------------------------------------------------------------|----------------------|--------|-------|
| 1 | C ⁻ | Carbon | -1.000 | 2.381 |
| 2 | CH ₃ ⁻ | Methanide | -0.671 | 2.000 |
| 3 | H ₂ C ⁻ —CH ₃ | Ethanide | -0.556 | 1.911 |
| | H ₂ C ⁻ — CH ₃ | | -0.205 | 1.766 |
| 4 | H ₃ C— C ⁻ (H)—CH ₃ | Propan-2-ide | -0.434 | 1.815 |
| 5 | $\begin{array}{c} \text{CH}_3 \\ \\ \text{H}_3\text{C}-\text{C}^--\text{CH}_3 \end{array}$ | 2-methylpropan-2-ide | -0.318 | 1.727 |
| 6 | | Pentan-3-ide | -0.385 | 1.774 |
| | | | -0.124 | 1.688 |
| | | | -0.160 | 1.736 |
| 7 | | Pent-1-en-3-ide | -0.233 | 1.687 |
| | | | -0.120 | 1.699 |
| | | | -0.106 | 1.680 |
| 8 | | Penta-1,4-dien-3-ide | 0.006 | 1.666 |
| 9 | H ₂ C=**CH ⁻ | Ethenide | -0.509 | 1.885 |
| | H ₂ C =CH ⁻ | | -0.295 | 1.824 |
| 10 | HC≡**C ⁻ | Ethyne | -0.600 | 2.099 |
| | HC≡ C ⁻ | | -0.405 | 1.857 |
| 11 | C ≡ C ⁻ | Ethyne-1,2-diide | -1.000 | 2.344 |

| | | | | |
|----|--|--------------------|--------|-------|
| 12 | | Chloromethanide | -0.484 | 1.871 |
| 13 | | Dichloromethanide | -0.321 | 1.750 |
| 14 | | Chloroform (anion) | -0.174 | 1.646 |
| 15 | | Benzen-1-ide | -0.411 | 1.861 |
| | | | -0.138 | 1.697 |
| | | | -0.127 | 1.675 |
| 16 | | Cyclopropanide | -0.512 | 1.877 |
| | | | -0.192 | 1.716 |
| 17 | | Cyclobutanide | -0.442 | 1.820 |
| | | | -0.123 | 1.684 |
| 18 | | Cyclopentanide | -0.369 | 1.726 |
| | | | -0.104 | 1.669 |

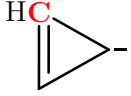
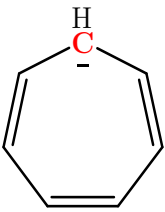
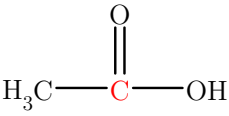
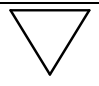
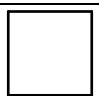
| | | | | |
|----|-------------------------------------------------------------------------------------|-----------------------------|--------|-------|
| 19 |  | Cyclohexanide | -0.360 | 1.725 |
| |  | | -0.092 | 1.667 |
| 20 |  | Cycloheptanide | -0.398 | 1.770 |
| |  | | -0.091 | 1.667 |
| 21 |  | Benzo[d][1,3]dithiol-2-ide | -0.443 | 1.888 |
| 22 |  | 4-oxocyclohex-2-en-1-ide | -0.174 | 1.681 |
| |  | | 0.060 | 1.571 |
| 23 |  | 4-oxocyclobut-2-en-1-ide | -0.315 | 1.713 |
| |  | | 0.072 | 1.588 |
| 24 |  | 2-methylenecyclohexan-1-ide | -0.238 | 1.680 |
| |  | | -0.057 | 1.630 |

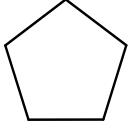
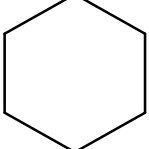
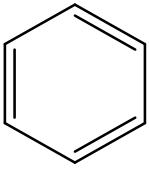
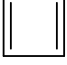
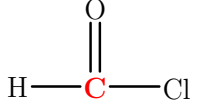
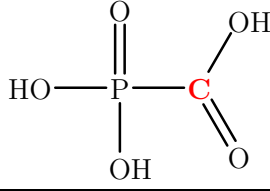
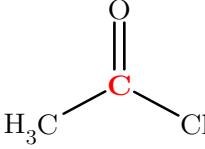
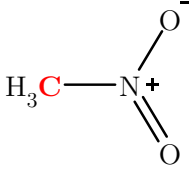
| | | | | |
|----|--|-------------------------------------|--------|-------|
| 25 | | (Phenylsulfinyl)methanide | -0.383 | 1.802 |
| 26 | | (Methylsulfinyl)methanide | -0.424 | 1.826 |
| | | | -0.158 | 1.739 |
| 27 | | 2-methoxy-2-oxoethan-1-ide | -0.361 | 1.771 |
| | | | 0.091 | 1.550 |
| 28 | | Cyanomethanide | -0.400 | 1.812 |
| 29 | | 2-oxopropan-1-ide | -0.340 | 1.775 |
| 30 | | 1,3-dimethoxy-1,3-dioxopropan-2-ide | -0.235 | 1.650 |
| | | | 0.154 | 1.526 |
| 31 | | Cyanide | -0.510 | 2.069 |
| 32 | | Prop-2-en-1-ide | -0.362 | 1.797 |

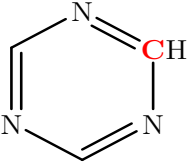
| | | | | |
|----|--|-----------------------------|--------|-------|
| 33 | | Cyclopenta-2,4-dien-1-ide | -0.193 | 1.697 |
| 34 | | (Chlorosulfonyl)methanide | -0.273 | 1.754 |
| 35 | | 2-oxoethan-1-ide | -0.550 | 1.888 |
| 36 | | Cyano(phenyl)methanide | -0.221 | 1.684 |
| 37 | | 5-cyano-2-nitrobenzen-1-ide | -0.339 | 1.813 |
| 38 | | 2-aminobenzen-1-ide | -0.399 | 1.834 |
| | | | -0.015 | 1.603 |
| 39 | | 3-aminobenzen-1-ide | -0.410 | 1.860 |
| | | | -0.005 | 1.585 |

| | | | | |
|----|-------------------------------------------------------------------------------------|----------------------------|--------|--------|
| 40 |  | 4-aminobenzen-1-ide | -0.415 | 1.861 |
| |  | | -0.018 | 1.5824 |
| 41 |  | Phenylmethanide | -0.474 | 1.831 |
| |  | | -0.016 | 1.634 |
| 42 |  | 3-methylbut-2-en-2-ide | -0.412 | 1.851 |
| |  | | -0.124 | 1.638 |
| 43 |  | (E)-3-chlorobut-2-en-2-ide | -0.362 | 1.802 |
| |  | (E)-3-chlorobut-2-en-2-ide | -0.064 | 1.659 |
| 44 |  | Prop-1-yn-1-ide | -0.629 | 2.081 |
| 45 |  | Propan-1-ide | -0.528 | 1.892 |
| 46 |  | 2-methylpropan-1-ide | -0.510 | 1.879 |

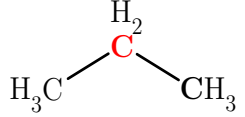
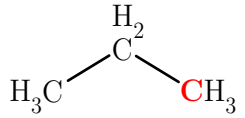
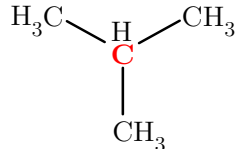
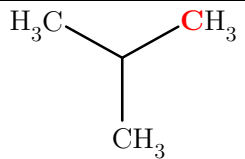
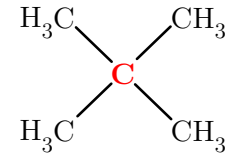
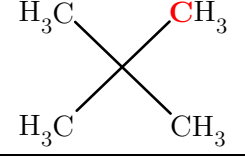
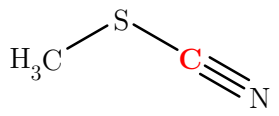
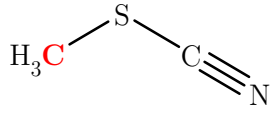
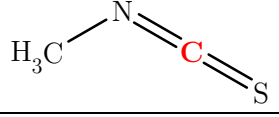
| | | | | |
|----|--|---------------------------|--------|-------|
| 47 | | 2,2-dimethylpropan-1-ide | -0.491 | 1.865 |
| 48 | | 2-methylcyclopropan-1-ide | -0.481 | 1.860 |
| | | | -0.118 | 1.646 |
| 49 | | endo-5H-norborborneide | -0.410 | 1.799 |
| 50 | | exo-5H-norborborneide | -0.436 | 1.817 |
| 51 | | Bromomethanide | -0.431 | 1.873 |
| 52 | | Fluoromethanide | -0.535 | 1.875 |
| 53 | | Diphenylmethanide | -0.200 | 1.662 |
| 54 | | Triphenylmethanide | -0.132 | 1.596 |
| 55 | | Cycloprop-2-en-1-ide | -0.562 | 1.943 |

| | | | | |
|----|-------------------------------------------------------------------------------------|------------------------|--------|-------|
| |  | | -0.191 | 1.741 |
| 56 |  | Cycloheptatriene-1-ide | -0.261 | 1.733 |
| 57 | C | Carbon | 0.000 | 2.118 |
| 58 | CLi₄ | CLi4 | -0.790 | 2.128 |
| 59 | CH₄ | Methane | -0.186 | 1.780 |
| 60 | CH₃Br | Bromomethane | -0.058 | 1.745 |
| 61 | CH₂Br₂ | Dibromomethane | 0.025 | 1.723 |
| 62 | CHBr₃ | Bromoform | 0.085 | 1.713 |
| 63 | CBr₄ | Carbontetrabromide | 0.133 | 1.711 |
| 64 | CF₄ | Carbontetrafluoride | 0.280 | 1.369 |
| 65 | CO₂ | Carbon dioxide | 0.367 | 1.465 |
| 66 | CH₃OH | Methanol | -0.048 | 1.682 |
| 67 | LiCH₃ | Methyl lithium | -0.452 | 1.871 |
| 68 | CS₂ | Carbendisulfide | 0.082 | 1.729 |
| 69 | HCN | Hydrogen cyanide | 0.047 | 1.702 |
| 70 | H₃C—SH | Methanethiol | -0.119 | 1.742 |
| 71 | H₂C=CH₂ | Ethene | -0.111 | 1.744 |
| 72 | H₂C=C(Cl)H | Chloroethene | -0.108 | 1.728 |
| 73 | Cl—C(H)=C(H)—Cl | 1,2-dichloroethene | -0.013 | 1.670 |
| 74 | H₂C=CCl₂ | 1,1-dichloroethene | -0.106 | 1.714 |
| 75 | HC≡CH | Ethyne | -0.110 | 1.771 |
| 76 | HC≡CCl | Chloroethyne | -0.022 | 1.671 |
| 77 | H₃C—C≡N | Acetonitrile | 0.078 | 1.615 |
| 78 |  | Acetic acid | 0.226 | 1.699 |
| 79 |  | Cyclopropane | -0.106 | 1.677 |
| 80 |  | Cyclobutane | -0.085 | 1.665 |

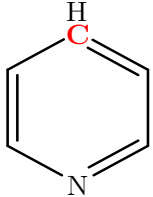
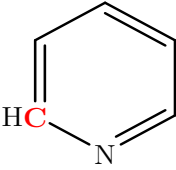
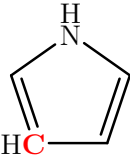
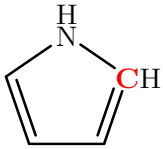
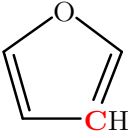
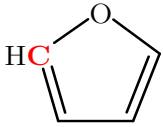
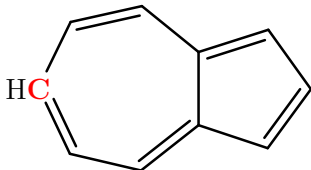
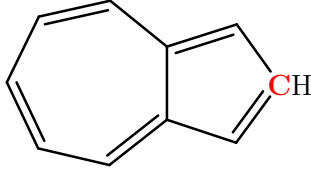
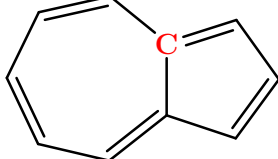
| | | | | |
|----|-------------------------------------------------------------------------------------|---------------------------|--------|-------|
| 81 |  | Cyclopentane | -0.083 | 1.658 |
| 82 |  | Cyclohexane | -0.081 | 1.657 |
| 83 |  | Benzene | -0.058 | 1.660 |
| 84 |  | Cyclobuta-1,3-diene | -0.064 | 1.686 |
| 85 | CO | Carbon monoxide | 0.102 | 1.872 |
| 86 | HCOOH | Formic acid | 0.197 | 1.564 |
| 87 | HCOH | Formaldehyde | 0.113 | 1.679 |
| 88 |  | Formyl chloride | 0.194 | 1.626 |
| 89 | $\text{H}_2\text{C}=\text{N}^+\equiv\text{N}^-$ | Diazomethane | -0.147 | 1.712 |
| 90 | $\text{O}=\text{N}-\text{CF}_3$ | Trifluoro(nitroso)methane | 0.238 | 1.400 |
| 91 |  | Phosphonoformic acid | 0.170 | 1.523 |
| 92 |  | Acetyl chloride | 0.224 | 1.701 |
| 93 |  | Nitromethane | -0.045 | 1.678 |
| 94 | $\text{H}_2\text{C}=\text{NH}$ | Methanimine | 0.004 | 1.704 |
| 95 | $\text{H}_2\text{C}=\text{C}=\text{CH}_2$ | Propa-1,2-diene | -0.006 | 1.669 |
| 96 | $\text{H}_2\text{C}=\underset{\text{H}}{\text{C}}-\text{CH}_3$ | Prop-1-ene | -0.053 | 1.676 |

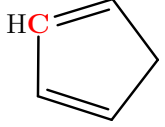
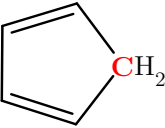
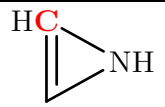
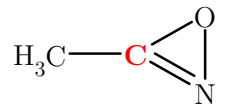
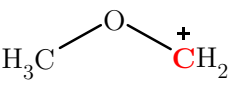
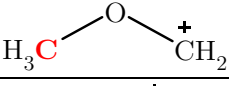
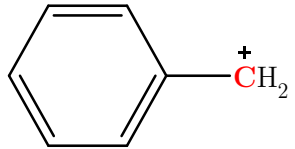
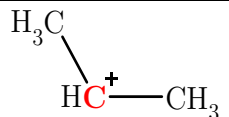
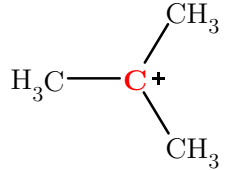
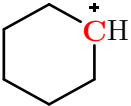
| | | | | |
|-----|-------------------------------------------------------------------------------------------------------------|-----------------------------------|--------|-------|
| 97 | $\begin{array}{c} \text{H} \\ \\ \text{F}_3\text{C}-\text{C}-\text{CF}_3 \\ \\ \text{OH} \end{array}$ | 1,1,1,3,3,3-hexafluoropropan-2-ol | 0.014 | 1.528 |
| 98 | $\begin{array}{c} \text{H} \\ \\ \text{H}-\text{C}-\text{CF}_3 \\ \\ \text{OH} \end{array}$ | 2,2,2-trifluoroethan-1-ol | -0.012 | 1.597 |
| 99 | $\begin{array}{c} \text{NO}_2 \\ \\ \text{O}_2\text{N}-\text{C}-\text{H} \\ \\ \text{NO}_2 \end{array}$ | Trinitromethane | 0.131 | 1.527 |
| 100 | $\begin{array}{c} \text{H} \\ \\ \text{Cl}_3\text{C}-\text{C}-\text{H} \\ \\ \text{NH}_2 \end{array}$ | 2,2,2-trichloroethan-1-amine | -0.030 | 1.623 |
| 101 | $\begin{array}{c} \text{H} \\ \\ \text{F}_3\text{C}-\text{C}-\text{H} \\ \\ \text{NH}_2 \end{array}$ | 2,2,2-trifluoroethan-1-amine | -0.040 | 1.610 |
| 102 | $\text{CH}_3\text{-Mg-Br}$ | Methylmagnesium bromide | -0.350 | 1.842 |
| 103 | $\text{CH}_3\text{-Mg-F}$ | Methylmagnesium fluoride | -0.347 | 1.844 |
| 104 | $\text{K}-\text{C}\equiv\text{N}$ | Cyanopotassium | 0.453 | 1.785 |
| 105 |  | 1,3,5-triazine | 0.113 | 1.595 |
| 106 | $\begin{array}{c} \text{O} \\ \\ \text{Cl}-\text{C}-\text{NH}_2 \end{array}$ | Carbamic chloride | 0.231 | 1.537 |

| | | | | |
|-----|----------------------------------------------------------|-----------------------|--------|-------|
| 107 | | Perchloroethene | 0.064 | 1.614 |
| 108 | $\text{H}_3\text{C}-\text{N}^+\equiv\text{C}^-$ | Isocyanomethane | -0.119 | 1.903 |
| 109 | $\text{HO}-\text{C}\equiv\text{N}$ | Cyanic acid | 0.159 | 1.534 |
| 110 | $\text{HO}-\text{N}^+\equiv\text{C}^-$ | Fulminic acid | -0.112 | 1.889 |
| 111 | | Carbonyl diisocyanate | 0.264 | 1.505 |
| 112 | | Carbonyl diisocyanate | 0.322 | 1.505 |
| 113 | o-carborane | o-carborane | -0.009 | 1.630 |
| 114 | m-carborane | m-carborane | -0.058 | 1.647 |
| 115 | p-carborane | p-carborane | -0.053 | 1.649 |
| 116 | $\text{H}_3\text{C}-\text{C}\equiv\text{N}^+-\text{O}^-$ | Acetonitrile oxide | 0.058 | 1.590 |
| 117 | | Naphthalene | -0.059 | 1.660 |
| | | | -0.004 | 1.587 |
| 118 | | Anthracene | -0.060 | 1.660 |
| | | | -0.005 | 1.587 |
| 119 | | Cyclooctatetraene | -0.051 | 1.673 |
| 120 | | 1,3,5-hexatriene | -0.055 | 1.671 |
| | | | -0.115 | 1.736 |
| 121 | $\text{H}_3\text{C}-\text{CH}_3$ | Ethane | -0.129 | 1.719 |

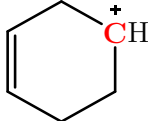
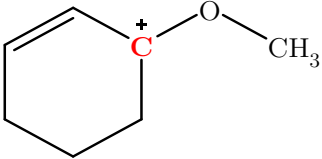
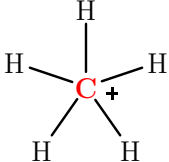
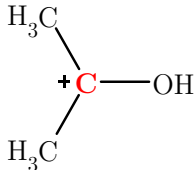
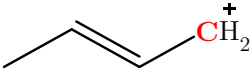
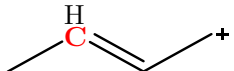
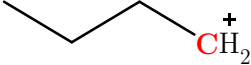
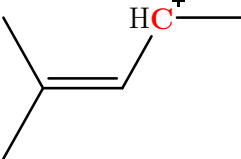
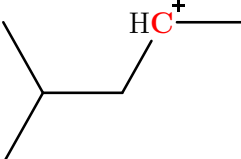
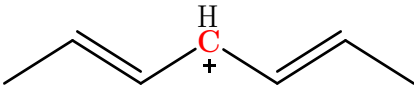
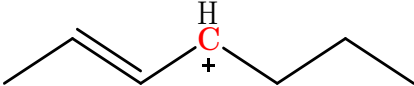
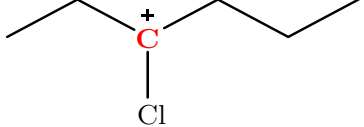
| | | | | |
|-----|-------------------------------------------------------------------------------------|----------------------------|--------|-------|
| 122 |  | Propane | -0.078 | 1.664 |
| |  | | -0.129 | 1.714 |
| 123 |  | Isobutane | -0.034 | 1.615 |
| |  | | -0.129 | 1.709 |
| 124 |  | Neopentane | 0.006 | 1.573 |
| |  | | -0.128 | 1.704 |
| 125 | $\text{CH}_3\text{-Ph}$ | Toulene | -0.122 | 1.712 |
| 126 | $\text{CH}_2\text{-Ph}_2$ | Diphenylmethane | -0.069 | 1.652 |
| 127 | CH-Ph_3 | Triphenylmethane | -0.021 | 1.602 |
| 128 | CHCl-Ph_2 | (Chloromethylene)dibenzene | 0.035 | 1.622 |
| 129 | CH_3F | Fluoromethane | -0.028 | 1.670 |
| 130 | CH_2F_2 | Difluoromethane | 0.095 | 1.568 |
| 131 | CHF_3 | Trifluoromethane | 0.192 | 1.469 |
| 132 |  | Thiocyanatomethane | 0.054 | 1.635 |
| |  | | -0.099 | 1.733 |
| 133 |  | Isothiocyanatomethane | 0.121 | 1.645 |

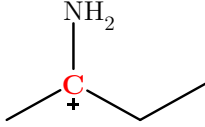
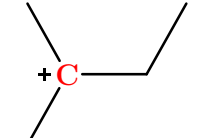
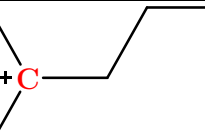
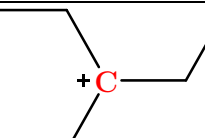
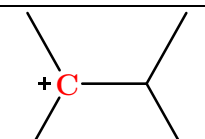
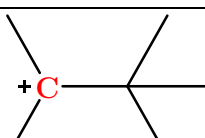
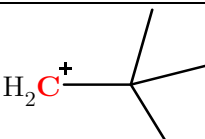
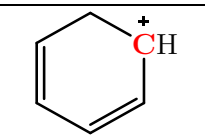
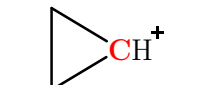
| | | | | |
|-----|--|--------------|--------|-------|
| | | | -0.024 | 1.694 |
| 134 | | Methanethial | -0.024 | 1.771 |
| 135 | | Methanamine | -0.079 | 1.698 |
| 136 | | Cyclopropene | -0.111 | 1.697 |
| | | | -0.065 | 1.685 |
| 137 | | Phenanthrene | 0.000 | 1.659 |
| | | | -0.006 | 1.587 |
| 138 | | Pentalene | -0.065 | 1.670 |
| | | | -0.029 | 1.582 |
| | | | -0.035 | 1.669 |

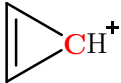
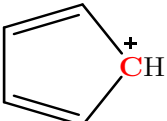
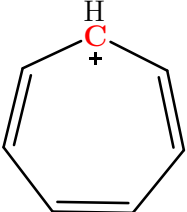
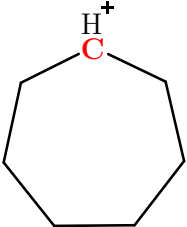
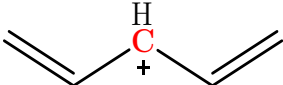
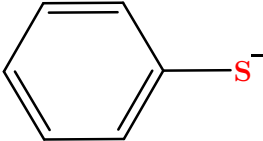
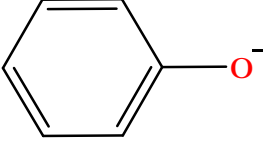
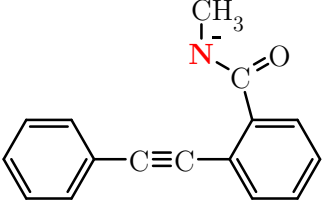
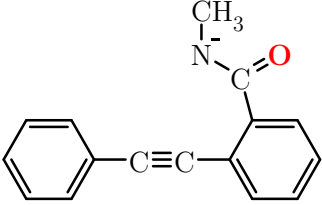
| | | | | |
|-----|-------------------------------------------------------------------------------------|----------|--------|-------|
| 139 |  | Pyridine | -0.035 | 1.658 |
| |  | | 0.016 | 1.628 |
| 140 |  | Pyrrole | -0.110 | 1.665 |
| |  | | -0.044 | 1.636 |
| 141 |  | Furan | -0.097 | 1.660 |
| |  | | 0.004 | 1.618 |
| 142 |  | Azulene | -0.029 | 1.660 |
| |  | | -0.061 | 1.667 |
| |  | | -0.010 | 1.591 |

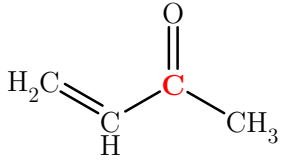
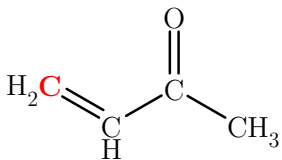
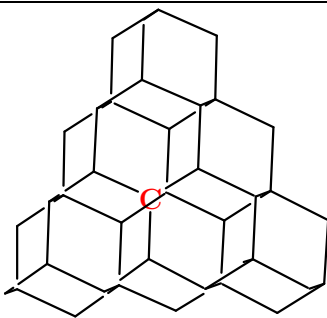
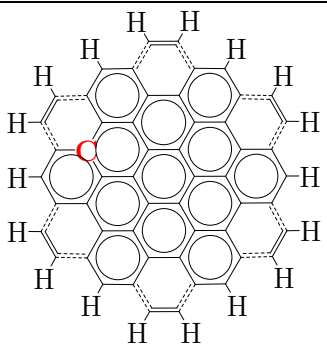

| | | | | |
|-----|-------------------------------------------------------------------------------------|------------------------|--------|-------|
| 143 |  | Cyclopentadiene | -0.072 | 1.667 |
| |  | | -0.078 | 1.659 |
| 144 |  | 1H-azirine | -0.02 | 1.670 |
| 145 | $\text{H}_3\text{C}-\text{N}=\text{C}=\text{O}$ | Isocyanatomethane | 0.235 | 1.511 |
| 146 | $\text{H}_3\text{C}-\text{O}-\text{N}^+\equiv\text{C}^-$ | (Isocyanooxy)methane | -0.123 | 1.893 |
| 147 | $\text{H}_3\text{C}-\text{O}-\text{C}\equiv\text{N}$ | Cyanatomethane | 0.156 | 1.532 |
| 148 |  | 3-methyl-1,2-oxazirine | 0.164 | 1.527 |
| 149 | C^+ | Carbon-cation | 1.000 | 2.017 |
| 150 | CH_3^+ | Methylium | 0.428 | 1.777 |
| 151 |  | Methoxymethyl cation | 0.286 | 1.658 |
| |  | | 0.06 | 1.687 |
| 152 | $\text{H}_3\text{C}-\text{CH}_2^+$ | Ethylium | 0.106 | 1.697 |
| | $\text{H}_3\text{C}^+-\text{CH}_2$ | | 0.105 | 1.697 |
| 153 |  | Phenylmethyl cation | 0.335 | 1.711 |
| 154 |  | Propan-2-ylum | 0.254 | 1.657 |
| 155 |  | 2-methylpropan-2-ylum | 0.254 | 1.610 |
| 156 |  | Cyclohexylum | 0.227 | 1.644 |

| | | | | |
|-----|--|---------------------------|--------|-------|
| | | | -0.033 | 1.636 |
| | | | -0.068 | 1.647 |
| 157 | | Cyclopentylum | 0.227 | 1.645 |
| 158 | | Methylcyclopentan-1-ylum | 0.234 | 1.594 |
| 159 | | Allylium | 0.268 | 1.652 |
| 160 | | Ethylium | 0.324 | 1.736 |
| | | | 0.324 | 1.736 |
| 161 | | 3-methylbut-2-en-2-ylum | 0.217 | 1.634 |
| 162 | | Benzene-1-ylum | 0.257 | 1.620 |
| | | | 0.021 | 1.653 |
| | | | -0.006 | 1.653 |
| 163 | | (E)-penta-2,4-dien-1-ylum | 0.079 | 1.721 |
| | | | 0.135 | 1.658 |

| | | | | |
|-----|-------------------------------------------------------------------------------------|-------------------------------|--------|-------|
| 164 |  | Cyclohex-3-en-1-ylum | 0.221 | 1.643 |
| 165 |  | 1-methoxycyclohex-2-en-1-ylum | 0.231 | 1.545 |
| 166 |  | Carbonium | -0.050 | 1.716 |
| 167 |  | 2-hydroxypropan-2-ylum | 0.314 | 1.563 |
| 168 |  | (E)-but-2-en-1-ylum | -0.076 | 1.695 |
| |  | | 0.181 | 1.658 |
| 169 |  | Butan-1-ylum | 0.221 | 1.650 |
| 170 |  | 4-methylpent-3-en-2-ylum | 0.120 | 1.656 |
| 171 |  | 4-methylpentan-2-ylum | 0.063 | 1.639 |
| 172 |  | (2E,5E)-hepta-2,5-dien-4-ylum | 0.115 | 1.657 |
| 173 |  | (E)-hept-2-en-4-ylum | 0.150 | 1.654 |
| 174 |  | 3-chlorohexan-3-ylum | 0.247 | 1.609 |

| | | | | |
|-----|-------------------------------------------------------------------------------------|-----------------------------|-------|-------|
| 175 |  | Butan-2-iminium | 0.209 | 1.567 |
| 176 |  | 2-methylbutan-2-ylum | 0.242 | 1.603 |
| 177 |  | 2-methylpentan-2-ylum | 0.241 | 1.604 |
| 178 |  | 3-methylpentan-3-ylum | 0.234 | 1.598 |
| 179 |  | 2,3-dimethylbutan-2-ylum | 0.236 | 1.601 |
| 180 |  | 2,3,3-trimethylbutan-2-ylum | 0.233 | 1.595 |
| 181 | $\text{H}_2\text{N}-\overset{+}{\text{C}}\text{H}_2$ | Methaniminium | 0.210 | 1.673 |
| 182 | $\text{HO}-\overset{+}{\text{C}}\text{H}_2$ | Hydroxymethylium | 0.338 | 1.661 |
| 183 | $\text{F}-\overset{+}{\text{C}}\text{H}_2$ | Flouromethylium | 0.437 | 1.640 |
| 184 | $\text{CN}-\overset{+}{\text{C}}\text{H}_2$ | Isocyanomethylium | 0.328 | 1.725 |
| 185 |  | 2,2-dimethylpropan-1-ylum | 0.330 | 1.725 |
| 186 |  | cyclohexa-2,4-dien-1-ylum | 0.111 | 1.654 |
| 187 |  | Cyclopropylum | 0.000 | 1.650 |

| | | | | |
|-----|-------------------------------------------------------------------------------------|---------------------------------|--------|-------|
| 188 |  | Cycloprop-2-en-1-ylum | 0.156 | 1.659 |
| 189 |  | Cyclopenta-2,4-dien-1-ylum | 0.230 | 1.662 |
| 190 |  | Cyclohepta-2,4,6-trien-1-ylum | -0.011 | 1.598 |
| 191 |  | Cycloheptylium | 0.148 | 1.631 |
| 192 |  | Penta-1,4-dien-3-ylum | 0.149 | 1.656 |
| 193 |  | Benzene thiolate | -0.561 | 2.028 |
| 194 |  | Phenolate | -0.817 | 1.364 |
| 195 |  | Deprotonated o-alkynylbenzamide | -0.364 | 1.198 |
| |  | | -0.478 | 1.108 |

| | | | | |
|-----|-------------------------------------------------------------------------------------|------------------------|--------|-------|
| 196 |  | Butenone | 0.173 | 1.179 |
| |  | | -0.071 | 1.303 |
| 197 |  | Diamond cluster model | -0.003 | 1.54 |
| 198 |  | Graphene cluster model | -0.002 | 1.587 |
| 199 |  | C ₆₀ | 0.00 | 1.597 |

References

1. Parr, R. G.; Weitao, Y., *Density-Functional Theory of Atoms and Molecules*. Oxford University Press: 1994.
2. Sholl, D.; Steckel, J. A., *Density Functional Theory: A Practical Introduction*. Wiley: 2011.
3. Koch, W.; Holthausen, M. C., *A Chemist's Guide to Density Functional Theory*. Wiley: 2015.
4. Soroush, M., *Computational Quantum Chemistry: Insights into Polymerization Reactions*. Elsevier Science: 2018.
5. Zheng, C.; Zheng, J.; You, S.-L., A DFT Study on Rh-Catalyzed Asymmetric Dearomatization of 2-Naphthols Initiated with C–H Activation: A Refined Reaction Mechanism and Origins of Multiple Selectivity. *ACS Catal.* **2016**, *6* (1), 262-271.
6. Kolář, M. H.; Hobza, P., Computer Modeling of Halogen Bonds and Other σ -hole Interactions. *Chem. Rev.* **2016**, *116* (9), 5155-5187.
7. Gilday, L. C.; Robinson, S. W.; Barendt, T. A.; Langton, M. J.; Mullaney, B. R.; Beer, P. D., Halogen Bonding in Supramolecular Chemistry. *Chem. Rev.* **2015**, *115* (15), 7118-7195.
8. Mahmudov, K. T.; Kopylovich, M. N.; Guedes da Silva, M. F. C.; Pombeiro, A. J. L., Non-covalent Interactions in the Synthesis of Coordination Compounds: Recent Advances. *Coord. Chem. Rev.* **2017**, *345*, 54-72.
9. Aakeröy, C. B.; Wijethunga, T. K.; Desper, J., Practical Crystal Engineering Using Halogen Bonding: A Hierarchy Based on Calculated Molecular Electrostatic Potential Surfaces. *J. Mol. Struct.* **2014**, *1072*, 20-27.
10. Ateş, Ö. D.; Zorlu, Y.; Kanmazalp, S. D.; Chumakov, Y.; Gürek, A. G.; Ayhan, M. M., Halogen Bonding Driven Crystal Engineering of Iodophthalonitrile Derivatives. *CrystEngComm* **2018**, *20* (27), 3858-3867.
11. de la Roza, A. O.; DiLabio, G. A., *Non-covalent Interactions in Quantum Chemistry and Physics: Theory and Applications*. Elsevier Science: 2017.
12. Bromley, S. T.; Woodley, S. M., *Computational Modelling of Nanoparticles*. Elsevier Science: 2018.

13. Bernales, V.; Ortuño, M. A.; Truhlar, D. G.; Cramer, C. J.; Gagliardi, L., Computational Design of Functionalized Metal-organic Framework Nodes for Catalysis. *ACS Cent. Sci.* **2018**, *4* (1), 5-19.
14. van Santen, R. A.; Sautet, P., *Computational Methods in Catalysis and Materials Science: An Introduction for Scientists and Engineers*. Wiley: 2015.
15. Giustino, F., *Materials Modelling Using Density Functional Theory: Properties and Predictions*. Oxford University Press: 2014.
16. Lunghi, A.; Sanvito, S., A Unified Picture of the Covalent Bond within Quantum-accurate Force Fields: From Organic Molecules to Metallic Complexes' Reactivity. *Sci. Adv.* **2019**, *5* (5), eaaw2210.
17. Lu, W.; Zhang, R.; Jiang, H.; Zhang, H.; Luo, C., Computer-aided Drug Design in Epigenetics. *Front. Chem.* **2018**, *6* (57).
18. Clark, D. E., What has Computer-aided Molecular Design Ever Done for Drug Discovery? *Expert Opin. Drug Discov.* **2006**, *1* (2), 103-110.
19. Ortiz, C. L. D.; Completo, G. C.; Nacario, R. C.; Nellas, R. B., Potential Inhibitors of Galactofuranosyltransferase 2 (GlfT2): Molecular Docking, 3D-QSAR, and In Silico ADMETox Studies. *Sci. Rep.* **2019**, *9* (1), 17096.
20. Ting, Z.; Danzhi, H.; Amedeo, C., Quantum Mechanical Methods for Drug Design. *Curr. Top. Med. Chem.* **2010**, *10* (1), 33-45.
21. Marenich, A. V.; Jerome, S. V.; Cramer, C. J.; Truhlar, D. G., Charge Model 5: An Extension of Hirshfeld Population Analysis for the Accurate Description of Molecular Interactions in Gaseous and Condensed Phases. *J. Chem. Theory Comput.* **2012**, *8* (2), 527-541.
22. Over, H.; Kim, Y. D.; Seitsonen, A. P.; Wendt, S.; Lundgren, E.; Schmid, M.; Varga, P.; Morgante, A.; Ertl, G., Atomic-Scale Structure and Catalytic Reactivity of the RuO₂(110) Surface. *Science* **2000**, *287* (5457), 1474.
23. Bauer, M. R.; Mackey, M. D., Electrostatic Complementarity as a Fast and Effective Tool to Optimize Binding and Selectivity of Protein-Ligand Complexes. *J. Med. Chem.* **2019**, *62* (6), 3036-3050.
24. Rathi, P. C.; Ludlow, R. F.; Verdonk, M. L., Practical High-Quality Electrostatic Potential Surfaces for Drug Discovery Using a Graph-Convolutional Deep Neural Network. *J. Med. Chem.* **2020**, *63* (16), 8778-8790.

25. Chessari, G.; Buck, I. M.; Day, J. E. H.; Day, P. J.; Iqbal, A.; Johnson, C. N.; Lewis, E. J.; Martins, V.; Miller, D.; Reader, M.; Rees, D. C.; Rich, S. J.; Tamanini, E.; Vitorino, M.; Ward, G. A.; Williams, P. A.; Williams, G.; Wilsher, N. E.; Woolford, A. J. A., Fragment-Based Drug Discovery Targeting Inhibitor of Apoptosis Proteins: Discovery of a Non-Alanine Lead Series with Dual Activity Against cIAP1 and XIAP. *J. Med. Chem.* **2015**, *58* (16), 6574-6588.
26. Chaloner, P., *Organic Chemistry: A Mechanistic Approach*. Taylor & Francis: 2014.
27. Li, D. Y.; Shi, K. J.; Mao, X. F.; Zhao, Z. L.; Wu, X. Y.; Liu, P. N., Selective Cyclization of Alkynols And Alkynylamines Catalyzed by Potassium Tert-Butoxide. *Tetrahedron* **2014**, *70* (39), 7022-7031.
28. Kundu, N. G.; Khan, M. W., Palladium-Catalysed Heteroannulation with Terminal Alkynes: a Highly Regio- and Stereoselective Synthesis of (Z)-3-Aryl(alkyl)idene Isoindolin-1-ones. *Tetrahedron* **2000**, *56* (27), 4777-4792.
29. Krause, N.; Hoffmann-Röder, A., Recent Advances in Catalytic Enantioselective Michael Additions. *Synthesis* **2001**, *2*, 171-196.
30. Mondal, P.; Hazarika, K. K.; Deka, R. C., Reactivity of α,β -unsaturated Carbonyl Compounds Towards Nucleophilic Addition Reaction: A Local Hard-soft Acid-base Approach. *PhysChemComm* **2003**, *6* (6), 24-27.
31. Hammer, B.; Morikawa, Y.; Nørskov, J. K., CO Chemisorption at Metal Surfaces and Overlayers. *Phys. Rev. Lett.* **1996**, *76* (12), 2141-2144.
32. Chen, M.; Bates, S. P.; van Santen, R. A.; Friend, C. M., The Chemical Nature of Atomic Oxygen Adsorbed on Rh(111) and Pt(111): A Density Functional Study. *J. Phys. Chem. B* **1997**, *101* (48), 10051-10057.
33. Denis, P. A.; Iribarne, F., Comparative Study of Defect Reactivity in Graphene. *J. Phys. Chem. C* **2013**, *117* (37), 19048-19055.
34. OuYang, F.; Huang, B.; Li, Z.; Xiao, J.; Wang, H.; Xu, H., Chemical Functionalization of Graphene Nanoribbons by Carboxyl Groups on Stone-Wales Defects. *J. Phys. Chem. C* **2008**, *112* (31), 12003-12007.
35. Kudur Jayaprakash, G.; Casillas, N.; Astudillo-Sánchez, P. D.; Flores-Moreno, R., Role of Defects on Regioselectivity of Nano Pristine Graphene. *J. Phys. Chem. A* **2016**, *120* (45), 9101-9108.
36. Denis, P. A., Heteroatom Promoted Cycloadditions for Graphene. *ChemistrySelect* **2016**, *1* (17), 5497-5500.

37. Geerlings, P.; De Proft, F.; Langenaeker, W., Conceptual Density Functional Theory. *Chem. Rev.* **2003**, *103* (5), 1793-1874.
38. Ayers, P. W., An Elementary Derivation of the Hard/Soft-acid/base Principle. *J. Chem. Phys.* **2005**, *122* (14), 141102.
39. Yang, W.; Parr, R. G., Hardness, Softness, and the Fukui Function in the Electronic Theory of Metals and Catalysis. *Proc. Natl. Acad. Sci. U.S.A* **1985**, *82* (20), 6723-6726.
40. Beker, W.; Szarek, P.; Komorowski, L.; Lipinski, J., Reactivity Patterns of Imidazole, Oxazole, and Thiazole As Reflected by the Polarization Justified Fukui Functions. *J. Phys. Chem. A* **2013**, *117* (7), 1596-1600.
41. Mendoza-Huizar, L. H., Analysis of the Chemical Reactivity of Aminocyclopyrachlor Herbicide Through the Fukui Function. *J. Serb. Chem. Soc.* **2015**, *80* (6), 767-777.
42. Fukui, K., Role of Frontier Orbitals in Chemical Reactions. *Science* **1982**, *218* (4574), 747-754.
43. Geerlings, P.; De Proft, F., HSAB Principle: Applications of its Global and Local Forms in Organic Chemistry. *Int. J. Quantum Chem* **2000**, *80* (2), 227-235.
44. Langenaeker, W.; de Proft, F.; Geerlings, P., Development of Local Hardness-Related Reactivity Indices: Their Application in a Study of the SE at Monosubstituted Benzenes within the HSAB Context. *J. Phys. Chem.* **1995**, *99* (17), 6424-6431.
45. Mendez, F.; Garcia-Garibay, M. A., A Hard–Soft Acid–Base and DFT Analysis of Singlet–Triplet Gaps and the Addition of Singlet Carbenes to Alkenes. *J. Org. Chem.* **1999**, *64* (19), 7061-7066.
46. Chattaraj, P. K.; Fuentealba, P.; Gómez, B.; Contreras, R., Woodward–Hoffmann Rule in the Light of the Principles of Maximum Hardness and Minimum Polarizability: DFT and Ab Initio SCF Studies. *J. Am. Chem. Soc.* **2000**, *122* (2), 348-351.
47. Balawender, R.; Komorowski, L.; De Proft, F.; Geerlings, P., Derivatives of Molecular Valence as a Measure of Aromaticity. *J. Phys. Chem. A* **1998**, *102* (48), 9912-9917.
48. Sarmah, P.; Deka, R. C., Solvent Effect on the Reactivity of CIS-platinum (II) complexes: A Density Functional Approach. *Int. J. Quantum Chem* **2008**, *108* (8), 1400-1409.

49. Panina, N. S.; Calligaris, M., Density Functional Study of Linkage Isomerism in Dimethyl Sulfoxide Ru(III) and Rh(III) Complexes. *Inorg. Chim. Acta* **2002**, *334*, 165-171.
50. Bania, K. K.; Deka, R. C., Influence of Zeolite Framework on the Structure, Properties, and Reactivity of Cobalt Phenanthroline Complex: A Combined Experimental and Computational Study. *J. Phys. Chem. C* **2011**, *115* (19), 9601-9607.
51. Islam, N.; Kaya, S., *Conceptual Density Functional Theory and Its Application in the Chemical Domain*. Apple Academic Press: 2018.
52. Frau, J.; Hernández-Haro, N.; Glossman-Mitnik, D., Computational Prediction of the pK_a s of Small Peptides Through Conceptual DFT Descriptors. *Chem. Phys. Lett.* **2017**, *671*, 138-141.
53. Putz, M. V.; Mingos, D. M. P., *Applications of Density Functional Theory to Chemical Reactivity*. Springer Berlin Heidelberg: 2013.
54. Pearson, R. G., *Chemical Hardness: Applications from Molecules to Solids*. Wiley: 1998.
55. Jayakumar, N.; Kolandaivel, P., Studies of Isomer Stability Using the Maximum Hardness Principle (MHP). *Int. J. Quantum Chem* **2000**, *76* (5), 648-655.
56. Padmanabhan, J.; Parthasarathi, R.; Subramanian, V.; Chattaraj, P. K., Molecular Structure, Reactivity, and Toxicity of the Complete Series of Chlorinated Benzenes. *J. Phys. Chem. A* **2005**, *109* (48), 11043-11049.
57. Senthilkumar, K.; Kolandaivel, P., Hartree-Fock and Density Functional Theory Studies on Ionization and Fragmentation of Halomethane Molecules by Positron Impact. *Mol. Phys.* **2002**, *100* (24), 3817-3822.
58. Shankar, R.; Senthilkumar, K.; Kolandaivel, P., Calculation of Ionization Potential and Chemical Hardness: A Comparative Study of Different Methods. *Int. J. Quantum Chem* **2009**, *109* (4), 764-771.
59. Anderson, J. S. M.; Melin, J.; Ayers, P. W., Conceptual Density-Functional Theory for General Chemical Reactions, Including Those That Are Neither Charge- nor Frontier-Orbital-Controlled. 1. Theory and Derivation of a General-Purpose Reactivity Indicator. *J. Chem. Theory Comput.* **2007**, *3* (2), 358-374.
60. Berger, G., Using Conceptual Density Functional Theory to Rationalize Regioselectivity: A Case Study on the Nucleophilic Ring-opening of Activated Aziridines. *Comp. Theor. Chem.* **2013**, *1010*, 11-18.

61. Falicov, L. M.; Somorjai, G. A., Correlation Between Catalytic Activity and Bonding and Coordination Number of Atoms and Molecules on Transition Metal Surfaces: Theory and Experimental Evidence. *Proc. Natl. Acad. Sci. U.S.A* **1985**, *82* (8), 2207-2211.
62. Carey, F. A.; Sundberg, R. J., *Advanced Organic Chemistry: Part A: Structure and Mechanisms*. Springer US: 2007.
63. Ren, J. H.; Brauman, J. I., Energy Deposition in S_N2 Reaction Products and Kinetic Energy Effects on Reactivity. *J. Phys. Chem. A* **2002**, *106* (15), 3804-3813.
64. Bader, R. F. W., *Atoms in Molecules: A Quantum Theory*. Clarendon Press: 1994.
65. Ayers, P. W.; Parr, R. G.; Nagy, A., Local Kinetic Energy and Local Temperature in The Density-Functional Theory of Electronic Structure. *Int. J. Quantum Chem* **2002**, *90* (1), 309-326.
66. Liu, S., Steric Effect: A Quantitative Description from Density Functional Theory. *J. Chem. Phys.* **2007**, *126* (24), 244103.
67. Politzer, P.; Murray, J. S.; Bulat, F. A., Average Local Ionization Energy: A Review. *J. Mol. Model.* **2010**, *16* (11), 1731-1742.
68. Silvi, B.; Savin, A., Classification of Chemical Bonds Based on Topological Analysis of Electron Localization Functions. *Nature* **1994**, *371* (6499), 683-686.
69. Becke, A. D.; Edgecombe, K. E., A Simple Measure of Electron Localization in Atomic and Molecular Systems. *J. Chem. Phys.* **1990**, *92* (9), 5397-5403.
70. Morell, C.; Grand, A.; Toro-Labbé, A., New Dual Descriptor for Chemical Reactivity. *J. Phys. Chem. A* **2005**, *109* (1), 205-212.
71. Cárdenas, C.; Rabi, N.; Ayers, P. W.; Morell, C.; Jaramillo, P.; Fuentealba, P., Chemical Reactivity Descriptors for Ambiphilic Reagents: Dual Descriptor, Local Hypersoftness, and Electrostatic Potential. *J. Phys. Chem. A* **2009**, *113* (30), 8660-8667.
72. Martinez-Araya, J. I., Why is the Dual Descriptor a More Accurate Local Reactivity Descriptor Than Fukui Functions? *J. Math. Chem.* **2015**, *53* (2), 451-465.
73. Roos, G.; Geerlings, P.; Messens, J., Enzymatic Catalysis: The Emerging Role of Conceptual Density Functional Theory. *J. Phys. Chem. B* **2009**, *113* (41), 13465-13475.

74. Ayers, P. L.; Boyd, R. J.; Bultinck, P.; Caffarel, M.; Carbó-Dorca, R.; Causá, M.; Cioslowski, J.; Contreras-Garcia, J.; Cooper, D. L.; Coppens, P.; Gatti, C.; Grabowsky, S.; Lazzeretti, P.; Macchi, P.; Martín Pendás, Á.; Popelier, P. L. A.; Ruedenberg, K.; Rzepa, H.; Savin, A.; Sax, A.; Schwarz, W. H. E.; Shahbazian, S.; Silvi, B.; Solà, M.; Tsirelson, V., Six Questions on Topology in Theoretical Chemistry. *Comp. Theor. Chem.* **2015**, *1053*, 2-16.
75. Pauling, L., The Nature of The Chemical Bond. Application of Results Obtained from the Quantum Mechanics and from a Theory of Paramagnetic Susceptibility to the Structure of Molecules. *J. Am. Chem. Soc.* **1931**, *53* (4), 1367-1400.
76. Hoffmann, R., Building Bridges Between Inorganic and Organic Chemistry (Nobel Lecture). *Angew. Chem. Int. Ed.* **1982**, *21* (10), 711-724.
77. Klopman, G., Chemical Reactivity and the Concept of Charge- and Frontier-controlled Reactions. *J. Am. Chem. Soc.* **1968**, *90* (2), 223-234.
78. Woodward, R. B.; Hoffmann, R., Stereochemistry of Electrocyclic Reactions. *J. Am. Chem. Soc.* **1965**, *87* (2), 395-397.
79. Hoffmann, H. M. R., The Ene Reaction. *Angew. Chem. Int. Ed.* **1969**, *8* (8), 556-577.
80. Fleming, I., *Molecular Orbitals and Organic Chemical Reactions*. Wiley: 2011.
81. Varbanov, H. P.; Jakupec, M. A.; Roller, A.; Jensen, F.; Galanski, M.; Keppler, B. K., Theoretical Investigations and Density Functional Theory Based Quantitative Structure–activity Relationships Model for Novel Cytotoxic Platinum(IV) Complexes. *J. Med. Chem.* **2013**, *56* (1), 330-344.
82. DeChancie, J.; Houk, K. N., The Origins of Femtomolar Protein–Ligand Binding: Hydrogen-Bond Cooperativity and Desolvation Energetics in the Biotin–(Strept)Avidin Binding Site. *J. Am. Chem. Soc.* **2007**, *129* (17), 5419-5429.
83. Friesner, R. A.; Guallar, V., Ab-initio Quantum Chemical and Mixed Quantum Mechanics/Molecular Mechanics (QM/MM) Methods for Studying Enzymatic Catalysis. *Annu. Rev. Phys. Chem.* **2005**, *56* (1), 389-427.
84. Akimov, A. V.; Prezhdo, O. V., Large-Scale Computations in Chemistry: A Bird’s Eye View of a Vibrant Field. *Chem. Rev.* **2015**, *115* (12), 5797-5890.
85. Hirayama, T.; Okaniwa, M.; Banno, H.; Kakei, H.; Ohashi, A.; Iwai, K.; Ohori, M.; Mori, K.; Gotou, M.; Kawamoto, T.; Yokota, A.; Ishikawa, T., Synthetic Studies on Centromere-Associated Protein-E (CENP-E) Inhibitors: 2. Application of Electrostatic Potential Map (EPM) and Structure-Based Modeling to Imidazo[1,2-

a]pyridine Derivatives as Anti-Tumor Agents. *J. Med. Chem.* **2015**, *58* (20), 8036-8053.

86. Jiang, D.; Chen, Z., *Graphene Chemistry: Theoretical Perspectives*. Wiley: 2013.
87. Janesko, B. G.; Wiberg, K. B.; Scalmani, G.; Frisch, M. J., Electron Delocalization Range in Atoms and on Molecular Surfaces. *J. Chem. Theory Comput.* **2016**, *12* (7), 3185-3194.
88. Mehmood, A.; Janesko, B. G., An Orbital-overlap Complement to Atomic Partial Charge. *Angew. Chem. Int. Ed.* **2017**, *56* (24), 6878-6881.
89. Janesko, B. G.; Scalmani, G.; Frisch, M. J., Quantifying Solvated Electrons' Delocalization. *Phys. Chem. Chem. Phys.* **2015**, *17* (28), 18305-18317.
90. Mehmood, A.; Jones, S. I.; Tao, P.; Janesko, B. G., An Orbital-Overlap Complement to Ligand and Binding Site Electrostatic Potential Maps. *J. Chem. Inf. Model.* **2018**, *58* (9), 1836-1846.
91. Mehmood, A.; Janesko, B. G., The Electron Delocalization Range in Stretched Bonds. *Int. J. Quantum Chem* **2016**, *116* (23), 1783-1795.
92. Janesko, B. G.; Scalmani, G.; Frisch, M. J., How Far Do Electrons Delocalize? *J. Chem. Phys.* **2014**, *141* (14), 144104.
93. Janesko, B. G.; Wiberg, K. B.; Scalmani, G.; Frisch, M. J., Electron Delocalization Range in Atoms and on Molecular Surfaces. *J. Chem. Theory Comput.* **2016**, *12* (7), 3185-3194.
94. Frisch, M. J.; Trucks, G. W.; Schlegel, H. B.; Scuseria, G. E.; Robb, M. A.; Cheeseman, J. R.; Scalmani, G.; Barone, V.; Petersson, G. A.; Nakatsuji, H.; Li, X.; Caricato, M.; Marenich, A. V.; Bloino, J.; Janesko, B. G.; Gomperts, R.; Mennucci, B.; Hratchian, H. P.; Ortiz, J. V.; Izmaylov, A. F.; Sonnenberg, J. L.; Williams; Ding, F.; Lipparini, F.; Egidi, F.; Goings, J.; Peng, B.; Petrone, A.; Henderson, T.; Ranasinghe, D.; Zakrzewski, V. G.; Gao, J.; Rega, N.; Zheng, G.; Liang, W.; Hada, M.; Ehara, M.; Toyota, K.; Fukuda, R.; Hasegawa, J.; Ishida, M.; Nakajima, T.; Honda, Y.; Kitao, O.; Nakai, H.; Vreven, T.; Throssell, K.; Montgomery Jr., J. A.; Peralta, J. E.; Ogliaro, F.; Bearpark, M. J.; Heyd, J. J.; Brothers, E. N.; Kudin, K. N.; Staroverov, V. N.; Keith, T. A.; Kobayashi, R.; Normand, J.; Raghavachari, K.; Rendell, A. P.; Burant, J. C.; Iyengar, S. S.; Tomasi, J.; Cossi, M.; Millam, J. M.; Klene, M.; Adamo, C.; Cammi, R.; Ochterski, J. W.; Martin, R. L.; Morokuma, K.; Farkas, O.; Foresman, J. B.; Fox, D. J. *Gaussian 16 Rev. C.01*, Wallingford, CT, 2016.

95. Lu, T.; Chen, F., Multiwfn: A Multifunctional Wavefunction Analyzer. *J. Comput. Chem.* **2012**, *33* (5), 580-592.
96. Bader, R. F. W.; Carroll, M. T.; Cheeseman, J. R.; Chang, C., Properties of Atoms in Molecules: Atomic Volumes. *J. Am. Chem. Soc.* **1987**, *109* (26), 7968-7979.
97. Bader, R. F. W.; Henneker, W. H.; Cade, P. E., Molecular Charge Distributions and Chemical Binding. *J. Chem. Phys.* **1967**, *46* (9), 3341-3363.
98. Pearson, R. G., Hard and Soft Acids and Bases. *J. Am. Chem. Soc.* **1963**, *85* (22), 3533-3539.
99. Pearson, R. G., Hard and Soft Acids and Bases, HSAB, Part 1: Fundamental Principles. *J. Chem. Educ.* **1968**, *45* (9), 581.
100. Pearson, R. G., Hard and Soft Acids and Bases, HSAB, Part II: Underlying Theories. *J. Chem. Educ.* **1968**, *45* (10), 643.
101. Pearson, R. G., Hard and Soft Acids and Bases-The Evolution of a Chemical Concept. *Coord. Chem. Rev.* **1990**, *100*, 403-425.
102. Boldyrev, A. I.; Wang, L.-S., All-Metal Aromaticity and Antiaromaticity. *Chem. Rev.* **2005**, *105* (10), 3716-3757.
103. Politzer, P.; Murray, J. S.; Clark, T., Halogen Bonding and Other σ -hole Interactions: A Perspective. *Phys. Chem. Chem. Phys.* **2013**, *15* (27), 11178-11189.
104. Shaik, S.; Danovich, D.; Silvi, B.; Lauvergnat, D. L.; Hiberty, P. C., Charge-Shift Bonding—A Class of Electron-Pair Bonds That Emerges from Valence Bond Theory and is Supported by the Electron Localization Function Approach. *Chem. Eur. J.* **2005**, *11* (21), 6358-6371.
105. Cohen, A. J.; Mori-Sánchez, P.; Yang, W., Challenges for Density Functional Theory. *Chem. Rev.* **2012**, *112* (1), 289-320.
106. Hollett, J. W.; McKemmish, L. K.; Gill, P. M. W., The Nature of Electron Correlation in a Dissociating Bond. *J. Chem. Phys.* **2011**, *134* (22), 224103.
107. Rassolov, V. A.; Ratner, M. A.; Pople, J. A., Electron Correlation in Chemical Bonds. *J. Chem. Phys.* **2000**, *112* (9), 4014-4019.
108. VandeVondele, J.; Sprik, M., A Molecular Dynamics Study of The Hydroxyl Radical in Solution Applying Self-Interaction-Corrected Density Functional Methods. *Phys. Chem. Chem. Phys.* **2005**, *7* (7), 1363-1367.

109. Hellgren, M.; Caruso, F.; Rohr, D. R.; Ren, X.; Rubio, A.; Scheffler, M.; Rinke, P., Static Correlation and Electron Localization in Molecular Dimers from the Self-Consistent RPA and GW Approximation. *Phys. Rev. B* **2015**, *91* (16), 165110.
110. Scuseria, G. E.; Schaefer, H. F., Diatomic Chromium (Cr₂): Application of the Coupled Cluster Method Including All Single and Double Excitation (CCSD). *Chem. Phys. Lett.* **1990**, *174* (5), 501-503.
111. Becke, A. D.; Roussel, M. R., Exchange Holes in Inhomogeneous Systems: A Coordinate-space Model. *Phys. Rev. A* **1989**, *39* (8), 3761-3767.
112. Gerratt, J.; Cooper, D. L.; Karadakov, P. B.; Raimondi, M., Modern Valence Bond Theory. *Chem. Soc. Rev.* **1997**, *26* (2), 87-100.
113. Mo, Y.; Song, L.; Wu, W.; Cao, Z.; Zhang, Q., Electronic Delocalization: A Quantitative Study from Modern Ab Initio Valence Bond Theory. *J. Theor. Comput. Chem.* **2002**, *01* (01), 137-151.
114. Mo, Y.; Peyerimhoff, S. D., Theoretical Analysis of Electronic Delocalization. *J. Chem. Phys.* **1998**, *109* (5), 1687-1697.
115. Foster, J. P.; Weinhold, F., Natural Hybrid Orbitals. *J. Am. Chem. Soc.* **1980**, *102* (24), 7211-7218.
116. Fulton, R. L., On the Delocalization of Electrons in Atoms and Molecules. *J. Phys. Chem. A* **2004**, *108* (52), 11691-11702.
117. Zubarev, D. Y.; Boldyrev, A. I., Developing Paradigms of Chemical Bonding: Adaptive Natural Density Partitioning. *Phys. Chem. Chem. Phys.* **2008**, *10* (34), 5207-5217.
118. Bader, R. F. W., A Quantum Theory of Molecular Structure and its Applications. *Chem. Rev.* **1991**, *91* (5), 893-928.
119. Wagner, K.; Kohout, M., Atomic Shell Structure Based on Inhomogeneity Measures of the Electron Density. *Theor. Chem. Acc.* **2010**, *128* (1), 39-46.
120. Scherer, W.; Sirsch, P.; Shorokhov, D.; Tafipolsky, M.; McGrady, G. S.; Gullo, E., Valence Charge Concentrations, Electron Delocalization and β -Agostic Bonding in d₀ Metal Alkyl Complexes. *Chem. Eur. J.* **2003**, *9* (24), 6057-6070.
121. de Silva, P.; Korchowiec, J.; Wesolowski, T. A., Revealing the Bonding Pattern from the Molecular Electron Density Using Single Exponential Decay Detector: An Orbital-free Alternative to the Electron Localization Function. *ChemPhysChem* **2012**, *13* (15), 3462-3465.

122. Mok, D. K. W.; Neumann, R.; Handy, N. C., Dynamical and Nondynamical Correlation. *J. Phys. Chem.* **1996**, *100* (15), 6225-6230.
123. Coulson, C. A.; Fischer, I., XXXIV. Notes on the Molecular Orbital Treatment of the Hydrogen Molecule. *Lond. Edinb. Dubl. Phil. Mag.* **1949**, *40* (303), 386-393.
124. Janesko, B. G., Topological Analysis of the Electron Delocalization Range. *J. Comput. Chem.* **2016**, *37* (21), 1993–2005.
125. Burdett, J. K.; McCormick, T. A., Electron Localization in Molecules and Solids: The Meaning of ELF. *J. Phys. Chem. A* **1998**, *102* (31), 6366-6372.
126. Ponec, R.; Cooper, D. L., Anatomy of Bond Formation. Bond Length Dependence of the Extent of Electron Sharing in Chemical Bonds. *J. Mol. Struc-THEOCHEM* **2005**, *727* (1–3), 133-138.
127. Fulton, R. L.; Mixon, S. T., Sharing of Electrons in Molecules: Basin-Basin and Basin-Point Sharing Indices for Some Simple Molecules. *J. Phys. Chem.* **1995**, *99* (24), 9768-9783.
128. Sandoval-Lira, J.; Hô, M.; Hernández-Esparza, R.; Ramírez, J. C.; Hernández-Pérez, J. M., Characterizing Off-diagonal Regions of One-electron Density Matrix. *Theor. Chem. Acc.* **2016**, *135* (6), 1-10.
129. Bowen, H. C.; Linnett, J. W., 195. Binding in the Hydrogen Molecule and its Ion. *J. Chem. Soc. (Resumed)* **1963**, (0), 1064-1068.
130. Coulson, C. A.; Bell, R. P., Kinetic Energy, Potential Energy and Force in Molecule Formation. *Trans. Faraday Soc.* **1945**, *41* (0), 141-149.
131. Schmidt, M. W.; Ivanic, J.; Ruedenberg, K., The Physical Origin of Covalent Bonding. In *The Chemical Bond*, Wiley-VCH Verlag GmbH & Co. KGaA: 2014; pp 1-68.
132. Walton, J. R.; Rivera–Rivera, L. A.; Lucchese, R. R.; Bevan, J. W., Canonical Approaches to Applications of the Virial Theorem. *J. Phys. Chem. A* **2016**, *120* (5), 817-823.
133. Bacskey, G. B.; Nordholm, S., Covalent Bonding: The Fundamental Role of the Kinetic Energy. *J. Phys. Chem. A* **2013**, *117* (33), 7946-7958.
134. Ruedenberg, K.; Schmidt, M. W., Why Does Electron Sharing Lead to Covalent Bonding? A Variational Analysis. *J. Comput. Chem.* **2007**, *28* (1), 391-410.
135. Wilson, C. W.; Goddard, W. A., The Role of Kinetic Energy in Chemical Binding. *Theor. Chim. Acta.* **1972**, *26* (3), 195-210.

136. Ruedenberg, K., The Physical Nature of the Chemical Bond. *Rev. Mod. Phys.* **1962**, *34*, 326-376.
137. Nordholm, S., Delocalization - The Key Concept of Covalent Bonding. *J. Chem. Educ.* **1988**, *65*, 581-584.
138. Bacsckay, G. B.; Nordholm, S., Covalent Bonding: The Fundamental Role of the Kinetic Energy. *J. Phys. Chem. A* **2013**, *117*, 7946-7958.
139. Ruedenberg, K., The Physical Nature of the Chemical Bond. *Rev. Mod. Phys.* **1962**, *34* (2), 326-376.
140. Cohen, A. J.; Mori-Sánchez, P.; Yang, W., Insights into Current Limitations of Density Functional Theory. *Science* **2008**, *321*, 792.
141. Luo, F.; McBane, G. C.; Kim, G.; Giese, C. F.; Gentry, W. R., The Weakest Bond: Experimental Observation of Helium Dimer. *J. Chem. Phys.* **1993**, *98* (4), 3564-3567.
142. García-Revilla, M.; Popelier, P. L. A.; Francisco, E.; Martín Pendás, Á., Nature of Chemical Interactions from the Profiles of Electron Delocalization Indices. *J. Chem. Theory Comput.* **2011**, *7* (6), 1704-1711.
143. Sanderson, R. T., An Interpretation of Bond Lengths and a Classification of Bonds. *Science* **1951**, *114* (2973), 670-672.
144. Perdew, J. P.; Parr, R. G.; Levy, M.; Balduz, J. L., Density-Functional Theory for Fractional Particle Number: Derivative Discontinuities of the Energy. *Phys. Rev. Lett.* **1982**, *49* (23), 1691-1694.
145. Shaik, S.; Maitre, P.; Sini, G.; Hiberty, P. C., The Charge-Shift Bonding Concept. Electron-Pair Bonds with Very Large Ionic-Covalent Resonance Energies. *J. Am. Chem. Soc.* **1992**, *114* (20), 7861-7866.
146. Rodríguez-Mayorga, M.; Ramos-Cordoba, E.; Salvador, P.; Solà, M.; Matito, E., Bonding Description of the Harpoon Mechanism. *Mol. Phys.* **2016**, *114* (7-8), 1345-1355.
147. Weiner, B.; Ohrn, Y., Correlated Electronic States of the Lithium Hydride Molecule Studied with the Polarization Propagator. *J. Phys. Chem.* **1987**, *91* (3), 563-570.
148. Mulliken, R. S., The Low Electronic States of Simple Heteropolar Diatomic Molecules. I. General Survey. *Phys. Rev.* **1936**, *50* (11), 1017-1027.
149. Frisch, M. J.; Trucks, G. W.; Schlegel, H. B.; Scuseria, G. E.; Robb, M. A.; Cheeseman, J. R.; Scalmani, G.; Barone, V.; Mennucci, B.; Petersson, G. A.;

- Nakatsuji, H.; Caricato, M.; Li, X.; Hratchian, H. P.; Izmaylov, A. F.; Bloino, J.; Janesko, B. G.; Lipparini, F.; Zheng, G.; Sonnenberg, J. L.; Liang, W.; Hada, M.; Ehara, M.; Toyota, K.; Fukuda, R.; Hasegawa, J.; Ishida, M.; Nakajima, T.; Honda, Y.; Kitao, O.; Nakai, H.; T. Vreven; J. A. Montgomery, J.; Peralta, J. E.; Ogliaro, F.; Bearpark, M.; Heyd, J. J.; Brothers, E.; Kudin, K. N.; Staroverov, V. N.; Keith, T.; Kobayashi, R.; Normand, J.; Raghavachari, K.; Rendell, A.; Burant, J. C.; Iyengar, S. S.; Cossi, J. T.; Rega, N.; Millam, J. M.; Klene, M.; Knox, J. E.; Cross, J. B.; Bakken, V.; Adamo, C.; Jaramillo, J.; Gomperts, R.; Stratmann, R. E.; Yazyev, O.; Austin, A. J.; Cammi, R.; Pomelli, C.; Ochterski, J. W.; Martin, R. L.; Morokuma, K.; Zakrzewski, V. G.; Voth, G. A.; Salvador, P.; Dannenberg, J. J.; Dapprich, S.; Parandekar, P. V.; Mayhall, N. J.; Daniels, A. D.; Farkas, O.; Foresman, J. B.; Ortiz, J. V.; Cioslowski, J.; Fox, D. J. *Gaussian Development Version, Revision H.35*, Gaussian, Inc., Wallingford CT.: 2010.
150. Hohenberg, P.; Kohn, W., Inhomogeneous Electron Gas. *Phys. Rev.* **1964**, *136* (3B), B864-B871.
151. Kohn, W.; Sham, L. J., Self-Consistent Equations Including Exchange and Correlation Effects. *Phys. Rev.* **1965**, *140* (4A), A1133-A1138.
152. Becke, A. D., Density-functional Exchange-energy Approximation with Correct Asymptotic Behavior. *Phys. Rev. A* **1988**, *38* (6), 3098-3100.
153. Perdew, J. P.; Wang, Y., Accurate and Simple Analytic Representation of the Electron-gas Correlation Energy. *Phys. Rev. B* **1992**, *45* (23), 13244-13249.
154. Becke, A. D., Density-Functional Thermochemistry. II. The Effect of the Perdew–Wang Generalized-Gradient Correlation Correction. *J. Chem. Phys.* **1992**, *97* (12), 9173-9177.
155. Stephens, P. J.; Devlin, F. J.; Chabalowski, C. F.; Frisch, M. J., Ab Initio Calculation of Vibrational Absorption and Circular Dichroism Spectra Using Density Functional Force Fields. *J. Phys. Chem.* **1994**, *98* (45), 11623-11627.
156. Seeger, R.; Pople, J. A., Self-consistent Molecular Orbital Methods. XVIII. Constraints and Stability in Hartree–Fock Theory. *J. Chem. Phys.* **1977**, *66* (7), 3045-3050.
157. Handy, N. C.; Schaefer, H. F., On the Evaluation of Analytic Energy Derivatives for Correlated Wavefunctions. *J. Chem. Phys.* **1984**, *81* (11), 5031-5033.
158. Wiberg, K. B.; Hadad, C. M.; LePage, T. J.; Breneman, C. M.; Frisch, M. J., Analysis of the Effect of Electron Correlation on Charge Density Distributions. *J. Phys. Chem.* **1992**, *96* (2), 671-679.

159. Dunning, T. H., Gaussian Basis Sets for Use in Correlated Molecular Calculations. I. The Atoms Boron Through Neon and Hydrogen. *J. Chem. Phys.* **1989**, *90* (2), 1007-1023.
160. Woon, D. E.; Dunning, T. H., Gaussian Basis Sets for Use in Correlated Molecular Calculations. IV. Calculation of Static Electrical Response Properties. *J. Chem. Phys.* **1994**, *100* (4), 2975-2988.
161. Bacskay, G. B., A Quadratically Convergent Hartree-Fock (QC-SCF) Method. Application to Closed Shell Systems. *Chem. Phys.* **1981**, *61* (3), 385-404.
162. Sanderson, R. T., Atomic Charges in Monosubstituted Benzenes. *Science* **1955**, *122* (3170), 598-599.
163. Sanderson, R. T., Partial Charges on Atoms in Organic Compounds. *Science* **1955**, *121* (3137), 207-208.
164. Sanderson, R. T., Electronegativities in Inorganic Chemistry. III. *J. Chem. Educ.* **1954**, *31* (5), 238.
165. Ferguson, L. N., *Electron Structures of Organic Molecules*. Prentice-Hall: New York, 1952.
166. Anslyn, E. V.; Dougherty, D. A., *Modern Physical Organic Chemistry*. University Science: 2006.
167. Chermette, H., Chemical Reactivity Indexes in Density Functional Theory. *J. Comput. Chem.* **1999**, *20* (1), 129-154.
168. Politzer, P.; Murray, J. S.; Concha, M. C., σ -hole Bonding Between Like atoms; A Fallacy of Atomic Charges. *J. Mol. Model.* **2008**, *14* (8), 659-665.
169. Kemnitz, C. R.; Mackey, J. L.; Loewen, M. J.; Hargrove, J. L.; Lewis, J. L.; Hawkins, W. E.; Nielsen, A. F., Origin of Stability in Branched Alkanes. *Chem. Eur. J.* **2010**, *16* (23), 6942-6949.
170. Hansch, C.; Leo, A.; Taft, R. W., A Survey of Hammett Substituent Constants and Resonance and Field Parameters. *Chem. Rev.* **1991**, *91* (2), 165-195.
171. Anderson, A. G.; Nelson, J. A., Electrophilic Substitution of Azulene. *J. Am. Chem. Soc.* **1950**, *72* (8), 3824-3825.
172. Brown, R. D., A Quantum-mechanical Investigation of the Azulene Molecule. Part I. *Trans. Faraday Soc.* **1948**, *44* (0), 984-987.

173. Kass, S. R., Cyclopropenyl Anion: An Energetically Nonaromatic Ion. *J. Org. Chem.* **2013**, *78* (14), 7370-7372.
174. Freeman, P. K.; George, D. E.; Rao, V. N. M., Factors Controlling the Reactions of Nortricyclyl and Dehydronorbornyl Chloride with Sodium and with Magnesium. *J. Org. Chem.* **1964**, *29* (7), 1682-1684.
175. Stille, J. K.; Sannes, K. N., Allylcarbinyl-cyclopropylcarbinyl Norbornenyl-nortricyclyl Anion Rearrangement. Evidence for a Symmetrical Intermediate. *J. Am. Chem. Soc.* **1972**, *94* (24), 8494-8496.
176. Sauers, R. R., A Computational Study of Proton and Electron Affinities. *Tetrahedron* **1999**, *55* (33), 10013-10026.
177. Li, L.; Janesko, B. G., 3-Methyleneisindolin-1-one Assembly via Base- and CuI/l-Proline-Catalyzed Domino Reaction: Mechanism of Regioselective Anionic Cyclization. *J. Org. Chem.* **2016**, *81* (22), 10802-10808.
178. Vasilevsky, S. F.; Mikhailovskaya, T. y. F.; Mamatyuk, V. I.; Salnikov, G. E.; Bogdanchikov, G. A.; Manoharan, M.; Alabugin, I. V., Tuning Selectivity of Anionic Cyclizations: Competition between 5-Exo and 6-Endo-Dig Closures of Hydrazides of o-Acetylenyl Benzoic Acids and Based-Catalyzed Fragmentation/Recyclization of the Initial 5-Exo-Dig Products. *J. Org. Chem.* **2009**, *74* (21), 8106-8117.
179. Li, L.; Wang, M.; Zhang, X.; Jiang, Y.; Ma, D., Assembly of Substituted 3-Methyleneisindolin-1-ones via a CuI/l-Proline-Catalyzed Domino Reaction Process of 2-Bromobenzamides and Terminal Alkynes. *Org. Lett.* **2009**, *11* (6), 1309-1312.
180. Haruta, M., When Gold Is Not Noble: Catalysis by Nanoparticles. *Chem. Rec.* **2003**, *3* (2), 75-87.
181. Häkkinen, H.; Yoon, B.; Landman, U.; Li, X.; Zhai, H.-J.; Wang, L.-S., On the Electronic and Atomic Structures of Small Au_N⁻ (N = 4–14) Clusters: A Photoelectron Spectroscopy and Density-Functional Study. *J. Phys. Chem. A* **2003**, *107* (32), 6168-6175.
182. Li, X.; Kiran, B.; Cui, L.-F.; Wang, L.-S., Magnetic Properties in Transition-Metal-Doped Gold Clusters: M@Au₆ (M = Ti, V, Cr). *Phys. Rev. Lett.* **2005**, *95* (25), 253401.
183. Yoon, B.; Häkkinen, H.; Landman, U.; Wörz, A. S.; Antonietti, J.-M.; Abbet, S.; Judai, K.; Heiz, U., Charging Effects on Bonding and Catalyzed Oxidation of CO on Au₈ Clusters on MgO. *Science* **2005**, *307* (5708), 403-407.

184. Kryachko, E. S.; Remacle, F., The Magic Gold Cluster Au₂₀. *Int. J. Quantum Chem* **2007**, *107* (14), 2922-2934.
185. Pyykkö, P., Theoretical Chemistry of Gold. II. *Inorg. Chim. Acta* **2005**, *358* (14), 4113-4130.
186. Furche, F.; Ahlrichs, R., Adiabatic Time-dependent Density Functional Methods for Excited State Properties. *J. Chem. Phys.* **2002**, *117* (16), 7433-7447.
187. Lin, L.; Claes, P.; Gruene, P.; Meijer, G.; Fielicke, A.; Nguyen, M. T.; Lievens, P., Far-Infrared Spectra of Yttrium-Doped Gold Clusters Au_nY (n = 1–9). *ChemPhysChem* **2010**, *11* (9), 1932-1943.
188. Yuan, D. W.; Wang, Y.; Zeng, Z., Geometric, Electronic, and Bonding Properties of Au_NM (N = 1–7, M = Ni, Pd, Pt) Clusters. *J. Chem. Phys.* **2005**, *122* (11), 114310.
189. Yuan, H. K.; Kuang, A. L.; Tian, C. L.; Chen, H., Structural and Electronic Properties of Au_n–xPt_x (n = 2–14; x ≤ n) Clusters: The Density Functional Theory Investigation. *AIP Advances* **2014**, *4* (3), 037107.
190. Zhang, M.; He, L.-M.; Zhao, L.-X.; Feng, X.-J.; Luo, Y.-H., Tuning Magnetic Moments by 3d Transition-Metal-Doped Au₆ Clusters. *J. Phys. Chem. C* **2009**, *113* (16), 6491-6496.
191. Li, Y.-F.; Kuang, X.-Y.; Wang, S.-J.; Zhao, Y.-R., Geometries, Stabilities, and Electronic Properties of Small Anion Mg-Doped Gold Clusters: A Density Functional Theory Study. *J. Phys. Chem. A* **2010**, *114* (43), 11691-11698.
192. Nhat, P. V.; Nguyen, M. T., Trends in Structural, Electronic and Energetic Properties of Bimetallic Vanadium-gold Clusters Au_nV with n = 1-14. *Phys. Chem. Chem. Phys.* **2011**, *13* (36), 16254-16264.
193. Zhang, M.; Zhang, H.; Zhao, L.; Li, Y.; Luo, Y., Low-Energy Isomer Identification, Structural Evolution, and Magnetic Properties in Manganese-Doped Gold Clusters MnAu_n (n = 1–16). *J. Phys. Chem. A* **2012**, *116* (6), 1493-1502.
194. Ruibin, D.; Xiaoshuang, C.; Huxian, Z.; Xiaofang, W.; Haibo, S.; Zonglin, D.; Lu, W., Structural, Electronic and Magnetic Properties of Ag_nFe Clusters (n ≤ 15): Local Magnetic Moment Interacting with Delocalized Electrons. *J. Phys. B: At., Mol. Opt. Phys.* **2011**, *44* (3), 035102.
195. Torres, M. B.; Fernández, E. M.; Balbás, L. C., Theoretical Study of Structural, Electronic, and Magnetic Properties of Au_nM⁺ Clusters (M = Sc, Ti, V, Cr, Mn, Fe, Au; n ≤ 9). *Phys. Rev. B* **2005**, *71* (15), 155412.

196. Torres, M. B.; Fernández, E. M.; Balbás, L. C., Theoretical Study of Oxygen Adsorption on Pure Au_{n+1}^+ and Doped MAu_n^+ Cationic Gold Clusters for $M = \text{Ti, Fe}$ and $n = 3-7$. *J. Phys. Chem. A* **2008**, *112* (29), 6678-6689.
197. Frisch, M. J.; Trucks, G. W.; Schlegel, H. B.; Scuseria, G. E.; Robb, M. A.; Cheeseman, J. R.; Scalmani, G.; Barone, V.; Mennucci, B.; Petersson, G. A.; Nakatsuji, H.; Caricato, M.; Li, X.; Hratchian, H. P.; Bloino, J.; Janesko, B. G.; Izmaylov, A. F.; Marenich, A.; Lipparini, F.; Zheng, G.; Sonnenberg, J. L.; Liang, W.; Hada, M.; Ehara, M.; Toyota, K.; Fukuda, R.; Hasegawa, J.; Ishida, M.; Nakajima, T.; Honda, Y.; Kitao, O.; Nakai, H.; Vreven, T.; Throssell, K.; Montgomery, J. A., Jr.; Peralta, J. E.; Ogliaro, F.; Bearpark, M.; Heyd, J. J.; Brothers, E.; Kudin, K. N.; Staroverov, V. N.; Keith, T.; Kobayashi, R.; Normand, J.; Raghavachari, K.; Rendell, A.; Burant, J. C.; Iyengar, S. S.; Tomasi, J.; Cossi, M.; Rega, N.; Millam, J. M.; Klene, M.; Knox, J. E.; Cross, J. B.; Bakken, V.; Adamo, C.; Jaramillo, J.; Gomperts, R.; Stratmann, R. E.; Yazyev, O.; Austin, A. J.; Cammi, R.; Pomelli, C.; Ochterski, J. W.; Martin, R. L.; Morokuma, K.; Zakrzewski, V. G.; Voth, G. A.; Salvador, P.; Dannenberg, J. J.; Dapprich, S.; Parandekar, P. V.; Mayhall, N. J.; Daniels, A. D.; Farkas, O.; Foresman, J. B.; Ortiz, J. V.; Cioslowski, J.; Fox, D. J. *Gaussian Development Version, Revision I.02+*; Gaussian, Inc.; Wallingford, CT, 2014.
198. Lee, C.; Yang, W.; Parr, R. G., Development of the Colle-Salvetti Correlation-energy Formula Into a Functional of the Electron Density. *Phys. Rev. B* **1988**, *37*, 785.
199. Miehlich, B.; Savin, A.; Stoll, H.; Preuss, H., Results Obtained With the Correlation Energy Density Functionals of Becke and Lee, Yang and Parr. *Chem. Phys. Lett.* **1989**, *157* (3), 200-206.
200. Iikura, H.; Tsuneda, T.; Yanai, T.; Hirao, K., A Long-Range Correction Scheme for Generalized-Gradient-Approximation Exchange Functionals. *J. Chem. Phys.* **2001**, *115* (8), 3540-3544.
201. Tomasi, J.; Mennucci, B.; Cammi, R., Quantum Mechanical Continuum Solvation Models. *Chem. Rev.* **2005**, *105* (8), 2999-3094.
202. Wang, Y.; Perdew, J. P., Correlation Hole of the Spin-Polarized Electron Gas, With Exact Small-Wave-Vector and High-Density Scaling. *Phys. Rev. B* **1991**, *44* (24), 13298-13307.
203. Wadt, W. R.; Hay, P. J., Ab Initio Effective Core Potentials for Molecular Calculations. Potentials for Main Group Elements Na To Bi. *J. Chem. Phys.* **1985**, *82* (1), 284-298.

204. Hay, P. J.; Wadt, W. R., Ab Initio Effective Core Potentials for Molecular Calculations. Potentials for K to Au Including the Outermost Core Orbitals. *J. Chem. Phys.* **1985**, *82* (1), 299-310.
205. Friesner, R. A.; Guallar, V., Ab-initio Quantum Chemical and Mixed Quantum Mechanics/Molecular Mechanics (QM/MM) Methods for Studying Enzymatic Catalysis. *Annu. Rev. Phys. Chem.* **2005**, *56*, 389-427.
206. Mendgen, T.; Steuer, C.; Klein, C. D., Privileged Scaffolds or Promiscuous Binders: A Comparative Study on Rhodanines and Related Heterocycles in Medicinal Chemistry. *J. Med. Chem.* **2012**, *55* (2), 743-753.
207. Paton, R. S.; Goodman, J. M., Hydrogen Bonding and π -Stacking: How Reliable are Force Fields? A Critical Evaluation of Force Field Descriptions of Nonbonded Interactions. *J. Chem. Inf. Model.* **2009**, *49* (4), 944-955.
208. Yilmazer, N. D.; Heitel, P.; Schwabe, T.; Korth, M., Benchmark of Electronic Structure Methods for Protein–Ligand Interactions Based on High-Level Reference Data. *J. Theor. Comput. Chem.* **2015**, *14* (01), 1540001.
209. Sherrill, C. D.; Sumpter, B. G.; Sinnokrot, M. O.; Marshall, M. S.; Hohenstein, E. G.; Walker, R. C.; Gould, I. R., Assessment of Standard Force Field Models Against High-quality Ab Initio Potential Curves for Prototypes of π - π , CH/ π , and SH/ π Interactions. *J. Comput. Chem.* **2009**, *30* (14), 2187-2193.
210. Ehrlich, S.; Göller, A. H.; Grimme, S., Towards full Quantum-Mechanics-based Protein–Ligand Binding Affinities. *ChemPhysChem* **2017**, *18* (8), 898-905.
211. Wheeler, R. A.; Spellmeyer, D. C., *Annual Reports in Computational Chemistry, Vol. 6*. Elsevier: 2010.
212. Leach, A. R.; Shoichet, B. K.; Peishoff, C. E., Prediction of Protein–ligand Interactions. Docking and Scoring: Successes and Gaps. *J. Med. Chem.* **2006**, *49* (20), 5851-5855.
213. Yan, Y.; Wang, W.; Sun, Z.; Zhang, J. Z. H.; Ji, C., Protein–ligand Empirical Interaction Components for Virtual Screening. *J. Chem. Inf. Model.* **2017**, *57* (8), 1793-1806.
214. Liu, Z.; Su, M.; Han, L.; Liu, J.; Yang, Q.; Li, Y.; Wang, R., Forging the Basis for Developing Protein–ligand Interaction Scoring Functions. *Acc. Chem. Res.* **2017**, *50* (2), 302-309.

215. Hirayama, T.; Okaniwa, M.; Imada, T.; Ohashi, A.; Ohori, M.; Iwai, K.; Mori, K.; Kawamoto, T.; Yokota, A.; Tanaka, T.; Ishikawa, T., Synthetic Studies of Centromere-associated Protein-E (CENP-E) Inhibitors: 1.Exploration of Fused Bicyclic Core Scaffolds Using Electrostatic Potential Map. *Bioorg. Med. Chem.* **2013**, *21* (17), 5488-5502.
216. Honig, B.; Nicholls, A., Classical Electrostatics in Biology and Chemistry. *Science* **1995**, *268* (5214), 1144-1149.
217. Zhu, X.; Yu, W.; McBride, R.; Li, Y.; Chen, L.-M.; Donis, R. O.; Tong, S.; Paulson, J. C.; Wilson, I. A., Hemagglutinin Homologue from H17N10 Bat Influenza Virus Exhibits Divergent Receptor-Binding and pH-Dependent Fusion Activities. *Proc. Natl. Acad. Sci. U.S.A* **2013**, *110* (4), 1458-1463.
218. Jagusch, C.; Negri, M.; Hille, U. E.; Hu, Q.; Bartels, M.; Jahn-Hoffmann, K.; Mendieta, M. A. E. P. B.; Rodenwaldt, B.; Müller-Vieira, U.; Schmidt, D.; Lauterbach, T.; Recanatini, M.; Cavalli, A.; Hartmann, R. W., Synthesis, Biological Evaluation and Molecular Modelling Studies of Methyleneimidazole Substituted Biaryls as Inhibitors of Human 17 α -hydroxylase-17,20-lyase (CYP17). Part I: Heterocyclic Modifications of the Core Structure. *Bioorg. Med. Chem.* **2008**, *16* (4), 1992-2010.
219. Holstein, J. J.; Hubschle, C. B.; Dittrich, B., Electrostatic Properties of Nine Fluoroquinolone Antibiotics Derived Directly from their Crystal Structure Refinements. *CrystEngComm* **2012**, *14* (7), 2520-2531.
220. Wandtke, C. M.; Lübben, J.; Dittrich, B., Molecular Electrostatic Potentials from Invariom Point Charges. *ChemPhysChem* **2016**, *17* (14), 2238-2246.
221. Bak, J. M.; Domagala, S.; Hubschle, C.; Jelsch, C.; Dittrich, B.; Dominiak, P. M., Verification of Structural and Electrostatic Properties Obtained by the Use of Different Pseudoatom Databases. *Acta Cryst. A* **2011**, *67* (2), 141-153.
222. Van Damme, S.; Bultinck, P., 3D QSAR Based on Conceptual DFT Molecular Fields: Antituberculosic Activity. *J. Mol. Stru-THEOCHEM* **2010**, *943* (1), 83-89.
223. Faver, J.; Merz, K. M., Utility of the Hard/Soft Acid–Base Principle via the Fukui Function in Biological Systems. *J. Chem. Theory Comput.* **2010**, *6* (2), 548-559.
224. Galanakis, D.; Davis, C. A.; Ganellin, C. R.; Dunn, P. M., Synthesis and Quantitative Structure–Activity Relationship of a Novel Series of Small Conductance Ca²⁺-Activated K⁺ Channel Blockers Related to Dequalinium. *J. Med. Chem.* **1996**, *39* (2), 359-370.

225. Bultinck, P.; Carbó-Dorca, R., Molecular Quantum Similarity Using Conceptual DFT Descriptors. *J. Chem. Sci* **2005**, *117* (5), 425-435.
226. Norbury, A. H.; Sinha, A. I. P., The Co-ordination of Ambidentate Ligands. *Q. Rev. Chem. Soc.* **1970**, *24* (1), 69-94.
227. Bayer, E. A.; Wilchek, M., Application of Avidin-Biotin Technology to Affinity-based Separations. *J. Chromatogr. A* **1990**, *510*, 3-11.
228. Wilchek, M.; Bayer, E. A., Avidin-Biotin Technology Ten Years On: Has it Lived up to its Expectations? *Trends Biochem. Sci.* **1989**, *14* (10), 408-412.
229. Green, N. M., Avidin. 1. The Use of [¹⁴C]biotin for Kinetic Studies and for Assay. *Biochem. J* **1963**, *89* (3), 585-591.
230. Livnah, O.; Bayer, E. A.; Wilchek, M.; Sussman, J. L., Three-dimensional Structures of Avidin and the Avidin-Biotin Complex. *Proc. Natl. Acad. Sci. U.S.A* **1993**, *90* (11), 5076-5080.
231. Rekharsky, M. V.; Mori, T.; Yang, C.; Ko, Y. H.; Selvapalam, N.; Kim, H.; Sobransingh, D.; Kaifer, A. E.; Liu, S.; Isaacs, L.; Chen, W.; Moghaddam, S.; Gilson, M. K.; Kim, K.; Inoue, Y., A Synthetic Host-Guest System Achieves Avidin-Biotin Affinity by Overcoming Enthalpy-Entropy Compensation. *Proc. Natl. Acad. Sci. U.S.A* **2007**, *104* (52), 20737-20742.
232. Qi, X.; Chan, W. L.; Read, R. J.; Zhou, A.; Carrell, R. W., Temperature-Responsive Release of Thyroxine and its Environmental Adaptation in Australians. *Proc. Royal Soc. B-Biol Sci* **2014**, *281* (1779).
233. Cheng, S.-Y.; Leonard, J. L.; Davis, P. J., Molecular Aspects of Thyroid Hormone Actions. *Endocrine Reviews* **2010**, *31* (2), 139-170.
234. Robbins, J., New Ideas in Thyroxine-Binding Globulin Biology. *J. Clin. Endocrinol. Metab.* **2000**, *85* (11), 3994-3995.
235. Zhou, A.; Wei, Z.; Read, R. J.; Carrell, R. W., Structural Mechanism for the Carriage and Release of Thyroxine in the Blood. *Proc. Natl. Acad. Sci. U.S.A* **2006**, *103* (36), 13321-13326.
236. Wei, W.; Sun, Y.; Zhu, M.; Liu, X.; Sun, P.; Wang, F.; Gui, Q.; Meng, W.; Cao, Y.; Zhao, J., Structural Insights and the Surprisingly Low Mechanical Stability of the Au-S Bond in the Gold-Specific Protein GolB. *J. Am. Chem. Soc.* **2015**, *137* (49), 15358-15361.

237. Checa, S. K.; Soncini, F. C., Bacterial Gold Sensing and Resistance. *BioMetals* **2011**, *24* (3), 419-427.
238. Checa, S. K.; Espariz, M.; Audero, M. E. P.; Botta, P. E.; Spinelli, S. V.; Soncini, F. C., Bacterial Sensing of and Resistance to Gold Salts. *Mol. Microbiol.* **2007**, *63* (5), 1307-1318.
239. Jian, X.; Wasinger, E. C.; Lockard, J. V.; Chen, L. X.; He, C., Highly Sensitive and Selective Gold(I) Recognition by a Metalloregulator in *Ralstonia Metallidurans*. *J. Am. Chem. Soc.* **2009**, *131* (31), 10869-10871.
240. Wei, W.; Zhu, T.; Wang, Y.; Yang, H.; Hao, Z.; Chen, P. R.; Zhao, J., Engineering a Gold-Specific Regulon for Cell-based Visual Detection and Recovery of Gold. *Chem. Sci.* **2012**, *3* (6), 1780-1784.
241. Pearson, R. G., Absolute Electronegativity and Hardness: Application to Inorganic Chemistry. *Inorg. Chem.* **1988**, *27* (4), 734-740.
242. Appel, M. J.; Bertozzi, C. R., Formylglycine, a Post-Translationally Generated Residue with Unique Catalytic Capabilities and Biotechnology Applications. *ACS Chem. Biol.* **2015**, *10* (1), 72-84.
243. Hudak, J. E.; Barfield, R. M.; de Hart, G. W.; Grob, P.; Nogales, E.; Bertozzi, C. R.; Rabuka, D., Synthesis of Heterobifunctional Protein Fusions Using Copper-Free Click Chemistry and the Aldehyde Tag. *Angew. Chem. Int. Ed.* **2012**, *51* (17), 4161-4165.
244. Meury, M.; Knop, M.; Seebeck, F. P., Structural Basis for Copper–Oxygen Mediated C–H Bond Activation by the Formylglycine-Generating Enzyme. *Angew. Chem. Int. Ed.* **2017**, *56* (28), 8115-8119.
245. Smith, E. L.; Giddens, J. P.; Iavarone, A. T.; Godula, K.; Wang, L.-X.; Bertozzi, C. R., Chemoenzymatic Fc Glycosylation via Engineered Aldehyde Tags. *Bioconjugate Chem.* **2014**, *25* (4), 788-795.
246. Carrico, I. S.; Carlson, B. L.; Bertozzi, C. R., Introducing Genetically Encoded Aldehydes into Proteins. *Nat. Chem. Biol.* **2007**, *3*, 321.
247. Rush, J. S.; Bertozzi, C. R., New Aldehyde Tag Sequences Identified by Screening Formylglycine Generating Enzymes in Vitro and in Vivo. *J. Am. Chem. Soc.* **2008**, *130* (37), 12240-12241.

248. Knop, M.; Engi, P.; Lemnar, R.; Seebeck, F. P., In Vitro Reconstitution of Formylglycine-Generating Enzymes Requires Copper(I). *ChemBioChem* **2015**, *16* (15), 2147-2150.
249. Schmidt, B.; Selmer, T.; Ingendoh, A.; Figurat, K. v., A Novel Amino Acid Modification in Sulfatases that is Defective in Multiple Sulfatase Deficiency. *Cell* **1995**, *82* (2), 271-278.
250. Dierks, T.; Dickmanns, A.; Preusser-Kunze, A.; Schmidt, B.; Mariappan, M.; von Figura, K.; Ficner, R.; Rudolph, M. G., Molecular Basis for Multiple Sulfatase Deficiency and Mechanism for Formylglycine Generation of the Human Formylglycine-Generating Enzyme. *Cell* **2005**, *121* (4), 541-552.
251. Knop, M.; Dang, T. Q.; Jeschke, G.; Seebeck, F. P., Copper is a Cofactor of the Formylglycine-Generating Enzyme. *ChemBioChem* **2017**, *18* (2), 161-165.
252. Solioz, M.; Odermatt, A., Copper and Silver Transport by CopB-ATPase in Membrane Vesicles of *Enterococcus Hirae*. *J. Biol. Chem.* **1995**, *270* (16), 9217-9221.
253. Petris, M. J.; Mercer, J. F.; Culvenor, J. G.; Lockhart, P.; Gleeson, P. A.; Camakaris, J., Ligand-regulated Transport of the Menkes Copper P-type ATPase Efflux Pump from the Golgi Apparatus to the Plasma Membrane: A Novel Mechanism of Regulated Trafficking. *EMBO J.* **1996**, *15* (22), 6084-6095.
254. Changela, A.; Chen, K.; Xue, Y.; Holschen, J.; Outten, C. E.; O'Halloran, T. V.; Mondragón, A., Molecular Basis of Metal-Ion Selectivity and Zeptomolar Sensitivity by CueR. *Science* **2003**, *301* (5638), 1383-1387.
255. Philips, S. J.; Canalizo-Hernandez, M.; Yildirim, I.; Schatz, G. C.; Mondragón, A.; O'Halloran, T. V., Allosteric Transcriptional Regulation via Changes in the Overall Topology of the Core Promoter. *Science* **2015**, *349* (6250), 877-881.
256. Rensing, C.; Fan, B.; Sharma, R.; Mitra, B.; Rosen, B. P., CopA: An *Escherichia coli* Cu(I)-translocating P-type ATPase. *Proc. Natl. Acad. Sci. U.S.A* **2000**, *97* (2), 652-656.
257. Lu, Z. H.; Solioz, M., Copper-induced Proteolysis of the CopZ Copper Chaperone of *Enterococcus Hirae*. *J. Biol. Chem.* **2001**, *276* (51), 47822-47827.
258. Gitschier, J.; Moffat, B.; Reilly, D.; Wood, W. I.; Fairbrother, W. J., Solution Structure of the Fourth Metal-binding Domain from the Menkes Copper-transporting ATPase. *Nat. Struct. Biol.* **1998**, *5*, 47.

259. Baell, J. B.; Holloway, G. A., New Substructure Filters for Removal of Pan Assay Interference Compounds (PAINS) from Screening Libraries and for Their Exclusion in Bioassays. *J. Med. Chem.* **2010**, *53* (7), 2719-2740.
260. Tomašić, T.; Peterlin Mašič, L., Rhodanine as a Scaffold in Drug Discovery: A Critical Review of its Biological Activities and Mechanisms of Target Modulation. *Expert Opin. Drug Discov.* **2012**, *7* (7), 549-560.
261. Nitsche, C.; Schreier, V. N.; Behnam, M. A. M.; Kumar, A.; Bartenschlager, R.; Klein, C. D., Thiazolidinone–Peptide Hybrids as Dengue Virus Protease Inhibitors with Antiviral Activity in Cell Culture. *J. Med. Chem.* **2013**, *56* (21), 8389-8403.
262. Gregory, L.; Armen, P.; Frederic, R. L., Trifluoromethyl Ethers and –Thioethers as Tools for Medicinal Chemistry and Drug Discovery. *Curr. Top. Med. Chem.* **2014**, *14* (7), 941-951.
263. Macrae, C. F.; Edgington, P. R.; McCabe, P.; Pidcock, E.; Shields, G. P.; Taylor, R.; Towler, M.; van de Streek, J., Mercury: Visualization and Analysis of Crystal Structures. *J. Appl. Crystallogr.* **2006**, *39* (3), 453-457.
264. D.A. Case, D. S. C., T.E. Cheatham, III, T.A. Darden, R.E. Duke, T.J. Giese, H. Gohlke, A.W. Goetz, D. Greene, N. Homeyer, S. Izadi, A. Kovalenko, T.S. Lee, S. LeGrand, P. Li, C. Lin, J. Liu, T. Luchko, R. Luo, D. Mermelstein, K.M. Merz, G. Monard, H. Nguyen, I. Omelyan, A. Onufriev, F. Pan, R. Qi, D.R. Roe, A. Roitberg, C. Sagui, C.L. Simmerling, W.M. Botello-Smith, J. Swails, R.C. Walker, J. Wang, R.M. Wolf, X. Wu, L. Xiao, D.M. York and P.A. Kollman *AMBER 2017*, AMBER 2017, University of California, San Francisco, 2017.
265. Frisch, M. J.; Trucks, G. W.; Schlegel, H. B.; Scuseria, G. E.; Robb, M. A.; Cheeseman, J. R.; Scalmani, G.; Barone, V.; Mennucci, B.; Petersson, G. A.; Nakatsuji, H.; Caricato, M.; Li, X.; Hratchian, H. P.; Izmaylov, A. F.; Bloino, J.; Zheng, G.; Sonnenberg, J. L.; Hada, M.; Ehara, M.; Toyota, K.; Fukuda, R.; Hasegawa, J.; Ishida, M.; Nakajima, T.; Honda, Y.; Kitao, O.; Nakai, H.; Vreven, T.; Montgomery Jr., J. A.; Peralta, J. E.; Ogliaro, F.; Bearpark, M. J.; Heyd, J.; Brothers, E. N.; Kudin, K. N.; Staroverov, V. N.; Kobayashi, R.; Normand, J.; Raghavachari, K.; Rendell, A. P.; Burant, J. C.; Iyengar, S. S.; Tomasi, J.; Cossi, M.; Rega, N.; Millam, N. J.; Klene, M.; Knox, J. E.; Cross, J. B.; Bakken, V.; Adamo, C.; Jaramillo, J.; Gomperts, R.; Stratmann, R. E.; Yazyev, O.; Austin, A. J.; Cammi, R.; Pomelli, C.; Ochterski, J. W.; Martin, R. L.; Morokuma, K.; Zakrzewski, V. G.; Voth, G. A.; Salvador, P.; Dannenberg, J. J.; Dapprich, S.;

- Daniels, A. D.; Farkas, Ö.; Foresman, J. B.; Ortiz, J. V.; Cioslowski, J.; Fox, D. J. *Gaussian 09*, Gaussian, Inc.: Wallingford, CT, USA, 2009.
266. Becke, A. D., Density-functional Thermochemistry. III. The Role of Exact Exchange. *J. Chem. Phys.* **1993**, *98* (7), 5648-5652.
267. Lee, C.; Yang, W.; Parr, R. G., Development of the Colle-Salvetti Correlation-energy Formula Into a Functional of the Electron Density. *Phys. Rev. B* **1988**, *37* (2), 785-789.
268. Vosko, S. H.; Wilk, L.; Nusair, M., Accurate Spin-dependent Electron Liquid Correlation Energies for Local Spin Density Calculations: A Critical Analysis. *Can. J. Phys.* **1980**, *58* (8), 1200-1211.
269. Stephens, P. J.; Devlin, F. J.; Chabalowski, C. F.; Frisch, M. J., Ab Initio Calculation of Vibrational Absorption and Circular Dichroism Spectra Using Density Functional Force Fields. *J. Phys. Chem.* **1994**, *98* (45), 11623-11627.
270. Barone, V.; Cossi, M., Quantum Calculation of Molecular Energies and Energy Gradients in Solution by a Conductor Solvent Model. *J. Phys. Chem. A* **1998**, *102* (11), 1995-2001.
271. Li, P.; Merz, K. M., MCPB.py: A Python Based Metal Center Parameter Builder. *J. Chem. Inf. Model.* **2016**, *56* (4), 599-604.
272. Maier, J. A.; Martinez, C.; Kasavajhala, K.; Wickstrom, L.; Hauser, K. E.; Simmerling, C., ff14SB: Improving the Accuracy of Protein Side Chain and Backbone Parameters from ff99SB. *J. Chem. Theory Comput.* **2015**, *11* (8), 3696-3713.
273. Jorgensen, W. L.; Madura, J. D., Quantum and Statistical Mechanical Studies of Liquids. 25. Solvation and Conformation of Methanol in Water. *J. Am. Chem. Soc.* **1983**, *105* (6), 1407-1413.
274. Zwanzig, R., Nonlinear Generalized Langevin Equations. *J. Stat. Phys.* **1973**, *9* (3), 215-220.
275. Miyamoto, S.; Kollman, P. A., Settle: An Analytical Version of the SHAKE and RATTLE Algorithm for Rigid Water Models. *J. Comput. Chem.* **1992**, *13* (8), 952-962.
276. Vreven, T.; Byun, K. S.; Komáromi, I.; Dapprich, S.; Montgomery, J. A.; Morokuma, K.; Frisch, M. J., Combining Quantum Mechanics Methods with Molecular Mechanics Methods in ONIOM. *J. Chem. Theory Comput.* **2006**, *2* (3), 815-826.

277. Chai, J.-D.; Head-Gordon, M., Long-range Corrected Hybrid Density Functionals With Damped Atom-Atom Dispersion Corrections. *Phys. Chem. Chem. Phys.* **2008**, *10* (44), 6615-6620.
278. Cornell, W. D.; Cieplak, P.; Bayly, C. I.; Gould, I. R.; Merz, K. M.; Ferguson, D. M.; Spellmeyer, D. C.; Fox, T.; Caldwell, J. W.; Kollman, P. A., A Second Generation Force Field for the Simulation of Proteins, Nucleic Acids, and Organic Molecules. *J. Am. Chem. Soc.* **1995**, *117* (19), 5179-5197.
279. Humphrey, W.; Dalke, A.; Schulten, K., VMD: Visual Molecular Dynamics. *J. Mol. Graph.* **1996**, *14* (1), 33-38.
280. Lewis, G. N., *Valence and the Structure of Atoms and Molecules*. Dover Publications: 1923.
281. Lewis, G. N., Acids and Bases. *J. Franklin Inst.* **1938**, *226* (3), 293-313.
282. Chen, T.; Hefter, G.; Marcus, Y., Relationships Among Solvent Softness Scales. *J. Solution Chem.* **2000**, *29* (3), 201-216.
283. Pearson, R. G., Acids and Bases. *Science* **1966**, *151* (3707), 172-177.
284. Reichardt, C.; Welton, T., *Solvents and Solvent Effects in Organic Chemistry*. Wiley: 2011.
285. Bogachev, N. A.; Gorbunov, A. O.; Tikhomirova, A. A.; Pushikhina, O. S.; Skripkin, M. Y.; Nikolskii, A. B., Solubility of d-elements Salts in Organic and Aqueous-organic Solvents: I. Copper, Cobalt, and Cadmium Sulfates. *Russ. J. Gen. Chem.* **2015**, *85* (11), 2509-2512.
286. Gorbunov, A. O.; Tsyruľnikov, N. A.; Tikhomirova, A. A.; Bogachev, N. A.; Skripkin, M. Y.; Nikolskii, A. B.; Pestova, O. N., Solubility of d-element Salts in Organic and Aqueous-organic Solvents: II. Effect of Halocomplex Formation on Solubility of Cobalt Bromide and Chloride and Nickel Chloride. *Russ. J. Gen. Chem.* **2016**, *86* (4), 771-777.
287. Payehghadr, M.; Hashemi, S. E., Solvent Effect on Complexation Reactions. *J. Incl. Phenom. Macrocycl. Chem.* **2017**, *89* (3), 253-271.
288. Claisen, L., Über C-Alkylierung (Kernalkylierung) von Phenolen. *Angew. Chem.* **1923**, *36* (65), 478-479.

289. Kornblum, N.; Berrigan, P. J.; le Noble, W. J., Chemical Effects Arising from Selective Solvation: Selective Solvation as a Factor in the Alkylation of Ambident Anions. *J. Am. Chem. Soc.* **1960**, *82* (5), 1257-1258.
290. Kornblum, N.; Berrigan, P. J.; Le Noble, W. J., Solvation as a Factor in the Alkylation of Ambident Anions: The Importance of the Hydrogen Bonding Capacity of the Solvent. *J. Am. Chem. Soc.* **1963**, *85* (8), 1141-1147.
291. Hughes, E. D.; Ingold, C. K., 55. Mechanism of Substitution at a Saturated Carbon Atom. Part IV. A Discussion of Constitutional and Solvent Effects on the Mechanism, Kinetics, Velocity, and Orientation of Substitution. *J. Chem. Soc. (Resumed)* **1935**, (0), 244-255.
292. Hughes, E. D., Mechanism and Kinetics of Substitution at a Saturated Carbon Atom. *Trans. Faraday Soc.* **1941**, *37* (0), 603-631.
293. Cooper, K. A.; Dhar, M. L.; Hughes, E. D.; Ingold, C. K.; MacNulty, B. J.; Woolf, L. I., 417. Mechanism of Elimination Reactions. Part VII. Solvent Effects on Rates and Product-proportions in uni- and bi-molecular Substitution and Elimination Reactions of Alkyl Halides and Sulphonium Salts in Hydroxylic Solvents. *J. Chem. Soc. (Resumed)* **1948**, (0), 2043-2049.
294. Greenwald, R.; Chaykovsky, M.; Corey, E. J., The Wittig Reaction Using Methylsulfinyl Carbanion-Dimethyl Sulfoxide 1. *J. Org. Chem.* **1963**, *28* (4), 1128-1129.
295. Laoire, C. O.; Mukerjee, S.; Abraham, K. M.; Plichta, E. J.; Hendrickson, M. A., Influence of Nonaqueous Solvents on the Electrochemistry of Oxygen in the Rechargeable Lithium–Air Battery. *J. Phys. Chem. C* **2010**, *114* (19), 9178-9186.
296. Marcus, Y., The Use of Chemical Probes for the Characterization of Solvent Mixtures. Part 2. Aqueous Mixtures. *J. Chem. Soc., Perkin Trans. 2* **1994**, (8), 1751-1758.
297. Allen, C. J.; Hwang, J.; Kautz, R.; Mukerjee, S.; Plichta, E. J.; Hendrickson, M. A.; Abraham, K. M., Oxygen Reduction Reactions in Ionic Liquids and the Formulation of a General ORR Mechanism for Li–Air Batteries. *J. Phys. Chem. C* **2012**, *116* (39), 20755-20764.
298. Peppel, T.; Köckerling, M.; Geppert-Rybczyńska, M.; Ralys, R. V.; Lehmann, J. K.; Verevkin, S. P.; Heintz, A., Low-Viscosity Paramagnetic Ionic Liquids with Doubly Charged $[\text{Co}(\text{NCS})_4]^{2-}$ Ions. *Angew. Chem. Int. Ed.* **2010**, *49* (39), 7116-7119.

299. Tsurumaki, A.; Trequattrini, F.; Palumbo, O.; Panero, S.; Paolone, A.; Navarra, M. A., The Effect of Ether-functionalisation in Ionic Liquids Analysed by DFT Calculation, Infrared Spectra, and Kamlet–Taft Parameters. *Phys. Chem. Chem. Phys.* **2018**, *20* (12), 7989-7997.
300. Tsurumaki, A.; Kagimoto, J.; Ohno, H., Properties of Polymer Electrolytes Composed of Poly(ethylene oxide) and Ionic Liquids According to Hard and Soft Acids and Bases Theory. *Polym. Adv. Technol.* **2011**, *22* (8), 1223-1228.
301. Marcus, Y., Linear Solvation Energy Relationships: A Scale Describing the "Softness" of Solvents. *J. Phys. Chem.* **1987**, *91* (16), 4422-4428.
302. Persson, I.; Sandström, M.; Goggin, P. L., On the Coordinating Properties of Some Solvents. A Vibrational Spectroscopic Study Of Mercury(II) Halides and Antimony(V) Chloride in Solution; New Concepts for Lewis Basicity Scales of Solvents. *Inorg. Chim. Acta* **1987**, *129* (2), 183-197.
303. Laurence, C.; Queignec-Cabanetos, M.; Dziembowska, T.; Queignec, R.; Wojtkowiak, B., 1-Iodoacetylenes. 1. Spectroscopic Evidence of Their Complexes with Lewis Bases. A Spectroscopic Scale of Soft Basicity. *J. Am. Chem. Soc.* **1981**, *103* (10), 2567-2573.
304. Gritzner, G., Solvent Effects on Half-wave Potentials. *J. Phys. Chem.* **1986**, *90* (21), 5478-5485.
305. Gutmann, V.; Wychera, E., Coordination Reactions in Non Aqueous Solutions - The role of the Donor Strength. *Inorg. Nucl. Chem. Letters* **1966**, *2* (9), 257-260.
306. Maria, P. C.; Gal, J. F., A Lewis Basicity Scale for Nonprotogenic Solvents: Enthalpies of Complex Formation with Boron Trifluoride in Dichloromethane. *J. Phys. Chem.* **1985**, *89* (7), 1296-1304.
307. Oshima, T.; Arikata, S.; Nagai, T., Solvent Effects in the Reaction of Diazodiphenylmethane with Tetracycanoethylene: a New Empirical Parameter of Solvent Basicity. *J. Chem. Res., Synop.* **1981**, 204-205.
308. Dong, D. C.; Winnik, M. A., The Py Scale of Solvent Polarities. Solvent Effects on The Vibronic Fine Structure of Pyrene Fluorescence and Empirical Correlations with Et And Y Values. *Photochem. Photobiol.* **1982**, *35* (1), 17-21.
309. Katritzky, A. R.; Tamm, T.; Wang, Y.; Sild, S.; Karelson, M., QSPR Treatment of Solvent Scales. *J. Chem. Inf. Comput. Sci.* **1999**, *39* (4), 684-691.

310. Gutmann, V., Empirical Parameters for Donor and Acceptor Properties of Solvents. *Electrochim. Acta* **1976**, *21* (9), 661-670.
311. Persson, I., Solvation and Complex Formation in Strongly Solvating Solvents. In *Pure Appl. Chem.*, 1986; Vol. 58, p 1153.
312. Sandström, M.; Persson, I.; Persson, P., A Study of Solvent Electron-pair Donor Ability and Lewis Basicity Scales. *Acta Chem. Scand* **1990**, *44* (7), 653-675.
313. Armand, M.; Endres, F.; MacFarlane, D. R.; Ohno, H.; Scrosati, B., Ionic-liquid Materials for the Electrochemical Challenges of the Future. *Nat. Mater* **2009**, *8*, 621.
314. Wilkes, J. S., A Short History of Ionic Liquids—From Molten Salts to Neoteric Solvents. *Green Chem.* **2002**, *4* (2), 73-80.
315. Van Aken, K. L.; Beidaghi, M.; Gogotsi, Y., Formulation of Ionic-Liquid Electrolyte To Expand the Voltage Window of Supercapacitors. *Angew. Chem. Int. Ed.* **2015**, *54* (16), 4806-4809.
316. Hayes, R.; Warr, G. G.; Atkin, R., Structure and Nanostructure in Ionic Liquids. *Chem. Rev.* **2015**, *115* (13), 6357-6426.
317. MacFarlane, D. R.; Tachikawa, N.; Forsyth, M.; Pringle, J. M.; Howlett, P. C.; Elliott, G. D.; Davis, J. H.; Watanabe, M.; Simon, P.; Angell, C. A., Energy Applications of Ionic Liquids. *Energy Environ. Sci.* **2014**, *7* (1), 232-250.
318. Zhao, Y.; Wang, J.; Wang, H.; Li, Z.; Liu, X.; Zhang, S., Is There Any Preferential Interaction of Ions of Ionic Liquids with DMSO and H₂O? A Comparative Study from MD Simulation. *J. Phys. Chem. B* **2015**, *119* (22), 6686-6695.
319. Dogonadze, R. R.; Kalman, E.; Kornyshev, A. A., *The Chemical Physics of Solvation: Theory of solvation*. Elsevier: 1985.
320. Anderson, J. L.; Ding, J.; Welton, T.; Armstrong, D. W., Characterizing Ionic Liquids On the Basis of Multiple Solvation Interactions. *J. Am. Chem. Soc.* **2002**, *124* (47), 14247-14254.
321. Fujii, K.; Fujimori, T.; Takamuku, T.; Kanzaki, R.; Umebayashi, Y.; Ishiguro, S.-i., Conformational Equilibrium of Bis(trifluoromethanesulfonyl) Imide Anion of a Room-Temperature Ionic Liquid: Raman Spectroscopic Study and DFT Calculations. *J. Phys. Chem. B* **2006**, *110* (16), 8179-8183.
322. Umebayashi, Y.; Fujimori, T.; Sukizaki, T.; Asada, M.; Fujii, K.; Kanzaki, R.; Ishiguro, S.-i., Evidence of Conformational Equilibrium of 1-Ethyl-3-

- methylimidazolium in Its Ionic Liquid Salts: Raman Spectroscopic Study and Quantum Chemical Calculations. *J. Phys. Chem. A* **2005**, *109* (40), 8976-8982.
323. Singh, D. K.; Cha, S.; Nam, D.; Cheong, H.; Joo, S.-W.; Kim, D., Raman Spectroscopic Study on Alkyl Chain Conformation in 1-Butyl-3-methylimidazolium Ionic Liquids and their Aqueous Mixtures. *ChemPhysChem* **2016**, *17* (19), 3040-3046.
324. Xu, A.; Zhang, Y.; Zhao, Y.; Wang, J., Cellulose Dissolution at Ambient Temperature: Role of Preferential Solvation of Cations of Ionic Liquids by a Cosolvent. *Carbohydr. Polym.* **2013**, *92* (1), 540-544.
325. Zhao, Y.; Liu, X.; Wang, J.; Zhang, S., Insight into the Cosolvent Effect of Cellulose Dissolution in Imidazolium-Based Ionic Liquid Systems. *J. Phys. Chem. B* **2013**, *117* (30), 9042-9049.
326. Gupta, K. M.; Jiang, J., Cellulose Dissolution and Regeneration in Ionic Liquids: A Computational Perspective. *Chem. Eng. Sci.* **2015**, *121*, 180-189.
327. Becke, A. D., A New Mixing of Hartree-Fock and Local Density-functional Theories. *J. Chem. Phys.* **1993**, *98* (2), 1372-1377.
328. Francel, M. M.; Pietro, W. J.; Hehre, W. J.; Binkley, J. S.; Gordon, M. S.; DeFrees, D. J.; Pople, J. A., Self-consistent Molecular Orbital Methods. XXIII. A Polarization-type Basis Set for Second-row Elements. *J. Chem. Phys.* **1982**, *77* (7), 3654-3665.
329. Hariharan, P. C.; Pople, J. A., Accuracy of AH n Equilibrium Geometries by Single Determinant Molecular Orbital Theory. *Mol. Phys.* **1974**, *27* (1), 209-214.
330. Hariharan, P. C.; Pople, J. A., The Influence of Polarization Functions on Molecular Orbital Hydrogenation Energies. *Theor. Chim. Acta.* **1973**, *28* (3), 213-222.
331. Hehre, W. J.; Ditchfield, R.; Pople, J. A., Self-Consistent Molecular Orbital Methods. XII. Further Extensions of Gaussian-Type Basis Sets for Use in Molecular Orbital Studies of Organic Molecules. *J. Chem. Phys.* **1972**, *56* (5), 2257-2261.
332. Ditchfield, R.; Hehre, W. J.; Pople, J. A., Self-Consistent Molecular-Orbital Methods. IX. An Extended Gaussian-Type Basis for Molecular-Orbital Studies of Organic Molecules. *J. Chem. Phys.* **1971**, *54* (2), 724-728.
333. Lu, T.; Chen, F., Quantitative Analysis of Molecular Surface Based on Improved Marching Tetrahedra Algorithm. *J. Mol. Graphics Modell.* **2012**, *38*, 314-323.
334. Banhart, F.; Kotakoski, J.; Krasheninnikov, A. V., Structural Defects in Graphene. *ACS Nano* **2011**, *5* (1), 26-41.

335. Eftekhari, A.; Garcia, H., The Necessity of Structural Irregularities for the Chemical Applications of Graphene. *Mater Today Chem.* **2017**, *4*, 1-16.
336. Raccichini, R.; Varzi, A.; Passerini, S.; Scrosati, B., The Role of Graphene for Electrochemical Energy Storage. *Nat. Mater* **2014**, *14*, 271.
337. Jia, Y.; Zhang, L.; Du, A.; Gao, G.; Chen, J.; Yan, X.; Brown, C. L.; Yao, X., Defect Graphene as a Trifunctional Catalyst for Electrochemical Reactions. *Adv. Mater.* **2016**, *28* (43), 9532-9538.
338. Xu, X.; Liu, C.; Sun, Z.; Cao, T.; Zhang, Z.; Wang, E.; Liu, Z.; Liu, K., Interfacial Engineering in Graphene Bandgap. *Chem. Soc. Rev.* **2018**, *47* (9), 3059-3099.
339. Bellunato, A.; Arjmandi Tash, H.; Cesa, Y.; Schneider, G. F., Chemistry at the Edge of Graphene. *ChemPhysChem* **2016**, *17* (6), 785-801.
340. Son, Y.-W.; Cohen, M. L.; Louie, S. G., Half-metallic Graphene Nanoribbons. *Nature* **2006**, *444* (7117), 347-349.
341. Robertson, A. W.; Allen, C. S.; Wu, Y. A.; He, K.; Olivier, J.; Neethling, J.; Kirkland, A. I.; Warner, J. H., Spatial Control of Defect Creation in Graphene at the Nanoscale. *Nat. Commun.* **2012**, *3*, 1144.
342. Cantele, G.; Lee, Y.-S.; Ninno, D.; Marzari, N., Spin Channels in Functionalized Graphene Nanoribbons. *Nano Lett.* **2009**, *9* (10), 3425-3429.
343. Ugeda, M. M.; Brihuega, I.; Hiebel, F.; Mallet, P.; Veuillen, J.-Y.; Gómez-Rodríguez, J. M.; Ynduráin, F., Electronic and Structural Characterization of Divacancies in Irradiated Graphene. *Phys. Rev. B* **2012**, *85* (12), 121402.
344. Ma, Y.; Lehtinen, P. O.; Foster, A. S.; Nieminen, R. M., Magnetic Properties of Vacancies in Graphene and Single-walled Carbon Nanotubes. *New J. Phys.* **2004**, *6*, 68-68.
345. Lehtinen, P. O.; Foster, A. S.; Ma, Y.; Krasheninnikov, A. V.; Nieminen, R. M., Irradiation-Induced Magnetism in Graphite: A Density Functional Study. *Phys. Rev. Lett.* **2004**, *93* (18), 187202.
346. Yazyev, O. V.; Helm, L., Defect-induced Magnetism in Graphene. *Phys. Rev. B* **2007**, *75* (12), 125408.
347. Pidatella, A.; Mazzarello, R., Defect-Induced Magnetism in Graphene: An Ab Initio Study. In *Correlations in Condensed Matter under Extreme Conditions: A Tribute to*

Renato Pucci on the Occasion of his 70th Birthday, Angilella, G. G. N.; La Magna, A., Eds. Springer International Publishing: Cham, 2017; pp 195-214.

348. Ni, Z. H.; Ponomarenko, L. A.; Nair, R. R.; Yang, R.; Anissimova, S.; Grigorieva, I. V.; Schedin, F.; Blake, P.; Shen, Z. X.; Hill, E. H.; Novoselov, K. S.; Geim, A. K., On Resonant Scatterers As a Factor Limiting Carrier Mobility in Graphene. *Nano Lett.* **2010**, *10* (10), 3868-3872.
349. Chen, J.-H.; Cullen, W. G.; Jang, C.; Fuhrer, M. S.; Williams, E. D., Defect Scattering in Graphene. *Phys. Rev. Lett.* **2009**, *102* (23), 236805.
350. Jing, N.; Xue, Q.; Ling, C.; Shan, M.; Zhang, T.; Zhou, X.; Jiao, Z., Effect of Defects on Young's Modulus of Graphene Sheets: A Molecular Dynamics Simulation. *RSC Adv.* **2012**, *2* (24), 9124-9129.
351. Thomas, S.; Mrudul, M. S.; Ajith, K. M.; Valsakumar, M. C., Young's Modulus of Defective Graphene Sheet from Intrinsic Thermal Vibrations. *J. Phys.: Conf. Ser.* **2016**, *759*, 012048.
352. Dettori, R.; Cadelano, E.; Colombo, L., Elastic Fields and Moduli in Defected Graphene. *J. Phys.: Condens. Matter* **2012**, *24* (10), 104020.
353. Kotakoski, J.; Meyer, J. C.; Kurasch, S.; Santos-Cottin, D.; Kaiser, U.; Krasheninnikov, A. V., Stone-Wales-type Transformations in Carbon Nanostructures Driven by Electron Irradiation. *Phys. Rev. B* **2011**, *83* (24), 245420.
354. Pantelides, S. T.; Puzyrev, Y.; Tsetseris, L.; Wang, B., Defects and Doping and their Role in Functionalizing Graphene. *MRS Bull.* **2012**, *37* (12), 1187-1194.
355. Boukhvalov, D. W.; Katsnelson, M. I., Chemical Functionalization of Graphene with Defects. *Nano Lett.* **2008**, *8* (12), 4373-4379.
356. Ci, L.; Song, L.; Jin, C.; Jariwala, D.; Wu, D.; Li, Y.; Srivastava, A.; Wang, Z. F.; Storr, K.; Balicas, L.; Liu, F.; Ajayan, P. M., Atomic Layers of Hybridized Boron Nitride and Graphene Domains. *Nat. Mater* **2010**, *9*, 430.
357. Cretu, O.; Krasheninnikov, A. V.; Rodríguez-Manzo, J. A.; Sun, L.; Nieminen, R. M.; Banhart, F., Migration and Localization of Metal Atoms on Strained Graphene. *Phys. Rev. Lett.* **2010**, *105* (19), 196102.
358. Lahiri, J.; Lin, Y.; Bozkurt, P.; Oleynik, I. I.; Batzill, M., An Extended Defect in Graphene as a Metallic Wire. *Nat. Nanotechnol.* **2010**, *5*, 326.

359. Carr, L. D.; Lusk, M. T., Graphene Gets Designer Defects. *Nat. Nanotechnol.* **2010**, *5*, 316.
360. Sarkar, S.; Bekyarova, E.; Niyogi, S.; Haddon, R. C., Diels–Alder Chemistry of Graphite and Graphene: Graphene as Diene and Dienophile. *J. Am. Chem. Soc.* **2011**, *133* (10), 3324-3327.
361. Cao, Y.; Osuna, S.; Liang, Y.; Haddon, R. C.; Houk, K. N., Diels–Alder Reactions of Graphene: Computational Predictions of Products and Sites of Reaction. *J. Am. Chem. Soc.* **2013**, *135* (46), 17643-17649.
362. Denis, P. A., Organic Chemistry of Graphene: The Diels–Alder Reaction. *Chem. Eur. J.* **2013**, *19* (46), 15719-15725.
363. Navalon, S.; Dhakshinamoorthy, A.; Alvaro, M.; Garcia, H., Carbocatalysis by Graphene-Based Materials. *Chem. Rev.* **2014**, *114* (12), 6179-6212.
364. Qi, W.; Su, D., Metal-Free Carbon Catalysts for Oxidative Dehydrogenation Reactions. *ACS Catal.* **2014**, *4* (9), 3212-3218.
365. Sahoo, S.; Suib, S. L.; Alpay, S. P., Graphene Supported Single Atom Transition Metal Catalysts for Methane Activation. *ChemCatChem* **2018**, *10* (15), 3229-3235.
366. Xu, L.; Yang, L.-M.; Ganz, E., Mn–graphene Single-atom Catalyst Evaluated for CO Oxidation by Computational Screening. *Theor. Chem. Acc.* **2018**, *137* (7), 98.
367. Ito, Y.; Cong, W.; Fujita, T.; Tang, Z.; Chen, M., High Catalytic Activity of Nitrogen and Sulfur Co-Doped Nanoporous Graphene in the Hydrogen Evolution Reaction. *Angew. Chem.* **2015**, *127* (7), 2159-2164.
368. Pykal, M.; Jurečka, P.; Karlický, F.; Otyepka, M., Modelling of Graphene Functionalization. *Phys. Chem. Chem. Phys.* **2016**, *18* (9), 6351-6372.
369. Wan, W.; Wang, H., First-Principles Investigation of Adsorption and Diffusion of Ions on Pristine, Defective and B-doped Graphene. *Mater. Corros.* **2015**, *8* (9), 163-6178.
370. Haldar, S.; Kolář, M.; Sedlák, R.; Hobza, P., Adsorption of Organic Electron Acceptors on Graphene-like Molecules: Quantum Chemical and Molecular Mechanical Study. *J. Phys. Chem. C* **2012**, *116* (48), 25328-25336.
371. Peralta-Inga, Z.; Murray, J. S.; Edward Grice, M.; Boyd, S.; O'Connor, C. J.; Politzer, P., Computational Characterization of Surfaces of Model Graphene Systems. *J. Mol. Stru-THEOCHEM* **2001**, *549* (1), 147-158.

372. Hernández Rosas, J. J.; Ramírez Gutiérrez, R. E.; Escobedo-Morales, A.; Chigo Anotá, E., First Principles Calculations of The Electronic and Chemical Properties of Graphene, Graphane, and Graphene Oxide. *J. Mol. Model.* **2011**, *17* (5), 1133-1139.
373. Cortés Arriagada, D., Global and Local Reactivity Indexes Applied to Understand the Chemistry of Graphene Oxide and Doped Graphene. *J. Mol. Model.* **2013**, *19* (2), 919-930.
374. Kudur Jayaprakash, G.; Swamy, B. E. K.; Casillas, N.; Flores-Moreno, R., Analytical Fukui and Cyclic Voltammetric Studies on Ferrocene Modified Carbon Electrodes and Effect of Triton X-100 by Immobilization Method. *Electrochim. Acta* **2017**, *258*, 1025-1034.
375. Jayaprakash, G. K.; Flores-Moreno, R., Quantum Chemical Study of Triton X-100 Modified Graphene Surface. *Electrochim. Acta* **2017**, *248*, 225-231.
376. Pašti, I. A.; Jovanović, A.; Dobrota, A. S.; Mentus, S. V.; Johansson, B.; Skorodumova, N. V., Atomic Adsorption on Graphene with a Single Vacancy: Systematic DFT Study Through the Periodic Table of Elements. *Phys. Chem. Chem. Phys.* **2018**, *20* (2), 858-865.
377. Fair, K. M.; Cui, X. Y.; Li, L.; Shieh, C. C.; Zheng, R. K.; Liu, Z. W.; Delley, B.; Ford, M. J.; Ringer, S. P.; Stampfl, C., Hydrogen Adsorption Capacity of Adatoms on Double Carbon Vacancies of Graphene: A Trend Study from First Principles. *Phys. Rev. B* **2013**, *87* (1), 014102.
378. Zhou, L.-J.; Hou, Z. F.; Wu, L.-M., First-Principles Study of Lithium Adsorption and Diffusion on Graphene with Point Defects. *J. Phys. Chem. C* **2012**, *116* (41), 21780-21787.
379. Gürel, H. H.; Özçelik, V. O.; Ciraci, S., Dissociative Adsorption of Molecules on Graphene and Silicene. *J. Phys. Chem. C* **2014**, *118* (47), 27574-27582.
380. Esrafilı, M. D.; Mohammad-Valipour, R.; Mousavi-Khoshdel, S. M.; Nematollahi, P., A Comparative Study of CO Oxidation on Nitrogen- and Phosphorus-Doped Graphene. *ChemPhysChem* **2015**, *16* (17), 3719-3727.
381. Kropp, T.; Mavrikakis, M., Transition Metal Atoms Embedded in Graphene: How Nitrogen Doping Increases CO Oxidation Activity. *ACS Catal.* **2019**, 6864-6868.
382. Cordero, B.; Gómez, V.; Platero-Prats, A. E.; Revés, M.; Echeverría, J.; Cremades, E.; Barragán, F.; Alvarez, S., Covalent Radii Revisited. *Dalton Trans.* **2008**, (21), 2832-2838.

383. Jiang, K.; Siahrostami, S.; Zheng, T.; Hu, Y.; Hwang, S.; Stavitski, E.; Peng, Y.; Dynes, J.; Gangisetty, M.; Su, D.; Attenkofer, K.; Wang, H., Isolated Ni Single Atoms in Graphene Nanosheets for High-performance CO₂ Reduction. *Energy Environ. Sci.* **2018**, *11* (4), 893-903.
384. Zhao, Y.; Truhlar, D. G., The M06 Suite of Density Functionals for Main Group Thermochemistry, Thermochemical Kinetics, Noncovalent Interactions, Excited States, and Transition Elements: Two New Functionals and Systematic Testing of Four M06-Class Functionals and 12 Other Functionals. *Theor. Chem. Acc.* **2008**, *120* (1), 215-241.
385. Weigend, F.; Ahlrichs, R., Balanced Basis Sets of Split Valence, Triple Zeta Valence and Quadruple Zeta Valence Quality for H to Rn: Design and Assessment of Accuracy. *Phys. Chem. Chem. Phys.* **2005**, *7* (18), 3297-3305.
386. Brinck, T.; Murray, J. S.; Politzer, P., Surface Electrostatic Potentials of Halogenated Methanes as Indicators of Directional Intermolecular Interactions. *Int. J. Quantum Chem* **1992**, *44* (S19), 57-64.
387. Clark, T.; Hennemann, M.; Murray, J. S.; Politzer, P., Halogen Bonding: The sigma-hole. Proceedings of "Modeling Interactions in Biomolecules II", Prague, September 5th-9th, 2005. *J. Mol. Model.* **2007**, *13* (2), 291-6.
388. Politzer, P.; Murray, J. S.; Clark, T.; Resnati, G., The σ -hole Revisited. *Phys. Chem. Chem. Phys.* **2017**, *19* (48), 32166-32178.
389. Metrangolo, P.; Murray, J. S.; Pilati, T.; Politzer, P.; Resnati, G.; Terraneo, G., Fluorine-Centered Halogen Bonding: A Factor in Recognition Phenomena and Reactivity. *Cryst. Growth Des.* **2011**, *11* (9), 4238-4246.
390. Politzer, P.; Murray, J. S., Halogen Bonding and Beyond: Factors Influencing the Nature of CN-R and SiN-R Complexes with F-Cl and Cl₂. *Theor. Chem. Acc.* **2012**, *131* (2), 1114.
391. Mukherjee, A.; Tothadi, S.; Desiraju, G. R., Halogen Bonds in Crystal Engineering: Like Hydrogen Bonds yet Different. *Acc. Chem. Res.* **2014**, *47* (8), 2514-2524.
392. Politzer, P.; Murray, J. S.; Clark, T., Halogen Bonding: An Electrostatically-driven Highly Directional Noncovalent Interaction. *Phys. Chem. Chem. Phys.* **2010**, *12* (28), 7748-7757.
393. Murray, J. S.; Riley, K. E.; Politzer, P.; Clark, T., Directional Weak Intermolecular Interactions: σ -hole Bonding. *Aust. J. Chem.* **2010**, *63* (12), 1598-1607.

394. Murray-Rust, P.; Motherwell, W. D. S., Computer Retrieval and Analysis of Molecular Geometry. 4. Intermolecular Interactions. *J. Am. Chem. Soc.* **1979**, *101* (15), 4374-4376.
395. Murray-Rust, P.; Stallings, W. C.; Monti, C. T.; Preston, R. K.; Glusker, J. P., Intermolecular Interactions of the Carbon-fluorine Bond: The Crystallographic Environment of Fluorinated Carboxylic Acids and Related Structures. *J. Am. Chem. Soc.* **1983**, *105* (10), 3206-3214.
396. Ramasubbu, N.; Parthasarathy, R.; Murray-Rust, P., Angular Preferences of Intermolecular Forces Around Halogen Centers: Preferred Directions of Approach of Electrophiles and Nucleophiles Around Carbon-Halogen Bond. *J. Am. Chem. Soc.* **1986**, *108* (15), 4308-4314.
397. Desiraju, G. R.; Parthasarathy, R., The Nature of Halogen...Halogen Interactions: Are Short Halogen Contacts Due to Specific Attractive Forces or Due to Close Packing of Non-spherical Atoms? *J. Am. Chem. Soc.* **1989**, *111* (23), 8725-8726.
398. Lu, Y.; Zou, J.; Wang, H.; Yu, Q.; Zhang, H.; Jiang, Y., Triangular Halogen Trimers. A DFT Study of the Structure, Cooperativity, and Vibrational Properties. *J. Phys. Chem. A* **2005**, *109* (51), 11956-11961.
399. Wang, F.-F.; Hou, J.-H.; Li, Z.-R.; Wu, D.; Li, Y.; Lu, Z.-Y.; Cao, W.-L., Unusual Halogen-bonded complex $\text{FBr}^{\delta+}\cdots\delta+\text{BrF}$ and Hydrogen-bonded Complex $\text{FBr}^{\delta+}\cdots\delta+\text{HF}$ Formed by Interactions Between Two Positively Charged Atoms of Different Polar Molecules. *J. Chem. Phys.* **2007**, *126* (14), 144301.
400. Eskandari, K.; Lesani, M., Does Fluorine Participate in Halogen Bonding? *Chem. Eur. J.* **2015**, *21* (12), 4739-4746.
401. Riley, K. E.; Murray, J. S.; Politzer, P.; Concha, M. C.; Hobza, P., $\text{Br}\cdots\text{O}$ Complexes as Probes of Factors Affecting Halogen Bonding: Interactions of Bromobenzenes and Bromopyrimidines with Acetone. *J. Chem. Theory Comput.* **2009**, *5* (1), 155-163.
402. Politzer, P.; Murray, J. S.; Concha, M. C., Halogen Bonding and the Design of New Materials: Organic Bromides, Chlorides and Perhaps Even Fluorides as Donors. *J. Mol. Model.* **2007**, *13* (6), 643-650.
403. Valerio, G.; Raos, G.; Meille, S. V.; Metrangolo, P.; Resnati, G., Halogen Bonding in Fluoroalkylhalides: A Quantum Chemical Study of Increasing Fluorine Substitution. *J. Phys. Chem. A* **2000**, *104* (8), 1617-1620.

404. Lim, J. Y. C.; Beer, P. D., Sigma-Hole Interactions in Anion Recognition. *Chem* **2018**, *4* (4), 731-783.
405. Wang, W.; Ji, B.; Zhang, Y., Chalcogen Bond: A Sister Noncovalent Bond to Halogen Bond. *J. Phys. Chem. A* **2009**, *113* (28), 8132-8135.
406. Brezgunova, M. E.; Lieffrig, J.; Aubert, E.; Dahaoui, S.; Fertey, P.; Lebègue, S.; Ángyán, J. G.; Fourmigué, M.; Espinosa, E., Chalcogen Bonding: Experimental and Theoretical Determinations from Electron Density Analysis. Geometrical Preferences Driven by Electrophilic–Nucleophilic Interactions. *Cryst. Growth Des.* **2013**, *13* (8), 3283-3289.
407. Del Bene, J. E.; Alkorta, I.; Sanchez-Sanz, G.; Elguero, J., Structures, Energies, Bonding, and NMR Properties of Pnicogen Complexes $H_2XP:NXH_2$ ($X = H, CH_3, NH_2, OH, F, Cl$). *J. Phys. Chem. A* **2011**, *115* (46), 13724-13731.
408. Zahn, S.; Frank, R.; Hey-Hawkins, E.; Kirchner, B., Pnicogen Bonds: A New Molecular Linker? *Chem. Eur. J.* **2011**, *17* (22), 6034-6038.
409. Scheiner, S., The Pnicogen Bond: Its Relation to Hydrogen, Halogen, and Other Noncovalent Bonds. *Acc. Chem. Res.* **2013**, *46* (2), 280-288.
410. Bauzá, A.; Mooibroek, T. J.; Frontera, A., Tetrel-Bonding Interaction: Rediscovered Supramolecular Force? *Angew. Chem. Int. Ed.* **2013**, *52* (47), 12317-12321.
411. Stenlid, J. H.; Johansson, A. J.; Brinck, T., σ -holes on Transition Metal Nanoclusters and Their Influence on the Local Lewis Acidity. *Crystals* **2017**, *7* (7), 222.
412. Stenlid, J. H.; Brinck, T., Extending the σ -hole Concept to Metals: An Electrostatic Interpretation of the Effects of Nanostructure in Gold and Platinum Catalysis. *J. Am. Chem. Soc.* **2017**, *139* (32), 11012-11015.
413. Shields, Z. P.; Murray, J. S.; Politzer, P., Directional Tendencies of Halogen and Hydrogen bonds. *Int. J. Quantum Chem* **2010**, *110* (15), 2823-2832.
414. Duarte, D. J. R.; Sosa, G. L.; Peruchena, N. M.; Alkorta, I., Halogen Bonding. The Role of the Polarizability of the Electron-pair Donor. *Phys. Chem. Chem. Phys.* **2016**, *18* (10), 7300-7309.
415. Clark, T.; Politzer, P.; Murray, J. S., Correct Electrostatic Treatment of Noncovalent Interactions: The Importance of Polarization. *Wiley Interdiscip. Rev. Comput. Mol. Sci.* **2015**, *5* (2), 169-177.

416. Pinter, B.; Nagels, N.; Herrebout, W. A.; De Proft, F., Halogen Bonding from a Hard and Soft Acids and Bases Perspective: Investigation by Using Density Functional Theory Reactivity Indices. *Chem. Eur. J.* **2013**, *19* (2), 519-530.
417. Syzgantseva, O. A.; Tognetti, V.; Joubert, L., On the Physical Nature of Halogen Bonds: A QTAIM Study. *J. Phys. Chem. A* **2013**, *117* (36), 8969-8980.
418. Grabowski, S. J., QTAIM Characteristics of Halogen Bond and Related Interactions. *J. Phys. Chem. A* **2012**, *116* (7), 1838-1845.
419. Sjoberg, P.; Murray, J. S.; Brinck, T.; Politzer, P., Average Local Ionization Energies on the Molecular Surfaces of Aromatic Systems as Guides to Chemical Reactivity. *Can. J. Chem.* **1990**, *68* (8), 1440-1443.
420. Foroutan-Nejad, C.; Shahbazian, S.; Marek, R., Toward a Consistent Interpretation of the QTAIM: Tortuous Link between Chemical Bonds, Interactions, and Bond/Line Paths. *Chem. Eur. J.* **2014**, *20* (32), 10140-10152.
421. Wang, W.; Wong, N.-B.; Zheng, W.; Tian, A., Theoretical Study on the Blueshifting Halogen Bond. *J. Phys. Chem. A* **2004**, *108* (10), 1799-1805.
422. Del Bene, J. E.; Alkorta, I.; Elguero, J., Do Traditional, Chlorine-shared, and Ion-pair Halogen Bonds Exist? An Ab Initio Investigation of FCl:CNX Complexes. *J. Phys. Chem. A* **2010**, *114* (49), 12958-12962
423. Schrödinger, E., Quantisierung als Eigenwertproblem I. *Ann. Phys. (Berl.)* **1926**, *384* (4), 361-376.
424. Schrödinger, E., Quantisierung als Eigenwertproblem II. *Ann. Phys. (Berl.)* **1926**, *384* (6), 489-527.
425. Schrödinger, E., Quantisierung als Eigenwertproblem III. *Ann. Phys. (Berl.)* **1926**, *385* (13), 437-490.
426. Szabo, A.; Ostlund, N. S., *Modern Quantum Chemistry: Introduction to Advanced Electronic Structure Theory*. McGraw-Hill: New York, 1989.
427. Born, M.; Oppenheimer, R., Zur Quantentheorie der Molekeln. *Ann. Phys. (Berl.)* **1927**, *389* (20), 457-484.
428. Dirac, P. A. M., A New Notation for Quantum Mechanics. *Math. Proc. Cambridge Philos. Soc.* **1939**, *35* (3), 416-418.
429. Hartree, D. R., *The Calculation of Atomic Structures*. J. Wiley & Sons: New York, 1957.

430. McQuarrie, D. A., *Quantum Chemistry*. University Science Books: California, 2008.
431. Hartree, D. R., The Wave Mechanics of an Atom with a Non-Coulomb Central Field. Part I. Theory and Methods. *Math. Proc. Cambridge Philos. Soc.* **1928**, *24* (1), 89-110.
432. Hartree, D. R., The Wave Mechanics of an Atom with a Non-Coulomb Central Field. Part II. Some Results and Discussion. *Math. Proc. Cambridge Philos. Soc.* **1928**, *24* (1), 111-132.
433. Slater, J. C., The Theory of Complex Spectra. *Phys. Rev.* **1929**, *34* (10), 1293-1322.
434. Dirac, P. A. M.; Fowler, R. H., On the Theory of Quantum Mechanics. *P. Roy. Soc. A - Math Phy.* **1926**, *112* (762), 661-677.
435. Roothaan, C. C. J., New Developments in Molecular Orbital Theory. *Rev. Mod. Phys.* **1951**, *23* (2), 69-89.
436. Hall, G. G.; Lennard-Jones, J. E., The Molecular Orbital Theory of Chemical Valency VIII. A Method of Calculating Ionization Potentials. *P. Roy. Soc. A - Math Phy.* **1951**, *205* (1083), 541-552.
437. Blinder, S. M., Chapter 1 - Introduction to the Hartree-Fock method. In *Mathematical Physics in Theoretical Chemistry*, Blinder, S. M.; House, J. E., Eds. Elsevier: 2019; pp 1-30.
438. Jensen, F., *Introduction to Computational Chemistry*. 2nd ed.; Wiley: 2007.
439. Leszczynski, J., *Handbook of Computational Chemistry*. Springer: 2012.
440. David Sherrill, C.; Schaefer, H. F., The Configuration Interaction Method: Advances in Highly Correlated Approaches. In *Adv. Quantum Chem.*, Löwdin, P.-O.; Sabin, J. R.; Zerner, M. C.; Brändas, E., Eds. Academic Press: 1999; Vol. 34, pp 143-269.
441. Spellmeyer, D., *Annual Reports in Computational Chemistry*. Elsevier Science: 2005.
442. van Dam, H. J. J.; van Lenthe, J. H.; Ruttink, P. J. A., Exact Size Consistency of Multireference Møller–Plesset Perturbation Theory. *Int. J. Quantum Chem* **1999**, *72* (6), 549-558.
443. Helgaker, T.; Jorgensen, P.; Olsen, J., *Molecular Electronic-Structure Theory*. Wiley: 2014.
444. Møller, C.; Plesset, M. S., Note on an Approximation Treatment for Many-Electron Systems. *Phys. Rev.* **1934**, *46* (7), 618-622.

445. Jambrina, P. G.; Aldegunde, J., Chapter 20 - Computational Tools for the Study of Biomolecules. In *Computer Aided Chemical Engineering*, Martín, M.; Eden, M. R.; Chemmangattuvalappil, N. G., Eds. Elsevier: 2016; Vol. 39, pp 583-648.
446. Grimme, S., Improved Second-order Møller–Plesset Perturbation Theory by Separate Scaling of Parallel- and Antiparallel-spin Pair Correlation Energies. *J. Chem. Phys.* **2003**, *118* (20), 9095-9102.
447. Del Ben, M.; Hutter, J.; VandeVondele, J., Second-Order Møller–Plesset Perturbation Theory in the Condensed Phase: An Efficient and Massively Parallel Gaussian and Plane Waves Approach. *J. Chem. Theory Comput.* **2012**, *8* (11), 4177-4188.
448. Walker, R. C.; Goetz, A. W., *Electronic Structure Calculations on Graphics Processing Units: From Quantum Chemistry to Condensed Matter Physics*. Wiley: 2016.
449. III, G. D. P.; Bartlett, R. J., A Full Coupled-cluster Singles and Doubles Model: The Inclusion of Disconnected Triples. *J. Chem. Phys.* **1982**, *76* (4), 1910-1918.
450. Shavitt, I.; Bartlett, R. J., *Many-Body Methods in Chemistry and Physics: MBPT and Coupled-Cluster Theory*. Cambridge University Press: 2009.
451. Hohenstein, E. G.; Sherrill, C. D., Wavefunction Methods for Noncovalent Interactions. *Wiley Interdiscip. Rev. Comput. Mol. Sci.* **2012**, *2* (2), 304-326.
452. Raghavachari, K.; Trucks, G. W.; Pople, J. A.; Head-Gordon, M., A Fifth-Order Perturbation Comparison of Electron Correlation Theories. *Chem. Phys. Lett.* **1989**, *157* (6), 479-483.
453. Staroverov, V. N., Density-Functional Approximations for Exchange and Correlation. In *A Matter of Density*, Sukumar, N., Ed. Wiley: 2012; pp 125-156.
454. Scuseria, G. E.; Staroverov, V. N., Chapter 24 - Progress in the Development of Exchange-correlation Functionals. In *Theory and Applications of Computational Chemistry*, Dykstra, C. E.; Frenking, G.; Kim, K. S.; Scuseria, G. E., Eds. Elsevier: Amsterdam, 2005; pp 669-724.
455. Filatov, M.; Thiel, W., A New Gradient-corrected Exchange-correlation Density Functional. *Mol. Phys.* **1997**, *91* (5), 847-860.
456. Perdew, J. P.; Chevary, J. A.; Vosko, S. H.; Jackson, K. A.; Pederson, M. R.; Singh, D. J.; Fiolhais, C., Atoms, Molecules, Solids, and Surfaces: Applications of the Generalized Gradient Approximation for Exchange and Correlation. *Phys. Rev. B* **1992**, *46* (11), 6671-6687.

457. Perdew, J. P., In *Electronic Structure of Solids '91*, Ziesche, P.; Eschrig, H., Eds. Akademie Verlag: Berlin, 1991.
458. Perdew, J. P., Density-functional Approximation for the Correlation Energy of the Inhomogeneous Electron Gas. *Phys. Rev. B* **1986**, *33* (12), 8822-8824.
459. Perdew, J. P.; Burke, K.; Ernzerhof, M., Generalized Gradient Approximation Made Simple. *Phys. Rev. Lett.* **1996**, *77* (18), 3865-3868.
460. Tao, J.; Perdew, J. P.; Staroverov, V. N.; Scuseria, G. E., Climbing the Density Functional Ladder: Nonempirical Meta-Generalized Gradient Approximation Designed for Molecules and Solids. *Phys. Rev. Lett.* **2003**, *91* (14), 146401.
461. Sun, J.; Ruzsinszky, A.; Perdew, J. P., Strongly Constrained and Appropriately Normed Semilocal Density Functional. *Phys. Rev. Lett.* **2015**, *115* (3), 036402.
462. Mardirossian, N.; Ruiz Pestana, L.; Womack, J. C.; Skylaris, C.-K.; Head-Gordon, T.; Head-Gordon, M., Use of the rVV10 Nonlocal Correlation Functional in the B97M-V Density Functional: Defining B97M-rV and Related Functionals. *J. Phys. Chem. Lett.* **2017**, *8* (1), 35-40.
463. Dombroski, J. P.; Taylor, S. W.; Gill, P. M. W., KWIK: Coulomb Energies in O(N) Work. *J. Phys. Chem.* **1996**, *100* (15), 6272-6276.
464. Adamson, R. D.; Dombroski, J. P.; Gill, P. M. W., Chemistry Without Coulomb Tails. *Chem. Phys. Lett.* **1996**, *254* (5), 329-336.
465. Gill, P. M. W.; Adamson, R. D., A Family of Attenuated Coulomb Operators. *Chem. Phys. Lett.* **1996**, *261* (1), 105-110.
466. Walker, M.; Harvey, A. J. A.; Sen, A.; Dessent, C. E. H., Performance of M06, M06-2X, and M06-HF Density Functionals for Conformationally Flexible Anionic Clusters: M06 Functionals Perform Better than B3LYP for a Model System with Dispersion and Ionic Hydrogen-Bonding Interactions. *J. Phys. Chem. A* **2013**, *117* (47), 12590-12600.
467. Perdew, J. P.; Ernzerhof, M.; Burke, K., Rationale for Mixing Exact Exchange with Density Functional Approximations. *J. Chem. Phys.* **1996**, *105* (22), 9982-9985.
468. Adamo, C.; Barone, V., Toward Reliable Density Functional Methods Without Adjustable Parameters: The PBE0 Model. *J. Chem. Phys.* **1999**, *110* (13), 6158-6170.

469. Yanai, T.; Tew, D. P.; Handy, N. C., A New Hybrid Exchange–correlation Functional Using the Coulomb-attenuating Method (CAM-B3LYP). *Chem. Phys. Lett.* **2004**, *393* (1), 51-57.
470. Vydrov, O. A.; Scuseria, G. E., Assessment of a Long-range Corrected Hybrid Functional. *J. Chem. Phys.* **2006**, *125* (23), 234109.
471. Chai, J.-D.; Head-Gordon, M., Systematic Optimization of Long-range Corrected Hybrid Density Functionals. *J. Chem. Phys.* **2008**, *128* (8), 084106.
472. Furche, F., Developing the Random Phase Approximation into A Practical Post-Kohn–Sham Correlation Model. *J. Chem. Phys.* **2008**, *129* (11), 114105.
473. Grimme, S., Semiempirical Hybrid Density Functional with Perturbative Second-order Correlation. *J. Chem. Phys.* **2006**, *124* (3), 034108.
474. Gill, P. M. W., Molecular Integrals Over Gaussian Basis Functions. *Adv. Quantum Chem.* **1994**, *25*, 141-205.
475. Boys, S. F., Electronic Wave Functions-I. A General Method of Calculation for the Stationary States of any Molecular System. *P. Roy. Soc. A - Math Phys.* **1950**, *200* (1063), 542-554.
476. Slater, J. C., Atomic Shielding Constants. *Phys. Rev.* **1930**, *36* (1), 57-64.
477. Cioslowski, J., *Many-Electron Densities and Reduced Density Matrices*. Springer US: 2012.
478. Dirac, P. A. M., Note on Exchange Phenomena in the Thomas Atom. *Math. Proc. Cambridge Philos. Soc.* **1930**, *26* (3), 376-385.
479. Schmider, H.; Edgecombe, K. E.; Smith, V. H.; Weyrich, W., One-particle Density Matrices Along the Molecular Bonds in Linear Molecules. *J. Chem. Phys.* **1992**, *96* (11), 8411-8419.
480. Gadre, S. R.; Kulkarni, S. A.; Pathak, R. K., Reduced First-order Density Matrices and "Exchange-only" Correlation Factors for Some Closed-shell Atomic Systems. *Phys. Rev. A* **1989**, *40* (8), 4224-4231.
481. Anderson, P. W., Localized Orbitals for Molecular Quantum Theory. I. The Hückel Theory. *Phys. Rev.* **1969**, *181* (1), 25-32.
482. Karasiev, V. V.; Jones, R. S.; Trickey, S. B.; Harris, F. E., Properties of Constraint-based Single-point Approximate Kinetic Energy Functionals. *Phys. Rev. B* **2009**, *80* (24), 245120.

483. Bader, R. F. W.; Streitwieser, A.; Neuhaus, A.; Laidig, K. E.; Speers, P., Electron Delocalization and the Fermi Hole. *J. Am. Chem. Soc.* **1996**, *118* (21), 4959-4965.
484. Bader, R. F. W.; Stephens, M. E., Spatial Localization of the Electronic Pair and Number Distributions in Molecules. *J. Am. Chem. Soc.* **1975**, *97* (26), 7391-7399.
485. Weyrich, W., Interpretation of Momentum Densities. *Acta Cryst. A* **1987**, *43* (a1), C320.
486. Hückel, E., Quantentheoretische Beiträge zum Benzolproblem. *Zeitschrift für Physik* **1931**, *70* (3), 204-286.
487. Mayer, I., Charge, Bond Order and Valence in the Ab Initio SCF Theory. *Chem. Phys. Lett.* **1983**, *97* (3), 270-274.
488. Wiberg, K. B., Application of the Pople-Santry-Segal CNDO Method to the Cyclopropylcarbinyl and Cyclobutyl Cation and to Bicyclobutane. *Tetrahedron* **1968**, *24* (3), 1083-1096.
489. Tretiak, S.; Mukamel, S., Density Matrix Analysis and Simulation of Electronic Excitations in Conjugated and Aggregated Molecules. *Chem. Rev.* **2002**, *102* (9), 3171-3212.
490. Head-Gordon, M.; Grana, A. M.; Maurice, D.; White, C. A., Analysis of Electronic Transitions as the Difference of Electron Attachment and Detachment Densities. *J. Phys. Chem.* **1995**, *99* (39), 14261-14270.
491. Plasser, F.; Wormit, M.; Dreuw, A., New Tools for the Systematic Analysis and Visualization of Electronic Excitations. I. Formalism. *J. Chem. Phys.* **2014**, *141* (2), 024106.
492. Cioslowski, J.; Mixon, S. T., Covalent Bond Orders in the Topological Theory of Atoms in Molecules. *J. Am. Chem. Soc.* **1991**, *113* (11), 4142-4145.
493. Fulton, R. L.; Mixon, S. T., Comparison of Covalent Bond Indexes and Sharing Indexes. *J. Phys. Chem.* **1993**, *97* (29), 7530-7534.
494. Bader, R. F. W.; Heard, G. L., The Mapping of the Conditional Pair Density Onto the Electron Density. *J. Chem. Phys.* **1999**, *111* (19), 8789-8798.
495. R. C. Bocchicchio, L. L., A. Torre, On the Definition of Bond Orders at Correlated Level. *Chem. Phys. Lett.* **2003**, *374*, 567-571.

496. Bultinck, P.; Cooper, D. L.; Ponec, R., Influence of Atoms-in-Molecules Methods on Shared-Electron Distribution Indices and Domain-Averaged Fermi Holes. *J. Phys. Chem. A* **2010**, *114* (33), 8754-8763.
497. Alcoba, D. R.; Lain, L.; Torre, A.; Bochicchio, R. C., A Study of the Partitioning of the First-Order Reduced Density Matrix According to the Theory of Atoms in Molecules. *J. Chem. Phys.* **2005**, *123* (14), 144113.
498. Vanfleteren, D.; Van Neck, D.; Bultinck, P.; Ayers, P. W.; Waroquier, M., Stockholder Projector Analysis: A Hilbert-Space Partitioning of The Molecular One-Electron Density Matrix with Orthogonal Projectors. *J. Chem. Phys.* **2012**, *136* (1), 014107.
499. Vanfleteren, D.; Van Neck, D.; Bultinck, P.; Ayers, P. W.; Waroquier, M., Partitioning of the Molecular Density Matrix Over Atoms and Bonds. *J. Chem. Phys.* **2010**, *132* (16), 164111.
500. Savin, A.; Nesper, R.; Wengert, S.; Fässler, T. F., ELF: The Electron Localization Function. *Angew. Chem. Int. Ed.* **1997**, *36* (17), 1808-1832.
501. Savin, A.; Becke, A. D.; Flad, J.; Nesper, R.; Preuss, H.; von Schnering, H. G., A New Look at Electron Localization. *Angew. Chem. Int. Ed.* **1991**, *30* (4), 409-412.
502. Feixas, F.; Matito, E.; Duran, M.; Sola, M.; Silvi, B., Electron Localization Function at the Correlated Level: A Natural Orbital Formulation. *J. Chem. Theory Comput.* **2010**, *6*, 2736-2742.
503. Fradera, X.; Austen, M. A.; Bader, R. F. W., The Lewis Model and Beyond. *J. Phys. Chem. A* **1999**, *103* (2), 304-314.
504. Johnson, E. R.; Keinan, S.; Mori-Sánchez, P.; Contreras-García, J.; Cohen, A. J.; Yang, W., Revealing Noncovalent Interactions. *J. Am. Chem. Soc.* **2010**, *132* (18), 6498-6506.
505. Bader, R. F. W.; Gatti, C., A Green's Function for the Density. *Chem. Phys. Lett.* **1998**, *287* (3-4), 233-238.
506. Szczepanik, D. W.; Żak, E.; Dyduch, K.; Mrozek, J., Electron Delocalization Index Based on Bond Order Orbitals. *Chem. Phys. Lett.* **2014**, *593*, 154-159.
507. Kohout, M., A Measure of Electron Localizability. *Int. J. Quantum Chem* **2004**, *97* (1), 651-658.

508. Matito, E.; Sola, M.; Salvador, P.; Duran, M., Electron Sharing Indexes at the Correlated Level. Application to Aromaticity Calculations. *Faraday Discuss.* **2007**, *135* (0), 325-345.
509. Schmider, H., A Parity Function for Studying the Molecular Electronic Structure. *J. Chem. Phys.* **1996**, *105* (24), 11134-11142.
510. Schmider, H. L.; Becke, A. D., Chemical Content of the Kinetic Energy Density. *J. Mol. Struc-THEOCHEM* **2000**, *527* (1-3), 51-61.
511. Schmider, H. L.; Becke, A. D., Two Functions of the Density Matrix and Their Relation to the Chemical Bond. *J. Chem. Phys.* **2002**, *116* (8), 3184-3193.
512. Becke, A. D., A Real-space Model of Nondynamical Correlation. *J. Chem. Phys.* **2003**, *119* (6), 2972-2977.
513. Proynov, E.; Liu, F.; Kong, J., Analyzing Effects of Strong Correlation Within Kohn-Sham Density Functional Theory. *Phys. Rev. A.* **2013**, *88* (3), 032510.
514. Proynov, E. I., On the Maximum Number of 'odd' Electrons in a Molecule. *J. Mol. Struct.: THEOCHEM* **2006**, *762* (1), 159-163.
515. Takatsuka, K.; Fueno, T.; Yamaguchi, K., Distribution of Odd Electrons in Ground-State Molecules. *Theor. Chim. Acta (Berl.)* **1978**, *48*, 175-183.
516. Meister, J.; Schwarz, W. H. E., Principal Components of Ionicity. *J. Phys. Chem.* **1994**, *98* (33), 8245-8252.
517. Wiberg, K. B.; Rablen, P. R., Comparison of Atomic Charges Derived via Different Procedures. *J. Comput. Chem.* **1993**, *14* (12), 1504-1518.
518. Hirshfeld, F. L., Bonded-atom Fragments for Describing Molecular Charge Densities. *Theor. Chim. Acta.* **1977**, *44* (2), 129-138.
519. Saha, S.; Roy, R. K.; Ayers, P. W., Are the Hirshfeld and Mulliken Population Analysis Schemes Consistent with Chemical Intuition? *Int. J. Quantum Chem* **2009**, *109* (9), 1790-1806.
520. Lu, T.; Chen, F., Atomic Dipole Moment Corrected Hirshfeld Population Method. *J. Theor. Comput. Chem.* **2012**, *11* (01), 163-183.
521. Bultinck, P.; Alsenoy, C. V.; Ayers, P. W.; Carbó-Dorca, R., Critical Analysis and Extension of the Hirshfeld Atoms in Molecules. *J. Chem. Phys.* **2007**, *126* (14), 144111.

522. Vanpoucke, D. E. P.; Bultinck, P.; Van Driessche, I., Extending Hirshfeld-I to Bulk and Periodic Materials. *J. Comput. Chem.* **2013**, *34* (5), 405-417.
523. Fonseca Guerra, C.; Handgraaf, J.-W.; Baerends, E. J.; Bickelhaupt, F. M., Voronoi Deformation Density (VDD) Charges: Assessment of the Mulliken, Bader, Hirshfeld, Weinhold, and VDD Methods for Charge Analysis. *J. Comput. Chem.* **2004**, *25* (2), 189-210.
524. Gatti, C.; Macchi, P., *Modern Charge-Density Analysis*. Springer: 2012.
525. Becke, A. D., A Multicenter Numerical Integration Scheme for Polyatomic Molecules. *J. Chem. Phys.* **1988**, *88* (4), 2547-2553.
526. Mei, Y.; Simmonett, A. C.; Pickard, F. C.; DiStasio, R. A.; Brooks, B. R.; Shao, Y., Numerical Study on the Partitioning of the Molecular Polarizability into Fluctuating Charge and Induced Atomic Dipole Contributions. *J. Phys. Chem. A* **2015**, *119* (22), 5865-5882.
527. Scrocco, E.; Tomasi, J. In *The Electrostatic Molecular Potential as a Tool for the Interpretation of Molecular Properties*, Springer Berlin Heidelberg: 1973; pp 95-170.
528. Scrocco, E.; Tomasi, J., Electronic Molecular Structure, Reactivity and Intermolecular Forces: An Euristic Interpretation by Means of Electrostatic Molecular Potentials. In *Adv. Quantum Chem.*, Löwdin, P.-O., Ed. Academic Press: 1978; Vol. 11, pp 115-193.
529. Stewart, R. F., On the Mapping of Electrostatic Properties from Bragg Diffraction Data. *Chem. Phys. Lett.* **1979**, *65* (2), 335-342.
530. Politzer, P.; Truhlar, D. G., *Chemical Applications of Atomic and Molecular Electrostatic Potentials: Reactivity, Structure, Scattering, and Energetics of Organic, Inorganic, and Biological Systems*. Springer US: 2013.
531. Murray, J. S.; Politzer, P., The Electrostatic Potential: An Overview. *Wiley Interdiscip. Rev. Comput. Mol. Sci.* **2011**, *1* (2), 153-163.
532. Politzer, P.; Laurence, P. R.; Jayasuriya, K., Molecular Electrostatic Potentials: An Effective Tool for The Elucidation of Biochemical Phenomena. *Environ. Health Perspect.* **1985**, *61*, 191-202.
533. Naray-Szabo, G.; Ferenczy, G. G., Molecular Electrostatics. *Chem. Rev.* **1995**, *95* (4), 829-847.
534. Agudelo, W. A.; Patarroyo, M. E., Quantum Chemical Analysis of MHC-peptide Interactions for Vaccine Design. *Mini Rev Med Chem* **2010**, *10* (8), 746-758.

535. Halldin Stenlid, J.; Johansson, A. J.; Brinck, T., The Local Electron Attachment Energy and the Electrostatic Potential as Descriptors of Surface-Adsorbate Interactions. *Phys. Chem. Chem. Phys.* **2019**, *21* (31), 17001-17009.
536. Li, G.; Stenlid, J. H.; Ahlquist, M. S. G.; Brinck, T., Utilizing the Surface Electrostatic Potential to Predict the Interactions of Pt and Ni Nanoparticles with Lewis Acids and Bases- σ -Lumps and σ -holes Govern the Catalytic Activities. *J. Phys. Chem. C* **2020**, *124* (27), 14696-14705.
537. Murray, J. S.; Politzer, P., Statistical Analysis of the Molecular Surface Electrostatic Potential: An Approach to Describing Noncovalent Interactions in Condensed Phases. *J. Mol. Stru-THEOCHEM* **1998**, *425* (1), 107-114.
538. Politzer, P.; Murray, J. S., Computational Prediction of Condensed Phase Properties from Statistical Characterization of Molecular Surface Electrostatic Potentials. *Fluid Phase Equilib.* **2001**, *185* (1), 129-137.
539. Sen, K. D.; Politzer, P., Characteristic Features of the Electrostatic Potentials of Singly Negative Monoatomic Ions. *J. Chem. Phys.* **1989**, *90* (8), 4370-4372.
540. Jeffrey, G. A.; Piniella, J. F., *The Application of Charge Density Research to Chemistry and Drug Design*. Springer US: 2012.
541. Pendas, A.; Shaik, S.; Novoa, J. J.; Gavezzotti, A.; Popelier, P.; Contreras-Garcia, J.; Arunan, E.; Gobetto, R.; Bacchi, A.; Politzer, P., *Intermolecular Interactions in Crystals: Fundamentals of Crystal Engineering*. Royal Society of Chemistry: 2017.
542. Coppens, P., Experimental Electron Densities and Chemical Bonding. *Angew. Chem. Int. Ed.* **1977**, *16* (1), 32-40.
543. Feil, D., Electron Density Distribution in Molecular Crystals: Exploring the Boundary Between X-Ray Diffraction and Quantum Chemistry. *Chemica Scripta* **1986**, *26* (3), 395 - 408
544. Peter Politzer, J. S. M., Molecular Electrostatic Potentials and Chemical Reactivity. In *Rev. Comput. Chem.*, Kenny B. Lipkowitz, D. B. B., Ed. VCH, New York: 1991; pp 273-312.
545. Politzer, P.; Riley, K. E.; Bulat, F. A.; Murray, J. S., Perspectives on Halogen Bonding and Other σ -hole Interactions: Lex Parsimoniae (Occam's Razor). *Comp. Theor. Chem.* **2012**, *998*, 2-8.
546. Clark, T.; Murray, J. S.; Politzer, P., Role of Polarization in Halogen Bonds. *Aust. J. Chem.* **2014**, *67* (3), 451-456.

547. Politzer, P.; Murray, J. S.; Clark, T., σ -hole Bonding: A Physical Interpretation. In *Halogen Bonding I: Impact on Materials Chemistry and Life Sciences*, Metrangolo, P.; Resnati, G., Eds. Springer International Publishing: Cham, 2015; pp 19-42.
548. Politzer, P.; Murray, J. S.; Clark, T., Mathematical Modeling and Physical Reality in Noncovalent Interactions. *J. Mol. Model.* **2015**, *21* (3), 52.
549. Murray, J. S.; Shields, Z. P.-I.; Seybold, P. G.; Politzer, P., Intuitive and Counterintuitive Non-covalent Interactions of Aromatic π Regions with the Hydrogen and the Nitrogen of HCN. *J. Comput. Sci.* **2015**, *10*, 209-216.
550. Parr, R. G.; Pearson, R. G., Absolute Hardness: Companion Parameter to Absolute Electronegativity. *J. Am. Chem. Soc.* **1983**, *105* (26), 7512-7516.

VITA

| | |
|--------------------------|----------------------------------------------------------------------------------------------------------------------------------------------------------------------------------------------------------------------------------------------------------------------------------------------------------------------------------------------------------------------------------------------------------------------------------------------|
| Personal Background | Arshad Mehmood Bahawalpur, 63100, Punjab, Pakistan |
| Education | M.Sc. Chemistry The Islamia University of Bahawalpur, Pakistan, 2009 M.Phil. Physical Chemistry The Islamia University of Bahawalpur, Pakistan, 2011 |
| Experience | Research Assistantship Texas Christian University, Fort Worth, 2016-2020 Teaching Assistantship Texas Christian University, Fort Worth, 2015-2016 Lecturership GC University Lahore, Pakistan, 2012-2015 |
| Professional Memberships | American Chemical Society, American Physical Society, American Crystallographic Association |
| Awards and Honors | Best Oral Presentation Award 51 st ACS Meeting-in-miniature, April 21, 2018, Dallas, TX. Wiley Best Poster Award 27 th Austin Symposium on Molecular Structure and Dynamics at Dallas, March 3-5, 2018, Dallas, TX. Chaired the General Interest Session 66 th Annual Meeting of American Crystallographic Association, July 22-26, 2016, Denver, CO. |
| Selected Publications | Mehmood, A.; Janesko, B. G., <i>J. Solution Chem</i> 2020, 49, 614-628. Mehmood, A.; Jones, S. I.; Tao, P.; Janesko, B. G., <i>J. Chem. Inf. Model.</i> 2018, 58 (9), 1836-1846. Mehmood, A.; Janesko, B. G., <i>J. Mass Spectrom.</i> 2018, 53 (5), 432-434. Mehmood, A.; Janesko, B. G., <i>Angew. Chem. Int. Ed.</i> 2017, 56 (24), 6878-6881. Mehmood, A.; Janesko, B. G., <i>J. Quantum Chem</i> 2016, 116 (23), 1783-1795. |

ABSTRACT

A COMPUTATIONAL TOOLKIT TO UNDERSTAND ORBITAL OVERLAP AND CHEMICAL REACTIVITY

by Arshad Mehmood, Ph.D., 2020
Department of Chemistry & Biochemistry
Texas Christian University

Dissertation Advisor: Benjamin G. Janesko, Associate Professor of Chemistry

Computational chemistry has become a standard tool for investigations in all branches of chemistry. Visualizing and interpreting electronic structure simulations, and predicting the chemical reactivity requires interpretative tools. However, in several cases, the widely used tools such as electrostatic potential (ESP) and partial atomic charges (Q) provide inconclusive information. Similarly, use of frontier molecular orbitals as interpretive tools is limited to visualize one orbital at a time. A comprehensive understanding of reactivity requires information about the nature of all occupied orbitals because the majority of chemical reactions are controlled by the synergy of electrostatics and orbital overlap effects.

Orbital overlap distance, $D(\vec{r})$, complements the ESP maps by quantifying the size of “test orbital” that maximizes its overlaps with a system’s occupied orbitals at a point \vec{r} . Compact orbitals tend to have smaller values of $D(\vec{r})$, as compared to the diffuse orbitals. We applied the combination of ESP and $D(\vec{r})$ surface maps to rationalize the binding of ligands and metal ions to proteins and extended their applications to medicinal chemistry by quantifying the chemistry of promiscuous binders and predicting centromere-associated

protein E inhibitors. We used this combination to distinguish the relative nature of carbon atoms at the defect sites of graphene sheet and to visualize σ -holes on molecules of group IV to VII elements and transition metal nanoclusters. Our studies established that quantitative analysis of molecular ESP and $D(\vec{r})$ surfaces can predict binding energies of σ -holes interactions, acid–base binding affinities, stability constants, and interactions of metal ions to graphene defects. We used this quantitative analysis to predict values of empirical solvent softness scales, develop a solvent versatility scale, and model the Marcus μ -values of ionic liquids.

Our second tool, atomic average overlap distance, D_A , distinguishes the compact, chemically stable atoms from chemically soft and unstable atoms. We used Q_A and D_A to capture trends in aromaticity, nucleophilicity, allotrope stability, and substituent effects.

We used the mother tool, $\text{EDR}(\vec{r}; d)$, to analyze the stretched and compressed bonds. $\text{EDR}(\vec{r}; d)$ captures aspects of fractional occupancy and left-right correlation in stretched covalent bonds.

This dissertation introduces the diverse applications of this toolkit to the major fields of chemical sciences.